

Towards Stable Cobalt-based Fischer-Tropsch Catalysts

Citation for published version (APA):

van Koppen, L. M. (2023). *Towards Stable Cobalt-based Fischer-Tropsch Catalysts*. [Phd Thesis 1 (Research TU/e / Graduation TU/e), Chemical Engineering and Chemistry]. Eindhoven University of Technology.

Document status and date:

Published: 13/09/2023

Document Version:

Publisher's PDF, also known as Version of Record (includes final page, issue and volume numbers)

Please check the document version of this publication:

- A submitted manuscript is the version of the article upon submission and before peer-review. There can be important differences between the submitted version and the official published version of record. People interested in the research are advised to contact the author for the final version of the publication, or visit the DOI to the publisher's website.
- The final author version and the galley proof are versions of the publication after peer review.
- The final published version features the final layout of the paper including the volume, issue and page numbers.

[Link to publication](#)

General rights

Copyright and moral rights for the publications made accessible in the public portal are retained by the authors and/or other copyright owners and it is a condition of accessing publications that users recognise and abide by the legal requirements associated with these rights.

- Users may download and print one copy of any publication from the public portal for the purpose of private study or research.
- You may not further distribute the material or use it for any profit-making activity or commercial gain
- You may freely distribute the URL identifying the publication in the public portal.

If the publication is distributed under the terms of Article 25fa of the Dutch Copyright Act, indicated by the "Taverne" license above, please follow below link for the End User Agreement:

www.tue.nl/taverne

Take down policy

If you believe that this document breaches copyright please contact us at:

openaccess@tue.nl

providing details and we will investigate your claim.

Towards Stable Cobalt-based Fischer-Tropsch Catalysts

PROEFSCHRIFT

ter verkrijging van de graad van doctor aan de Technische Universiteit Eindhoven, op gezag
van de rector magnificus prof.dr. S.K. Lenaerts,
voor een commissie aangewezen door het College voor Promoties, in het openbaar te
verdedigen op woensdag 13 september 2023 om 13:30 uur

door

Lukas Martin van Koppen

geboren te Rotterdam

Dit proefschrift is goedgekeurd door de promotoren en de samenstelling van de promotiecommissie is als volgt:

Voorzitter:	prof.dr.ir. R. Tuinier
1 ^e promotor:	prof.dr.ir. E.J.M. Hensen
Co-promotoren:	dr. A.I. Dugulan (Technische Universiteit Delft) dr. G.L. Bezemer (Shell Global Solutions International B.V.)
Leden:	prof.dr. A. Urakawa (Technische Universiteit Delft) prof.dr.-ing. M. Claeys (University of Cape Town) prof.dr.ir. J. van der Schaaf prof dr.ir. M. van Sint Annaland

Het onderzoek of ontwerp dat in dit proefschrift wordt beschreven is uitgevoerd in overeenstemming met de TU/e Gedragscode Wetenschapsbeoefening.

To my parents

Luke van Koppen

Towards Stable Cobalt-based Fischer-Tropsch Catalysts

A catalogue record is available from the Eindhoven University of Technology Library

ISBN: 978-90-386-5816-2

Copyright © 2023 by Lukas M. van Koppen



The work described in this thesis has been carried out at the Laboratory of Inorganic Materials & Catalysis at the Eindhoven University of Technology, and at the Laboratory of the Reactor Institute Delft at the Delft University of Technology. We acknowledge the financial support from Shell Global Solutions International B.V.

Cover design: Luke van Koppen

Printed by: Gildeprint

Table of contents

Content	Page
Chapter 1: Introduction and scope	1
Chapter 2: Sintering and carbidization under simulated high conversion on a cobalt-based Fischer-Tropsch catalyst; manganese oxide as a structural promotor	17
Appendix A	47
Chapter 3: Manganese as a structural promoter in silica-supported cobalt Fischer-Tropsch catalysts under simulated high conversion conditions	53
Appendix B	77
Chapter 4: Elucidating deactivation of titania-supported cobalt Fischer-Tropsch catalysts under simulated high conversion conditions	81
Appendix C	111
Chapter 5: Tuning stability of titania-supported Fischer-Tropsch catalysts: impact of surface area and noble metal promotion	119
Appendix D	151
Chapter 6: Summary and Outlook	161
Acknowledgements	165
List of publications	169
Curriculum Vitae	171

Chapter 1

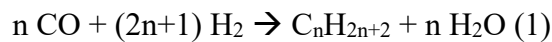
Introduction and scope

1.1 Introduction

In a landscape of growing inequality and inequity, humanity faces one of our greatest challenges yet, climate disaster. Since the onset of the industrial revolution, global temperature has been rising [1]. This can be directly correlated to the emission of anthropogenic greenhouse gasses, especially CO₂ [2]. The Glasgow Pact recently reevaluated the Paris Climate agreement and found that even under those pledges a dramatic global temperature increase of 2.7 – 3.7 °C could be reached, which led to further refining the pledges to reduce carbon dioxide emissions to net zero by midcentury [3]. Much of these global emissions stem from power generation and consumption [4]. Power generation by burning of fossil resources can in principle be relatively easily replaced by renewable energy sources like wind farms and solar panels. In 2021, already 29% of all global power generation was through renewables [5]. However, whilst renewable power generation can adequately replace gas- and coal-fired power plants, other chemicals such as transportation fuels as well as many bulk and fine chemicals still require fossil sources of carbon as a feedstock. A prime example are transportation fuels such as gasoline, kerosene and diesel. While a significant part of the mobility needs can be covered by renewable energy through the use of electric vehicles using batteries, there will remain a strong need for liquid fuels for heavy duty transport including aviation. Despite recent development in for instance synthesizing synthetic kerosene [6], processes for synthetic hydrocarbon fuels are far from commercial practice. Besides their high current cost, there is also a mismatch with the very large global demand for liquid hydrocarbon fuels. This also holds for most of the chemicals produced by the chemical industry. The discrepancy between the need for many chemical products and swift climate action to avoid disaster emphasizes the importance of alternative liquid hydrocarbons production. Key to the transition to a more sustainable economy are technologies that can convert various carbon-containing feedstocks to liquid products, i.e. XTL (anything-to-liquids) processes. [7]

1.2 Fischer-Tropsch synthesis

One of the major XTL technologies is the Fischer-Tropsch synthesis (FTS) process. This is a well-studied industrial process with a long history. The first patent filed by Franz Fischer and Hans Tropsch will celebrate its 100th birthday in 2025 [8]. This technology was quickly adopted in Germany to produce synthetic fuels and reduce their dependence on crude oil imports. The FTS process refers to the conversion of synthesis gas (often abbreviated as syngas), a mixture of carbon monoxide and hydrogen, to longer chain hydrocarbons. A simplified representation is given by Equation 1, showing the formation of alkanes from the synthesis gas feed [9].



Many products formed in the FTS reaction can also be directly obtained through oil refining. Throughout its history, the Fischer-Tropsch process has seen appeal when oil prices were high. The main advantages of FTS are the high purity of the product as the syngas feed can be easily cleaned, and the tunability of the reaction and its products. The Fischer-Tropsch reaction is a polymerization reaction of CH_x monomers that form *in situ*. The value of n in Equation 1 determines the chain length of the hydrocarbon product. For instance, if diesel were desired, one would require n to be in the range of 12-18. However, as with most polymerization reactions, a wide distribution of products with different carbon numbers is obtained. As such, products like (undesired) methane ($n = 1$), and lower-value naphtha ($n = 4-11$) are obtained. The distribution of hydrocarbon products obtained in the Fischer-Tropsch reaction can be reasonably described by the Anderson-Schulz-Flory (ASF) distribution [10]–[12]. The main parameter of the ASF is the chain-growth probability factor (α), which is defined by Equation 2 [13] where R_p is the rate of propagation and R_t is the rate of termination.

$$\alpha = \frac{R_p}{R_p + R_t} \quad (2)$$

As the product distribution directly follows from the reaction kinetics, it can be tuned by changing the experimental conditions. This versatility allows the reaction to be operated to produce mainly heavy, light or intermediate carbon products. Whilst current commercial FTS operations use natural gas and coal as carbonaceous feedstock, synthesis gas can alternatively be obtained from renewable sources. For instance, gasification of biomass can also be used to produce synthesis gas [14], while the reverse water-gas shift (rWGS) reaction can convert CO_2 (e.g., obtained from direct air capture) to CO. This can be done by the thermocatalytic rWGS reaction using green hydrogen [15]–[17] or

direct electrochemical CO₂ reduction using renewable electricity [18]. Such sustainable methods of generating syngas would allow for the production of renewable hydrocarbons through the Fischer-Tropsch synthesis.

1.3 Catalysis

For the successful commercial exploitation of FTS, a catalyst is required. This is not uncommon in the chemical industry with nearly 90% of all chemical processes utilizing a catalyst during one or more of the reaction steps [19]. Well-known examples of catalytic processes are the Haber-Bosch process to convert nitrogen to ammonia, which is essential for the production of artificial fertilizer, and the three-way catalyst installed in the exhaust system of gasoline cars to reduce noxious emissions. The primary function of a catalyst is to accelerate the chemical reaction. The catalyst does this by forming bonds with the reacting molecules, allowing them to react more easily i.e., with a lower activation energy allowing for instance operation at milder conditions. After the product is formed in this manner, the bond with the catalyst is broken and it returns to its original state, ready for another cycle. This catalytic cycle is schematically shown in Figure 1. Whilst the overall reaction thermodynamics remain unchanged, the catalyst opens a new reaction pathway with a lower energy barrier than the uncatalyzed reaction, resulting in improved reaction kinetics. Heterogeneous catalysts are most widely used in the chemical industry, because they are usually solids that can be easily separated from the gaseous and liquid reactants, which is a challenge in homogeneous catalysis [20]. Typical heterogeneous catalysts contain an active phase, usually in the form of metal nanoparticles, which is stabilized on a carrier material that is often inert to the reaction. The role of the carrier or support material is to anchor and disperse the active metal species, providing mechanical and thermal stability during the catalytic reaction [21]. Typical support materials are porous metal oxides such as SiO₂, Al₂O₃ and TiO₂ [22], [23]. Transition metals often form the active phase with a preference for iron, cobalt, nickel and copper given their abundance as compared to precious group metals such as platinum, palladium and rhodium.

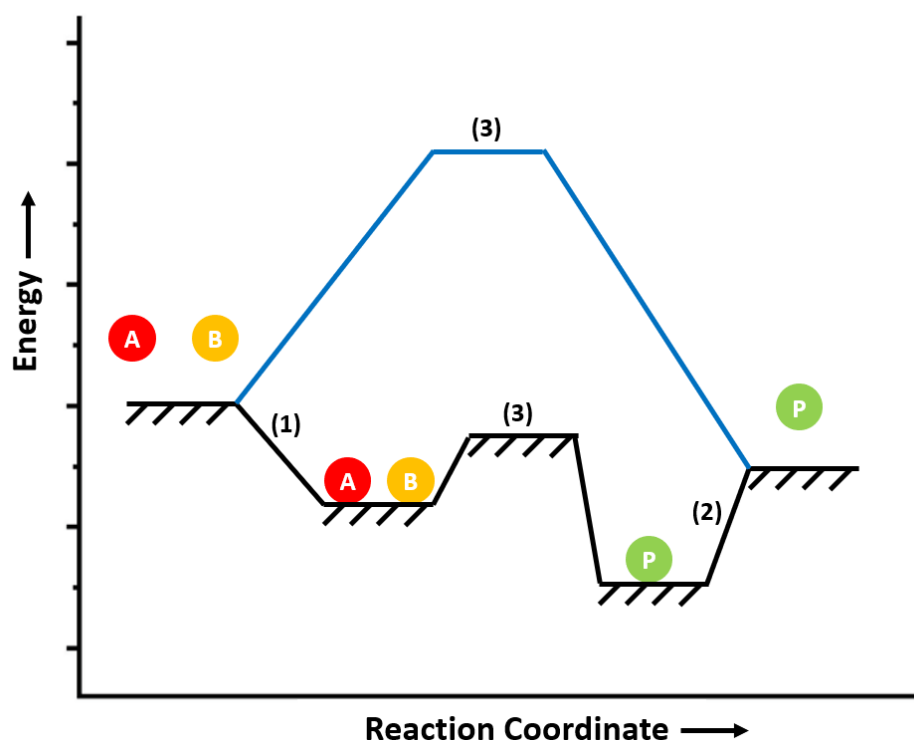


Figure 1: Cartoon representation of the energy diagram of a catalyzed reaction (black) and a non-catalyzed reaction (blue). The elementary reaction steps include (1) reactant adsorption, (2) product desorption and (3) reaction.

The preference for transition metals as the active phase in active catalysts can be understood by considering Sabatier's principle, which dictates that the bond between the active metal and the reactant/product needs to be sufficiently strong to adsorb and activate the reactant but not too strong as this would prevent desorption of the product and thus poison the active sites. This optimum in terms of bond strength leads to the typically observed volcano plots, where a maximum in catalytic performance is observed for intermediate bond strength between the metal and the desired reactants/products as shown schematically in Figure 2. The bond strength between metals and atoms and molecules depends on their position in the periodic table. This means that transition metals close to one another in the periodic table will show comparable performance in a particular catalytic reaction. For example, for Fischer-Tropsch synthesis both cobalt [24] and iron [25] are industrially used, while ruthenium has been shown to be an excellent FTS catalyst [26], though being too expensive to be of practical importance.

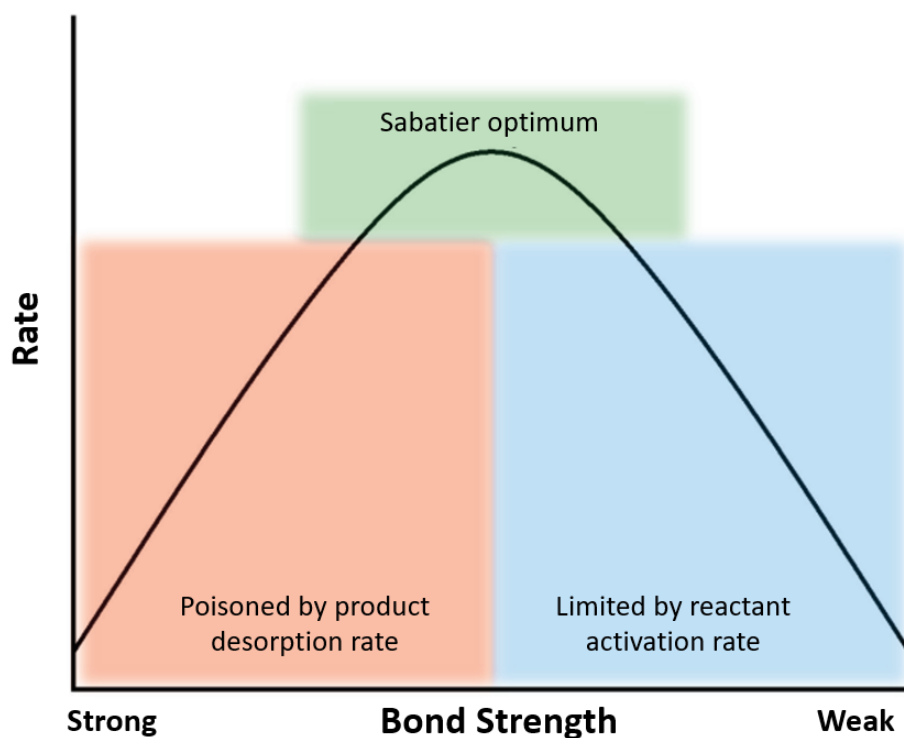


Figure 2: Schematic representation of the volcano plot of the qualitative Sabatier principle (adapted from [27]).

1.4 Fischer-Tropsch catalysts

Both cobalt and iron are used in industrial catalysts for the FTS reaction. A drawback of iron-based catalysts is their water-gas shift (WGS) activity [12], while the much lower price of iron compared to cobalt is a clear benefit as well as their better tolerance to contaminants [28]. The intrinsic WGS activity of iron-based FTS catalysts can be a benefit when syngas derived from coal with a relatively low H_2/CO ratio needs to be upgraded. The use of cobalt-based catalysts typically results in higher conversion rates with a higher selectivity towards long-chain hydrocarbons [24]. The low WGS activity makes cobalt-based catalysts preferred for converting syngas from natural gas. Besides studies focusing on the activity of cobalt-based catalysts [29]–[33], there is also a clear need to better understand their deactivation under relevant industrial conditions [29]–[34]. The aim of such studies is to understand structure-performance relations, not only aimed at improving the catalytic activity but also to improve the stability, which is of great practical importance.

1.4.1 Particle size effect

The impact of the particle size of the active metal phase is important for all heterogenous catalytic processes. As the catalytic reactions take place on the surface of metallic particles, the rate can in a

first approximation be increased by reducing the particle size. This increases the dispersion which is the fraction of metal atoms in a particle at the surface. As such, it would seem advantageous to use atomically dispersed metal atoms to achieve the highest possible activity. Although the field of so-called single-atom catalysis is burgeoning [35], many reactions require a particular ensemble of surface atoms. For Fischer-Tropsch catalysis, Bezemer et al. [36] found a strong particle size effect when studying cobalt-based catalysts with particle sizes in the range of 2.6-27 nm. The catalytic activity per surface atom (turnover frequency, TOF) was found to increase when the particle size increased from 2.6 to 6 nm. A further increase of the particle size to 27 nm did not change the TOF. This implies a strong preference for 6 nm cobalt particles for the FTS reaction, as it represents the highest cobalt-weight based activity. Moreover, it was found that the selectivity towards long-chain hydrocarbons decreased when the cobalt particles became smaller than 6 nm. These dependencies can be explained by the concept of structure-sensitive reactions [37]–[39], implying that the catalytic activity is not proportional to the amount of available metal surface area. This demonstrates that not all surface atoms are equal in catalysis as already earlier predicted by Taylor. Based on quantum-chemical studies of surface reactivity, it has now been firmly established that particular elementary reaction steps require different optimum surface atom ensembles for optimum performance [40]. Relevant to the FTS reaction, step-edge sites are preferred for low-barrier CO dissociation. Similar to N₂ dissociation relevant to Haber-Bosch ammonia synthesis, such step-edge sites are stabilized better on larger particles. In subsequent work, Den Breejen et al. [41] found that cobalt particles smaller than 6 nm had a low coverage by CH_x monomers during the FTS reaction and a higher coverage of strongly bonded CO. This is consistent with the insight that small particles lack sites for CO dissociation, resulting in a lower TOF. This goes together with a higher methane selectivity. As such, it is important to control the size of cobalt nanoparticles for successful FTS exploitation.

1.4.2 Cobalt deactivation

Given its importance to commercial FTS, deactivation has been thoroughly studied, identifying various mechanisms [32], [42]. The main pathways of cobalt catalyst deactivation are (i) poisoning, (ii) carbon effects, (iii) cobalt sintering, (iv) cobalt oxidation and (v) strong metal-support interactions (SMSI). The active cobalt phase can be poisoned by sulfur-containing compounds, which are typically present when synthesis gas is obtained from coal or biomass. It has been found that one sulfur atom can poison up to two metallic cobalt sites [43]. Also, nitrogen-containing compounds [44] and alkali metals [45], [46] can poison the active cobalt sites. This explains why cleaning of the syngas is important to successful FTS. Different from this deactivation pathway, the other ones cannot

be countered by syngas pretreatment, as they are the result of the formed products under industrial conditions. Carbon effects not only refers to the deposition of heavy wax products with high carbon numbers on the active sites, but also to the transformation of the metallic cobalt particles to cobalt carbides through the interaction of cobalt with carbon [47]. Sintering is a direct result of the high operating temperatures of FTS and the exothermic nature of the reaction, at these elevated temperatures cobalt becomes highly mobile and will seek to agglomerate to larger particles [48], [49]. Ostwald ripening involving mobile atomic cobalt species [50], [51] and particle coalescence [51] where entire particles are mobile [52], have been suggested as sintering mechanisms. Oxidation of the active metallic cobalt can occur due to the reaction of metallic cobalt with water, especially at high CO conversion, which will increase the partial pressure of steam. It has been observed that increasing steam to hydrogen ratios will result in cobalt oxidation [29], [53], [54]. Typical cobalt particle sizes used in FTS catalysts are large enough to render bulk oxidation thermodynamically unfavorable [55]. SMSI refers to strong interactions of metals with the metal oxide support material that can lead to surface or even bulk metal-support compounds (MSC). This has been most notably observed for reducible oxide supports such as TiO_2 [56] but MSC can also be formed with irreducible oxides like SiO_2 [56], [57] and Al_2O_3 [58]–[60].

1.4.3 Promoters

Promoters are typically added to catalysts in small amounts as compared to the active metal and the support material. They are added to improve the performance in terms of activity, selectivity or stability. Promoters can be classified as either structural or electronic [61]. Structural promoters typically improve the dispersion of the active phase, thus increasing the number of active sites, increase the reducibility, or make the active metal less prone to sintering. Electronic promoters assist the reaction by withdrawing or donating electrons from the metal, thus changing the intrinsic reactivity of the active sites. The main promoters of interest for FTS are noble metal promoters like rhenium or platinum [23], [62]–[65], which are structural promoters as they assist the reducibility of cobalt. Manganese has been extensively studied as a promoter for cobalt and it appears to function both as a structural and an electronic promoter [66]–[70].

1.5 Mössbauer Spectroscopy

Characterization of the active phase in catalysts is of utmost importance to formulate structure-performance relations, which can guide the design and synthesis of improved catalysts. The most valuable characterization is done under close to practical conditions, although this can also be very challenging given the often high temperature and pressure used in industrial chemical processes. This also applies to cobalt FTS catalysts, which are nowadays often studied under close to practical conditions. Synchrotron-based characterization techniques can be very valuable for in situ/operando studies as the high-energy X-rays can easily penetrate reactors [65], [71]–[73]. Mössbauer spectroscopy, which is more easily accessible than synchrotron techniques, is based on nuclear resonance, where a γ -ray produced from an energy transition in an atom will excite the same transition in another atom. Nuclear resonance is only possible if the γ -ray does not lose any energy upon emission and absorption, as otherwise it would not carry enough energy to excite the same transition in the second atom. These nuclear events without energy loss, are referred to as recoilless, and they can be measured because in the solid lattice both recoiling and non-recoiling events occur in a quantum superposition with certain probabilities. This effect was first explained and measured by Rudolf L. Mössbauer [74] and is accordingly referred to as the Mössbauer effect. In order to measure Mössbauer spectroscopy, specific isotopes are required that decay through an excited state that exhibits the Mössbauer effect, preferably with a convenient half-life. Furthermore, since the probability for a recoilless event is directly proportional to the energy of the γ -radiation, low energy transitions are desired. Of the Mössbauer active elements ^{57}Fe is by far the most used and accessible [75], [76], since the relevant $^{57\text{m}}\text{Fe}$ to ^{57}Fe transition emits a γ -ray of only 14.4 keV, and $^{57\text{m}}\text{Fe}$ is formed during the decay of the parent isotope, ^{57}Co , which has a half-life of 270 days.

1.5.1 Hyperfine Interactions

Nuclear resonance can only occur if the absorbing and emitting nucleus are experiencing the same environment, because the nucleus is coupled to its surroundings by hyperfine interactions. For example, no resonance would be observed if the source would be metallic iron, and the absorber iron oxide. For this reason, the energy of the source needs to be varied to measure a wider spectrum, and this is done with a relativistic doppler shift by moving the emitter towards and away from the absorber at a constant acceleration [77]. Doing so allows the analysis of a full Mössbauer spectrum, which as a result of its hyperfine interactions can provide key information about the structure, valence and coordination of the subject material. The three relevant hyperfine interactions are (i) isomer shift, (ii) electric quadrupole splitting, and (iii) magnetic hyperfine field, which are exemplified in Figure 3.

The isomer shift is a result of the Coulomb interactions between the positively charged protons in the nucleus and the negatively charged electrons and represents the difference in spherical electron densities at the nuclear sites in the emitting and absorbing atoms. Because the electron density affects the relevant Mössbauer energy transition, a difference in electron densities between the emitting and absorbing atoms results in a shift in the energy spectrum. Due to its direct correlation to the electron density, this isomer shift can be used to identify the valence and thus the oxidation state of the absorbing atom.

A non-spherical electronic charge distribution around the nucleus results in electric quadrupole splitting, because a gradient in the electric field will cause a splitting of the Mössbauer transition energy levels (E_0). An electric quadrupole interaction will be observed if at least one of the relevant nuclear states has a nuclear quadrupole moment ($I > \frac{1}{2}$), as is the case for ^{57m}Fe . If an electric field gradient is non-zero at the nucleus, the nuclear state with a nuclear quadrupole moment will degenerate into two separate states, resulting in two separate peaks being observed in the Mössbauer spectrum with a distance that is directly proportional with the quadrupole splitting. This information provides insight into the coordination of the probed atom.

Finally, in the presence of a magnetic field, a nuclear state with a nuclear moment will show dipole interaction with the magnetic field. This will result in the nuclear state to degenerate into a number of states proportional to the spin of the relevant nuclear states (I), also known as the Zeeman effect [78]. In ^{57}Fe Mössbauer, the Zeeman effect results in 6 separate transitions, 2 from ^{57}Fe and 4 from ^{57m}Fe , and thus we will observe 6 peaks in the Mössbauer spectrum. The distance between the outer peaks is directly proportional to the strength of the magnetic field, which allows the local magnetic field to be measured. Even when no external magnetic field is applied, nuclei such as metallic iron will show a magnetic field due to the unpaired spins of its valence electrons and the magnetic ordering of the atoms surrounding it. This magnetic field strength does not only give insight into the magnetic nature of the probed material, but also to its metallic domain size, because the local field strength was found to be strongly dependent on the particle size [79].

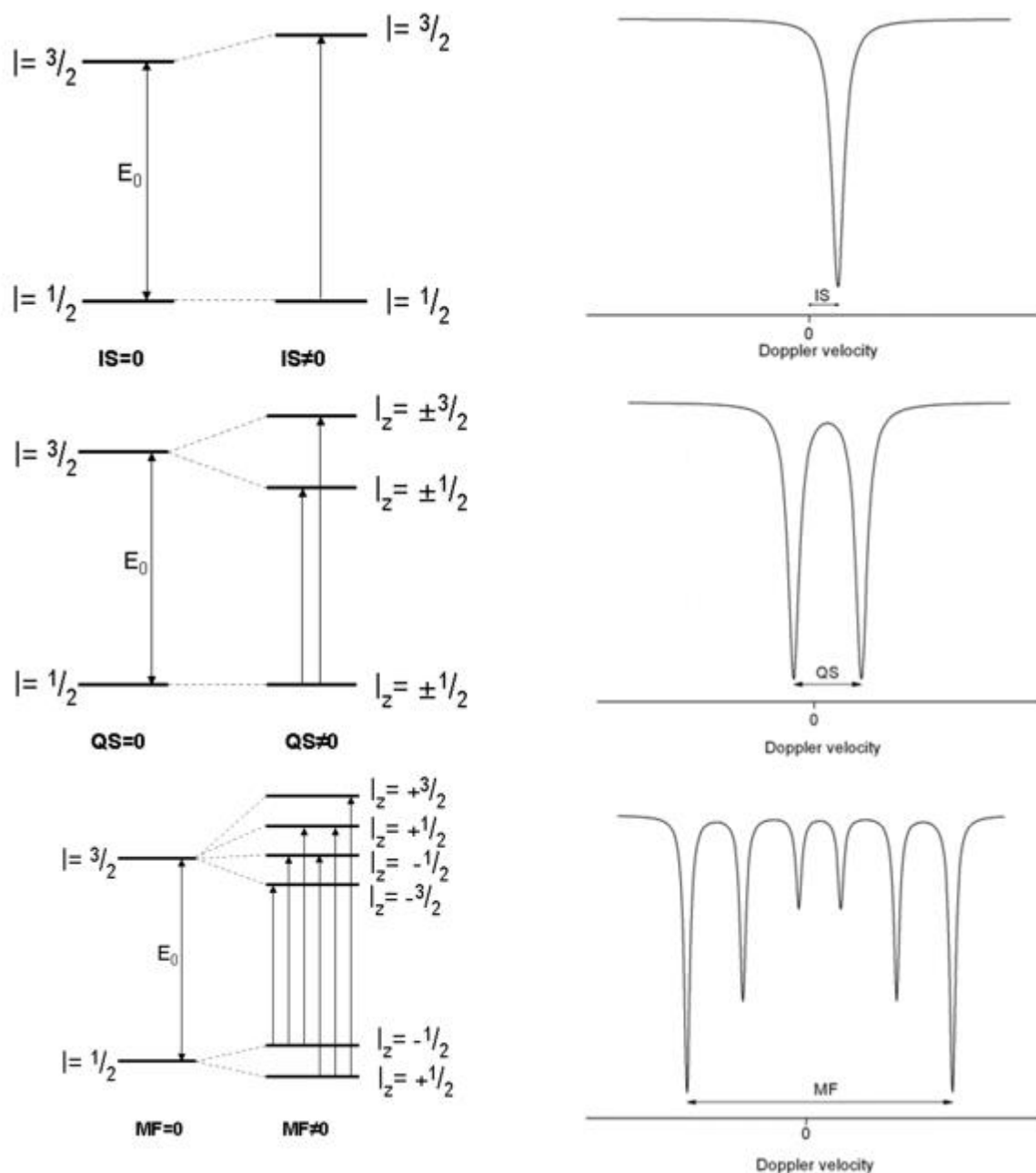


Figure 3: Hyperfine interactions observed in Mössbauer spectroscopy. (a) isomer shift, (b) electric quadrupole splitting and (c) magnetic hyperfine field. Adapted from [80].

1.5.2 Mössbauer Emission Spectroscopy

Whilst cobalt itself does not have a Mössbauer isotope, the use of Mössbauer Emission Spectroscopy (MES) in conventional transmission mode allows the measurement of cobalt-containing compounds. Using an *in situ* MES cell, the cobalt-containing catalyst spiked with ^{57}Co , which decays to $^{57\text{m}}\text{Fe}$, can be studied under high pressure and at high temperature [81]. This technique has already been

used extensively to study cobalt catalysts both for the FTS reaction [82] and for hydrotreating reactions (CoMo-sulfides) [83]–[86]. Mössbauer emission spectroscopy can provide key information about the valence, coordination, spin and particle size of the cobalt phases present in the catalytic system under realistic industrial conditions.

1.6 Scope of this thesis

The aim of this work is to understand the deactivation pathways of cobalt-based FTS catalysts using Mössbauer emission spectroscopy. This technique allows to study the evolution of cobalt in FTS catalysts. The objective is to understand the role of the support (carbon, titania and silica) on the stability of the active cobalt phase. Use is made of a high-pressure/high-temperature *in situ* MES cell to investigate the cobalt catalysts under industrially relevant conditions, specifically the high CO conversion conditions that lead to high steam partial pressures. The role of manganese and platinum as potential structural promoters is also studied. Manganese is investigated for its ability to suppress sintering, while the role of platinum is studied to speed up cobalt oxide reduction. Combined with complementary characterization such as transmission electron microscopy and X-ray electron spectroscopy and catalytic activity measurements, better insight into deactivation of supported cobalt catalysts is targeted.

In **Chapter 2** deactivation of carbon-supported cobalt is investigated as a function of the steam partial pressure using carbon nanofibers as an inert support. Cobalt catalysts supported on carbon nanofibers are investigated by Mössbauer spectroscopy under FTS conditions as a function of the steam partial pressure. The role of manganese on the evolution of cobalt is studied as well. Mössbauer spectroscopy is complemented with *ex situ* TEM, STEM-EDX, and plug-flow reactor activity measurements, to achieve clear structure-activity relations.

The role of manganese as a promotor is further investigated in **Chapter 3**. For this purpose, silica-supported cobalt catalysts with and without the manganese oxide promoter are prepared and the role of platinum as reduction promoter is studied as well. Increasing humid Fischer-Tropsch conditions are applied to the catalysts to study the stability of cobalt on the stronger oxidic support material, with and without the manganese oxide promoter. Additional characterization and activity tests allow achieving a thorough understanding of the detrimental effects of the deactivation behavior.

Chapter 4 focuses on the reducible oxide titania as a support material for cobalt. A total of 4 cobalt catalysts with cobalt weight loadings between 2% and 8% are prepared. The stability of these titania-supported catalysts is studied under increasing humid conditions to study the deactivation on this

more reactive support. These measurements are complemented with XRD, TEM, STEM-EDX and XPS characterization and fixed-bed activity tests. The formation of oxidic cobalt is nearly constant, independent to the cobalt loading, indicating the support surface area is limiting cobalt oxidation.

This latter aspect leads to a comparative study of titania supports with varying surface area in **Chapter 5**. To achieve this, cobalt catalysts with similar loadings are prepared on two titania support materials with higher surface area than the typical P25 titania. The role of platinum is investigated in improving the reducibility as well as resistance to cobalt oxidation. Humid Fischer-Tropsch conditions are applied to study the oxidation behavior of cobalt under simulated high CO conversion conditions and compared with previous results obtained with P25 titania.

The main findings of this work are summarized in Chapter 6, which also contains a brief outlook.

Bibliography

- [1] NOAA National Centers for Environmental information, “Climate at a Glance: Global Time Series,” Apr. 20, 2023. <https://www.ncei.noaa.gov/access/monitoring/climate-at-a-glance/global/time-series> (accessed Apr. 20, 2023).
- [2] A. A. Lacis, G. A. Schmidt, D. Rind, and R. A. Ruedy, “Atmospheric CO₂ : Principal Control Knob Governing Earth’s Temperature,” *Science* (1979), vol. 330, no. 6002, pp. 356–359, 2010, doi: 10.1126/science.1190653.
- [3] UNFCCC, “Report no. FCCC/PA/CMA/2021/10/Add.1,” 2022.
- [4] H. Ritchie, M. Roser, and P. Rosado, “CO₂ and Greenhouse Gas Emissions,” <https://ourworldindata.org/co2-and-greenhouse-gas-emissions>, 2020.
- [5] IEA, “Renewable Electricity,” IEA, Paris <https://www.iea.org/reports/renewable-electricity>, License: CC BY 4.0, 2022.
- [6] Shell Global, “Synthetic Kerosene,” <https://www.shell.com/business-customers/aviation/the-future-of-energy/sustainable-aviation-fuel/synthetic-kerosene.html>, May 2023.
- [7] D. L. King and A. de Klerk, “Overview of Feed-to-Liquid (XTL) Conversion,” in *ACS Symposium Series*, 2011, pp. 1–24. doi: 10.1021/bk-2011-1084.ch001.
- [8] A. de Klerk, “Fischer-Tropsch Process,” in *Kirk-Othmer Encyclopedia of Chemical Technology*, Hoboken, NJ, USA: John Wiley & Sons, Inc., 2013. doi: 10.1002/0471238961.fiscdekl.a01.
- [9] M. E. Dry, “The Fischer-Tropsch process: 1950–2000,” *Catal. Today*, vol. 71, no. 3–4, pp. 227–241, 2002, doi: 10.1016/S0920-5861(01)00453-9.
- [10] P. J. Flory, “Molecular Size Distribution in Linear Condensation Polymers ¹,” *J. Am. Chem. Soc.*, vol. 58, no. 10, pp. 1877–1885, 1936, doi: 10.1021/ja01301a016.
- [11] R. A. Friedel and R. B. Anderson, “Composition of Synthetic Liquid Fuels. I. Product Distribution and Analysis of C₅ — C₈ Paraffin Isomers from Cobalt Catalyst ¹,” *J. Am. Chem. Soc.*, vol. 72, no. 3, pp. 1212–1215, 1950, doi: 10.1021/ja01159a039.
- [12] G. P. van der Laan and A. A. C. M. Beenackers, “Kinetics and Selectivity of the Fischer–Tropsch Synthesis: A Literature Review,” *Catal. Rev.*, vol. 41, no. 3–4, pp. 255–318, 1999, doi: 10.1081/CR-100101170.
- [13] E. Rytter, N. E. Tsakoumis, and A. Holmen, “On the selectivity to higher hydrocarbons in Co-based Fischer-Tropsch synthesis,” *Catal. Today*, vol. 261, pp. 3–16, 2016, doi: 10.1016/j.cattod.2015.09.020.
- [14] G. Maschio, A. Lucchesi, and G. Stoppato, “Production of syngas from biomass,” *Bio. Tech.*, vol. 48, no. 2, pp. 119–126, 1994, doi: 10.1016/0960-8524(94)90198-8.
- [15] P. Ebrahimi, A. Kumar, and M. Khraisheh, “A Review of CeO₂ Supported Catalysts for CO₂ Reduction to CO through the Reverse Water Gas Shift Reaction,” *Catalysts*, vol. 12, no. 10, p. 1101, 2022, doi: 10.3390/catal12101101.
- [16] L. Pastor-Pérez, F. Baibars, E. Le Sache, H. Arellano-García, S. Gu, and T. R. Reina, “CO₂ valorisation via Reverse Water-Gas Shift reaction using advanced Cs doped Fe-Cu/Al₂O₃ catalysts,” *J. of CO₂ Util.*, vol. 21, pp. 423–428, 2017, doi: 10.1016/j.jcou.2017.08.009.
- [17] M. González-Castaño, B. Dorneanu, and H. Arellano-García, “The reverse water gas shift reaction: a process systems engineering perspective,” *React. Chem. Eng.*, vol. 6, no. 6, pp. 954–976, 2021, doi: 10.1039/D0RE00478B.
- [18] K. Zhao, Q. Bkour, X. Hou, S. W. Kang, J. C. Park, M. G. Norton, J.-I. Yang, and S. Ha, “Reverse water gas shift reaction over CuFe/Al₂O₃ catalyst in solid oxide electrolysis cell,” *Chem. Eng. J.*, vol. 336, pp. 20–27, 2018, doi: 10.1016/j.cej.2017.11.028.
- [19] “Recognizing the Best in Innovation: Breakthrough Catalyst,” *R&D Magazine*, p. 20, Sep. 2005.
- [20] J. A. Dumesic, G. W. Huber, and M. Boudart, in *Handbook of Heterogeneous Catalysis*, Weinheim, Germany: Wiley-VCH Verlag GmbH & Co. KGaA, 2008, pp. 1–15. doi: 10.1002/9783527610044.
- [21] E. F. Gallei, M. Hesse, and E. Schwab, in *Handbook of Heterogenous Catalysis*, Weinheim, Germany: Wiley-VCH Verlag GmbH & Co. KGaA, 2008, pp. 57–66.
- [22] S. J. Tauster, S. C. Fung, R. T. K. Baker, and J. A. Horsley, “Strong Interactions in Supported-Metal Catalysts,” *Science*, vol. 211, no. 4487, pp. 1121–1125, 1981, doi: 10.1126/science.211.4487.1121.
- [23] S. J. Tauster, S. C. Fung, and R. L. Garten, “Strong metal-support interactions. Group 8 noble metals supported on titanium dioxide,” *J. Am. Chem. Soc.*, vol. 100, no. 1, pp. 170–175, 1978, doi: 10.1021/ja00469a029.
- [24] E. Iglesia, “Design, synthesis, and use of cobalt-based Fischer-Tropsch synthesis catalysts,” *Appl. Catal. A Gen.*, vol. 161, no. 1–2, pp. 59–78, 1997, doi: 10.1016/S0926-860X(97)00186-5.
- [25] E. de Smit and B. M. Weckhuysen, “The renaissance of iron-based Fischer–Tropsch synthesis: on the multifaceted catalyst deactivation behaviour,” *Chem. Soc. Rev.*, vol. 37, no. 12, p. 2758, 2008, doi: 10.1039/b805427d.
- [26] W.-Z. Li, J.-X. Liu, J. Gu, W. Zhou, S.-Y. Yao, R. Si, Y. Guo, H.-Y. Su, C.-H. Yan, W.-X. Li, Y.-W. Zhang, and D. Ma, “Chemical Insights into the Design and Development of Face-Centered Cubic Ruthenium Catalysts for Fischer–Tropsch Synthesis,” *J. Am. Chem. Soc.*, vol. 139, no. 6, pp. 2267–2276, 2017, doi: 10.1021/jacs.6b10375.
- [27] W. L. Vrijburg, “Nickel-based catalysts for CO₂ hydrogenation,” Technische Universiteit Eindhoven, Eindhoven, 2019.

- [28] W. Ma, G. Jacobs, D. E. Sparks, B. Todić, D. B. Bukur, and B. H. Davis, “Quantitative comparison of iron and cobalt based catalysts for the Fischer-Tropsch synthesis under clean and poisoning conditions,” *Catal. Today*, vol. 343, pp. 125–136, 2020, doi: 10.1016/j.cattod.2019.04.011.
- [29] J. van de Loosdrecht, B. Balzhinimaev, J. A. Dalmon, J. W. Niemantsverdriet, S. V. Tsybulya, A. M. Saib, P. J. van Berge, and J. L. Visagie, “Cobalt Fischer-Tropsch synthesis: Deactivation by oxidation?,” *Catal. Today*, vol. 123, no. 1–4, pp. 293–302, 2007, doi: 10.1016/j.cattod.2007.02.032.
- [30] T. O. Eschemann and K. P. de Jong, “Deactivation Behavior of Co/TiO₂ Catalysts during Fischer–Tropsch Synthesis,” *ACS Catal.*, vol. 5, no. 6, pp. 3181–3188, 2015, doi: 10.1021/acscatal.5b00268.
- [31] M. Wolf, N. Fischer, and M. Claeys, “Water-induced deactivation of cobalt-based Fischer–Tropsch catalysts,” *Nat. Catal.*, vol. 3, no. 12, pp. 962–965, 2020, doi: 10.1038/s41929-020-00534-5.
- [32] N. E. Tsakoumis, M. Rønning, Ø. Borg, E. Rytter, and A. Holmen, “Deactivation of cobalt based Fischer-Tropsch catalysts: A review,” *Catal. Today*, vol. 154, no. 3–4, pp. 162–182, 2010, doi: 10.1016/j.cattod.2010.02.077.
- [33] A. Carvalho, V. V. Ordonsky, Y. Luo, M. Marinova, A. R. Muniz, N. R. Marcilio, and A. Y. Khodakov, “Elucidation of deactivation phenomena in cobalt catalyst for Fischer-Tropsch synthesis using SSITKA,” *J. Catal.*, vol. 344, pp. 669–679, 2016, doi: 10.1016/j.jcat.2016.11.001.
- [34] E. Rytter and A. Holmen, “Deactivation and Regeneration of Commercial Type Fischer-Tropsch Co-Catalysts—A Mini-Review,” *Catalysts*, vol. 5, no. 2, pp. 478–499, 2015, doi: 10.3390/catal5020478.
- [35] X.-F. Yang, A. Wang, B. Qiao, J. Li, J. Liu, and T. Zhang, “Single-Atom Catalysts: A New Frontier in Heterogeneous Catalysis,” *Acc. Chem. Res.*, vol. 46, no. 8, pp. 1740–1748, 2013, doi: 10.1021/ar300361m.
- [36] G. L. Bezemer, J. H. Bitter, H. P. C. E. Kuipers, H. Oosterbeek, J. E. Holewijn, X. Xu, F. Kapteijn, A. J. van Dillen, and K. P. de Jong, “Cobalt Particle Size Effects in the Fischer–Tropsch Reaction Studied with Carbon Nanofiber Supported Catalysts,” *J. Am. Chem. Soc.*, vol. 128, no. 12, pp. 3956–3964, 2006, doi: 10.1021/ja058282w.
- [37] H. S. Taylor, “A theory of the catalytic surface,” *Proceedings of the Royal Society of London. Series A, Containing Papers of a Mathematical and Physical Character*, vol. 108, no. 745, pp. 105–111, 1925, doi: 10.1098/rspa.1925.0061.
- [38] M. Boudart, “Heterogeneity of Metal Surfaces,” *J. Am. Chem. Soc.*, vol. 74, no. 14, pp. 3556–3561, 1952, doi: 10.1021/ja01134a029.
- [39] M. Boudart and M. A. McDonald, “Structure sensitivity of hydrocarbon synthesis from carbon monoxide and hydrogen,” *J. Phys. Chem.*, vol. 88, no. 11, pp. 2185–2195, 1984, doi: 10.1021/j150655a004.
- [40] R. A. van Santen, M. M. Ghouri, S. Shetty, and E. M. H. Hensen, “Structure sensitivity of the Fischer–Tropsch reaction; molecular kinetics simulations,” *Catal. Sci. Tech.*, vol. 1, no. 6, p. 891, 2011, doi: 10.1039/c1cy00118c.
- [41] J. P. den Breejen, P. B. Radstake, G. L. Bezemer, J. H. Bitter, V. Frøseth, A. Holmen, and K. P. de Jong, “On the Origin of the Cobalt Particle Size Effects in Fischer–Tropsch Catalysis,” *J. Am. Chem. Soc.*, vol. 131, no. 20, pp. 7197–7203, 2009, doi: 10.1021/ja901006x.
- [42] C. H. Bartholomew, “Mechanisms of catalyst deactivation,” *Appl. Catal. A Gen.*, vol. 212, no. 1–2, pp. 17–60, 2001, doi: 10.1016/S0926-860X(00)00843-7.
- [43] P. Agrawal, J. R. Katzer, and W. H. Manogue, “Methanation over transition metal catalysts III. Co/Al₂O₃ in sulfur-poisoning studies,” *J. Catal.*, vol. 69, no. 2, pp. 327–344, 1981, doi: 10.1016/0021-9517(81)90169-X.
- [44] V. V. Ordonsky, A. Carvalho, B. Legras, S. Paul, M. Virginie, V. L. Sushkevich, and A. Y. Khodakov, “Effects of co-feeding with nitrogen-containing compounds on the performance of supported cobalt and iron catalysts in Fischer–Tropsch synthesis,” *Catal. Today*, vol. 275, pp. 84–93, 2016, doi: 10.1016/j.cattod.2015.12.015.
- [45] A. H. Lillebø, E. Patanou, J. Yang, E. A. Blekkan, and A. Holmen, “The effect of alkali and alkaline earth elements on cobalt based Fischer-Tropsch catalysts,” *Catal. Today*, vol. 215, pp. 60–66, 2013, doi: 10.1016/j.cattod.2013.03.030.
- [46] C. M. Balonek, A. H. Lillebø, S. Rane, E. Rytter, L. D. Schmidt, and A. Holmen, “Effect of alkali metal impurities on Co-Re catalysts for Fischer-Tropsch synthesis from biomass-derived syngas,” *Catal. Letters*, vol. 138, no. 1–2, pp. 8–13, 2010, doi: 10.1007/s10562-010-0366-4.
- [47] M. Claeys, M. E. Dry, E. van Steen, E. du Plessis, P. J. van Berge, A. M. Saib, and D. J. Moodley, “In situ magnetometer study on the formation and stability of cobalt carbide in Fischer–Tropsch synthesis,” *J. Catal.*, vol. 318, pp. 193–202, 2014, doi: 10.1016/j.jcat.2014.08.002.
- [48] D. Moodley, M. Claeys, E. van Steen, P. van Helden, D. Kistamurthy, K.-J. Weststrate, H. Niemantsverdriet, A. Saib, W. Erasmus, and J. van de Loosdrecht, “Sintering of cobalt during FTS: Insights from industrial and model systems,” *Catal. Today*, vol. 342, pp. 59–70, 2020, doi: 10.1016/j.cattod.2019.03.059.
- [49] M. Rahmati, M. S. Safdari, T. H. Fletcher, M. D. Argyle, and C. H. Bartholomew, “Chemical and Thermal Sintering of Supported Metals with Emphasis on Cobalt Catalysts during Fischer-Tropsch Synthesis,” *Chem. Rev.*, vol. 120, no. 10, pp. 4455–4533, May 27, 2020, doi: 10.1021/acs.chemrev.9b00417.
- [50] D. Kistamurthy, A. M. Saib, D. J. Moodley, J. W. Niemantsverdriet, and C. J. Weststrate, “Ostwald ripening on a planar Co/SiO₂ catalyst exposed to model Fischer–Tropsch synthesis conditions,” *J. Catal.*, vol. 328, pp. 123–129, 2015, doi: 10.1016/j.jcat.2015.02.017.

- [51] W. Janse Van Rensburg, P. Van Helden, D. J. Moodley, M. Claeys, M. A. Petersen, and E. Van Steen, "Role of Transient Co-Subcarbonyls in Ostwald Ripening Sintering of Cobalt Supported on γ -Alumina Surfaces," *J. of Phys. Chem. C*, vol. 121, no. 31, pp. 16739–16753, 2017, doi: 10.1021/acs.jpcc.7b01907.
- [52] C. E. Klierer, S. L. Soled, and G. Kiss, "Morphological transformations during Fischer-Tropsch synthesis on a titania-supported cobalt catalyst," *Catal. Today*, vol. 323, pp. 233–256, 2019, doi: 10.1016/j.cattod.2018.05.021.
- [53] P. J. Van Berge, J. Van De Loosdrecht, S. Barradas, and A. M. Van Der Kraan, "Oxidation of cobalt based Fischer-Tropsch catalysts as a deactivation mechanism," *Catal. Today*, vol. 58, no. 4, pp. 321–334, 2000, doi: 10.1016/S0920-5861(00)00265-0.
- [54] C. Lancelot, V. V. Ordonsky, O. Stéphan, M. Sadeqzadeh, H. Karaca, M. Lacroix, D. Curulla-Ferré, F. Luck, P. Fongarland, A. Griboval-Constant, and A. Y. Khodakov, "Direct Evidence of Surface Oxidation of Cobalt Nanoparticles in Alumina-Supported Catalysts for Fischer-Tropsch Synthesis," *ACS Catal.*, vol. 4, no. 12, pp. 4510–4515, 2014, doi: 10.1021/cs500981p.
- [55] E. van Steen, M. Claeys, M. E. Dry, J. van de Loosdrecht, E. L. Viljoen, and J. L. Visagie, "Stability of Nanocrystals: Thermodynamic Analysis of Oxidation and Re-reduction of Cobalt in Water/Hydrogen Mixtures," *J. Phys. Chem. B*, vol. 109, no. 8, pp. 3575–3577, 2005, doi: 10.1021/jp045136o.
- [56] C. Qiu, Y. Odarchenko, Q. Meng, P. Cong, M. A. W. Schoen, A. Kleibert, T. Forrest, and A. M. Beale, "Direct observation of the evolving metal-support interaction of individual cobalt nanoparticles at the titania and silica interface," *Chem. Sci.*, vol. 11, no. 48, pp. 13060–13070, 2020, doi: 10.1039/D0SC03113E.
- [57] M. Wolf, H. Kotzé, N. Fischer, and M. Claeys, "Size dependent stability of cobalt nanoparticles on silica under high conversion Fischer-Tropsch environment," *Farad. Dis.*, vol. 197, pp. 243–268, 2017, doi: 10.1039/C6FD00200E.
- [58] H. Karaca, J. Hong, P. Fongarland, P. Roussel, A. Griboval-Constant, M. Lacroix, K. Hortmann, O. V. Safonova, and A. Y. Khodakov, "In situ XRD investigation of the evolution of alumina-supported cobalt catalysts under realistic conditions of Fischer-Tropsch synthesis," *Chem. Commun.*, vol. 46, no. 5, pp. 788–790, 2010, doi: 10.1039/B920110F.
- [59] E. Rytter, Ø. Borg, N. E. Tsakoumis, and A. Holmen, "Water as key to activity and selectivity in Co Fischer-Tropsch synthesis: γ -alumina based structure-performance relationships," *J. Catal.*, vol. 365, pp. 334–343, 2018, doi: 10.1016/j.jcat.2018.07.003.
- [60] M. Sadeqzadeh, S. Chambrey, J. Hong, P. Fongarland, F. Luck, D. Curulla-Ferré, D. Schweich, J. Bousquet, and A. Y. Khodakov, "Effect of different reaction conditions on the deactivation of alumina-supported cobalt Fischer-Tropsch catalysts in a milli-fixed-bed reactor: Experiments and modeling," *Ind. Eng. Chem. Res.*, vol. 53, no. 17, pp. 6913–6922, 2014, doi: 10.1021/ie4040303.
- [61] B. E. Koel and J. Kim, in *Handbook of Heterogeneous Catalysis*, Weinheim, Germany: Wiley-VCH Verlag GmbH & Co. KGaA, 2008, pp. 1593–1624.
- [62] J. H. Den Otter, S. R. Nijveld, and K. P. De Jong, "Synergistic Promotion of Co/SiO₂ Fischer-Tropsch Catalysts by Niobia and Platinum," *ACS Catal.*, vol. 6, no. 3, pp. 1616–1623, 2016, doi: 10.1021/acscatal.5b02418.
- [63] G. Jacobs, P. M. Patterson, Y. Zhang, T. Das, J. Li, and B. H. Davis, "Fischer-Tropsch synthesis: deactivation of noble metal-promoted Co/Al₂O₃ catalysts," *Appl. Catal. A Gen.*, vol. 233, no. 1–2, pp. 215–226, 2002, doi: 10.1016/S0926-860X(02)00147-3.
- [64] T. O. Eschemann, J. Oenema, and K. P. de Jong, "Effects of noble metal promotion for Co/TiO₂ Fischer-Tropsch catalysts," *Catal. Today*, vol. 261, pp. 60–66, 2016, doi: 10.1016/j.cattod.2015.06.016.
- [65] G. Jacobs, Y. Ji, B. H. Davis, D. Cronauer, A. J. Kropf, and C. L. Marshall, "Fischer-Tropsch synthesis: Temperature programmed EXAFS/XANES investigation of the influence of support type, cobalt loading, and noble metal promoter addition to the reduction behavior of cobalt oxide particles," *Appl. Catal. A Gen.*, vol. 333, no. 2, pp. 177–191, 2007, doi: 10.1016/j.apcata.2007.07.027.
- [66] S. Colley, R. G. Copperthwaite, G. J. Hutchings, and M. Van der Riet, "Carbon monoxide hydrogenation using cobalt manganese oxide catalysts: initial catalyst optimization studies," *Ind. Eng. Chem. Res.*, vol. 27, no. 8, pp. 1339–1344, 1988, doi: 10.1021/ie00080a001.
- [67] J. Paterson, M. Peacock, R. Purves, R. Partington, K. Sullivan, G. Sunley, and J. Wilson, "Manipulation of Fischer-Tropsch Synthesis for Production of Higher Alcohols Using Manganese Promoters," *Chem. Cat. Chem.*, vol. 10, no. 22, pp. 5154–5163, 2018, doi: 10.1002/cctc.201800883.
- [68] J. P. den Breejen, A. M. Frey, J. Yang, A. Holmen, M. M. van Schooneveld, F. M. F. de Groot, O. Stephan, J. H. Bitter, and K. P. de Jong, "A Highly Active and Selective Manganese Oxide Promoted Cobalt-on-Silica Fischer-Tropsch Catalyst," *Top. Catal.*, vol. 54, no. 13–15, pp. 768–777, 2011, doi: 10.1007/s11244-011-9703-0.
- [69] G. L. Bezemer, P. Radstake, U. Falke, H. Oosterbeek, H. Kuipers, A. Van Dillen, and K. De Jong, "Investigation of promoter effects of manganese oxide on carbon nanofiber-supported cobalt catalysts for Fischer-Tropsch synthesis," *J. Catal.*, vol. 237, no. 1, pp. 152–161, 2006, doi: 10.1016/j.jcat.2005.10.031.
- [70] F. Morales, E. de Smit, F. de Groot, T. Visser, and B. Weckhuysen, "Effects of manganese oxide promoter on the CO and H₂ adsorption properties of titania-supported cobalt Fischer-Tropsch catalysts," *J. Catal.*, vol. 246, no. 1, pp. 91–99, 2007, doi: 10.1016/j.jcat.2006.11.014.

- [71] F. Morales, D. Grandjean, F. M. F. de Groot, O. Stephan, and B. M. Weckhuysen, "Combined EXAFS and STEM-EELS study of the electronic state and location of Mn as promoter in Co-based Fischer–Tropsch catalysts," *Phys. Chem. Chem. Phys.*, vol. 7, no. 4, pp. 568–572, 2005, doi: 10.1039/B418286C.
- [72] N. E. Tsakoumis, R. Dehghan, R. E. Johnsen, A. Voronov, W. Van Beek, J. C. Walmsley, Ø. Borg, E. Rytter, D. Chen, M. Rønning, and A. Holmen, "A combined in situ XAS-XRPD-Raman study of Fischer-Tropsch synthesis over a carbon supported Co catalyst," *Catal. Today*, vol. 205, pp. 86–93, 2013, doi: 10.1016/j.cattod.2012.08.041.
- [73] A. Rochet, V. Moizan, F. Diehl, C. Pichon, and V. Briois, "Quick-XAS and Raman operando characterisation of a cobalt alumina-supported catalyst under realistic Fischer-Tropsch reaction conditions," *Catal. Today*, vol. 205, pp. 94–100, 2013, doi: 10.1016/j.cattod.2012.08.021.
- [74] R. L. Mössbauer, "Kernresonanzfluoreszenz von Gammastrahlung in Ir^{191} ," *Zeitschrift für Physik*, vol. 151, no. 2, pp. 124–143, 1958, doi: 10.1007/BF01344210.
- [75] G. M. Bancroft, A. G. Maddock, and R. G. Burns, "Applications of the Mössbauer effect to silicate mineralogy—I. Iron silicates of known crystal structure," *Geochim. Cosmochim. Acta.*, vol. 31, no. 11, pp. 2219–2246, 1967, doi: 10.1016/0016-7037(67)90062-2.
- [76] J. Jung, M. Fricke, G. Hampel, and J. Hesse, " ^{57}Fe Mössbauer effect studies on the magnetism of iron-rich bcc, fcc and hcp phases of $\text{Fe}_{100-\text{c}}\text{Mn}_{\text{c}}$," *Hyperfine Interact.*, vol. 72, no. 4, pp. 375–388, 1992, doi: 10.1007/BF02397691.
- [77] G. K. Wertheim, "Chemical effects of nuclear transformations in Moessbauer spectroscopy," *Acc. Chem. Res.*, vol. 4, no. 11, pp. 373–379, 1971, doi: 10.1021/ar50047a003.
- [78] P. Zeeman, "XXXII. On the influence of magnetism on the nature of the light emitted by a substance," *The London, Edinburgh, and Dublin Philosophical Magazine and Journal of Science*, vol. 43, no. 262, pp. 226–239, 1897, doi: 10.1080/14786449708620985.
- [79] S. Mørup, H. Topsøe, and B. S. Clausen, "Magnetic Properties of Microcrystals Studied by Mössbauer Spectroscopy," *Phys. Scr.*, vol. 25, pp. 713–719, 1982.
- [80] M. P. Steenvoorden and N. van Dijk, "Beschrijving van een Mössbauer-spectrometer", 2015.
- [81] M. W. J. Crajé, A. M. Van der Kraan, J. Van de Loosdrecht, and P. J. Van Berge, "The application of Mössbauer emission spectroscopy to industrial cobalt based Fischer-Tropsch catalysts," *Catal. Today*, vol. 71, no. 3–4, pp. 369–379, 2002, doi: 10.1016/S0920-5861(01)00464-3.
- [82] G. L. Bezemer, T. J. Remans, A. P. van Bavel, and A. I. Dugulan, "Direct Evidence of Water-Assisted Sintering of Cobalt on Carbon Nanofiber Catalysts during Simulated Fischer–Tropsch Conditions Revealed with in Situ Mössbauer Spectroscopy," *J. Am. Chem. Soc.*, vol. 132, no. 25, pp. 8540–8541, 2010, doi: 10.1021/ja103002k.
- [83] C. Wivel, R. Candia, B. S. Clausen, S. Mørup, and H. Topsøe, "On the catalytic significance of a CoMoS phase in CoMo Al_2O_3 hydrodesulfurization catalysts: Combined in situ Mössbauer emission spectroscopy and activity studies," *J. Catal.*, vol. 68, no. 2, pp. 453–463, 1981, doi: 10.1016/0021-9517(81)90115-9.
- [84] H. Topsøe, B. S. Clausen, R. Candia, C. Wivel, and S. Mørup, "In situ Mossbauer emission spectroscopy studies of unsupported and supported sulfided Co-Mo hydrodesulfurization catalysts: Evidence for and nature of a Co-Mo-S phase," *J. Catal.*, vol. 68, no. 2, pp. 433–452, 1981, doi: 10.1016/0021-9517(81)90114-7.
- [85] C. Wivel, B. S. Clausen, R. Candia, S. Mørup, and H. Topsøe, "Mössbauer Emission Studies of Calcined Co-Mo/ Al_2O_3 Catalysts: Catalytic Significance of Co Precursors," *J. Catal.*, vol. 87, no. 2, pp. 497–513, 1984, doi: 10.1016/0021-9517(84)90210-0.
- [86] M. W. J. Crajé, V. H. J. De Beer, J. A. R. Van Veen, and A. M. Van Der Kraan, "Sulfidation of Co/ Al_2O_3 and CoMo/ Al_2O_3 catalysts studied by mössbauer emission spectroscopy," *J. Catal.*, vol. 143, no. 2, pp. 601–615, 1993, doi: 10.1006/jcat.1993.1303.

Chapter 2

Sintering and carbidization under simulated high conversion on a cobalt-based Fischer-Tropsch catalyst; manganese oxide as a structural promotor

Abstract

The commercial application of cobalt-based Fischer-Tropsch synthesis (FTS) suffers from catalyst deactivation. One of the main deactivation mechanisms under industrial conditions is sintering. In this work, we explored the role of manganese oxide as a structural promoter against sintering in a carbon nanofiber supported cobalt model catalyst. We employed *in situ* Mössbauer emission spectroscopy to study cobalt sintering in synthesis gas as a function of the steam partial pressure, which mimics high CO conversion during FTS. Steam accelerates the sintering of non-promoted metallic cobalt particles. Model experiments point to a synergistic effect between carbon monoxide and steam on cobalt sintering. In the manganese-promoted case, sintering is significantly reduced, indicative of the structural stabilization of small cobalt particles by manganese oxide. Nevertheless, a fraction of cobalt particles in close interaction with manganese oxide carburized under these conditions, resulting in a lower catalytic activity.

This chapter was published as: L.M. van Koppen, A.I. Dugulan, G.L. Bezemer, and E.J.M. Hensen, *J. Catal.*, 2022, **413**, 106-118.

2.1 Introduction

Fischer-Tropsch synthesis, which refers to the conversion of synthesis gas to fuels and chemicals, is of growing importance for the valorization of diverse feedstocks. At the molecular level, Fischer-Tropsch synthesis (FTS) entails surface-catalyzed polymerization of *in situ* produced CH_x monomers formed by dissociation of adsorbed CO and subsequent hydrogenation of adsorbed carbon species [1]. There are currently two kinds of commercially viable low temperature FT catalysts based on either cobalt or iron. Cobalt catalysts are characterized by higher activity, higher chain-growth probability, and lower byproduct formation in comparison to iron catalysts. Moreover, different from iron, cobalt shows only very low activity in the water-gas shift reaction [2]. Therefore, cobalt catalysts are preferred when the synthesis gas is derived from natural gas and longer chain paraffins, and olefins are targeted. Whilst cobalt-based Fischer-Tropsch has many advantages, it also suffers from a strong particle size effect, requiring catalysts with a relatively high dispersion with an optimum around 6-8 nm [3] and good stability for successful exploitation [4].

Catalyst deactivation in cobalt-based Fischer-Tropsch synthesis is a major challenge, as catalyst replacement in the commonly deployed fixed-bed reactors can result in several weeks of interrupted production combined with the relatively high cost of cobalt. Therefore, improving the stability of cobalt-based FTS catalysts would be a substantial benefit in the commercial operation of the Fischer-Tropsch process [4]. Catalyst deactivation in cobalt-based Fischer-Tropsch is a complex process, which according to the state of the art can be categorized in long- and short-term deactivation profiles [5]. Deactivation after the start-up of the reaction has been studied extensively with every resurgence of Fischer-Tropsch research [4], [6], [7]. The short-term deactivation is often found to be reversible under mild hydrogen treatments [8]. In contrast, the long-term deactivation cannot be reversed, making it of operational significance. The complexity lies in the underlying causes of deactivation, which are many and range from poisoning to strong metal support interaction (SMSI) [4]. Poisoning is avoided industrially by extensive scrubbing of the feed and the use of proper guarding technology and can therefore usually be excluded as a reason for deactivation under realistic conditions. This leaves oxidation, SMSI, carbon deposits and sintering as mechanisms for long-term catalyst deactivation.

Sintering of the active metallic cobalt phase is typically found to be one of the main reasons for deactivation under FTS conditions [9]–[11]. Carbon nanofibers (CNF) as a support have an advantage in studying the sintering mechanism. As a result of the weak interaction between the support and the

metallic cobalt phase, sintering occurs on a much shorter timescale [12]–[15]. Carbon nanofiber catalysts have previously been used as model systems in order to understand the effect of cobalt particle size, and catalyst deactivation in Fischer-Tropsch synthesis [3], [8], [16]–[18]. The role of water, a main product in FTS, on deactivation has been under earlier investigation and studies have shown the potential impact on oxidation as well as sintering. Thermodynamic calculations have shown that spherical cobalt nanoparticles smaller than 4.4 nm are likely to be oxidised at the prevailing $\text{H}_2\text{O}/\text{H}_2$ ratio at FTS conditions [19]. Experimental investigations, however, not always detect bulk oxidation of cobalt under these (simulated) industrial FTS conditions which can be related to e.g. usage of larger cobalt particles, which are more resistant to oxidation, or the kinetic hindrance of water splitting [4], [16], [20]–[22]. The role of water on sintering has been established more convincingly. For instance, Kliewer et al. proposed that partial oxidation of cobalt by water led to oxide/hydroxide species prone to coalescence on a wetted support [12]. The group of Khodakov suggested a similar mechanism for the faster sintering of cobalt observed in the presence of water [23], whereas Ostwald ripening by sub-carbonyl species in the presence water has been hypothesized by Moodley et al. [6]. Additionally, recent *in situ* studies have shown that the formation of bulk cobalt carbides is possible under realistic Fischer-Tropsch conditions [24]–[26], although the process seems strongly kinetically inhibited. The formation of these cobalt carbides was reported to lead to a decrease in activity and an increase in methane selectivity [24].

Herein, we investigate the role of water on the deactivation of CNF-supported cobalt and manganese oxide-promoted cobalt catalysts. Manganese oxide has been investigated as a constituent of cobalt-based FTS catalysts already in the first half of the 20th century [27]. These early results showed the potential of manganese to reduce methane selectivity. Later pioneering studies using catalysts prepared by co-precipitation of cobalt and manganese improved our understanding of the role of manganese oxide as a support and selectivity promoter [28]–[31]. More recent work focused on manganese oxide as a promoter for supported cobalt FTS catalysts [32]–[35], in which a positive impact on the chain-growth probability was observed. In the present work, we focus on the role of manganese oxide as a structural promoter to reduce cobalt sintering. The sintering of cobalt is investigated under actual reaction conditions at elevated pressure by *in situ* Mössbauer emission spectroscopy (MES) [36]. A previous ^{57}Co MES study showed that water increases cobalt sintering [16]. The MES measurements are supplemented by XPS, TEM and STEM-EDX characterization, while the catalytic performance is measured in a microflow reactor.

2.2. Experimental section

2.2.1 Catalyst preparation

Carbon nanofibers (CNF) (surface area $200 \text{ m}^2 \text{ g}^{-1}$, total pore volume of 0.46 ml g^{-1}) were synthesized according to literature [37]. All the supported catalysts were prepared by incipient wetness impregnation preparation followed by drying in air at 120°C for 6 hours. The impregnation solutions were obtained by dissolving the appropriate amount of $\text{Co}(\text{NO}_3)_2 \cdot 6\text{H}_2\text{O}$ ($\geq 98.0\%$, Sigma Aldrich) and $\text{Mn}(\text{NO}_3)_2 \cdot 3\text{H}_2\text{O}$ ($\geq 97.0\%$, Sigma Aldrich) in dehydrated ethanol. Two catalysts were prepared with a cobalt loading of 4 wt%, one unpromoted and the other promoted by manganese oxide in a Co/Mn atomic ratio of 5. These samples are denoted by Co(4)/CNF and Co(4)Mn/CNF, respectively. Another Co-Mn catalyst with a cobalt loading of 10 wt% Co and the same Co/Mn ratio of 5 is denoted by Co(10)Mn/CNF. A part of the impregnation solutions was spiked with radioactive ^{57}Co by adding an appropriate amount of a solution containing 90 MBq ^{57}Co in 0.1 M HNO_3 , while the other part was spiked with the same amount of a 0.1 M HNO_3 solution without radioactive cobalt. In this way, two comparable samples were obtained with nearly identical cobalt loading, one being doped with approximately $0.3 \text{ }\mu\text{g}$ of ^{57}Co for the Mössbauer measurements. The radioactive samples were used for Mössbauer spectroscopy.

2.2.2 Characterization

Electron microscopy

The surface average particle size and particle size distribution were determined with transmission electron microscopy (TEM). TEM measurements were performed on a FEI Tecnai 20 electron microscope operated at an electron acceleration voltage of 200 kV with a LaB_6 filament. Typically, a small amount of the sample was ground and suspended in pure ethanol, sonicated, and dispersed over a Cu grid with a holey carbon film.

The nanoscale distribution of elements in the samples was studied using scanning transmission electron microscopy–energy-dispersive X-ray spectroscopy (STEM-EDX). Measurements were carried out on a FEI cubed Cs-corrected Titan operating at 300 kV. Samples were crushed, sonicated in ethanol, and dispersed on a holey Cu support grid. Elemental analysis was done with an Oxford Instruments EDX detector X-MaxN 100TLE.

***In situ* Mössbauer emission spectroscopy**

Mössbauer emission spectroscopy (MES) was carried out at different temperatures using a constant acceleration spectrometer set up in a triangular mode with a moving single-line $\text{K}_4\text{Fe}(\text{CN})_6 \cdot 3\text{H}_2\text{O}$ absorber enriched in ^{57}Fe . The velocity scale was calibrated with a $^{57}\text{Co}:\text{Rh}$ source and a sodium nitroprusside absorber. Zero velocity corresponds to the peak position of the $\text{K}_4\text{Fe}(\text{CN})_6 \cdot 3\text{H}_2\text{O}$ absorber measured with the $^{57}\text{Co}:\text{Rh}$ source, positive velocities corresponding to the absorber moving towards the source.

To be able to measure under *in situ* Fischer-Tropsch conditions, an earlier described high pressure MES cell is used [36]. The cell is equipped with a beryllium window above the sample cup which ensures a leak tight system whilst still allowing the gamma rays to pass through. Additionally, the use of water cooling as well as various O-rings allow this cell to pass all safety requirements of working with radiation and high pressures of dangerous gasses. Furthermore, the use of a metal mesh in the sample cup means both the radioactive probed catalyst as well as a non-radioactive counterpart can be loaded simultaneously without mixing. In this way the non-radioactive counterpart will experience the exact same conditions and make it possible to perform *ex situ* characterization on a used catalyst sample.

The Mössbauer spectra were fitted using the MossWinn 4.0 program [38]. The spectra of very small superparamagnetic species were fitted using the two-state magnetic relaxation model of Blume and Tjon, which assumes the presence of a fluctuating magnetic field that jumps between the values of $+H$ and $-H$ along the z -axis with an average frequency τ [39]. Here H typically equals 500 kOe and τ can vary between $1 \cdot 10^{-9}$ and $1 \cdot 10^{-12} \text{ s}^{-1}$. The Mössbauer spectra of larger particles were fitted using a hyperfine sextuplet, resulting from the local magnetic field experienced by bulk metallic particles. The experimental uncertainties in the calculated Mössbauer parameters, estimated using Monte Carlo iterations by the MossWinn 4.0 program, were as follows: IS and QS $\pm 0.01 \text{ mm s}^{-1}$ for the isomer shift and quadrupole splitting, respectively; $\pm 3\%$ for the spectral contribution; $\pm 3 \text{ kOe}$ for the hyperfine field.

Typically, 500 mg of radioactively probed and 100 mg of non-radioactive catalyst (sieve fraction 250-500 μm) was loaded into the reactor cell. Fischer-Tropsch experiments were performed *in situ* following reduction at 350 °C for 2 hours in 100 mL/min flow of pure H_2 . Reactions were done at 200 °C and 20 bars of pressure, the CO/H_2 was kept at 4 throughout, and steam was fed to achieve different relative humidities. Experiments were typically performed for 2 days; however, to achieve

a significant degree of oxidation at industrially relevant conditions this length was increased to 5 and 11 days for the treatments with a relative humidity of 25 and 57% respectively. The water was evaporated and mixed with the incoming feed gas using a Bronkhorst CEM W-102A-222K. Wax products were collected in a downstream hot catch pot, and water was retrieved in a subsequent cold catch pot. An online Trace GC Ultra from ThermoFischer equipped with a RT-Silica bond column and a flame ionization detector and a Stabilwax column and a thermal conductivity detector was used to analyse the gaseous Fischer-Tropsch products.

***Quasi in situ* X-ray photoelectron spectroscopy (XPS)**

The oxidation state of cobalt and manganese was studied by *quasi in situ* XPS using a Kratos AXIS Ultra 600 spectrometer equipped with a monochromatic Al K α X-ray source (Al K α 1486.6 eV). Survey scans were recorded at a pass energy of 160 eV, detailed region scans at 40 eV. The step size was 0.1 eV and the background pressure during the measurements was kept below 10⁻⁹ mbar.

A high-temperature reaction cell (Kratos, WX-530) was used to pre-treat the sample supported on an alumina stub, allowing *in vacuo* sample transfer into the analysis chamber. Reduction was performed in a pure H₂ flow at atmospheric pressure and 350 °C for 2h. After reduction, the reaction cell was evacuated to a pressure below 10⁻⁹ mbar. Then, the sample was cooled to 150 °C and transferred to the analysis chamber. Data analysis was done with the CasaXPS software (version 2.3.22PR1.0). The binding energy scale was corrected for surface charging by taking the C 1s peak of adventitious carbon as a reference at 284.8 eV.

2.2.3 Catalytic activity measurements

The catalytic performance was determined in a single-pass flow reactor system (Microactivity Reference unit, PID Eng&Tech) operated at a temperature of 220°C or 240 °C, a total pressure of 20 bar and a H₂/CO ratio of 4. In a typical experiment, 50 mg of catalyst (sieve fraction 125-250 μ m) mixed with SiC particles of the same sieve fraction was placed in a tubular reactor with an internal diameter of 9 mm. The temperature was controlled via a thermocouple, located in the centre of the catalytic bed. The reactor was first heated in a flow of H₂ to 350 °C at a rate of 5 °C/min. After a dwell time of 2 h, the reactor was cooled to 220°C and the gas feed composition was changed to reaction conditions. A gas-hourly space velocity (GHSV) of 1000 h⁻¹ was applied which resulted in a CO conversion of about 10 \pm 5%. A TRACE1300 GC from Scientific instrument equipped with a RT-Silica bond column and a flame ionization detector, and a Porabond-Q column and a thermal

conductivity detector was used to measure the products in the reactor effluent. The Weisz–Prater criterion was calculated to confirm operations did not run under internal mass transfer limitations. Under the applied reaction conditions, the production of CO₂ was not detected and the selectivity toward oxygenates on a molar carbon basis was less than 1%. Liquid products and waxes were collected in a downstream cold trap. To calculate the CO conversion independent of volume changes, the feed contained a known amount of Ar (i.e., 9 vol% Ar in CO was used). The CO (X_{CO}) conversion was determined in the following manner:

$$X_{CO} = 1 - \frac{F_{Ar,in}F_{CO,out}}{F_{CO,in}F_{Ar,out}}$$

where $F_{Ar,in}$ is the volumetric Ar flow in the reactor feed, $F_{CO,in}$ is the volumetric CO flow in the reactor feed, $F_{Ar,out}$ and $F_{CO,out}$ are the respective volumetric flows of Ar and CO out of the reactor system.

The carbon-based selectivity of hydrocarbon compound C_i (S_{Ci}) was calculated using:

$$S_{Ci} = \frac{F_{Ar,in}F_{Ci}v_i}{F_{Ar,out}F_{CO,in}X_{CO}}$$

where F_{Ci} is the volumetric flow of hydrocarbon compound C_i out of the reactor, and v_i is the stoichiometric factor of the hydrocarbon compound.

The cobalt time-yield (CTY) was determined using the following equation:

$$CTY = \frac{F_{CO,in}X_{CO}}{m_{Co}}$$

where m_{Co} is the weight of cobalt used in the catalytic reaction. These equations were also used to analyse the activity measured during *in situ* Mössbauer experiments.

2.3. Results and Discussion

2.3.1 Fresh catalyst characterization

Figure 1 shows representative TEM images of the as-prepared Co(4)/CNF, Co(4)Mn/CNF and Co(10)Mn/CNF catalysts. The images clearly show small cobalt oxide nanoparticles dispersed on the fibrous carbon strands of the support. The average size and size distribution of the cobalt phase were determined by measuring the size of about 150 particles in ca. 8 TEM images per sample. The average particle sizes of the Co(4)/CNF and Co(4)Mn/CNF samples were 4.0 ± 2.7 nm and 5.6 ± 3.3 nm, respectively. Thus, the presence of manganese oxide did not substantially affect the particle size of the cobalt phase in the catalyst precursor. The particles in the Co(10)Mn/CNF sample with a higher cobalt loading were larger with an average size of 11.8 ± 5.4 nm.

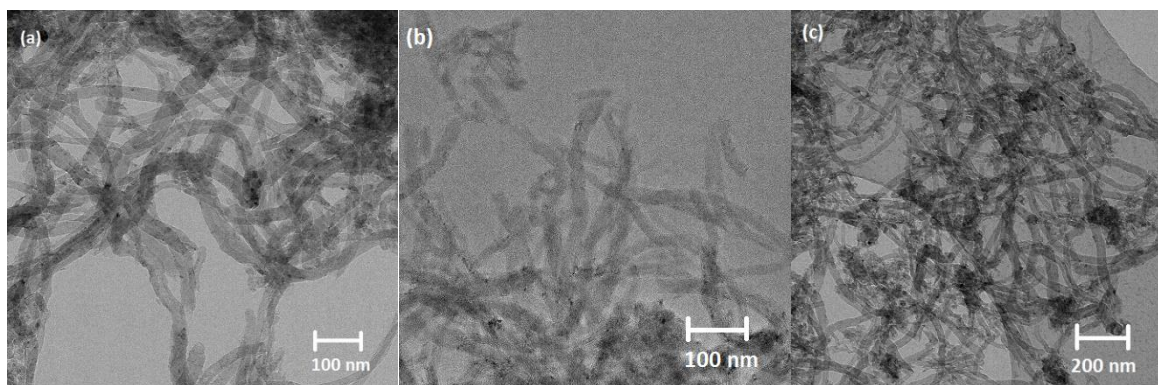


Figure 1. Representative TEM images of from left to right the as prepared (a) Co(4)/CNF, (b) Co(4)Mn/CNF, and (c) Co(10)Mn/CNF.

Mössbauer spectra measured for the fresh catalysts are shown in Figure 2a. All spectra contain a doublet corresponding to oxidic cobalt. This feature has an isomer shift (IS) of 0.2 mm s^{-1} and a quadrupole splitting (QS) of 0.7 mm s^{-1} , which can be assigned to Co^{3+} . The spectrum of the non-promoted Co(4)/CNF catalyst shows a secondary doublet with a spectral contribution of approximately 17%, an IS of 1.0 mm s^{-1} and a QS of 2.2 mm s^{-1} . These Mössbauer parameters are due to Co^{2+} . The observation of two different electronic states of cobalt in the fresh catalysts comes from the Auger cascade that follows the decay of the ^{57}Co probe [40]–[43]. It is important to note that both Co^{3+} and Co^{2+} contributions have been observed by MES in ^{57}Co -doped CoO, a compound in which all cobalt, before nuclear decay, is divalent [40]. This happens because the neighbouring Co^{2+} atoms can stabilize Co^{3+} formed during the Auger cascade of ^{57}Co long enough to be measured. As ^{57}Co probe atoms with more neighbouring Co^{2+} atoms are more likely to stabilize Co^{3+} , this

contribution can provide qualitative information about the dispersion of oxidic cobalt [44]–[46]. For instance, the increasing contribution of the Co^{3+} doublet with increasing cobalt loading on an alumina support could be attributed to a lower dispersion of cobalt oxide [47]. In the spectra of the fresh catalysts, we find the highest contribution of Co^{2+} for the non-promoted Co(4)/CNF sample. This suggests that this catalyst has the highest dispersion of oxidic cobalt. The high Co loading catalyst shows no contribution of Co^{2+} due to the lower dispersion of cobalt oxide.

2.3.2 *In situ* Mössbauer spectroscopy of reduced catalysts

Mössbauer spectra of the catalysts after reduction at 350 °C are given in Figure 2b. The singlet observed for the reduced Co(4)/CNF sample with an IS of 0.0 mm s⁻¹ is due to metallic cobalt. The presence of such a singlet instead of a sextuplet demonstrates that cobalt is present as small cobalt metal particles without magnetic ordering (i.e., < 6 nm)[16]. We will refer to this superparamagnetic (SPM) contribution as small metallic cobalt particles. The spectrum of the Co(4)Mn/CNF sample is different. It contains both singlet (ca. 76%) and sextuplet (ca. 17%) contributions of metallic cobalt. The sextuplet points to the presence of magnetically ordered cobalt metal particles, which is common for particles larger than 6 nm. The finding that this sample contains larger particles is in line with the TEM analysis (Figure 1). The particles represented by this sextuplet will be referred to as large metallic cobalt particles. Furthermore, the spectrum contains a small contribution (7%) of cobalt oxide. The related doublet has an IS of 1.0 mm s⁻¹ and a QS of 2.0 mm s⁻¹, which is indicative of small dispersed Co^{2+} -oxide particles that might be stabilized by their strong interaction with manganese oxide, which does not reduce under our applied conditions [48]. The Mössbauer spectrum of the promoted sample with a higher cobalt loading, Co(10)Mn/CNF, contains the signatures of small and large cobalt particles. Compared to Co(4)Mn/CNF, the sextuplet contribution of large metallic cobalt particles is larger (ca. 44%), which is in line with the presence of larger particles as determined by TEM.

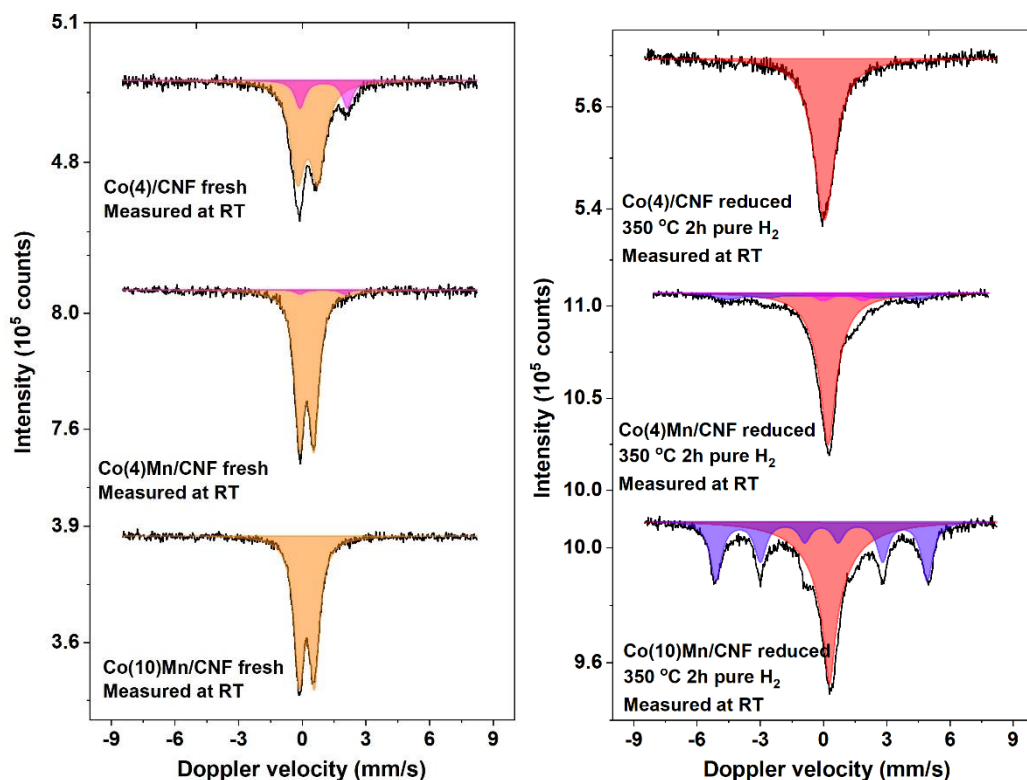


Figure 2. (a) Mössbauer spectra of fresh Co(4)/CNF, Co(4)Mn/CNF, and Co(10)Mn/CNF catalysts: black lines represent the experimental spectra, orange and magenta the fitted cobalt oxide doublets. (b) Mössbauer spectra of reduced Co(4)/CNF, Co(4)Mn/CNF, and Co(10)Mn/CNF catalysts at 350 °C, for 2 hours under pure hydrogen: black lines represent the experimental spectra, red the fitted metallic cobalt SPM singlet, blue the fitted bulk metallic cobalt sextuplet, and magenta the fitted cobalt oxide doublet.

2.3.3 *In situ* Fischer-Tropsch Mössbauer emission spectroscopy

In situ Mössbauer spectra were recorded for the three catalysts as a function of the steam partial pressure at a temperature of 200 °C, a total pressure of 20 bar and a H₂/CO ratio of 4. The steam partial pressure will be expressed as the relative humidity at the applied conditions. In Table A1 the reactant flows at the different experimental conditions are provided. Spectra were recorded for at least 48 h at each humidity step except for the relative humidity of 25% and 57% where the durations were prolonged to 5 and 11 days, respectively. These two treatments were longer, these conditions are most industrially relevant for commercial fixed-bed FTS operation. Moreover, in performing these long-term humidity tests, we aimed to achieve a high degree of deactivation to better understand the underlying deactivation mechanisms. The reported values of the Mössbauer parameters for these

prolonged treatments are obtained from the last two days at these conditions, to accurately report the state of the catalysts at the end of the test.

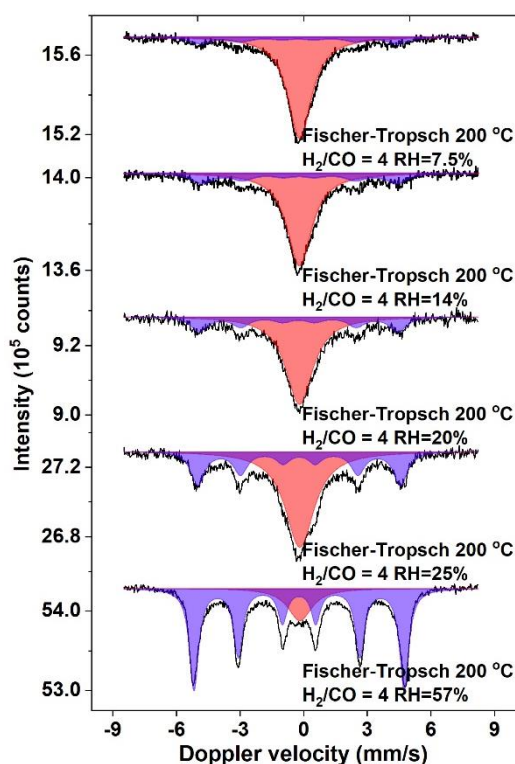


Figure 3. In situ Mössbauer spectra measured of the Co(4)/CNF catalyst during FTS conditions under increasing humidity: black lines represent the experimental spectra, red the fitted metallic cobalt SPM singlet, and blue the fitted bulk metallic cobalt sextuplet.

The spectra for the Co(4)/CNF sample exposed to these treatments contain two contributions of metallic cobalt (Figure 3). The singlet has an IS of -0.2 mm s^{-1} (recorded at $200 \text{ }^{\circ}\text{C}$), which corresponds to small metallic cobalt particles. The sextuplet representing large metallic cobalt particles has the same IS. The changes in the spectral contribution and hyperfine field (HF) of the sextuplet with increasing steam pressure provide qualitative information on the sintering behavior of the metallic cobalt phase. These and other Mössbauer parameters are given in Table A2. The increasing contribution of the sextuplet and concomitant decreasing contribution of the SPM phase clearly show that, with increasing relative humidity, small metallic cobalt particles sinter into larger ones. The increasing HF of the large metallic cobalt sextuplet underpins that the metallic cobalt particles grow when the humidity is increased. It is important to note that the extent of sintering was found to still be increasing during the last days on stream and would have further increased upon longer exposure time. As such the reported values do not reflect a fully deactivated catalyst. The

tendency of cobalt sintering under humid FTS conditions is stronger than observed under non-reactive conditions in previous Mössbauer measurements performed on similar Co/CNF catalysts [16]. Previous studies suggest that the sintering of cobalt during FTS on graphite occurs exclusively through partially oxidized cobalt [49], [50]. In our experiments we were unable to see any contributions of oxidic cobalt. However, the previously mentioned studies and the work of Moodley et al. [6] strongly suggests that this sintering occurs through an Ostwald ripening mechanism, which could explain why we are unable to see these short lived oxidic cobalt species as they migrate over the surface before re-reducing.

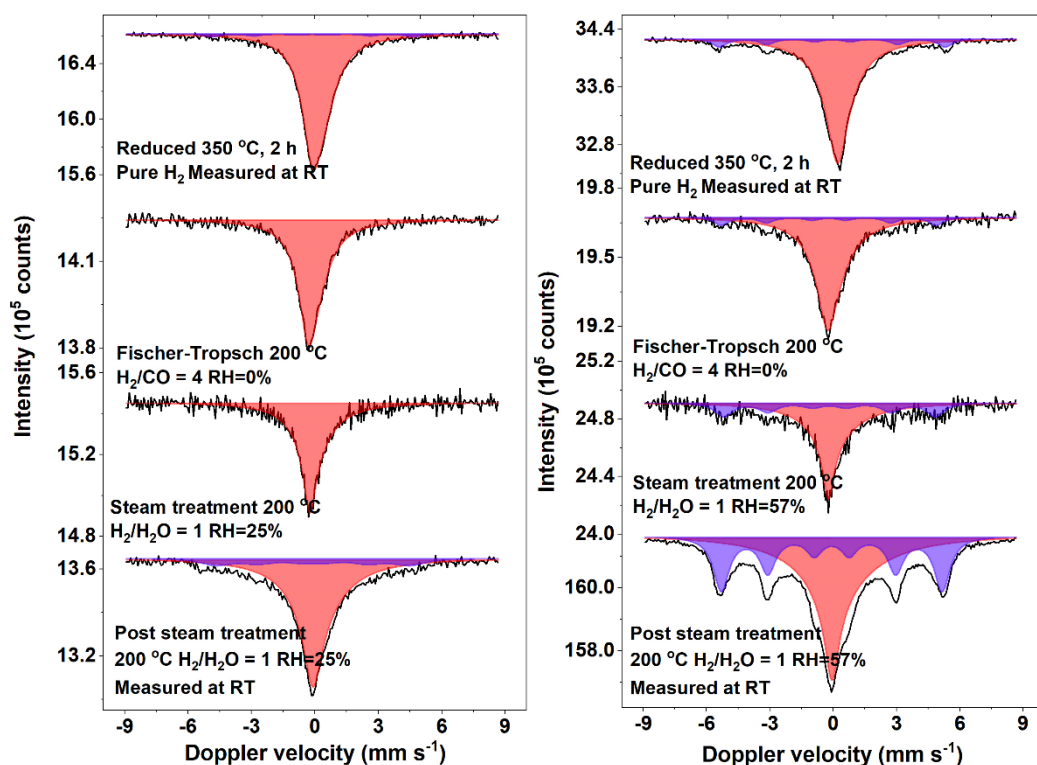


Figure 4. (a) *In situ* Mössbauer spectra measured of the Co(4)/CNF catalyst before, during and after steam treatment with a relative humidity of 25%: black lines represent the experimental spectra, red the fitted metallic cobalt SPM singlet, and blue the fitted bulk metallic cobalt sextuplet. (b) *In situ* Mössbauer spectra measured of the Co(4)/CNF catalyst before, during and after steam treatment with a relative humidity of 57%: black lines represent the experimental spectra, red the fitted metallic cobalt SPM singlet, and blue the fitted bulk metallic cobalt sextuplet.

Additional measurements were performed without CO in the feed to study the effect of exposure to a $\text{H}_2\text{O}/\text{H}_2$ mixture on the sintering of Co(4)/CNF. To this end, a freshly reduced Co(4)/CNF catalyst was exposed at 200 °C to a mixture of steam and hydrogen (molar ratio $\text{H}_2\text{O}/\text{H}_2 = 1$) diluted in two

different flows of inert to achieve relative humidity of 25% and 57% respectively (Table A3). The spectra corresponding to these steam treatment conditions are given in Figure 4. The SPM contributions in the freshly reduced catalysts differ slightly. Following an 11-day treatment at a relative humidity of 25%, the bulk cobalt contribution changed from 5% to 19% as measured at room temperature. At a higher relative humidity of 57%, the sextuplet contribution measured at room temperature increased from 12% after reduction to 41% after 11 days steam treatment. In Figure 5, the impact of process conditions on the fraction of sintered cobalt is plotted as a function of the relative humidity. A clear trend is seen that exposure to more humid conditions results in an increased amount of sintered cobalt particles, which points to the detrimental effect of H₂O. A much more severe sintering is seen for the experiment where both CO and H₂O were present, which points to a synergy between steam and CO on cobalt sintering under FTS conditions. In the cobalt-catalyzed FT reaction, the simultaneous presence of both CO and water cannot be prevented, although the reaction conditions can be moderated to reduce the relative humidity and hence suppress the sintering rate. This is in agreement with previous results found by Claeys et al. [9], who reported enhanced sintering in the presence of both CO and steam for cobalt on an alumina support.

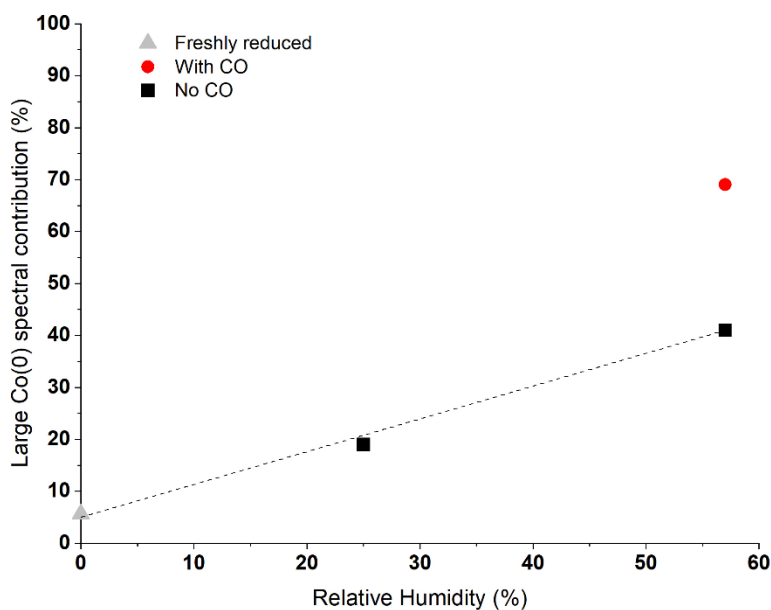


Figure 5. The contribution of relatively large metallic cobalt particles determined by Mössbauer spectroscopy at room temperature of a freshly reduced catalyst (grey) and after treatment under humid conditions without CO (black) and with CO (red).

Spectra measured for the promoted Co(4)Mn/CNF catalyst are given in Figure 6 and the corresponding Mössbauer fit parameters are listed in Table 1. Similar to the non-promoted Co(4)/CNF catalyst, these spectra show a singlet due to small metallic cobalt particles. The Co^{2+} contribution (7%) remaining after reduction indicates that reduction in the presence of manganese oxide is more difficult. This is in line with literature [32], [51]. Complete reduction of the cobalt phase was obtained after the first FTS conditions without steam, although during this and subsequent humid treatments no reduction of the manganese oxide promotor is expected [48]. During the experiment and different from Co(4)/CNF without manganese oxide, this sample does not undergo extensive sintering of small metallic cobalt particles into larger ones upon humid FTS treatments. Only after 11 days at the highest relative humidity of 57%, a contribution of larger cobalt particles is apparent from the observation of a sextuplet. Another difference with the manganese oxide-free sample is the appearance of a doublet with an IS of 0.0 mm s^{-1} and a QS of 0.8 mm s^{-1} (recorded at 200°C) at a relative humidity of 14%. This doublet can be attributed to cobalt carbide species, analogous to the Fe_xC phase found in previous Mössbauer results [52]. This assignment was further confirmed by carbidizing a cobalt catalyst under pure CO, which resulted in a dominant carbide phase (60%) with the same Mössbauer parameters as shown in Figure A4 (IS = 0.1 mm s^{-1} , QS = 0.8 mm s^{-1}). Thus, the manganese oxide-promoted catalyst was partially carbidized under the given experimental conditions.

Table 1 shows how the spectral contribution of this cobalt carbide phase evolved with increasing relative humidity. While initially an increasing steam partial pressure resulted in more extensive carbidization, the contribution of carbidized species did not further increase when the relative humidity was raised above 25%. The contribution of the cobalt carbide phase was about 20%. Contrary to previously observed cobalt metal sintering, the spectral contribution of carbide did not further increase when the treatment was prolonged to 11 days. The contribution measured during the first two days (19%) was equal to the one found during the final two days of treatment. This shows that the carbide phase is formed relatively fast upon application of the humid FTS conditions. At the end of these measurements, the carbidized sample was reduced in pure H_2 at 350°C for 2 h. The spectrum in Figure 7 shows that the Co_2C phase was converted to large metallic cobalt particles as evident from growth of the sextuplet which is indicative of large cobalt nanoparticles. Comparing the spectra of the re-reduced Co(4)Mn/CNF sample with the non-promoted Co(4)/CNF sample subjected to the same humidity treatments shows that, after the same treatment, the promoted catalyst contains 60% small metallic cobalt nanoparticles, while this amounts to 31% for the unpromoted catalyst. This difference indicates that the cobalt particles in the unpromoted Co(4)/CNF catalyst have grown more

than those in the promoted Co(4)Mn/CNF catalyst. These observations highlight that manganese oxide decreases sintering during humid FTS operation, although a small part of the metallic cobalt phase is carbidized.

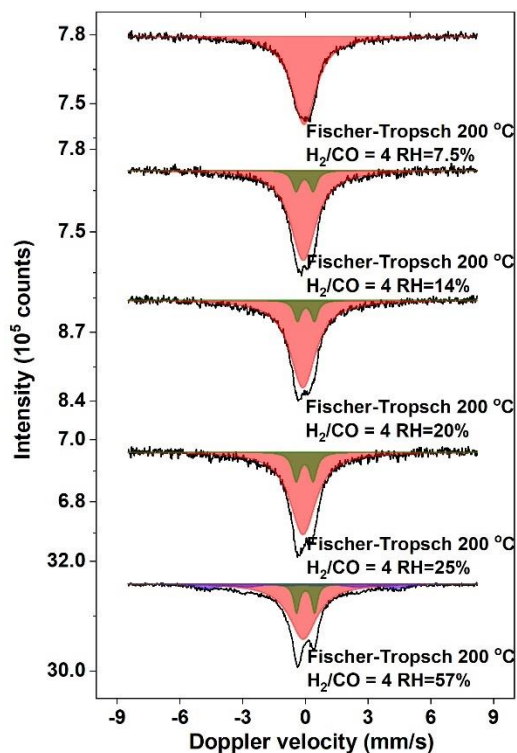


Figure 6. In situ Mössbauer spectra measured of the Co(4)Mn/CNF catalyst during FTS conditions under increasing humidity: black lines represent the experimental spectra, red the fitted metallic cobalt SPM singlet, blue the fitted bulk metallic cobalt

Table 1. Fit parameters of Mössbauer spectra of the Co(4)Mn/CNF catalyst after different treatments.

<i>Treatment</i>	<i>Temperature (°C)</i>	<i>Cobalt phase</i>	<i>Isomer Shift (mm s⁻¹)</i>	<i>Hyperfine Field (kOe)</i>	<i>Quadrupole Splitting (mm s⁻¹)</i>	<i>Spectral Contribution (%)</i>
<i>After reduction</i>	20	<i>Co(0) SPM</i>	0.2	-	-	76
		<i>Co(0) bulk</i>	-0.1	292	-	17
		<i>Co²⁺</i>	1.0	-	2.0	7

<i>During FT reaction</i>	200	<i>Co(0)</i>	0.0	-	-	100
		<i>SPM</i>				
<i>RH = 7.5%</i>	200	<i>Co(0)</i>	-0.1	-	-	100
		<i>SPM</i>				
<i>RH = 14%</i>	200	<i>Co(0)</i>	-0.1	-	-	88
		<i>SPM</i>				
		<i>Co₂C</i>	0.0	-	0.8	12
<i>RH = 20%</i>	200	<i>Co(0)</i>	-0.1	-	-	88
		<i>SPM</i>				
		<i>Co₂C</i>	0.0	-	0.8	12
<i>RH = 25%</i>	200	<i>Co(0)</i>	-0.1	-	-	82
		<i>SPM</i>				
		<i>Co₂C</i>	0.0	-	0.8	18
<i>RH = 57%</i>	200	<i>Co(0)</i>	-0.1	-	-	66
		<i>SPM</i>				
		<i>Co(0)</i>	-0.2	281	-	15
		<i>bulk</i>				
		<i>Co₂C</i>	0.0	-	0.9	19
<i>After reaction</i>	20	<i>Co(0)</i>	0.0	-	-	63
		<i>SPM</i>				
		<i>Co(0)</i>	-0.1	298	-	17
		<i>bulk</i>				
<i>Reduced</i>	20	<i>Co₂C</i>	0.1	-	0.8	20
		<i>Co(0)</i>	0.0	-	-	60
		<i>SPM</i>				
		<i>Co(0)</i>	-0.1	314	-	40
		<i>bulk</i>				

Previous studies on carbon-supported cobalt catalysts have shown that direct oxidation by water of the metallic cobalt particles is kinetically hindered in the absence of CO [22]. However, when CO was introduced, rapid oxidation to cobalt oxide occurred. The authors proposed a mechanism in which removal of adsorbed oxygen due to CO dissociation is hindered by water. Whilst no oxidic cobalt is

observed in our spectra, we find that part of cobalt carbidizes when both CO and steam are present. This carbidization might follow a similar mechanism as that postulated for oxidation, where carbon accumulates on the surface due to fast CO dissociation in the presence of the manganese oxide promoter and removal being hindered by water. The accumulation of carbon species on the surface would facilitate the formation of cobalt carbide. In a different study [24], it was shown that the formation of cobalt carbide can also occur under industrial FTS conditions when cobalt is supported on alumina. Although it was mentioned that cobalt carbide formation is strongly kinetically inhibited, it was noted that higher partial pressures of steam enhance carbidization in keeping with the findings in the present work.

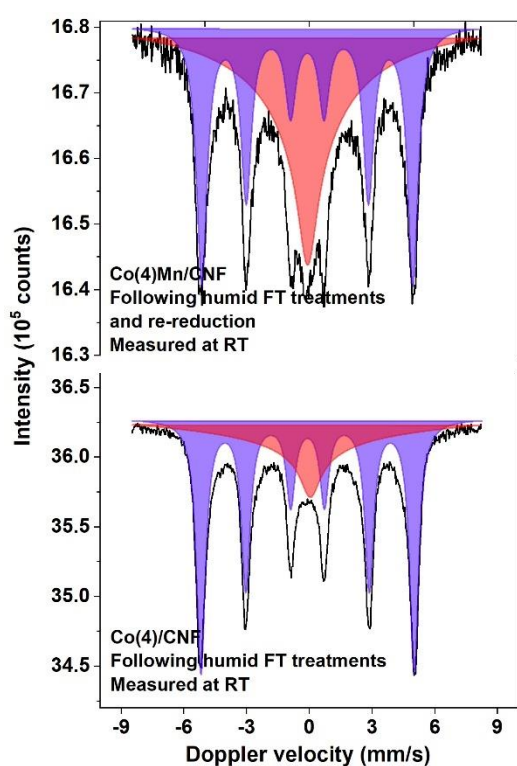


Figure 7. Mössbauer spectra measured on Co(4)Mn/CNF and Co(4)/CNF following the humid FTS treatments: black lines represent the experimental spectra, red the fitted metallic cobalt SPM singlet, and blue the fitted bulk metallic cobalt sextuplet.

Following the removal of the carbide phase with hydrogen at 350 °C, the Co(4)Mn/CNF catalyst was exposed to FTS conditions without co-feeding of steam. Different from the freshly reduced sample where exposure to a FTS feed mixture did not lead to structural changes, such exposure of the re-reduced catalyst initially treated under humid FTS conditions led to the formation of cobalt carbide. Figure 8 shows that a cobalt carbide doublet already appears after 6 h on stream under these mild

conditions. Following 48 h under FTS conditions, the spectral contribution of the carbide doublet increased to 25%, which is even higher than it was before re-reduction. Comparing the contributions of the two metallic cobalt phases, the formation of cobalt carbide mainly led to a decrease in the bulk metallic phase. The spectral contribution of this sextuplet dropped from 40% to 22% under FTS conditions, whereas the SPM contribution only decreased by 6%.

2.3.4 Understanding carbidization under FTS conditions

The above findings indicate that the steam treatment and re-reduction resulted in a larger propensity to carbidization of cobalt in the presence of manganese. Additional experiments to gain further insight into this aspect involved the exposure of a freshly reduced Co(4)Mn/CNF catalyst to a mixture of H₂O/H₂ without CO, followed by replacing the feed by a CO/H₂ mixture. This led to the formation of cobalt carbide as shown in Figure A5. From this, we infer that the observed more pronounced carbidization is caused by the high steam partial pressure under reducing conditions. From the finding that a catalyst, partially carbidized under humid FTS conditions and subsequently re-reduced, formed the same carbide phase under FTS conditions without steam co-feeding (Figure 8), we can infer that the change that induces carbidization cannot be reversed by a reduction step. Following a recent report that reduction-oxidation-reduction (ROR) treatment can lead to the redispersion of the metallic cobalt particles [4], [7], [12], a freshly reduced Co(4)Mn/CNF catalyst was exposed to a mixture of H₂O/H₂ in inert. Subsequently, the catalyst was exposed to a high partial pressure of steam in inert. In this oxidizing environment, the metallic cobalt particles were fully oxidized as can be appreciated from Figure A6. Following this oxidation step, the catalyst was re-reduced in pure hydrogen and subsequently exposed to FTS conditions without steam co-feeding. The resulting spectra also given in Figure A6 show that no carbide was formed under these conditions. This indicates that the changes in the structure caused by the high partial pressures of steam are reversible by a ROR treatment, potentially through the redispersion of the cobalt particles on the support or a reduced manganese-cobalt interaction.

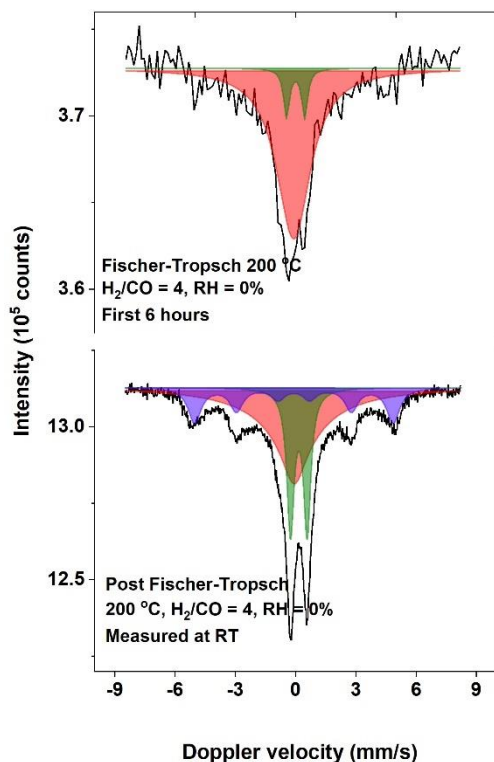


Figure 8. In situ Mössbauer spectra measured on the Co(4)Mn/CNF catalyst during dry Fischer-Tropsch conditions: black lines represent the experimental spectra, red the fitted metallic cobalt SPM singlet, blue the fitted bulk metallic cobalt sextuplet, and green the fitted cobalt carbide doublet.

We also investigated the tendency of carbidization for the Co(10)Mn/CNF catalyst. The Mössbauer spectrum of the reduced catalyst contains two contributions of metallic cobalt in the form of small and large particles (Figure 2). Compared to Co(4)Mn/CNF, this sample contains a contribution of larger metallic cobalt particles, in line with the larger particle size determined by TEM. The *in situ* spectra measured during the various humidity treatments are given in Figure 9, while the Mössbauer fit parameters are listed in Table A7. Different from Co(4)Mn/CNF, the cobalt carbide doublet for this sample was already observed at the lowest relative humidity of 7.5%. While the spectral parameters of this cobalt carbide doublet ($IS = 0.0 \text{ mm s}^{-1}$, $QS = 0.8 \text{ mm s}^{-1}$) are the same as those observed for the partially carbidized Co(4)Mn/CNF sample, the relative fraction of this cobalt carbide phase is larger for the Co(10)Mn/CNF sample (Figure 10). As before, it is observed that the degree of carbidization increases with relative humidity, further underpinning the role of steam in carbidization. Table A7 also shows that the HF of the sextuplet contribution representing larger metallic Co particles decreases during these humidity treatments. This agrees with the earlier conclusion that especially

relatively large metallic cobalt particles within the fraction of magnetically ordered cobalt particles are prone to carbidisation.

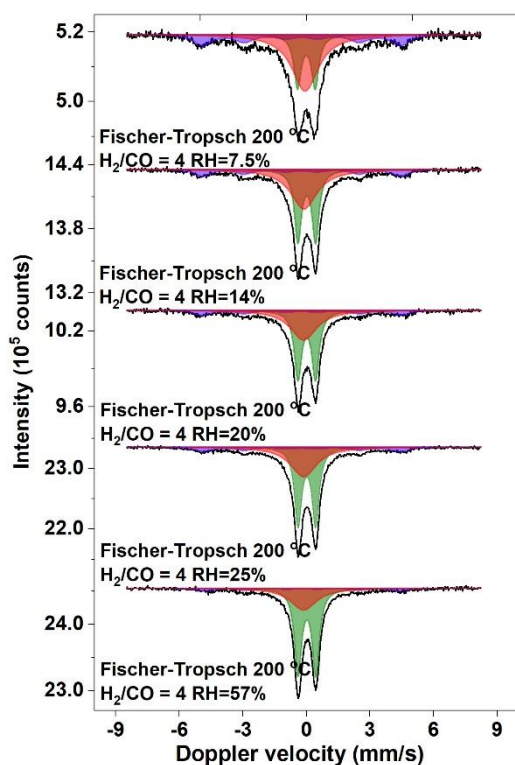


Figure 9. In situ Mössbauer spectra measured of the Co(10)Mn/CNF catalyst during Fischer-Tropsch conditions under increasing humidity: black lines represent the experimental spectra, red the fitted metallic cobalt SPM singlet, blue the fitted bulk metallic cobalt sextuplet, and green the fitted cobalt carbide doublet.

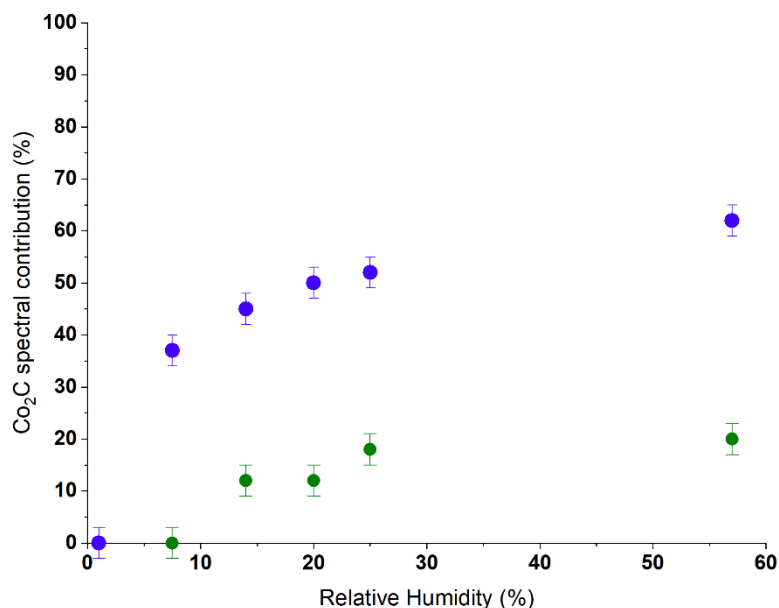


Figure 10. Spectral contribution of cobalt carbide during increasingly humid Fischer-Tropsch conditions: the green circles show the spectral contribution measured for the Co(4)Mn/CNF catalyst, and the blue circles show the spectral contribution for the Co(10)Mn/CNF catalyst. Error bars show the experimental uncertainty of the calculated spectral contribution.

2.3.5 Characterization of used catalysts

The catalysts were also characterized after the *in situ* Mössbauer spectroscopy measurements. For this, nonradioactive samples exposed to the same conditions as the radioactive samples were used placed in the same cell. Representative TEM images of the used catalysts are given in Figure 11. While small cobalt nanoparticles are observed for all catalysts, the manganese-promoted samples also contain larger agglomerates of particles, some of which are well above 50 nm in size. When determining the average particle size, the individual particles that make up these agglomerates were measured. Additionally, care was taken to distinguish between manganese oxide and cobalt particles by looking at the shape and contrast, as well as using EDX information. The average particle size for the used Co(4)/CNF and Co(4)Mn/CNF catalysts were 10.7 ± 6.6 nm and 11.6 ± 6.8 nm, respectively. This evidences that the cobalt phase has sintered in both catalysts. For the Co(10)Mn/CNF catalyst, the average particle size was 13.7 ± 7.7 nm, implying relatively speaking a smaller impact of the treatment on the initially larger particles.

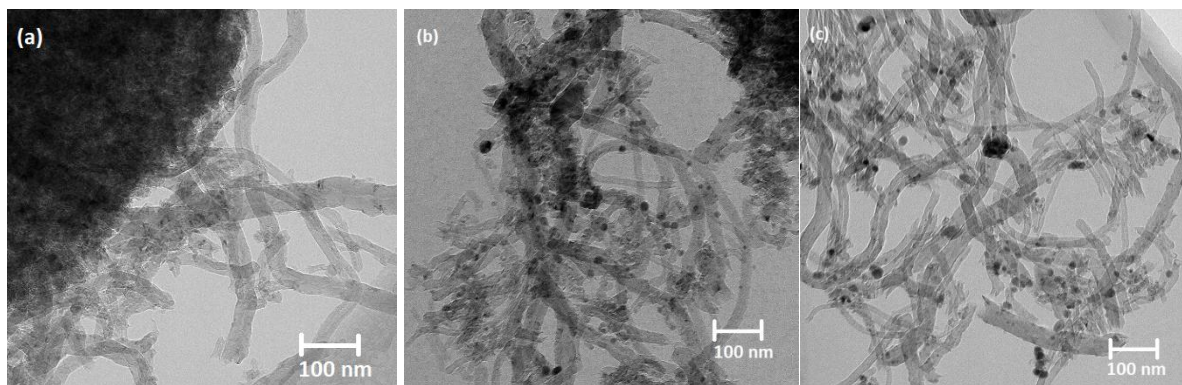


Figure 11. Representative TEM images of used (a) Co(4)/CNF, (b) Co(4)Mn/CNF, and (c) Co(10)Mn/CNF.

To better understand cobalt carbidization, EDX measurements were performed on fresh and used Co(4)Mn/CNF and Co(10)Mn/CNF catalysts. For each of these four samples, approximately 10 different EDX maps were measured on various spots of the sample to ensure the measurements were representative for their respective catalyst. EDX maps obtained on the freshly reduced and passivated Co(10)Mn/CNF catalysts are given in Figure 12. These maps show the proximity between cobalt and manganese with manganese being homogeneously dispersed on the support surface. Cobalt is present as nanoparticles with a size of about 10 nm with strong interactions with the manganese oxide promotor. The EDX maps in Figure 13 for the used Co(10)Mn/CNF are very different. This catalyst contains manganese oxide particles with sizes larger than 100 nm. Three of such large manganese oxide particles were observed in the 10 EDX maps obtained for this catalyst. These large particles interact with few cobalt particles. Consequently, large parts of the carbon support surface have become relatively poor in manganese oxide. Similar findings were observed for the used Co(4)Mn/CNF catalyst, which showed two very large manganese oxide particles on the 10 measured EDX maps. Their size was smaller than in the Co(10)Mn/CNF catalyst, which can be explained by the lower manganese content of the former. These maps provide a clearer understanding of the effects that humid FTS conditions have on the catalyst morphology. Not only cobalt but also manganese oxide appears to be mobile under humid FTS conditions. The high mobility of manganese oxide results in significant sintering into large particles, which exhibit a strong interaction with part of the metallic cobalt particles. It has been shown that the proximity of Co and Mn in the precursor facilitates the formation of cobalt carbide under FTS conditions [53]. Thus, we speculate that the larger cobalt particles that strongly interact with manganese oxide are carbidized under humid FTS conditions. Furthermore, these images as well as the TEM analysis suggest that promotion with manganese oxide

does not limit cobalt mobility to a significant extent on the carbon support. Whilst the presence of manganese oxide allows more of the cobalt to remain small as supported by the Mössbauer findings, the bulk particles sinter to a similar extent and are subsequently carbidized under reactive conditions.

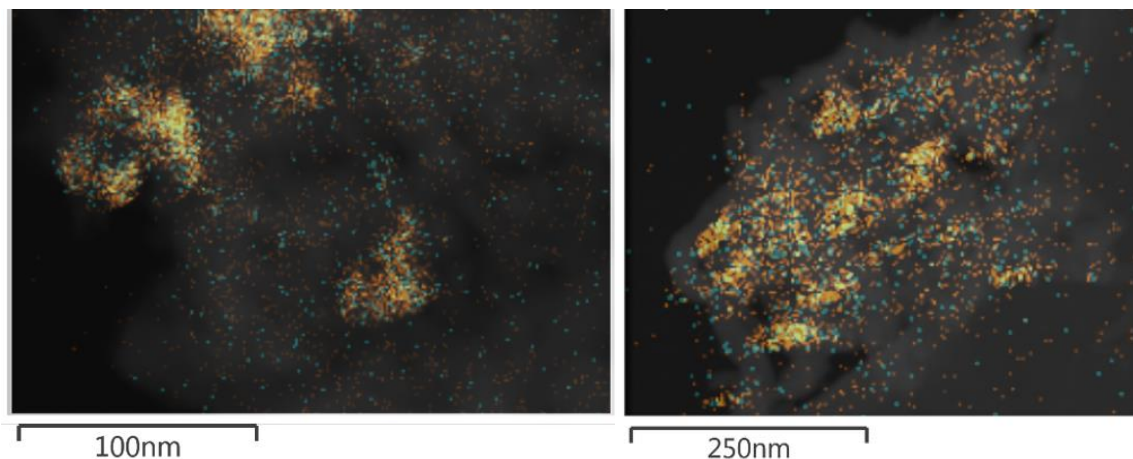


Figure 12. EDX mappings of a reduced and passivated Co(10)Mn/CNF catalyst: the manganese mapping is shown in teal and the cobalt mapping in orange.

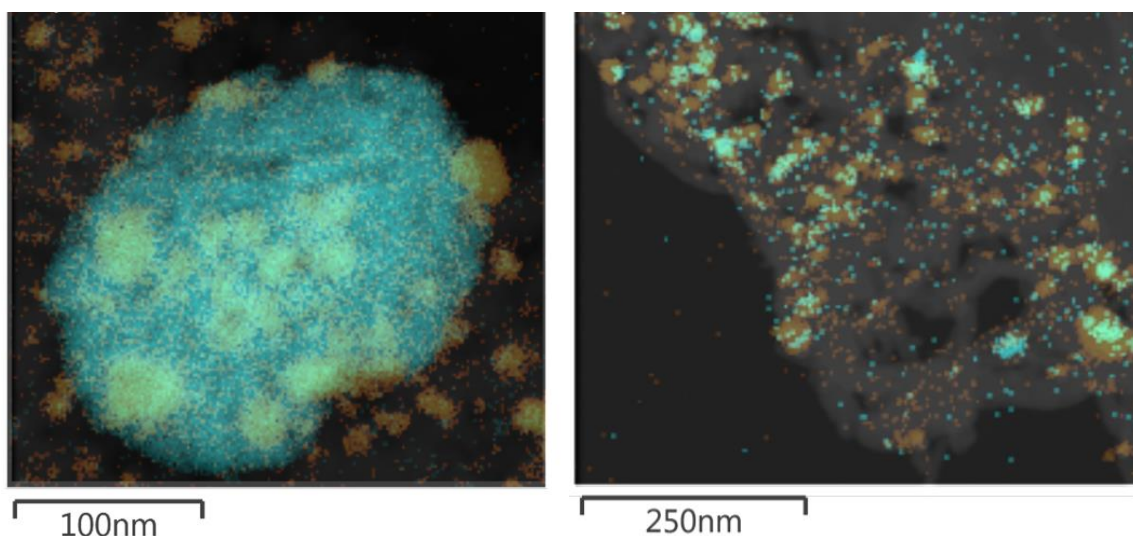


Figure 13. EDX mappings of a used Co(10)Mn/CNF catalyst: the manganese mapping is shown in teal and the cobalt mapping in orange.

Quasi in situ XPS was used to further investigate the apparent sintering of the used catalysts. These results, given in Figure A8 and Table A9, show the decrease in Co/C peak ratio for every used catalyst compared to their respective fresh counterpart. Additionally, for every catalyst a higher DOR after use was observed. These two findings indicate that indeed, all catalysts experienced sintering during the humid Mössbauer treatments.

2.3.6 Catalytic activity measurements

Besides catalytic activity measurements in the *in situ* MES cell, the performance of the cobalt catalysts was measured in a high-pressure plug-flow reactor at 220 °C, 20 bar, a H₂/CO ratio of 4, and a gas hourly space velocity of 6500 h⁻¹. The results for the fresh and used catalysts are collected in Table 2. Figure 14 plots the measured CTY values for the freshly reduced and used catalysts, alongside previously obtained values from literature [18] on similar carbon nanofiber supported cobalt catalysts measured at 220 °C, 1 bar and a H₂/CO ratio of 2. Turnover frequencies (TOFs) were determined for all freshly reduced catalysts as well as the non-promoted Co(4)/CNF catalyst based on the average particle size determined by TEM assuming spherical particle shape. We do not report TOFs for the used Co(4)Mn/CNF and Co(10)Mn/CNF catalysts, because these samples contain an appreciable amount of cobalt carbide.

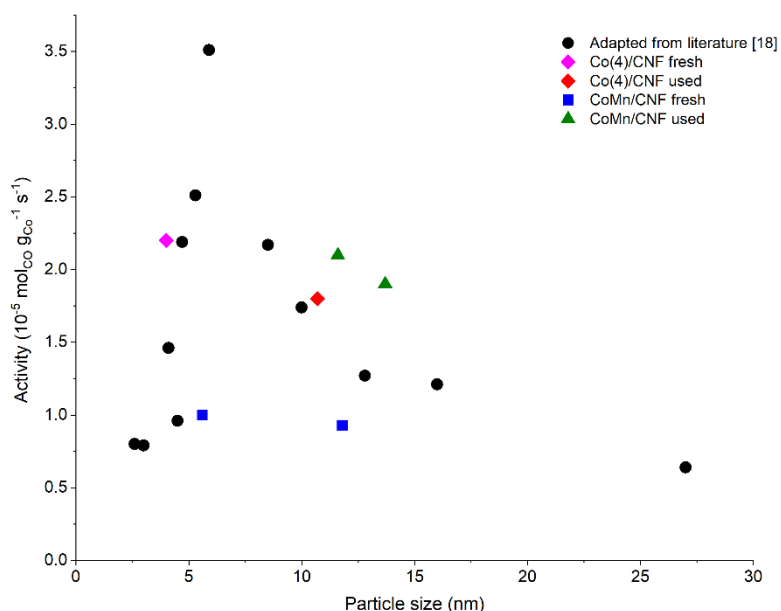


Figure 14. Correlation between the activity of carbon-supported cobalt catalysts and their particle size. In black previously reported activities adapted from literature [18], in magenta Co(4)/CNF fresh, in red Co(4)/CNF used, in blue Co(4)Mn/CNF and Co(10)Mn/CNF fresh, and in olive Co(4)Mn/CNF and Co(10)Mn/CNF used.

The Co(4)/CNF catalysts shows the expected loss in CTY activity after being exposed to humid FTS conditions, which can be explained by sintering of the metallic cobalt under humid FTS conditions. The activity only decreasing 20% versus an increase of the average cobalt particle size from 4.0 to 10.7 nm can be rationalized by the cobalt particle size effect. Upon sintering of cobalt particles smaller than 6-8 nm, the TOF of the surface atoms increases in accordance to the relation between catalytic

activity and cobalt particle size [18]. The manganese-promoted catalysts show a significantly lower activity than the unpromoted catalyst after reduction. However, one would expect a higher activity given the presence of larger particles in Co(4)Mn/CNF in comparison to Co(4)/CNF. Nevertheless, it has been established before that manganese can be present on the cobalt surface lowering the FT activity through overpromotion. For instance, manganese promotion of Co/CNF (cobalt-to-manganese ratio of 10) led to a decrease of the activity by 35% [32]. The cobalt-to-manganese ratio in the present study is higher, providing a possible explanation for the significant activity decrease of the freshly reduced catalyst as well as a lower TOF despite a more optimal cobalt particle size. After use under humid FTS conditions and despite an increase of the cobalt particle size, the catalytic activity of the Co(4)Mn/CNF sample was twice that of the freshly reduced catalyst. Two explanations can be put forward. First, the increase in the cobalt particle size will increase the intrinsic activity through the particle size effect. Second, manganese migration as evidenced from TEM analysis can explain this difference. As manganese agglomerated into large clusters, the residual catalyst surface would come much closer to the optimum cobalt-to-manganese ratio for activity, which was found to be around 100 [32]. An indication that cobalt and manganese are still associated in the used catalyst follows from the lower methane selectivity compared to the non-promoted catalyst. These findings are in keeping with the notion that manganese is a promoter for the activity of cobalt FTS catalysts at low surface concentrations [32], [51], [54].

The Co(10)Mn/CNF catalyst showed a similar activity increase upon use as the Co(4)Mn/CNF catalyst. A closer look reveals an interesting trend in the selectivity data. In the series tested, both Co(10)Mn/CNF samples had significantly increased C₂-C₄ selectivity compared to the other ones. Such a difference has been earlier reported under 20 bar FTS conditions for overpromoted catalysts but was accompanied with a higher methane selectivity. In this series, the methane selectivity was lowest for the sample with highest manganese content. Moreover, the increased C₂-C₄ selectivity was at expense of the C₅+ selectivity, which can be beneficial for obtaining of light olefins.

Comparing the selectivity data in Table 2, all used catalysts show an increase in C₅+ selectivity compared to their fresh counterparts, which goes together with a decrease in the methane selectivity. It is well known that larger cobalt particles are more selective to longer hydrocarbons, while small cobalt nanoparticles are more selective to methane ([18]). The differences noted between our catalysts can be explained by the sintering under FTS conditions. Specifically for the manganese-promoted catalysts, the decrease of the negative effects of manganese overpromotion will also contribute to the improved C₅+ selectivity.

Table 2. Catalytic performance data for the cobalt catalysts (plug-flow reactor operated at 220 °C, 20 bar and $H_2/CO = 4$, GHSV = 6500 h⁻¹)

^aTOF was based on the dispersion found by TEM, assuming spherical particles.

<i>Catalyst</i>	<i>Conversion (%)</i>	<i>C₁ selectivity (%)</i>	<i>C_{2-C4} selectivity (%)</i>	<i>C₅₊ selectivity (%)</i>	<i>CTY (10⁻⁵ mol_{CO} g_{Co}⁻¹ s⁻¹)</i>	<i>TOF^a (10⁻³ s⁻¹)</i>
Co(4)/CNF	2	27	9	64	2.2	4.7
Co(4)/CNF used	3	16	8	76	1.8	10.3
Co(4)Mn/CNF	7	21	8	71	1.0	3.0
Co(4)Mn/CNF used	3	10	8	82	2.1	-
Co(10)Mn/CNF	4	19	14	67	0.93	5.9
Co(10)Mn/CNF used	8	8	15	77	1.9	-

2.4. Conclusions

The use of *in situ* Mössbauer spectroscopy showed a synergy between carbon monoxide and steam on the sintering of manganese-free metallic cobalt particles during FTS. Sintering in the absence of either carbon monoxide or steam was much less severe compared to the case where both gases were present. This suggests enhanced mobility of cobalt in the presence of carbon monoxide and steam. No oxidation of cobalt was observed, even at the highest steam partial pressures. Mössbauer spectroscopy shows that a substantial part of the cobalt nanoparticles remains small (in the SPM phase) in the presence of the manganese promoter. While sintering was nearly absent without steam and cobalt remained completely in the metallic form, increasing steam partial pressure led to the transformation of part of the metallic cobalt phase to cobalt carbide. EDX mapping shows that these cobalt carbide particles are likely formed due to their strong interaction with manganese oxide. Such measurements also indicate the sintering of manganese oxide under humid conditions, with particles up to 100 nm being observed on the carbon nanofiber support. The cobalt carbide phase could be fully reduced into relatively large cobalt particles. The latter result confirms the suggestion from EDX

that the cobalt carbide particles were already sintered compared to the cobalt precursor. Carbidization was observed to be more severe at higher cobalt and manganese loadings. Overall, carbidization presented an alternative deactivation mechanism for the manganese-promoted cobalt nanoparticle catalyst.

Bibliography

- [1] E. Iglesia, "Design, synthesis, and use of cobalt-based Fischer-Tropsch synthesis catalysts," *Appl. Catal. A Gen.*, vol. 161, no. 1–2, pp. 59–78, 1997, doi: 10.1016/S0926-860X(97)00186-5.
- [2] E. Rytter, N. E. Tsakoumis, and A. Holmen, "On the selectivity to higher hydrocarbons in Co-based Fischer-Tropsch synthesis," *Catal. Today*, vol. 261, pp. 3–16, 2016, doi: 10.1016/j.cattod.2015.09.020.
- [3] J. P. den Breejen *et al.*, "On the Origin of the Cobalt Particle Size Effects in Fischer-Tropsch Catalysis," *J. Am. Chem. Soc.*, vol. 131, no. 20, pp. 7197–7203, 2009, doi: 10.1021/ja901006x.
- [4] N. E. Tsakoumis, M. Rønning, Ø. Borg, E. Rytter, and A. Holmen, "Deactivation of cobalt based Fischer-Tropsch catalysts: A review," *Catal. Today*, vol. 154, no. 3–4, pp. 162–182, 2010, doi: 10.1016/j.cattod.2010.02.077.
- [5] P. J. van Berge and R. C. Everson, "Cobalt as an alternative Fischer-Tropsch catalyst to iron for the production of middle distillates," in *Studies in Surface Science and Catalysis*, vol. 107, no. 15, pp. 207–212, 1997, doi: 10.1016/S0167-2991(97)80336-9.
- [6] D. Moodley *et al.*, "Sintering of cobalt during FTS: Insights from industrial and model systems," *Catal. Today*, vol. 342, pp. 59–70, 2020, doi: 10.1016/j.cattod.2019.03.059.
- [7] E. Rytter and A. Holmen, "Deactivation and regeneration of commercial type Fischer-Tropsch co-catalysts—A mini-review," *Catalysts*, vol. 5, no. 2, pp. 478–499, 2015, doi: 10.3390/catal5020478.
- [8] Z. Yu, Ø. Borg, D. Chen, E. Rytter, and A. Holmen, "Role of surface oxygen in the preparation and deactivation of carbon nanofiber supported cobalt Fischer-Tropsch catalysts," *Top. Catal.*, vol. 45, no. 1–4, pp. 69–74, 2007, doi: 10.1007/s11244-007-0242-7.
- [9] M. Claeys *et al.*, "Impact of Process Conditions on the Sintering Behavior of an Alumina-Supported Cobalt Fischer-Tropsch Catalyst Studied with an in Situ Magnetometer," *ACS Catal.*, vol. 5, no. 2, pp. 841–852, 2015, doi: 10.1021/cs501810y.
- [10] M. D. Argyle, T. S. Frost, and C. H. Bartholomew, "Cobalt Fischer-Tropsch catalyst deactivation modeled using generalized power law expressions," *Top. Catal.*, vol. 57, no. 6–9, pp. 415–429, 2014, doi: 10.1007/s11244-013-0197-9.
- [11] M. Rahmati, M. Safdari, T. H. Fletcher, M. D. Argyle, and C. H. Bartholomew, "Chemical and Thermal Sintering of Supported Metals with Emphasis on Cobalt Catalysts During Fischer-Tropsch Synthesis," *Chem. Rev.*, vol. 120, no. 10, pp. 4455–4533, 2020, doi: 10.1021/acs.chemrev.9b00417.
- [12] C. E. Kliewer, S. L. Soled, and G. Kiss, "Morphological transformations during Fischer-Tropsch synthesis on a titania-supported cobalt catalyst," *Catal. Today*, vol. 323, pp. 233–256, 2019, doi: 10.1016/j.cattod.2018.05.021.
- [13] T. O. Eschemann and K. P. de Jong, "Deactivation Behavior of Co/TiO₂ Catalysts during Fischer-Tropsch Synthesis," *ACS Catal.*, vol. 5, no. 6, pp. 3181–3188, 2015, doi: 10.1021/acscatal.5b00268.
- [14] M. Wolf *et al.*, "In-depth characterisation of metal-support compounds in spent Co/SiO₂ Fischer-Tropsch model catalysts," *Catal. Today*, vol. 342, pp. 71–78, 2020, doi: 10.1016/j.cattod.2019.01.065.
- [15] W. Zhou, J.-G. Chen, K.-G. Fang, and Y.-H. Sun, "The deactivation of Co/SiO₂ catalyst for Fischer-Tropsch synthesis at different ratios of H₂ to CO," *Fuel Process. Technol.*, vol. 87, no. 7, pp. 609–616, 2006, doi: 10.1016/j.fuproc.2006.01.008.
- [16] G. L. Bezemer, T. J. Remans, A. P. van Bavel, and A. I. Dugulan, "Direct Evidence of Water-Assisted Sintering of Cobalt on Carbon Nanofiber Catalysts during Simulated Fischer-Tropsch Conditions Revealed with in Situ Mössbauer Spectroscopy," *J. Am. Chem. Soc.*, vol. 132, no. 25, pp. 8540–8541, 2010, doi: 10.1021/ja103002k.
- [17] Z. Yu *et al.*, "Carbon Nanofiber Supported Cobalt Catalysts for Fischer-Tropsch Synthesis with High Activity and Selectivity," *Catal. Letters*, vol. 109, no. 1–2, pp. 43–47, 2006, doi: 10.1007/s10562-006-0054-6.
- [18] G. L. Bezemer *et al.*, "Cobalt particle size effects in the Fischer-Tropsch reaction studied with carbon nanofiber supported catalysts," *J. Am. Chem. Soc.*, vol. 128, no. 12, pp. 3956–3964, 2006, doi: 10.1021/ja058282w.
- [19] E. Van Steen, M. Claeys, M. E. Dry, J. Van De Loosdrecht, E. L. Viljoen, and J. L. Visagie, "Stability of nanocrystals: Thermodynamic analysis of oxidation and re-reduction of cobalt in water/hydrogen mixtures," *J. Phys. Chem. B*, vol. 109, no. 8, pp. 3575–3577, 2005, doi: 10.1021/jp045136o.
- [20] J. van de Loosdrecht *et al.*, "Cobalt Fischer-Tropsch synthesis: Deactivation by oxidation?," *Catal. Today*, vol. 123, no. 1–4, pp. 293–302, 2007, doi: 10.1016/j.cattod.2007.02.032.
- [21] H. Karaca *et al.*, "Structure and catalytic performance of Pt-promoted alumina-supported cobalt catalysts under realistic conditions of Fischer-Tropsch synthesis," *J. Catal.*, vol. 277, no. 1, pp. 14–26, 2011, doi: 10.1016/j.jcat.2010.10.007.
- [22] M. Wolf, B. K. Mutuma, N. J. Coville, N. Fischer, and M. Claeys, "Role of CO in the Water-Induced Formation of Cobalt Oxide in a High Conversion Fischer-Tropsch Environment," *ACS Catal.*, vol. 8, no. 5, pp. 3985–3989, 2018, doi: 10.1021/acscatal.7b04177.

- [23] M. Sadeqzadeh *et al.*, “Mechanistic Modeling of Cobalt Based Catalyst Sintering in a Fixed Bed Reactor under Different Conditions of Fischer–Tropsch Synthesis,” *Ind. Eng. Chem. Res.*, vol. 51, no. 37, pp. 11955–11964, 2012, doi: 10.1021/ie3006929.
- [24] M. Claeys *et al.*, “In situ magnetometer study on the formation and stability of cobalt carbide in Fischer–Tropsch synthesis,” *J. Catal.*, vol. 318, pp. 193–202, 2014, doi: 10.1016/j.jcat.2014.08.002.
- [25] G. Jacobs, P. M. Patterson, Y. Zhang, T. Das, J. Li, and B. H. Davis, “Fischer–Tropsch synthesis: deactivation of noble metal-promoted Co/Al₂O₃ catalysts,” *Appl. Catal. A Gen.*, vol. 233, no. 1–2, pp. 215–226, 2002, doi: 10.1016/S0926-860X(02)00147-3.
- [26] H. Karaca *et al.*, “In situ XRD investigation of the evolution of alumina-supported cobalt catalysts under realistic conditions of Fischer–Tropsch synthesis,” *Chem. Commun.*, vol. 46, no. 5, pp. 788–790, 2010, doi: 10.1039/B920110F.
- [27] H. H. Storch, N. Golumbic, and R. B. Anderson, *The Fischer-Tropsch and Related Synthesis*. New York: Wiley, 1951.
- [28] M. van der Riet, G. J. Hutchings, and R. G. Copperthwaite, “Selective formation of C₃ hydrocarbons from CO + H₂ using cobalt–manganese oxide catalysts,” *J. Chem. Soc., Chem. Commun.*, no. 10, pp. 798–799, 1986, doi: 10.1039/C39860000798.
- [29] S. Colley, R. G. Copperthwaite, G. J. Hutchings, and M. Van der Riet, “Carbon monoxide hydrogenation using cobalt manganese oxide catalysts: initial catalyst optimization studies,” *Ind. Eng. Chem. Res.*, vol. 27, no. 8, pp. 1339–1344, 1988, doi: 10.1021/ie00080a001.
- [30] G. J. Hutchings, M. van der Riet, and R. Hunter, “CO hydrogenation using cobalt/manganese oxide catalysts. Comments on the mechanism of carbon–carbon bond formation,” *J. Chem. Soc. Faraday Trans. 1 Phys. Chem. Condens. Phases*, vol. 85, no. 9, p. 2875, 1989, doi: 10.1039/f19898502875.
- [31] S. E. Colley, R. G. Copperthwaite, G. J. Hutchings, S. P. Terblanche, and M. M. Thackeray, “Identification of body-centred cubic cobalt and its importance in CO hydrogenation,” *Nature*, vol. 339, no. 6220, pp. 129–130, 1989, doi: 10.1038/339129a0.
- [32] G. L. Bezemer *et al.*, “Investigation of promoter effects of manganese oxide on carbon nanofiber-supported cobalt catalysts for Fischer–Tropsch synthesis,” *J. Catal.*, vol. 237, no. 1, pp. 152–161, 2006, doi: 10.1016/j.jcat.2005.10.031.
- [33] F. Morales *et al.*, “In situ X-ray absorption of Co/Mn/TiO₂ catalysts for fischer-tropsch synthesis,” *J. Phys. Chem. B*, vol. 108, no. 41, pp. 16201–16207, 2004, doi: 10.1021/jp0403846.
- [34] F. Morales, F. De Groot, O. Gijzeman, A. Mens, O. Stephan, and B. Weckhuysen, “Mn promotion effects in Co/TiO₂ Fischer–Tropsch catalysts as investigated by XPS and STEM-EELS,” *J. Catal.*, vol. 230, no. 2, pp. 301–308, 2005, doi: 10.1016/j.jcat.2004.11.047.
- [35] A. Y. Khodakov, W. Chu, and P. Fongarland, “Advances in the development of novel cobalt Fischer–Tropsch catalysts for synthesis of long-chain hydrocarbons and clean fuels,” *Chem. Rev.*, vol. 107, no. 5, pp. 1692–1744, 2007, doi: 10.1021/cr050972v.
- [36] M. W. J. Crajé, A. M. Van der Kraan, J. Van de Loosdrecht, and P. J. Van Berge, “The application of Mössbauer emission spectroscopy to industrial cobalt based Fischer–Tropsch catalysts,” *Catal. Today*, vol. 71, no. 3–4, pp. 369–379, 2002, doi: 10.1016/S0920-5861(01)00464-3.
- [37] M. K. Van Der Lee, A. Van Jos Dillen, J. H. Bitter, and K. P. De Jong, “Deposition precipitation for the preparation of carbon nanofiber supported nickel catalysts,” *J. Am. Chem. Soc.*, vol. 127, no. 39, pp. 13573–13582, 2005, doi: 10.1021/ja053038q.
- [38] Z. Klencsár, “MossWinn—methodological advances in the field of Mössbauer data analysis,” *Hyperfine Interact.*, vol. 217, no. 1–3, pp. 117–126, 2013, doi: 10.1007/s10751-012-0732-2.
- [39] M. Blume and J. A. Tjon, “Mössbauer Spectra in a Fluctuating Environment,” *Phys. Rev.*, vol. 165, no. 2, pp. 446–456, 1966, doi: 10.1103/PhysRev.165.456.
- [40] G. K. Wertheim, “Hyperfine Structure of Divalent and Trivalent Fe⁵⁷ in Cobalt Oxide,” *Phys. Rev.*, vol. 124, no. 3, pp. 764–767, 1961, doi: 10.1103/PhysRev.124.764.
- [41] G. K. Wertheim, “Chemical Effects of Nuclear Transformations in Mössbauer Spectroscopy,” *Acc. Chem. Res.*, vol. 4, no. 11, pp. 373–379, 1971, doi: 10.1021/ar50047a003.
- [42] H. Pollak, “Fe³⁺ Ion Lifetime in CoO Deduced from the Auger and Mössbauer Effects,” *Phys. State. Sol.*, vol. 2, pp. 720–724, 1962, doi: 10.1002/pssb.19620020609.
- [43] A. Cruset and J. M. Friedt, “Mossbauer Study of the Valence State of ⁵⁷Fe after ⁵⁷Co Decay in CoFe₂O₄,” *Phys. State. Sol.*, vol. 45, p. 189, 1971, doi: 10.1002/pssb.2220450120.
- [44] C. Wivel, B. S. Clausen, R. Candia, S. Mørup, and H. Topsøe, “Mössbauer Emission Studies of Calcined Co-Mo/Al₂O₃ Catalysts: Catalytic Significance of the Co Precursors,” *J. Catal.*, vol. 87, pp. 497–513, 1984, doi: 10.1016/0021-9517(84)90210-0.

- [45] H. Topsøe, B. S. Clausen, R. Candia, C. Wivel, and S. Mørup, "In situ Mössbauer emission spectroscopy studies of unsupported and supported sulfided Co-Mo hydrodesulfurization catalysts: Evidence for and nature of a Co-Mo-S phase," *J. Catal.*, vol. 68, no. 2, pp. 433–452, 1981, doi: 10.1016/0021-9517(81)90114-7.
- [46] J. A. R. Van Veen, E. Gerkema, A. M. Van Der Kraan, P. A. J. M. Hendriks, and H. Beens, "A ^{57}Co Mössbauer emission spectrometric study of some supported CoMo hydrodesulfurization catalysts," *J. Catal.*, vol. 133, no. 1, pp. 112–123, 1992, doi: 10.1016/0021-9517(92)90189-O.
- [47] M. W. J. Crajé, V. H. J. De Beer, J. A. R. Van Veen, and A. M. Van Der Kraan, "Sulfidation of $\text{Co}/\text{Al}_2\text{O}_3$ and $\text{CoMo}/\text{Al}_2\text{O}_3$ catalysts studied by mössbauer emission spectroscopy," *J. Catal.*, vol. 143, no. 2, pp. 601–615, 1993, doi: 10.1006/jcat.1993.1303.
- [48] F. Morales, D. Grandjean, A. Mens, F. M. F. de Groot, and B. M. Weckhuysen, "X-ray Absorption Spectroscopy of Mn/Co/TiO₂ Fischer–Tropsch Catalysts: Relationships between Preparation Method, Molecular Structure, and Catalyst Performance," *J. Phys. Chem. B*, vol. 110, no. 17, pp. 8626–8639, 2006, doi: 10.1021/jp0565958.
- [49] M. Wolf, N. Fischer, and M. Claeys, "Water-induced deactivation of cobalt-based Fischer–Tropsch catalysts," *Nat. Catal.*, vol. 3, no. 12, pp. 962–965, 2020, doi: 10.1038/s41929-020-00534-5.
- [50] M. Wolf, N. Fischer, and M. Claeys, "Capturing the interconnectivity of water-induced oxidation and sintering of cobalt nanoparticles during the Fischer–Tropsch synthesis in situ," *J. Catal.*, vol. 374, pp. 199–207, 2019, doi: 10.1016/j.jcat.2019.04.030.
- [51] F. Morales, E. de Smit, F. M. F. de Groot, T. Visser, and B. M. Weckhuysen, "Effects of manganese oxide promoter on the CO and H₂ adsorption properties of titania-supported cobalt Fischer–Tropsch catalysts," *J. Catal.*, vol. 246, no. 1, pp. 91–99, 2007, doi: 10.1016/j.jcat.2006.11.014.
- [52] F. R. Van den Berg, M. W. J. Crajé, A. M. Van der Kraan, and J. W. Geus, "Reduction behaviour of Fe/ZrO₂ and Fe/K/ZrO₂ Fischer–Tropsch catalysts," *Appl. Catal. A Gen.*, vol. 242, no. 2, pp. 403–416, 2003, doi: 10.1016/S0926-860X(02)00532-X.
- [53] Z. Li *et al.*, "Effects of Sodium on the Catalytic Performance of CoMn Catalysts for Fischer–Tropsch to Olefin Reactions," *ACS Catal.*, vol. 7, no. 5, pp. 3622–3631, 2017, doi: 10.1021/acscatal.6b03478.
- [54] J. P. Den Breejen *et al.*, "A highly active and selective manganese oxide promoted cobalt-on-silica Fischer–Tropsch catalyst," *Top. Catal.*, vol. 54, no. 13–15, pp. 768–777, 2011, doi: 10.1007/s11244-011-9703-0.

Appendix A

Table A1. Mössbauer experimental conditions for reactive Fischer-Tropsch humidity tests. All tests were performed at 200 °C with a total pressure of 20 bar.

<i>Reaction</i>	<i>He (mL/min)</i>	<i>H₂ (mL/min)</i>	<i>CO (mL/min)</i>	<i>Water (g/h)</i>	<i>Steam (mL/min)</i>
<i>RH = 0%</i>	75	20	5	0	0
<i>RH = 7.5%</i> <i>H₂/H₂O = 4</i>	55	20	5	0.24	5
<i>RH = 14%</i> <i>H₂/H₂O = 2</i>	55	20	5	0.48	10
<i>RH = 20%</i> <i>H₂/H₂O = 1.3</i>	55	20	5	0.72	15
<i>RH = 25%</i> <i>H₂/H₂O = 1</i>	55	20	5	0.96	20
<i>RH = 57%</i> <i>H₂/H₂O = 1</i>	0	20	5	0.96	20

Table A2: Fit parameters of Mössbauer spectra of the Co(4)/CNF catalyst after different treatments.

<i>Treatment</i>	<i>Temperature (°C)</i>	<i>Cobalt phase</i>	<i>Isomer Shift (mm s⁻¹)</i>	<i>Hyperfine Field (kOe)</i>	<i>Quadrupole Splitting (mm s⁻¹)</i>	<i>Spectral Contribution (%)</i>
<i>After reduction</i>	20	<i>Co(0) SPM</i>	0.0	-	-	100
<i>During FT reaction</i>	200	<i>Co(0) SPM</i>	-0.1	-	-	100
<i>RH = 7.5%</i>	200	<i>Co(0) SPM</i>	-0.2	-	-	80
		<i>Co(0) bulk</i>	-0.2	290	-	20
<i>RH = 14%</i>	200	<i>Co(0) SPM</i>	-0.2	-	-	75
		<i>Co(0) bulk</i>	-0.2	287	-	25

<i>RH = 20%</i>	200	<i>Co(0) SPM</i>	-0.2	-	-	75
		<i>Co(0) bulk</i>	-0.2	293	-	25
<i>RH = 25%</i>	200	<i>Co(0) SPM</i>	-0.2	-	-	65
		<i>Co(0) bulk</i>	-0.2	298	-	35
<i>RH = 57%</i>	200	<i>Co(0) SPM</i>	-0.2	-	-	45
		<i>Co(0) bulk</i>	-0.2	308	-	55
<i>After reaction</i>	20	<i>Co(0) SPM</i>	0.0	-	-	31
		<i>Co(0) bulk</i>	-0.1	317	-	69

Table A3: Mössbauer experimental conditions for non-reactive steam treatments. All tests were performed at 200 °C with a total pressure of 20 bar.

<i>Reaction</i>	<i>He (mL/min)</i>	<i>H₂ (mL/min)</i>	<i>CO (mL/min)</i>	<i>H₂O (g/h)</i>
<i>Fischer-Tropsch reaction</i>	75	20	5	0
<i>Steam treatment RH = 25%</i> <i>H₂/H₂O = 1</i>	55	20	0	0.96
<i>Steam treatment RH = 57%</i> <i>H₂/H₂O = 1</i>	5	20	0	0.96

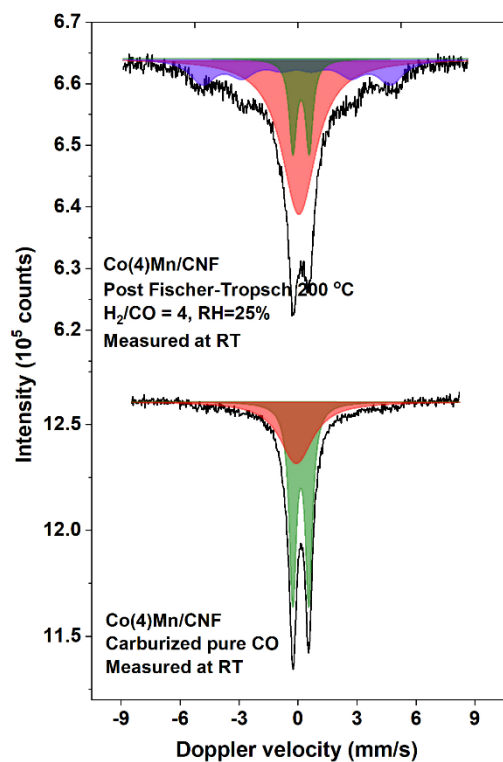


Figure A4. Mössbauer spectrum of the Co(4)Mn/CNF catalyst following a FT treatment with a relative humidity of 25%, and after carbidisation under pure CO at 220 °C and 8 bar pressure for 3 hours: black lines represent the experimental spectra, red the fitted metallic cobalt SPM singlet, blue the fitted bulk metallic cobalt sextuplet, and green the fitted cobalt carbide doublet.

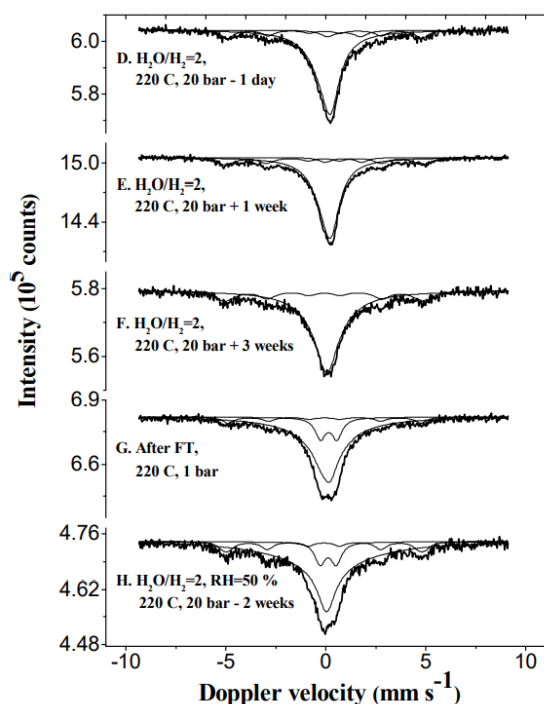


Figure A5. Mössbauer spectra measured on a Co(4)Mn/CNF catalyst. Shown is that following a steam treatment the catalyst is activated for carbidisation under regular Fischer-Tropsch conditions.

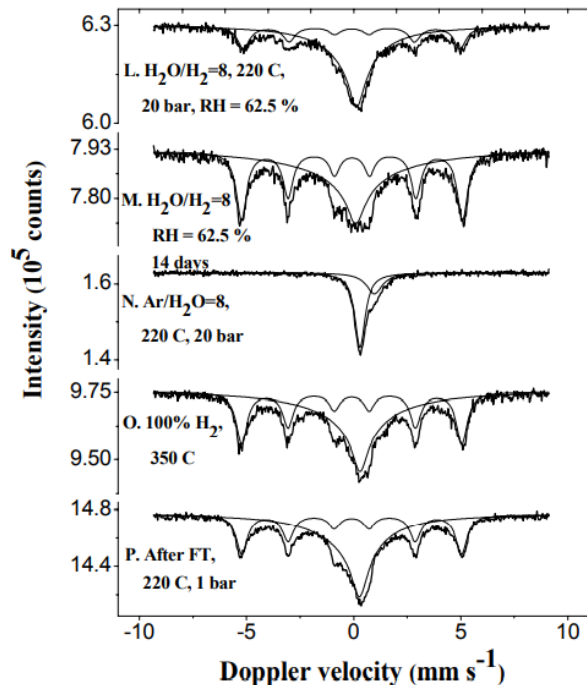


Figure A6. Mössbauer spectra measured on a Co(4)Mn/CNF catalyst. Shown is that following a steam treatment and complete oxidation of the metallic phase the catalyst is not activated for carbidisation under regular Fischer-Tropsch conditions.

Table A7. Fit parameters of Mössbauer spectra of the Co(10)Mn/CNF catalyst after different treatments.

<i>Treatment</i>	<i>Temperature</i> (°C)	<i>Cobalt phase</i>	<i>Isomer</i> <i>Shift</i> (mm s ⁻¹)	<i>Hyperfine</i> <i>Field</i> (kOe)	<i>Quadrupole</i> <i>Splitting</i> (mm s ⁻¹)	<i>Spectral</i> <i>Contribution</i> (%)
<i>After reduction</i>	20	<i>Co(0) SPM</i>	0.2	-	-	54
		<i>Co(0) bulk</i>	-0.1	312	-	46
<i>During FT reaction</i>	200	<i>Co(0) SPM</i>	0.0	-	-	72
		<i>Co(0) bulk</i>	-0.2	293	-	28
<i>RH = 7.5%</i>	200	<i>Co(0) SPM</i>	-0.1	-	-	50
		<i>Co(0) bulk</i>	-0.2	295	-	13
		<i>Co₂C</i>	0.0	-	0.8	37
<i>RH = 14%</i>	200	<i>Co(0) SPM</i>	-0.1	-	-	42
		<i>Co(0) bulk</i>	-0.2	294	-	13
		<i>Co₂C</i>	0.0	-	0.8	45
<i>RH = 20%</i>	200	<i>Co(0) SPM</i>	-0.1	-	-	38
		<i>Co(0) bulk</i>	-0.2	295	-	12
		<i>Co₂C</i>	0.0	-	0.8	50
<i>RH = 25%</i>	200	<i>Co(0) SPM</i>	-0.1	-	-	37
		<i>Co(0) bulk</i>	-0.2	292	-	11
		<i>Co₂C</i>	0.0	-	0.8	52
<i>RH = 57%</i>	200	<i>Co(0) SPM</i>	-0.1	-	-	29
		<i>Co(0) bulk</i>	-0.2	287	-	9
		<i>Co₂C</i>	0.0	-	0.8	62
<i>After reaction</i>	20	<i>Co(0) SPM</i>	0.0	-	-	21
		<i>Co(0) bulk</i>	-0.1	304	-	11
		<i>Co₂C</i>	0.1	-	0.8	68
<i>Reduced</i>	20	<i>Co(0) SPM</i>	0.0	-	-	15
		<i>Co(0) bulk</i>	-0.1	320	-	85

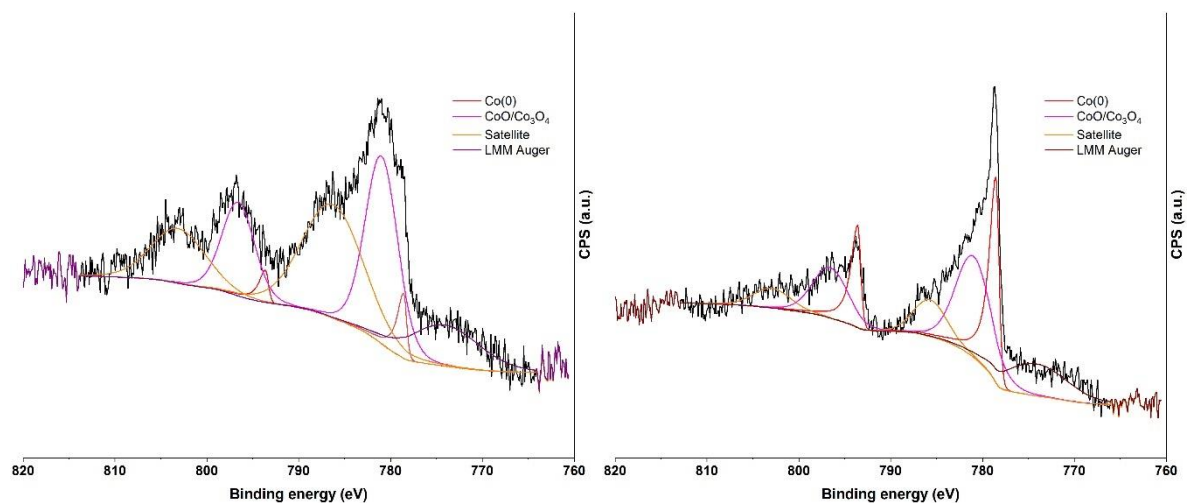


Figure A8. Cobalt 2p XPS spectra of Co(4)Mn/CNF after (a) reduction of the as-prepared catalyst and (b) reduction of the used catalyst (black: measured spectra; red: contribution of metallic cobalt; magenta: oxidic cobalt; orange: satellite peaks; brown: Auger peak).

Table A9. Peak ratios of cobalt to carbon for the as prepared and used catalyst following a reduction treatment in quasi in situ XPS.

Catalyst		Co/C peak ratio	DOR (%)
Co(4)/CNF	Reduced	0.014	35
	Used and reduced	0.010	51
Co(4)Mn/CNF	Reduced	0.024	11
	Used and reduced	0.012	41
Co(10)Mn/CNF	Reduced	0.036	23
	Used and reduced	0.020	55

Chapter 3

Manganese as a structural promoter in silica-supported cobalt Fischer-Tropsch catalysts under simulated high conversion conditions

Abstract

Understanding the deactivation mechanism of cobalt-based Fischer-Tropsch catalysts is of significant practical importance. Herein, we explored the role of manganese as a structural promotor on silica-supported cobalt nanoparticles under simulated high CO conversion conditions, i.e. high relative humidity. The structural changes in terms of cobalt dispersion and oxidation state were followed by *in situ* Mössbauer emission spectroscopy. The addition of manganese oxide to silica-supported cobalt enhanced the dispersion of metallic cobalt in the reduced catalysts. This higher cobalt dispersion, however, led to a stronger tendency of cobalt silicate formation under humid conditions. Without manganese, the cobalt particles sintered and the larger ones were prone to formation of cobalt carbide under high conversion conditions. As such, silica is not preferred as a support for practical FTS.

This chapter is being reviewed for publication in Journal of Catalysis.

3.1 Introduction

Fischer-Tropsch synthesis (FTS) is a surface-catalyzed polymerization reaction that converts a feed of synthesis gas ($\text{CO} + \text{H}_2$) to fuels and chemicals [1]. The current commercial exploitation of this technology mainly utilizes cobalt catalysts to convert synthesis gas derived from natural gas into primarily long-chain paraffins [2]. FTS also holds promise to convert feedstocks from renewable sources, such as biomass, which is crucial to the energy transition in which our dependence on fossil resources needs to decrease. Since cobalt-based FTS is dictated by a strong particle size effect, catalyst design is vitally important with an optimum size of cobalt nanoparticles around 6-8 nm [3], [4]. An important aspect of practical FTS is catalyst stability, which is broadly investigated [5].

Two dominant deactivation profiles can be discerned in cobalt-based FTS [6]. Short-term deactivation is well studied [5], [7], [8] and is the result of wax condensation and resulting diffusion limitations, which can typically be reversed by a mild hydrogen treatment [9]. Long-term deactivation, on the other hand, is often the result of structural changes of the catalyst and typically less reversible, making it significant in industrial practice. Long-term deactivation is not well understood with several factors contributing to the loss of catalytic activity over time. The most common ones are oxidation of the active metal phase [10]–[13], strong-metal support interactions (SMSI) [14]–[16], carbon deposition [17]–[19] and cobalt sintering [20]–[22].

In the study of deactivation, the role of the support plays an important role. Such studies employ model carbon support [4], [23], [24] or, of more practical relevance, oxide supports such as SiO_2 [16], [25], [26], Al_2O_3 [2], [27], [28] and TiO_2 [29]–[32]. Carbon represents a support with weak interaction with cobalt, which is an excellent model system to study sintering and other deactivation mechanisms [24]. In industrial applications, oxide supports are used, because the stronger interactions with cobalt lead to a better stability of the active phase. And it allows for catalyst regeneration through a oxidation and reduction cycle [8]. The interaction between cobalt and the support can also result in the formation of cobalt-support compounds [33], [34], which can also lead to significant irreversible deactivation, especially in the presence of steam [35], [36].

Water is a main product of the FTS reaction, because the main pathway for O removal from the surface upon CO dissociation is through the production of water. High partial pressures of steam (humidity) can facilitate cobalt deactivation, through oxidation, SMSI, carbide formation [24] or sintering. Thermodynamics dictate that spherical cobalt nanoparticles smaller than about 4 nm oxidize at relevant $\text{H}_2\text{O}/\text{H}_2$ ratios during FTS conditions [11]. However, bulk oxidation of supported cobalt

catalysts under (simulated) industrial FTS conditions is often not observed, which can be due to the fact that typical catalysts contain larger particles or due to kinetic limitations of water dissociation in simulated conditions, when tests are done in absence of CO [5], [10], [13], [37], [38]. The effect of steam on sintering under FTS conditions has also been investigated [21], [24], [38]. The combination of high partial pressure of steam and carbon monoxide accelerates agglomeration of the active metal phase. The exact mechanisms at play are still a matter of discussion. Kliewer et al. proposed that surface wetting by cobalt oxide/hydroxide species facilitates interaction between neighbouring metallic particles that results in coalescence [31]. In this regard, a narrow particle size distribution, well separated on the support is important to resist steam-induced sintering. On the other hand, Moodley et al. explained cobalt sintering by Ostwald ripening involving sub-carbonyl species as the dominant mechanism, which is also enhanced by the presence of water [7].

High coverage of the support by carbon deposits can also result in structural changes of the catalyst, and also the formation of cobalt carbides has been reported [39]. Whilst in iron-based FTS, iron carbide is the active phase, formation of cobalt carbide is undesired as it presents a much lower activity than metallic cobalt and also has a much lower selectivity towards heavy paraffins [40]–[42]. Thermodynamics show that cobalt carbides are stable under FTS conditions, implying that their formation is kinetically hindered [39].

Manganese oxide has been investigated as a constituent of cobalt-based FTS catalysts already in the first half of the 20th century [43]. These early results showed the potential of manganese to reduce methane selectivity. Later, pioneering studies using catalysts prepared by co-precipitation of cobalt and manganese led to better understanding of the role of manganese oxide as a support and selectivity promoter [44]–[47]. More recently the focus has been on manganese oxide as a promoter for supported cobalt FTS catalysts [23], [48]–[50], in which a positive impact on the chain-growth probability has been emphasized. However, concurrent work by Kimpel et al. [51] has shown that C₅₊ selectivity is only improved by manganese promotion when low operating pressures are used. And that at high operating pressures (10 to 30 bar) the addition of manganese leads to a reduction of the chain-growth probability. Contrary to their work, we focus on the structural effects of manganese promotion, and whether it can improve catalyst stability under high conversion conditions. In our previous study we looked at manganese promotion on a carbon supported system [24], and we observed the formation of cobalt carbide under industrial operating conditions. This formation was a direct result of the high mobility of both cobalt as well as manganese oxide under reaction conditions on the weakly interacting CNF support. And so, in the present work, we again focus on the role of

manganese oxide as a structural promoter but on a stronger interacting oxidic support, namely silica. Structural deactivation is investigated under FTS reaction conditions at elevated pressure by *in situ* Mössbauer emission spectroscopy (MES) [52]. The effect of water partial pressure on the deactivation is studied by feeding steam to the reactor to reach industrially relevant bottom bed conditions. Previous ^{57}Co MES studies showed that these high pressures of water increase cobalt sintering [24], [38] and can result in oxidation as well as strong-metal support interactions [36], [53]. The current MES measurements are supplemented by *quasi in situ* XPS, TEM and XRD characterization, while the catalytic performance is measured *in situ* and in a microflow reactor.

3.2. Experimental methods

3.2.1 Catalyst preparation

All supported catalysts were prepared by incipient wetness impregnation of X080 silica extrudates (Shell Global Solutions International B.V., pore volume 0.84 mL/g) followed by drying in air at 120 °C for 6 h. The impregnation solutions were obtained by dissolving the appropriate amount of $\text{Co}(\text{NO}_3)_2 \cdot 6\text{H}_2\text{O}$ ($\geq 98.0\%$, Sigma Aldrich) and $\text{Mn}(\text{NO}_3)_2 \cdot 3\text{H}_2\text{O}$ ($\geq 97.0\%$, Sigma Aldrich) in dehydrated ethanol, and mixing with a solution of $\text{Pt}(\text{NH}_3)_4(\text{NO}_3)_2$ ($\geq 99.995\%$, Sigma Aldrich) in deionized water to form a homogenous mixture. Three catalysts were prepared with a cobalt loading of 8 wt%, 0.08 wt% platinum and respectively 0, 0.8 and 1.6 wt% manganese. The resulting samples are denoted by $\text{CoMn}(x)\text{Pt}/\text{SiO}_2$, where x represents the intended manganese to cobalt ratio. Following impregnation and drying, the samples were calcined at 350 °C for 2 hours in stagnant air (rate 5 °C/min). Part of these calcined catalysts was spiked with radioactive ^{57}Co by pore volume impregnation using a solution containing 90 MBq ^{57}Co in 0.1 M HNO_3 . These radioactive samples were dried at 120 °C for 12 hours and subsequently used for Mössbauer spectroscopy.

3.2.2 Characterization

X-ray diffraction

X-ray diffraction (XRD) patterns were recorded on a Bruker D2 Phaser using a $\text{Cu K}\alpha$ radiation source and a 2 mm slit. Data was collected using a time per step of 0.15 min and a step size of 0.1° in the 2θ range of $10\text{--}65^\circ$. Background subtractions were applied, and reference spectra were obtained using the Diffrac.Eva software by Bruker.

***Quasi in situ* X-ray photoelectron spectroscopy**

The oxidation state and dispersion of cobalt was studied by *quasi in situ* XPS using a Kratos AXIS Ultra 600 spectrometer equipped with a monochromatic Al K α X-ray source (Al K α 1486.6 eV). Survey scans were recorded at a pass energy of 160 eV, detailed region scans at 40 eV. The step size was 0.1 eV and the background pressure during the measurements was kept below 10⁻⁹ mbar.

A high-temperature reaction cell (Kratos, WX-530) was used to pre-treat the sample supported on an alumina stub, allowing *in vacuo* sample transfer into the analysis chamber. Reduction was performed in a pure H₂ flow at atmospheric pressure and 350 °C for 2h. After reduction, the reaction cell was evacuated to a pressure below 10⁻⁹ mbar. Then, the sample was cooled to 150 °C and transferred to the analysis chamber. Data analysis was done with the CasaXPS software (version 2.3.22PR1.0). The binding energy scale was corrected for surface charging by taking the C 1s peak of adventitious carbon as a reference at 284.8 eV.

The degree of reduction (DOR) is calculated by comparing the peak areas corresponding to the fitted metallic and oxidic cobalt contributions, using a model as described by Biesinger et al. [54]. The Co/Si ratio is determined using a survey scan and comparing the peak areas of the Co2p and Si2p contributions.

Electron microscopy

Surface averaged particle sizes and particle size distributions were determined using transmission electron microscopy (TEM). TEM measurements were performed on a FEI Tecnai 20 electron microscope operated at an electron acceleration voltage of 200 kV with a LaB6 filament. Typically, a small amount of the sample was ground and suspended in pure ethanol, sonicated, and dispersed over a Cu grid with a holey carbon film.

***In situ* Mössbauer emission spectroscopy**

Mössbauer emission spectroscopy (MES) was carried out at various temperatures using a constant acceleration spectrometer set up in a triangular mode with a moving single-line K₄Fe(CN)₆·3H₂O absorber enriched in ⁵⁷Fe. The velocity scale was calibrated with a ⁵⁷Co:Rh source and a sodium nitroprusside absorber. Zero velocity corresponds to the peak position of the K₄Fe(CN)₆·3H₂O absorber measured with the ⁵⁷Co:Rh source, positive velocities correspond to the absorber moving towards the source. To be able to measure under *in situ* Fischer-Tropsch conditions, a high pressure MES cell is used [52], which is described in detail in literature [24].

Mössbauer spectra were fitted using the MossWinn 4.0 program [55]. The spectra of very small superparamagnetic species were fitted using the two-state magnetic relaxation model of Blume and Tjon, which assumes the presence of a fluctuating magnetic field which jumps between the values of $+H$ and $-H$ along the z -axis with an average frequency τ [56]. Here, H typically equals 500 kOe and τ can vary between 10^{-9} and 10^{-12} s $^{-1}$. The Mössbauer spectra of larger particles were fitted using a hyperfine sextuplet, resulting from the local magnetic field experienced by bulk metallic particles. The experimental uncertainties in the calculated Mössbauer parameters, estimated using Monte Carlo iterations by the MossWinn 4.0 program and including experimental uncertainties were as follows: IS and QS ± 0.01 mm s $^{-1}$ for the isomer shift and quadrupole splitting, respectively; $\pm 3\%$ for the spectral contribution; ± 3 kOe for the hyperfine field.

Typically, 300 mg of radioactivity-spiked and 100 mg of non-radioactive catalyst (sieve fraction 250-500 μm) was loaded into two separate compartments of the reactor cell. FTS experiments were performed *in situ* following reduction at 350 °C for 2 hours in 100 mL/min. flow of pure H₂. Reactions were done at 200 °C and 20 bar, while the CO/H₂ was kept at 4 throughout and steam was fed to vary the relative humidity. Water was evaporated and mixed with the incoming feed gas using a Bronkhorst controlled evaporator mixer (CEM). Wax products were collected in a downstream hot catch pot, and water was retrieved in a subsequent cold catch pot. An online Trace GC Ultra from Thermo Fisher Scientific equipped with a RT-Silica bond column and a flame ionization detector as well as a Stabilwax column and a thermal conductivity detector was used to analyse the gaseous products.

3.2.3 Catalytic activity measurements

The catalytic performance was determined in a single-pass flow reactor system (Microactivity Reference unit, PID Eng&Tech) operated at a temperature of 220°C or 240 °C, a total pressure of 20 bar and a H₂/CO ratio of 4. In a typical experiment, 50 mg of catalyst (sieve fraction 125-250 μm) mixed with SiC particles of the same sieve fraction to a total volume of 3 mL was placed in a tubular reactor with an internal diameter of 9 mm. The temperature was controlled via a thermocouple, located in the centre of the catalytic bed. Reduction was first performed in a flow of H₂ at 350 °C for 2 hours after heating at a rate of 5 °C/min. Subsequently, the reactor was cooled to 220°C and the gas feed composition was changed to reaction conditions. A space velocity (SV) of 60 L g_{cat} $^{-1}$ h $^{-1}$, was applied, which resulted in a CO conversion of approximately 5 %. A TRACE1300 GC instrument from Thermo Fisher Scientific equipped with a RT-Silica bond column and a flame ionization detector as well as a Porabond-Q column and a thermal conductivity detector was used to measure the gas

composition of the reactor effluent. The Weisz–Prater criterion was calculated to confirm the reactions did not run under internal mass transfer limitations. At the applied reaction conditions, no CO₂ was observed and the selectivity toward oxygenates on a molar carbon basis was less than 1%. Liquid products and waxes were collected in a cold trap placed after the reactor. Ar was used an internal standard in the CO/H₂ feed mixture. The CO conversion (X_{CO}) was determined in the following manner:

$$X_{CO} = 1 - \frac{F_{Ar,in}F_{CO,out}}{F_{CO,in}F_{Ar,out}} \quad (1)$$

where $F_{Ar,in}$ is the volumetric Ar flow in the reactor feed, $F_{CO,in}$ is the volumetric CO flow in the reactor feed, $F_{Ar,out}$ and $F_{CO,out}$ are the respective volumetric flows of Ar and CO out of the reactor system.

The carbon-based selectivity of hydrocarbon compound C_i (S_{Ci}) was calculated using:

$$S_{Ci} = \frac{F_{Ar,in}F_{Ci}v_i}{F_{Ar,out}F_{CO,in}X_{CO}} \quad (2)$$

where F_{Ci} is the volumetric flow of hydrocarbon compound C_i out of the reactor, and v_i is the stoichiometric factor of the hydrocarbon compound.

The cobalt time-yield (CTY) was determined using the following equation:

$$CTY = \frac{F_{CO,in}X_{CO}}{m_{Co}} \quad (3)$$

where m_{Co} is the weight of cobalt used in the catalytic reaction.

3.3. Results and Discussion

3.3.1 Fresh catalyst characterization

Figure 1 shows representative TEM images of the catalysts after calcination at 350 °C for 2 h in stagnant air. The average size and size distribution of the cobalt oxide nanoparticles was determined by analysing approximately 150 particles in ca. eight images per sample. The average particle sizes are given in Table 1. The particle size distribution of the calcined catalysts is not significantly affected by the presence of manganese, although the data can hint at a small decrease of the particle size with increasing manganese content.

Table 1. Average metal oxide particle size, Co/Si ratio, and reducibility of Co(Mn)Pt/SiO₂ catalysts.

Catalyst	Particle size (nm) ^a	Co/Si ^b (calcined)	Co/Si ^b (reduced)	DOR (%) ^c
CoPt/SiO ₂	6.1 ± 3.8	0.16	0.15	73
CoMn(0.1)Pt/SiO ₂	5.4 ± 2.6	0.21	-	-
CoMn(0.2)Pt/SiO ₂	5.2 ± 2.4	0.29	0.28	79

^a Determined by TEM analysis of calcined samples, ^b Atomic Co/Si ratio determined by XPS, ^c Degree of reduction determined by XPS.

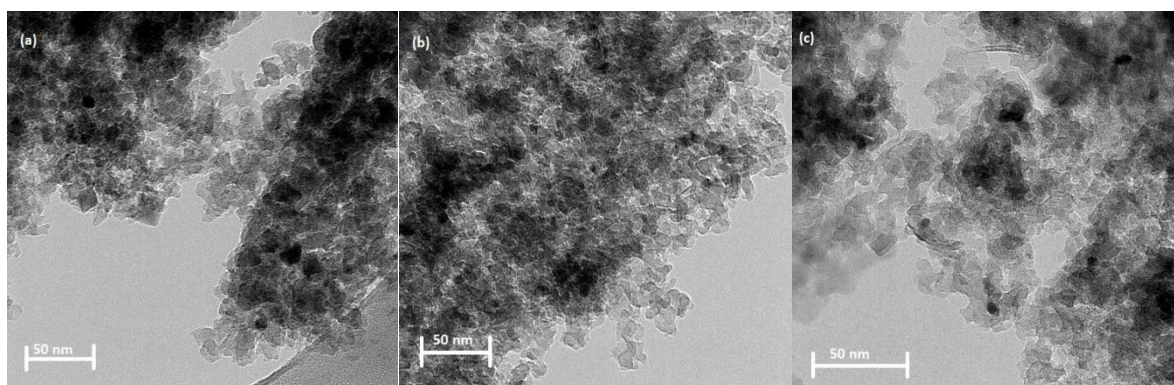


Figure 1. Representative TEM images of (a) CoPt/SiO₂, (b) CoMn(0.1)Pt/SiO₂ and (c) CoMn(0.2)Pt/SiO₂ following calcination at 350 °C for 2 in stagnant air.

The X-ray diffractograms of the calcined catalysts are given in Figure 2. All samples show the expected broad diffuse scattering feature of the amorphous silica support in addition to the diffraction lines of cobalt oxide (Co₃O₄). Although there are no diffraction features of manganese oxides in the

manganese-containing samples, a slight broadening of the main cobalt oxide diffraction line is observed, which may hint at a smaller size of the cobalt oxide phase. For the CoPt/SiO₂ catalyst a FWHM of 0.76° is found for the main diffraction peak at 36.8°, whereas this is 1.06° for the CoMn(0.2)Pt/SiO₂ sample. When using the Scherrer equation [57], assuming a shape factor of 0.9, this gives crystallite sizes in the range of 11.0 to 7.9 nm for the non-promoted and promoted sample respectively. These values are significantly higher than found through TEM which is likely caused by unaccounted for instrumental line broadening. But the data does clearly show the enhanced dispersity already in the oxidic precursor when manganese is present as a promotor, in good agreement with the TEM results.

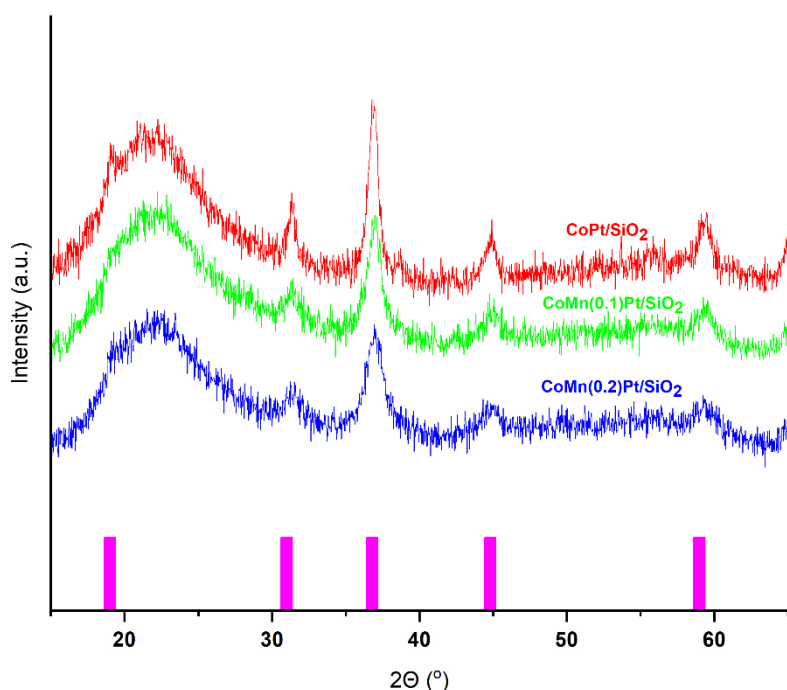


Figure 2. X-ray diffractograms of as-prepared CoMn(0.2)Pt/SiO₂ (blue), CoMn(0.1)Pt/SiO₂ (green), and CoPt/SiO₂ (red) following calcination at 350 °C (main Co₃O₄ reflections in magenta).

We then analysed the calcined and reduced state of the various catalysts by XPS. The cobalt spectra are given in Figure 3. Fitting of the Co 2p spectra was done using the model of Biesinger et al. [54]. The degree of reduction (DOR) upon reduction at 350 °C in pure hydrogen was determined from the metallic cobalt contribution to the Co 2p_{3/2} spectra. Both the non-promoted and promoted catalysts display a high DOR (Table 1). Table 1 also shows the Co/Si ratios before and after reduction. The finding that this ratio is nearly the same before and after reduction suggests that the reduction treatment does not lead to extensive sintering. This is likely the result of the interactions between the

silica support and cobalt, which is quite different from the extensive sintering seen for cobalt on titania [53], [58]. Comparison of the Co/Si ratios of CoPt/SiO₂ and CoMn(0.2)Pt/SiO₂ shows that manganese promotion leads to a higher cobalt dispersion in the oxidic precursor, which is maintained upon reduction. These findings are in good agreement with the TEM and XRD results, which also emphasized the positive effect of manganese on cobalt dispersion in the calcined catalyst. The Mn 2p XPS spectra before and after reduction are given in Figure B5. The Mn signal for the promoted catalysts in the calcined state was very weak. After reduction, clear Mn²⁺ contributions are observed for the CoMn(0.2)Pt/SiO₂ sample. This suggests that the reduction treatment resulted in an improved manganese dispersion, which has been earlier observed by Weckhuysen et al. [59] and was attributed to migration of manganese towards the support upon reduction of mixed oxide particles, although the formation of MnO on the surface of metallic cobalt can also contribute to the improved signal-to-noise ratio.

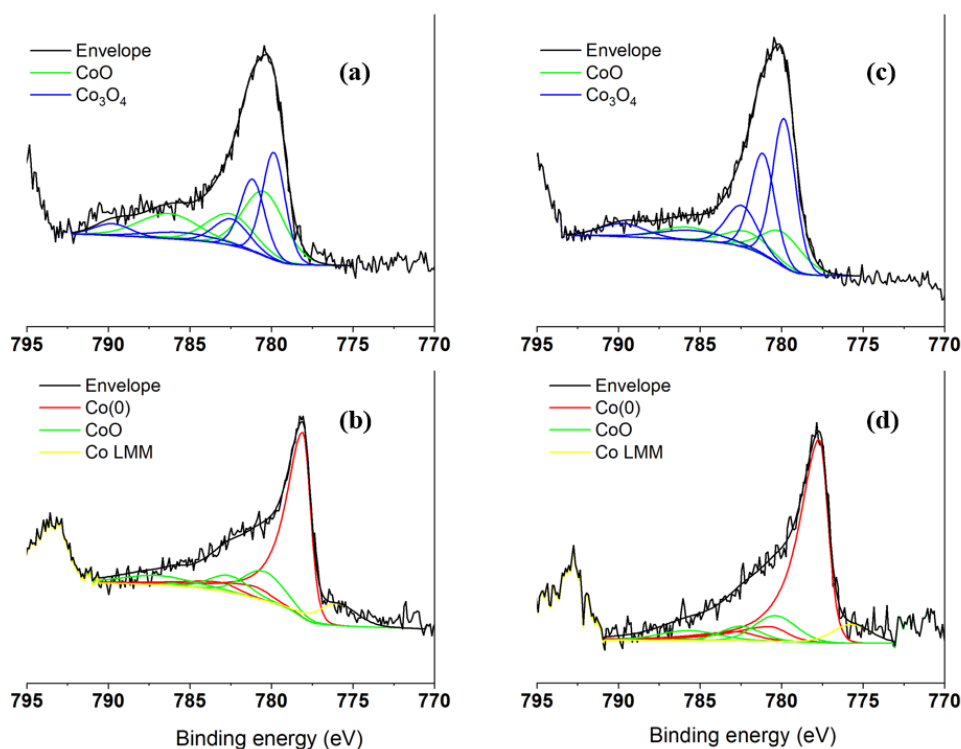


Figure 3. XPS spectra of CoPt/SiO₂ (a,b) and CoMn(0.2)Pt/SiO₂ (c,d) after (a,c) calcination and (b,d) subsequent reduction at 350 °C (black: experimental data and the fitted envelope; red: the fitted metallic Co(0) contributions; green: the fitted CoO contributions; blue: fitted Co₃O₄ contributions; yellow: the Co auger LMM peak; the XPS fit model was taken from Ref. [54]).

3.3.2 *In situ* Mössbauer emission spectroscopy of reduced catalysts

Mössbauer spectra of catalysts reduced in hydrogen at 350 °C for 2 h are given in Figure 4. The elevated noise observed on the CoMn(0.1)Pt/SiO₂ comes from the radioactive probe, which had decreased in activity due to its natural decay. Which resulted in fewer counts over the constant measurement time. The spectra contain two main contributions, namely a sextuplet with an isomer shift (IS) of -0.1 mm s⁻¹ and a hyperfine field (HF) between 310 and 317 kOe, and singlet with an IS of 0.0 mm s⁻¹. Both these features are related to metallic cobalt. The sextuplet represents a contribution of magnetically ordered cobalt metal particles, which is common when their size is larger than 6 nm [38]. The observed singlet indicates that the reduced catalyst also contains small superparamagnetic metallic particles without magnetic ordering, which is typical for particles smaller than 6 nm. The observation of significant contributions of both phases indicates that the reduced samples contain particles with sizes around the SPM cut-off of 6 nm. Compared to CoPt/SiO₂, the manganese-containing samples contain a significantly higher contribution of SPM cobalt. Additionally, the measured HF of the two manganese promoted catalysts is significantly lower (310 and 311 kOe) than for the non-promoted system (317 kOe). As the HF also follows from the domain size of magnetically ordered cobalt, this suggests that when manganese is present the metallic particles are smaller. Both these observations point towards the increased dispersity of cobalt after reduction when manganese is present as a promotor. It is important to note that the MES spectra do not contain evidence of doublets representative for cobalt oxide. This indicates a high reduction degree.

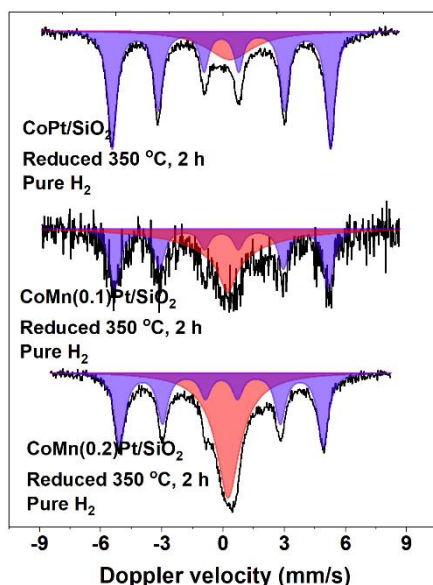


Figure 4. Mössbauer spectra of Co(Mn)Pt/SiO₂ catalysts after reduction at 350 °C in pure hydrogen: black lines represent the experimental spectra, blue the fitted bulk metallic cobalt and red the fitted SPM metallic cobalt singlet.

3.3.3 *In situ* Mössbauer emission spectroscopy during the FTS reaction

In situ Mössbauer spectra were recorded for the catalysts as a function of the steam partial pressure at a temperature of 200 °C, a total pressure of 20 bar, and a H₂/CO ratio of 4. The steam content in the feed is expressed as the relative humidity (RH) at the applied conditions. Table B1 details the feed compositions for the different experiments. Spectra were recorded for at least 48 h at each humidity step, except for RHs of 25% and 57% where the steam treatment was prolonged to 5 days and 11 days, respectively. This was done to understand the influence of prolonged exposure as encountered in industrial practice.

Under relative low humidity conditions up to RH = 25%, only minor changes are observed in the Mössbauer spectra (Figure 5a). The spectral contribution of the SPM phase did not decrease significantly for the promoted and non-promoted samples, as can be deduced from Table 2. The absence of a decreasing SPM metallic cobalt contribution indicates that significant sintering of the small metallic cobalt particles does not occur under these conditions.

When the humidity is further increased to RH = 57%, two new phases are observed in the Mössbauer spectra (Figure 5b). For CoPt/SiO₂, a Co₂C phase with a spectral contribution of 13% is present. This phase is characterized by an isomer shift (IS) of 0.0 mm s⁻¹ and a quadrupole splitting (QS) of 0.9

mm s⁻¹, as also reported for cobalt carbide formed in a carbon-supported cobalt catalyst [24]. The other phase appearing is a Co²⁺-containing phase with a spectral contribution of 4%. This feature is also observed in both promoted catalysts but with a significantly higher spectral contribution. The assignment of this doublet with an IS of 0.9 mm s⁻¹ and a QS of 1.8 mm s⁻¹ is based on the similarity of the Mössbauer parameters to previously observed Fe²⁺-doublets in ferrosilite (FeSiO₃) materials [60]. As such, this points towards the formation of metal-support compounds (MSC) under high humidity conditions. Different from CoPt/SiO₂, exposing the manganese-promoted catalysts to the highest RH did not lead to formation of cobalt carbide. This contrasts the formation of cobalt carbide in a manganese-promoted cobalt FTS catalyst supported on carbon nanofibers [24]. In the carbon-supported case, cobalt carbide formation was linked to cobalt being in close contact with larger manganese oxide agglomerates. The absence of cobalt carbide in the silica-supported samples containing manganese can be rationalized by the stronger metal-support interactions that decrease the mobility of cobalt and manganese. The formation of cobalt carbide in the non-promoted catalyst under high humidity conditions is likely the result of the increased CO partial pressure under these conditions. However, the high partial pressures of steam can also affect the phases present, as a previous study showed an increasing amount of cobalt carbide under *in situ* FTS conditions on an alumina support with increasing water partial pressure [39]. Another study of cobalt on alumina showed the importance of the metallic cobalt particle size, with larger cobalt particles (10-11 nm) being susceptible to carbidization under FTS conditions in contrast to smaller ones (6 nm) [37]. This observation is in agreement with our MES results which showed that the final reduction transformed carbide into a bulk sextuplet with highest associated HF in this study, indicative of largest cobalt particles. Such an effect of particle size on carbidization can well explain why cobalt carbide formation was not observed for the manganese-promoted samples in the present study as their metallic particles were significantly smaller. Thermodynamic calculations point towards the stability of cobalt carbide (Co₂C) under FTS conditions [39], [61]. This suggests that its formation under FTS conditions is strongly kinetically inhibited.

As previously discussed, the ratio of the SPM and magnetically ordered cobalt contributions is higher for the two manganese-promoted catalysts in comparison to their non-promoted counterparts. Following the high humidity treatment, these catalysts show a much higher spectral contribution of a cobalt-silicate phase, namely 33% for the CoMn(0.1)Pt/SiO₂ catalyst and 24% for the CoMn(0.2)Pt/SiO₂ sample. As the catalyst with a lower manganese loading shows a higher spectral contribution of the MSC, it is unlikely that cobalt-silicate formation is directly facilitated by

manganese oxide. Instead, it is reasonable to consider that the larger contribution of small metallic SPM cobalt particles causes the formation of more cobalt-silicate. It has been noted before that small metallic particles are more prone to oxidation and formation of MSCs [11] [16], [62]. The small difference in the amount of cobalt silicate between the two manganese-promoted catalysts cannot be due to differences in the particle size. These two catalysts contain nearly similarly sized cobalt particles, which follows from the similar initial SPM/sextuplet ratio and TEM imaging. Instead, the difference seems to stem from the rate at which cobalt silicate is formed. As the Mössbauer spectra are measured continuously over 11 days at a RH of 57%, we can follow the formation of the different phases in time. Table 2 shows that the SPM contribution declines faster in the CoMn(0.1)Pt/SiO₂ catalyst having dropped to 51% after 48 h in comparison to 60% after 48 h for CoMn(0.2)Pt/SiO₂. This decline in SPM content goes paired with the formation of cobalt-silicate, which contributed 25% after 48 hours for the CoMn(0.1)Pt/SiO₂ catalyst and only 7% after 48 hours for the CoMn(0.2)Pt/SiO₂ sample. The spectra recorded in inert following the high humidity test do not show significant differences anymore with cobalt-silicate contributions of 33% and 31% for CoMn(0.1)Pt/SiO₂ and CoMn(0.2)Pt/SiO₂ respectively (Tables B3 and B4). This means that the actual amount of cobalt-silicate formed is very similar for both promoted catalyst samples, although it is quite different from the non-promoted sample. The formation of the cobalt-silicate phase has concurrently led to a decrease in the SPM to sextuplet ratio, as can be seen in Table 2. This is a clear indication that smaller cobalt particles are more prone to forming MSCs. Thus, although manganese enhances cobalt dispersion, this also leads to a larger cobalt-silica interface, which can convert to inactive compounds under highly humid conditions.

Table 2. Contribution of SPM metallic cobalt determined through Mössbauer spectra measured at 200 °C, 20 bar pressure, H₂/CO = 4, and increasing relative humidity.

<i>Treatment</i>	<i>H₂O/H₂</i>	<i>Treatment length (hrs)</i>	<i>Spectral contribution SPM metallic cobalt (%)</i>		
			<i>CoPt/SiO₂</i>	<i>CoMn(0.1)Pt/SiO₂</i>	<i>CoMn(0.2)Pt/SiO₂</i>
RH 0%	0	48	47	66	69
RH 7.5%	0.25	48	50	N/A	65
RH 14%	0.50	48	49	N/A	67

RH 20%	0.75	48	48	N/A	69
RH 25%	1.0	48	48	70	68
	1.0	120	46	69	67
RH 57%	1.0	48	40	51	60
	1.0	120	39	48	53
	1.0	264	37	46	44

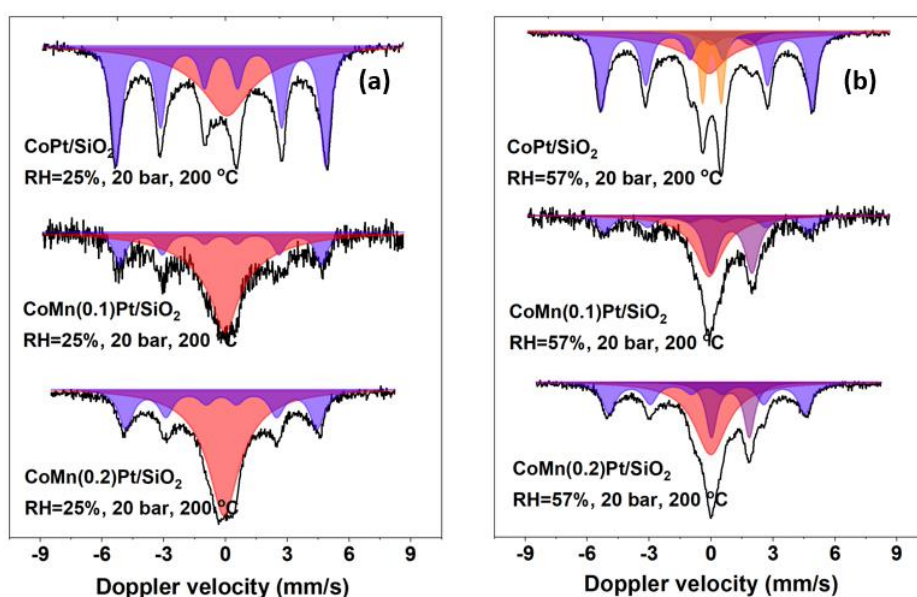


Figure 5. *In situ* Mössbauer spectra of the Co(Mn)Pt/SiO₂ catalysts under FTS conditions at a relative humidity of (a) 25%, and (b) 57%. The black lines represent the experimental spectra, the blue ones the fitted bulk metallic cobalt sextuplet, the red ones the small SPM metallic cobalt singlet, the orange ones the cobalt carbide doublet, and the purple ones the fitted oxidic cobalt doublet.

3.3.4 Characterization of used catalysts

The non-radioactive samples present in the Mössbauer cell during the consecutive humid FTS treatments were retrieved and further characterized. Representative TEM images of these catalysts are given in Figure 6. Next to the cobalt nanoparticles, the images show the typical microstructure of cobalt-silicate compounds as fibrous strands covering the silica surface. In agreement with the *in situ* Mössbauer findings, the manganese-promoted samples contain more of such cobalt-silicate structures. Contrary to the previous study on a carbon support [24], no large agglomerates of manganese oxide are observed for the used catalysts by TEM. This shows that the promoter is still

well dispersed over the silica support. The high contrast between the cobalt particles and the support highlights their metallic nature, their surface being passivated by wax or a thin oxide layer. However, we cannot exclude the possibility that manganese and cobalt are part of a mixed metal oxide as was previously observed on a titania support [63]. The average size of the spherical cobalt nanoparticles was determined from these TEM images. As such, it was found that the average particle sizes are 9.9 ± 5.2 nm for Co/SiO₂, 7.2 ± 3.8 nm for CoMn(0.1)Pt/SiO₂, and 7.7 ± 5.4 nm for CoMn(0.2)Pt/SiO₂. Comparing these results to size of the oxidic precursor particles (Table 1) shows that some sintering of the cobalt particles occurred during the humid FTS treatments. The observation that sintering is most severe for the unpromoted catalyst confirms that manganese helps stabilizing the dispersion of the cobalt nanoparticles in the silica-supported catalyst. Nevertheless, as discussed above and also evident from the TEM images, the higher cobalt dispersion in the presence of manganese leads to a stronger propensity towards formation of cobalt-silicate compounds under humid FTS conditions.

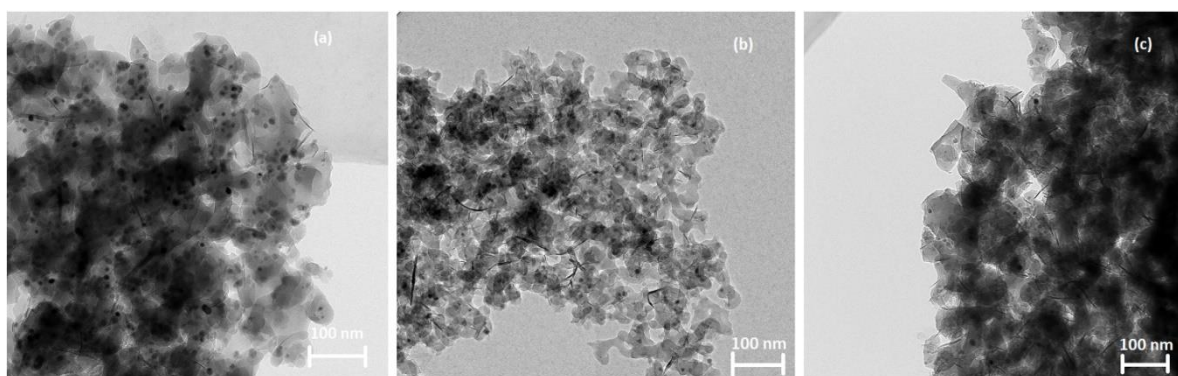


Figure 6. Representative TEM images of used (a) CoPt/SiO₂, (b) CoMn(0.1)Pt/SiO₂ and (c) CoMn(0.2)Pt/SiO₂ following humid FTS treatments.

3.3.5 Catalytic activity

The catalytic performance of CoPt/SiO₂ and CoMn(0.1)Pt/SiO₂ as measured on-stream during the Mössbauer measurements is given in Figure 7. Due to a technical issue with the TCD of the analysis equipment, the *in situ* activity of the CoMn(0.2)Pt/SiO₂ sample could not be measured. The CO conversion of CoPt/SiO₂ and CoMn(0.1)Pt/SiO₂ decreases with increasing RH of the feed. This is typical behaviour for cobalt FTS catalysts, although the opposite has also been reported [64], [65]. At short time scales, the beneficial kinetic impact of water on the FT conversion can be stronger than the deactivation, leading to a net increase of the FTS activity [66]. We also mention that the introduction of steam to the reactor feed results in a small decrease of the CO and H₂ partial pressures, which can affect the catalytic activity due to the negative reaction order in CO and positive order in H₂ [67],

[68]. These aspects render a detailed discussion of the catalytic performance challenging. Accordingly, we focus here on the main trends. The decline in activity between RH = 0% and 7.5% for the non-promoted catalyst is much steeper than the corresponding decline for the manganese-promoted sample. Mössbauer spectra do not show substantial changes for both samples upon an increase of the RH to 7.5%, with the SPM content and the total metallic cobalt contribution remaining unchanged. Therefore, the initial loss of activity might be a kinetic effect such as competitive adsorption of oxygen-containing species at the higher steam partial pressure. Such an effect can be offset by the presence of manganese in the promoted catalyst, as it has been shown that manganese promotion can also increase the rate of CO dissociation [49], [69]. Besides this initial difference, nevertheless, both catalysts show a gradual decline in activity at the higher humidity treatments, which can be correlated to a gradual transformation of the active cobalt phase into larger cobalt particles and the formation of less active cobalt carbide and cobalt silicate. Whilst the promoted catalyst shows a significantly larger fraction of cobalt silicates, its activity is still higher than that of the non-promoted sample. TEM analysis of the used sample showed less sintering of the metallic cobalt phase in the promoted catalysts with an average particle size closer to the optimum size of 6 nm. So, the improved activity of the promoted catalyst is likely the result of the strong cobalt particle size effect as well as the promotional effect of the promotor itself, confirming the promising role of manganese as a promotor [4]. The product distribution during these *in situ* Mössbauer measurements does not change much with the RH, except for the obvious increased CO₂ selectivity at the highest RH of 57%. This is most likely due to a larger contribution of the water-gas shift reaction at high partial pressures of steam. Unlike the non-promoted catalyst, the CoMn(0.1)Pt/SiO₂ catalyst shows a slightly higher methane selectivity at the expense of C₅₊ products at the highest RH. This is likely the result of the increased CO partial pressure under these conditions. It was previously found that at elevated CO partial pressure, the manganese oxide promotor shifted the product distribution towards more C₁ and C₂-C₄ products at the expense of C₅₊ products [23]. This effect of manganese is absent for the non-promoted catalyst.

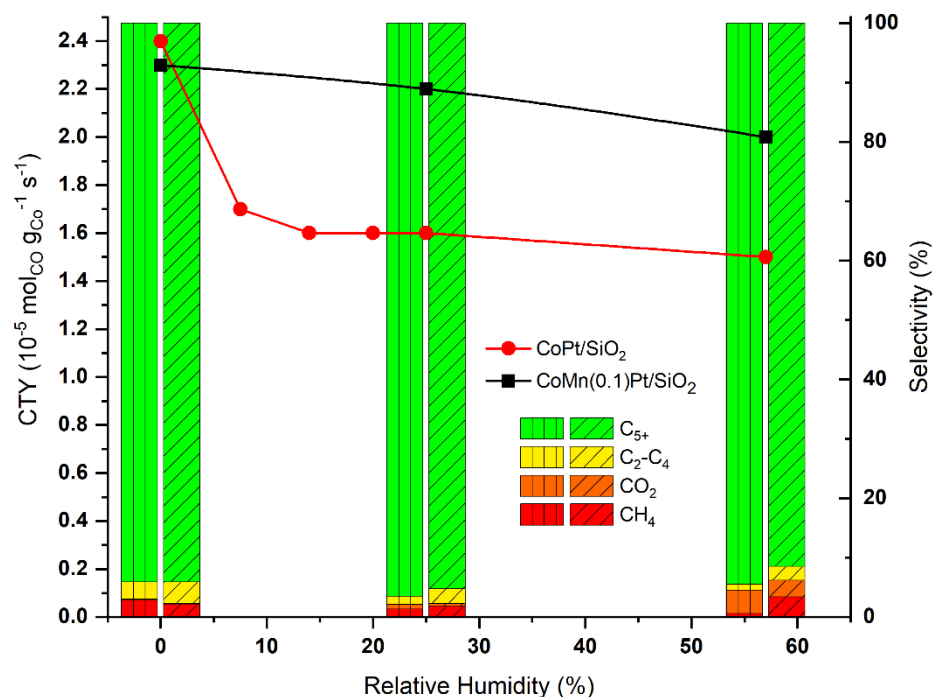


Figure 7. Catalytic performance at 200 °C, 20 bar pressure, $H_2/CO = 4$, and increasing relative humidity in terms of CTY and the product distribution for FTS measurements in the Mössbauer cell for the CoPt/SiO₂ (red dots) and the CoMn(0.1)Pt/SiO₂ catalyst (black squares). The carbon-based selectivity at the given humidity treatments is expressed as bar graphs for the CoPt/ catalyst (vertical line pattern) and the CoMn(0.1)Pt/SiO₂ catalyst (diagonal line pattern).

Besides the catalytic activity measurements in the *in situ* MES cell, the performance of the silica-supported cobalt catalysts was measured in a high-pressure fixed-bed plug-flow reactor at a temperature of 220 °C, a pressure of 20 bar, a H_2/CO ratio of 4, and a space velocity of 60 L g_{cat}⁻¹ h⁻¹. The corresponding results for fresh and used catalysts are given in Table 3. The activity normalized on the amount of cobalt (CTY) shows a clear effect of the manganese promotion, which was not observed in the Mössbauer experiments: the promoted samples are significantly less active than their non-promoted counterpart under these more representative test conditions. The observed average particle sizes for the two promoted catalysts given in Table 1 are slightly below the optimum size of 6 nm [4]. As such, a slightly lower activity is to be expected for these samples. As the decrease in activity is much more pronounced, we attribute this to overpromotion with manganese, where a substantial part of the cobalt surface is covered by manganese oxide. Previously, it was found that a manganese to cobalt ratio of 0.1 already led to a significant decrease of the FTS activity of a carbon nanofiber (CNF) supported cobalt catalyst [23]. The adverse effect of overpromotion seems to be

stronger for the silica-supported case, which may be due to the increased stability of manganese oxide. Compared to silica, manganese was found to be highly mobile on the CNF support [24]. Besides the decreased CTY values, the promoted catalysts also show a significant increase in the C₂-C₄ selectivity. This shift in selectivity has been previously reported for catalysts overpromoted with manganese oxide, where the strong interaction between cobalt and manganese in the oxidic precursor was emphasized [23]. Concurrent work by Kimpel et al. [51] has shown that manganese promotion leads to a lower chain-growth probability when operating the reaction at high pressure. They show that CO dissociation is enhanced by the manganese promotor, which was also recently reported by Gupta et al. [70]. And they propose the high carbon coverage results in a migration hindrance towards the step sites, which are highly active for C-C coupling.

From a comparison of the catalytic performance in the fresh and used state, it is clear that the catalysts significantly deactivated during the exposure to the various humid FTS treatments. The loss in CTY is more substantial for the non-promoted CoPt/SiO₂ catalyst. This is to be expected, as TEM showed more substantial sintering of cobalt, besides the formation of cobalt silicates. The less substantial activity loss for the manganese-promoted CoMn(0.2)Pt/SiO₂ catalyst is in line with the less severe sintering of the metallic cobalt phase, which can be attributed to the structural promotion of manganese.

However, a larger contribution of cobalt silicates was observed for the promoted catalyst. So, whilst the seemingly dominant deactivation due to sintering is likely less pronounced, additional deactivation occurs through formation of such inactive cobalt silicates. This deactivation goes in parallel with a shift in the product distribution with much of the selectivity towards C₂-C₄ products being lost in favour of methane and C₅₊ products. This could be the result of the increasing average particle size, as larger particles tend to favour C₅₊ selectivity. However, like the FTS activity measured in the Mössbauer cell at high humidity, an increase in methane selectivity is also observed, which would suggest the presence of smaller metallic particles. So instead, the selectivity shift could come from manganese oxide promotion being less pronounced in the spent catalyst. Such a shift was also observed in a previous study, where during prolonged time on stream the selectivity towards C₁ increased at the expense of C₂-C₄ products [71]. This is expected to be the result of manganese mobility under reaction conditions, as it migrates from the metal onto the support, weakening the promotion effect. As a result of this, the used catalyst benefits from reduced manganese overpromotion compared to the fresh sample, explained the lower selectivity towards C₂-C₄ products.

Table 3. Catalytic performance data for the cobalt catalysts (plug-flow reactor operated at 220 °C, 20 bar and $H_2/CO = 4$, $SV = 60 \text{ L g}_{\text{cat}}^{-1} \text{ h}^{-1}$)

<i>Catalyst</i>	<i>Conversion</i> (%)	<i>C₁</i> <i>selectivity</i> (%)	<i>C₂-C₄</i> <i>selectivity</i> (%)	<i>C₅+</i> <i>selectivity</i> (%)	<i>CTY</i> ($10^{-5} \text{ mol}_{\text{CO}}$ $\text{g}_{\text{Co}}^{-1} \text{ s}^{-1}$)
CoPt/SiO ₂	10	7	9	84	2.6
CoPt/SiO ₂ used	2	5	6	89	0.75
CoMn(0.2)Pt/SiO ₂	7	6	15	79	1.7
CoMn(0.2)Pt/SiO ₂ used	3	12	3	85	1.0
CoMn(0.1)Pt/SiO ₂	5	10	25	65	0.77

3.4. Conclusions

The effect of humidity during FTS conditions, representing high CO conversion conditions, on manganese-promoted cobalt supported by silica was investigated by Mössbauer spectroscopy, TEM and XPS. Promotion with manganese leads to a higher dispersion of the metallic cobalt particles in the reduced catalysts as compared to the unpromoted catalyst. *In situ* Mössbauer spectroscopy demonstrated that the enhanced dispersion of cobalt due to manganese promotion leads to a more intimate contact with the support, resulting in cobalt silicates at elevated relative humidity that are inactive for the FTS reaction. In the absence of manganese, carbidization of relatively large particles was observed as a possible deactivation mechanism under high relative humidity conditions. The metallic cobalt phase in the used catalysts (having undergone *in situ* Mössbauer spectroscopy from low to high relative humidity) has a significantly lower dispersion than the metallic phase in the freshly reduced state. Sintering is more pronounced in the absence of manganese oxide, demonstrating the beneficial role of manganese as a structural promoter in cobalt-based FTS catalysts. Despite this, catalysts without and with manganese suffered from serious deactivation upon exposure to high partial pressures of steam due to formation of less active cobalt phases. These findings highlight that silica is not a suitable support material for practical Fischer-Tropsch synthesis at bottom bed conditions with high CO conversion. Under mild conditions, however, the silica-supported cobalt exhibits excellent stability.

Bibliography

- [1] E. Iglesia, Design, synthesis, and use of cobalt-based Fischer-Tropsch synthesis catalysts, *Appl. Catal. A Gen.*, vol. 161, no. 1–2, pp. 59–78, 1997, doi: 10.1016/S0926-860X(97)00186-5.
- [2] E. Rytter, N. E. Tsakoumis, and A. Holmen, On the selectivity to higher hydrocarbons in Co-based Fischer-Tropsch synthesis, *Catal. Today*, vol. 261, pp. 3–16, 2016, doi: 10.1016/j.cattod.2015.09.020.
- [3] J. P. den Breejen, P. B. Radstake, G. L. Bezemer, J. H. Bitter, V. Frøseth, A. Holmen, and K. P. de Jong, On the Origin of the Cobalt Particle Size Effects in Fischer-Tropsch Catalysis, *J. Am. Chem. Soc.*, vol. 131, no. 20, pp. 7197–7203, 2009, doi: 10.1021/ja901006x.
- [4] G. L. Bezemer, J. H. Bitter, H. P. C. E. Kuipers, H. Oosterbeek, J. E. Holewijn, X. Xu, F. Kapteijn, A. J. van Dillen, and K. P. de Jong, Cobalt Particle Size Effects in the Fischer-Tropsch Reaction Studied with Carbon Nanofiber Supported Catalysts, *J. Am. Chem. Soc.*, vol. 128, no. 12, pp. 3956–3964, 2006, doi: 10.1021/ja058282w.
- [5] N. E. Tsakoumis, M. Rønning, Ø. Borg, E. Rytter, and A. Holmen, Deactivation of cobalt based Fischer-Tropsch catalysts: A review, *Catal. Today*, vol. 154, no. 3–4, pp. 162–182, 2010, doi: 10.1016/j.cattod.2010.02.077.
- [6] P. J. van Berge and R. C. Everson, Cobalt as an alternative Fischer-Tropsch catalyst to iron for the production of middle distillates, in *Studies in Surface Science and Catalysis*, vol. 107, no. 15, 1997, pp. 207–212. doi: 10.1016/S0167-2991(97)80336-9.
- [7] D. Moodley, M. Claeys, E. van Steen, P. van Helden, D. Kistamurthy, K.-J. Weststrate, H. Niemantsverdriet, A. Saib, W. Erasmus, and J. van de Loosdrecht, Sintering of cobalt during FTS: Insights from industrial and model systems, *Catal. Today*, vol. 342, pp. 59–70, 2020, doi: 10.1016/j.cattod.2019.03.059.
- [8] E. Rytter and A. Holmen, Deactivation and Regeneration of Commercial Type Fischer-Tropsch Co-Catalysts—A Mini-Review, *Catalysts*, vol. 5, no. 2, pp. 478–499, 2015, doi: 10.3390/catal5020478.
- [9] Z. Yu, Ø. Borg, D. Chen, E. Rytter, and A. Holmen, Role of surface oxygen in the preparation and deactivation of carbon nanofiber supported cobalt Fischer-Tropsch catalysts, *Top. Catal.*, vol. 45, no. 1–4, pp. 69–74, 2007, doi: 10.1007/s11244-007-0242-7.
- [10] M. Wolf, B. K. Mutuma, N. J. Coville, N. Fischer, and M. Claeys, Role of CO in the Water-Induced Formation of Cobalt Oxide in a High Conversion Fischer-Tropsch Environment, *ACS Catal.*, vol. 8, no. 5, pp. 3985–3989, 2018, doi: 10.1021/acscatal.7b04177.
- [11] E. Van Steen, M. Claeys, M. E. Dry, J. Van De Loosdrecht, E. L. Viljoen, and J. L. Visagie, Stability of nanocrystals: Thermodynamic analysis of oxidation and re-reduction of cobalt in water/hydrogen mixtures, *J. of Phys. Chem. B*, vol. 109, no. 8, pp. 3575–3577, 2005, doi: 10.1021/jp045136o.
- [12] P. J. Van Berge, J. Van De Loosdrecht, S. Barradas, and A. M. Van Der Kraan, Oxidation of cobalt based Fischer-Tropsch catalysts as a deactivation mechanism, *Catal. Today*, vol. 58, no. 4, pp. 321–334, 2000, doi: 10.1016/S0920-5861(00)00265-0.
- [13] J. van de Loosdrecht, B. Balzhinimaev, J. A. Dalmon, J. W. Niemantsverdriet, S. V. Tsybulya, A. M. Saib, P. J. van Berge, and J. L. Visagie, Cobalt Fischer-Tropsch synthesis: Deactivation by oxidation?, *Catal. Today*, vol. 123, no. 1–4, pp. 293–302, 2007, doi: 10.1016/j.cattod.2007.02.032.
- [14] W. Zhou, J.-G. Chen, K.-G. Fang, and Y.-H. Sun, The deactivation of Co/SiO₂ catalyst for Fischer-Tropsch synthesis at different ratios of H₂ to CO, *Fuel Processing Technology*, vol. 87, no. 7, pp. 609–616, 2006, doi: 10.1016/j.fuproc.2006.01.008.
- [15] G. Prieto, A. Martínez, P. Concepción, and R. Moreno-Tost, Cobalt particle size effects in Fischer-Tropsch synthesis: structural and in situ spectroscopic characterisation on reverse micelle-synthesised Co/ITQ-2 model catalysts, *J. Catal.*, vol. 266, no. 1, pp. 129–144, 2009, doi: 10.1016/j.jcat.2009.06.001.
- [16] M. Wolf, E. K. Gibson, E. J. Olivier, J. H. Neethling, C. R. A. Catlow, N. Fischer, and M. Claeys, In-depth characterisation of metal-support compounds in spent Co/SiO₂ Fischer-Tropsch model catalysts, *Catal. Today*, vol. 342, pp. 71–78, 2020, doi: 10.1016/j.cattod.2019.01.065.
- [17] C. H. Bartholomew, Mechanisms of catalyst deactivation, *Appl. Catal. A Gen.*, vol. 212, no. 1–2, pp. 17–60, Apr. 2001, doi: 10.1016/S0926-860X(00)00843-7.
- [18] M. Sadeqzadeh, S. Chambrey, J. Hong, P. Fongarland, F. Luck, D. Curulla-Ferré, D. Schweich, J. Bousquet, and A. Y. Khodakov, Effect of different reaction conditions on the deactivation of alumina-supported cobalt Fischer-Tropsch catalysts in a milli-fixed-bed reactor: Experiments and modeling, *Ind. Eng. Chem. Res.*, vol. 53, no. 17, pp. 6913–6922, 2014, doi: 10.1021/ie4040303.
- [19] A. M. Saib, D. J. Moodley, I. M. Ciobîc, M. M. Hauman, B. H. Sigwebela, C. J. Weststrate, J. W. Niemantsverdriet, and J. Van De Loosdrecht, Fundamental understanding of deactivation and regeneration of cobalt Fischer-Tropsch synthesis catalysts, *Catal. Today*, vol. 154, no. 3–4, pp. 271–282, 2010, doi: 10.1016/j.cattod.2010.02.008.
- [20] M. Rahmati, M. S. Safdari, T. H. Fletcher, M. D. Argyle, and C. H. Bartholomew, Chemical and Thermal Sintering of Supported Metals with Emphasis on Cobalt Catalysts during Fischer-Tropsch Synthesis, *Chemical Reviews*, vol. 120, no. 10, pp. 4455–4533, 2020. doi: 10.1021/acs.chemrev.9b00417.

- [21] M. Claeys, M. E. Dry, E. van Steen, P. J. van Berge, S. Booyens, R. Crous, P. van Helden, J. Labuschagne, D. J. Moodley, and A. M. Saib, Impact of Process Conditions on the Sintering Behavior of an Alumina-Supported Cobalt Fischer–Tropsch Catalyst Studied with an in Situ Magnetometer, *ACS Catal.*, vol. 5, no. 2, pp. 841–852, 2015, doi: 10.1021/cs501810y.
- [22] M. D. Argyle, T. S. Frost, and C. H. Bartholomew, Cobalt fischer-tropsch catalyst deactivation modeled using generalized power law expressions, *Top. Catal.*, vol. 57, no. 6–9, pp. 415–429, 2014, doi: 10.1007/s11244-013-0197-9.
- [23] G. L. Bezemer, P. Radstake, U. Falke, H. Oosterbeek, H. Kuipers, A. Van Dillen, and K. De Jong, Investigation of promoter effects of manganese oxide on carbon nanofiber-supported cobalt catalysts for Fischer–Tropsch synthesis, *J. Catal.*, vol. 237, no. 1, pp. 152–161, 2006, doi: 10.1016/j.jcat.2005.10.031.
- [24] L. M. van Koppen, A. I. Dugulan, G. L. Bezemer, and E. J. M. Hensen, Sintering and carbidization under simulated high conversion on a cobalt-based Fischer–Tropsch catalyst; manganese oxide as a structural promotor, *J. Catal.*, vol. 413, pp. 106–118, 2022, doi: 10.1016/j.jcat.2022.06.020.
- [25] A. Carvalho, V. V. Ordonsky, Y. Luo, M. Marinova, A. R. Muniz, N. R. Marcilio, and A. Y. Khodakov, Elucidation of deactivation phenomena in cobalt catalyst for Fischer–Tropsch synthesis using SSITKA, *J. Catal.*, vol. 344, pp. 669–679, 2016, doi: 10.1016/j.jcat.2016.11.001.
- [26] B. Ernst, S. Libs, P. Chaumette, and A. Kiennemann, Preparation and characterization of Fischer–Tropsch active Co/SiO₂ catalysts, *Appl. Catal. A Gen.*, vol. 186, no. 1–2, pp. 145–168, 1999, doi: 10.1016/S0926-860X(99)00170-2.
- [27] H. Karaca, J. Hong, P. Fongarland, P. Roussel, A. Griboval-Constant, M. Lacroix, K. Hortmann, O. V. Safonova, and A. Y. Khodakov, In situ XRD investigation of the evolution of alumina-supported cobalt catalysts under realistic conditions of Fischer–Tropsch synthesis, *Chem. Commun.*, vol. 46, no. 5, pp. 788–790, 2010, doi: 10.1039/B920110F.
- [28] A. Rochet, V. Moizan, F. Diehl, C. Pichon, and V. Briois, Quick-XAS and Raman operando characterisation of a cobalt alumina-supported catalyst under realistic Fischer–Tropsch reaction conditions, *Catal. Today*, vol. 205, pp. 94–100, 2013, doi: 10.1016/j.cattod.2012.08.021.
- [29] T. O. Eschemann and K. P. de Jong, Deactivation Behavior of Co/TiO₂ Catalysts during Fischer–Tropsch Synthesis, *ACS Catal.*, vol. 5, no. 6, pp. 3181–3188, 2015, doi: 10.1021/acscatal.5b00268.
- [30] T. O. Eschemann, J. H. Bitter, and K. P. De Jong, Effects of loading and synthesis method of titania-supported cobalt catalysts for Fischer–Tropsch synthesis, *Catal. Today*, vol. 228, pp. 89–95, 2014, doi: 10.1016/j.cattod.2013.10.041.
- [31] C. E. Kliever, S. L. Soled, and G. Kiss, Morphological transformations during Fischer–Tropsch synthesis on a titania-supported cobalt catalyst, *Catal. Today*, vol. 323, pp. 233–256, 2019, doi: 10.1016/j.cattod.2018.05.021.
- [32] M. Mehrbod, M. Martinelli, A. G. Martino, D. C. Cronauer, A. Jeremy Kropf, C. L. Marshall, and G. Jacobs, Fischer–Tropsch synthesis: Direct cobalt nitrate reduction of promoted Co/TiO₂ catalysts, *Fuel*, vol. 245, pp. 488–504, 2019, doi: 10.1016/j.fuel.2019.02.083.
- [33] S. J. Tauster, S. C. Fung, and R. L. Garten, Strong metal-support interactions. Group 8 noble metals supported on titanium dioxide, *J. Am. Chem. Soc.*, vol. 100, pp. 170–175, 1978, doi: 10.1021/ja00469a029.
- [34] S. J. Tauster, S. C. Fung, R. T. K. Baker, and J. A. Horsley, Strong Interactions in Supported-Metal Catalysts, *Science*, vol. 211, pp. 1121–1125, 1981, doi: 10.1126/science.211.4487.1121.
- [35] M. Wolf, E. K. Gibson, E. J. Olivier, J. H. Neethling, C. R. A. Catlow, N. Fischer, and M. Claeys, Water-Induced Formation of Cobalt-Support Compounds under Simulated High Conversion Fischer–Tropsch Environment, *ACS Catal.*, vol. 9, pp. 4902–4918, 2019, doi: 10.1021/acscatal.9b00160.
- [36] M. Wolf, N. Fischer, and M. Claeys, Water-induced deactivation of cobalt-based Fischer–Tropsch catalysts, *Nat. Catal.*, vol. 3, pp. 962–965, 2020, doi: 10.1038/s41929-020-00534-5.
- [37] H. Karaca, O. V. Safonova, S. Chambrey, P. Fongarland, P. Roussel, A. Griboval-Constant, M. Lacroix, and A. Y. Khodakov, Structure and catalytic performance of Pt-promoted alumina-supported cobalt catalysts under realistic conditions of Fischer–Tropsch synthesis, *J. Catal.*, vol. 277, pp. 14–26, 2011, doi: 10.1016/j.jcat.2010.10.007.
- [38] G. L. Bezemer, T. J. Remans, A. P. van Bavel, and A. I. Dugulan, Direct Evidence of Water-Assisted Sintering of Cobalt on Carbon Nanofiber Catalysts during Simulated Fischer–Tropsch Conditions Revealed with in Situ Mössbauer Spectroscopy, *J. Am. Chem. Soc.*, vol. 132, pp. 8540–8541, 2010, doi: 10.1021/ja103002k.
- [39] M. Claeys, M. E. Dry, E. van Steen, E. du Plessis, P. J. van Berge, A. M. Saib, and D. J. Moodley, In situ magnetometer study on the formation and stability of cobalt carbide in Fischer–Tropsch synthesis, *J. Catal.*, vol. 318, pp. 193–202, 2014, doi: 10.1016/j.jcat.2014.08.002.
- [40] T. Lin, K. Gong, C. Wang, Y. An, X. Wang, X. Qi, S. Li, Y. Lu, L. Zhong, and Y. Sun, Fischer–Tropsch Synthesis to Olefins: Catalytic Performance and Structure Evolution of Co₂C-Based Catalysts under a CO₂ Environment, *ACS Catal.*, vol. 9, pp. 9554–9567, 2019, doi: 10.1021/acscatal.9b02513.
- [41] Z. Li, L. Zhong, F. Yu, Y. An, Y. Dai, Y. Yang, T. Lin, S. Li, H. Wang, P. Gao, Y. Sun, and M. He, Effects of Sodium on the Catalytic Performance of CoMn Catalysts for Fischer–Tropsch to Olefin Reactions, *ACS Catal.*, vol. 7, no. 5, pp. 3622–3631, 2017, doi: 10.1021/acscatal.6b03478.
- [42] X. Wang, W. Chen, T. Lin, J. Li, F. Yu, Y. An, Y. Dai, H. Wang, L. Zhong, and Y. Sun, Effect of the support on cobalt carbide catalysts for sustainable production of olefins from syngas, *Cuihua Xuebao/Chinese Journal of Catalysis*, vol. 39, no. 12, pp. 1869–1880, 2018, doi: 10.1016/S1872-2067(18)63153-5.

- [43] H. H. Storch, The Fischer-Tropsch and Related Processes for Synthesis of Hydrocarbons by Hydrogenation of Carbon Monoxide, New York: Wiley, 1948, pp. 115–156. doi: 10.1016/S0360-0564(08)60674-4.
- [44] M. van der Riet, G. J. Hutchings, and R. G. Copperthwaite, Selective formation of C₃ hydrocarbons from CO + H₂ using cobalt–manganese oxide catalysts, *J. Chem. Soc., Chem. Commun.*, no. 10, pp. 798–799, 1986, doi: 10.1039/C39860000798.
- [45] S. Colley, R. G. Copperthwaite, G. J. Hutchings, and M. Van der Riet, Carbon monoxide hydrogenation using cobalt manganese oxide catalysts: initial catalyst optimization studies, *Ind. Eng. Chem. Res.*, vol. 27, no. 8, pp. 1339–1344, 1988, doi: 10.1021/ie00080a001.
- [46] G. J. Hutchings, M. van der Riet, and R. Hunter, CO hydrogenation using cobalt/manganese oxide catalysts. Comments on the mechanism of carbon–carbon bond formation, *Journal of the Chemical Society, Faraday Transactions 1: Physical Chemistry in Condensed Phases*, vol. 85, no. 9, pp. 2875, 1989, doi: 10.1039/f19898502875.
- [47] S. E. Colley, R. G. Copperthwaite, G. J. Hutchings, S. P. Terblanche, and M. M. Thackeray, Identification of body-centred cubic cobalt and its importance in CO hydrogenation, *Nature*, vol. 339, no. 6220, pp. 129–130, 1989, doi: 10.1038/339129a0.
- [48] F. Morales, F. M. F. De Groot, P. Glatzel, E. Kleimenov, H. Bluhm, M. Hävecker, A. Knop-Gericke, and B. M. Weckhuysen, In situ X-ray absorption of Co/Mn/TiO₂ catalysts for fischer-tropsch synthesis, *Journal of Physical Chemistry B*, vol. 108, no. 41, pp. 16201–16207, 2004, doi: 10.1021/jp0403846.
- [49] F. Morales, F. De Groot, O. Gijzeman, A. Mens, O. Stephan, and B. Weckhuysen, Mn promotion effects in Co/TiO₂ Fischer-Tropsch catalysts as investigated by XPS and STEM-EELS, *J. Catal.*, vol. 230, no. 2, pp. 301–308, 2005, doi: 10.1016/j.jcat.2004.11.047.
- [50] A. Y. Khodakov, W. Chu, and P. Fongarland, Advances in the development of novel cobalt Fischer-Tropsch catalysts for synthesis of long-chain hydrocarbons and clean fuels, *Chem. Rev.*, vol. 107, no. 5, pp. 1692–1744, 2007, doi: 10.1021/cr050972v.
- [51] T. F. Kimpel, J. X. Liu, W. Chen, R. Pestman, and E. J. M. Hensen, Pressure dependence and mechanism of Mn promotion in Co catalyzed Fischer-Tropsch reaction, *J. Catal.*, in review.
- [52] M. W. J. Crajé, A. M. Van der Kraan, J. Van de Loosdrecht, and P. J. Van Berge, The application of Mössbauer emission spectroscopy to industrial cobalt based Fischer-Tropsch catalysts, *Catal. Today*, vol. 71, no. 3–4, pp. 369–379, 2002, doi: 10.1016/S0920-5861(01)00464-3.
- [53] L. M. van Koppen, A. I. Dugulan, G. L. Bezemer, and E. J. M. Hensen, Elucidating deactivation of titania-supported cobalt Fischer-Tropsch catalysts under simulated high conversion conditions, *J. Catal.*, vol. 420, pp. 44–57, 2023, doi: 10.1016/j.jcat.2023.02.019.
- [54] M. C. Biesinger, B. P. Payne, A. P. Grosvenor, L. W. M. Lau, A. R. Gerson, and R. St. C. Smart, Resolving surface chemical states in XPS analysis of first row transition metals, oxides and hydroxides: Cr, Mn, Fe, Co and Ni, *Appl. Surf. Sci.*, vol. 257, no. 7, pp. 2717–2730, 2011, doi: 10.1016/j.apsusc.2010.10.051.
- [55] Z. Klencsár, MossWinn—methodological advances in the field of Mössbauer data analysis, *Hyperfine Interact.*, vol. 217, no. 1–3, pp. 117–126, 2013, doi: 10.1007/s10751-012-0732-2.
- [56] J. A. Tjon and M. Blume, Mössbauer Spectra in a Fluctuating Environment II. Randomly Varying Electric Field Gradients, *Physical Review*, vol. 165, no. 2, pp. 456–461, 1968, doi: 10.1103/PhysRev.165.456.
- [57] P. Scherrer, Estimation of the Size and Internal Structure of Colloidal Particles by Means of Röntgen, *Nachrichten von der Gesellschaft der Wissenschaften zu Göttingen*, vol. 2, pp. 96–100, 1918.
- [58] T. W. van Deelen, J. J. Nijhuis, N. A. Krans, J. Zečević, and K. P. de Jong, Preparation of Cobalt Nanocrystals Supported on Metal Oxides To Study Particle Growth in Fischer–Tropsch Catalysts, *ACS Catal.*, vol. 8, no. 11, pp. 10581–10589, 2018, doi: 10.1021/acscatal.8b03094.
- [59] F. Morales, D. Grandjean, F. M. F. de Groot, O. Stephan, and B. M. Weckhuysen, Combined EXAFS and STEM-EELS study of the electronic state and location of Mn as promoter in Co-based Fischer–Tropsch catalysts, *Phys. Chem. Chem. Phys.*, vol. 7, no. 4, pp. 568–572, 2005, doi: 10.1039/B418286C.
- [60] G. M. Bancroft, A. G. Maddock, and R. G. Burns, Applications of the Mössbauer effect to silicate mineralogy—I. Iron silicates of known crystal structure, *Geochim Cosmochim Acta*, vol. 31, no. 11, pp. 2219–2246, 1967, doi: 10.1016/0016-7037(67)90062-2.
- [61] L. C. Browning and P. H. Emmett, Equilibrium Measurements in the Ni₃C–Ni–CH₄–H₂ and Co₂C–Co–CH₄–H₂ Systems, *J. Am. Chem. Soc.*, vol. 74, no. 7, pp. 1680–1682, 1952, doi: 10.1021/ja01127a021.
- [62] M. Wolf, H. Kotzé, N. Fischer, and M. Claeys, Size dependent stability of cobalt nanoparticles on silica under high conversion Fischer–Tropsch environment, *Faraday Discuss.*, vol. 197, pp. 243–268, 2017, doi: 10.1039/C6FD00200E.
- [63] F. Morales, D. Grandjean, A. Mens, F. M. F. de Groot, and B. M. Weckhuysen, X-ray Absorption Spectroscopy of Mn/Co/TiO₂ Fischer–Tropsch Catalysts: Relationships between Preparation Method, Molecular Structure, and Catalyst Performance, *J. Phys. Chem. B*, vol. 110, no. 17, pp. 8626–8639, 2006, doi: 10.1021/jp0565958.

- [64] E. Rytter, Ø. Borg, N. E. Tsakoumis, and A. Holmen, Water as key to activity and selectivity in Co Fischer-Tropsch synthesis: γ -alumina based structure-performance relationships, *J. Catal.*, vol. 365, pp. 334–343, 2018, doi: 10.1016/j.jcat.2018.07.003.
- [65] E. Rytter and A. Holmen, Perspectives on the Effect of Water in Cobalt Fischer-Tropsch Synthesis, *ACS Catal.*, vol. 7, no. 8, pp. 5321–5328, 2017, doi: 10.1021/acscatal.7b01525.
- [66] Ø. Borg, Z. Yu, D. Chen, E. A. Blekkan, E. Rytter, and A. Holmen, The effect of water on the activity and selectivity for carbon nanofiber supported cobalt Fischer-Tropsch catalysts, *Top. Catal.*, vol. 57, no. 6–9, pp. 491–499, 2014, doi: 10.1007/s11244-013-0205-0.
- [67] W. Chen, R. Pestman, B. Zijlstra, I. A. W. Filot, and E. J. M. Hensen, Mechanism of Cobalt-Catalyzed CO Hydrogenation: 1. Methanation, *ACS Catal.*, vol. 7, no. 12, pp. 8050–8060, 2017, doi: 10.1021/acscatal.7b02757.
- [68] R. Pestman, W. Chen, and E. Hensen, Insight into the Rate-Determining Step and Active Sites in the Fischer-Tropsch Reaction over Cobalt Catalysts, *ACS Catal.*, vol. 9, no. 5, pp. 4189–4195, 2019, doi: 10.1021/acscatal.9b00185.
- [69] F. Morales, E. de Smit, F. de Groot, T. Visser, and B. Weckhuysen, Effects of manganese oxide promoter on the CO and H₂ adsorption properties of titania-supported cobalt Fischer-Tropsch catalysts, *J. Catal.*, vol. 246, no. 1, pp. 91–99, 2007, doi: 10.1016/j.jcat.2006.11.014.
- [70] S. S. Gupta, P. M. Shenai, J. Meeuwissen, G. L. Bezemer, and S. Shetty, Electronic Promotion Effects of Metal Oxides: A Case Study of MnO Impact on Fischer-Tropsch Catalysis, *The Journal of Physical Chemistry C*, vol. 125, no. 39, pp. 21390–21401, 2021, doi: 10.1021/acs.jpcc.1c05278.
- [71] M. van der Riet, R. G. Copperthwaite, and G. J. Hutchings, Formation of hydrocarbons from CO + H₂ using a cobalt-manganese oxide catalyst. A ¹³C isotopic study, *Journal of the Chemical Society, Faraday Transactions 1: Physical Chemistry in Condensed Phases*, vol. 83, no. 9, p. 2963, 1987, doi: 10.1039/f19878302963.

Appendix B

Table B1. Mössbauer experimental conditions for reactive Fischer-Tropsch humidity tests. All tests were performed at 200 °C with a total pressure of 20 bar.

<i>Reaction</i>	<i>He (mL/min)</i>	<i>H₂ (mL/min)</i>	<i>CO (mL/min)</i>	<i>Water (g/h)</i>	<i>Steam (mL/min)</i>
<i>RH = 0%</i>	75	20	5	0	0
<i>RH = 7.5%</i> <i>H₂/H₂O = 4</i>	55	20	5	0.24	5
<i>RH = 14%</i> <i>H₂/H₂O = 2</i>	55	20	5	0.48	10
<i>RH = 20%</i> <i>H₂/H₂O = 1.3</i>	55	20	5	0.72	15
<i>RH = 25%</i> <i>H₂/H₂O = 1</i>	55	20	5	0.96	20
<i>RH = 57%</i> <i>H₂/H₂O = 1</i>	0	20	5	0.96	20

Table B2. Fit parameters of Mössbauer spectra of the CoPt/SiO₂ catalyst after different treatments.

<i>Treatment</i>	<i>Temperature (°C)</i>	<i>Cobalt phase</i>	<i>Isomer Shift (mm s⁻¹)</i>	<i>Hyperfine Field (kOe)</i>	<i>Quadrupole Splitting (mm s⁻¹)</i>	<i>Spectral Contribution (%)</i>
<i>After reduction</i>	20	<i>Co(0) bulk</i>	-0.1	317	-	73
		<i>Co(0) SPM</i>	0.1	-	-	27
<i>During FTS reaction</i>	200	<i>Co(0) bulk</i>	-0.2	301	-	53
		<i>Co(0) SPM</i>	0.0	-	-	47
<i>RH = 7.5%</i>	200	<i>Co(0) bulk</i>	-0.2	301	-	50
		<i>Co(0) SPM</i>	0.0	-	-	50
<i>RH = 14%</i>	200	<i>Co(0) bulk</i>	-0.2	301	-	51
		<i>Co(0) SPM</i>	0.0	-	-	49

<i>RH = 20%</i>	200	<i>Co(0) bulk</i>	-0.2	301	-	52
		<i>Co(0) SPM</i>	0.0	-	-	48
<i>RH = 25%</i>	200	<i>Co(0) bulk</i>	-0.2	301	-	54
		<i>Co(0) SPM</i>	0.0	-	-	46
<i>RH = 57%</i>	200	<i>Co(0) bulk</i>	-0.2	301	-	46
		<i>Co(0) SPM</i>	0.0	-	-	37
		<i>Co²⁺</i>	0.9	-	1.8	4
		<i>Co₂C</i>	0.0	-	0.9	13
<i>After reaction</i>	20	<i>Co(0) bulk</i>	-0.1	317	-	54
		<i>Co(0) SPM</i>	0.1	-	-	19
		<i>Co²⁺</i>	1.0	-	2.5	12
		<i>Co₂C</i>	0.1	-	0.8	15
<i>Reduced</i>	20	<i>Co(0) bulk</i>	-0.1	320	-	75
		<i>Co(0) SPM</i>	0.1	-	-	14
		<i>Co²⁺</i>	1.0	-	2.5	11

Table B3. Fit parameters of Mössbauer spectra of the CoMn(0.1)Pt/SiO₂ catalyst after different treatments.

<i>Treatment</i>	<i>Temperature (°C)</i>	<i>Cobalt phase</i>	<i>Isomer Shift (mm s⁻¹)</i>	<i>Hyperfine Field (kOe)</i>	<i>Quadrupole Splitting (mm s⁻¹)</i>	<i>Spectral Contribution (%)</i>
<i>After reduction</i>	20	<i>Co(0) bulk</i>	-0.1	311	-	44
		<i>Co(0) SPM</i>	0.1	-	-	56
<i>During FTS reaction</i>	200	<i>Co(0) bulk</i>	-0.2	290	-	34
		<i>Co(0) SPM</i>	0.0	-	-	66
<i>RH = 25%</i>	200	<i>Co(0) bulk</i>	-0.2	289	-	31
		<i>Co(0) SPM</i>	0.0	-	-	69
<i>RH = 57%</i>	200	<i>Co(0) bulk</i>	-0.2	293	-	22
		<i>Co(0) SPM</i>	-0.1	-	-	46
		<i>Co²⁺</i>	0.9	-	1.9	32

<i>After reaction</i>	20	<i>Co(0) bulk</i>	-0.1	310	-	27
		<i>Co(0) SPM</i>	0.1	-	-	40
		<i>Co²⁺</i>	1.0	-	2.5	33
<i>Reduced</i>	20	<i>Co(0) bulk</i>	-0.1	312	-	27
		<i>Co(0) SPM</i>	0.0	-	-	34
		<i>Co²⁺</i>	1.0	-	2.5	39

Table B4. Fit parameters of Mössbauer spectra of the CoMn(0.2)Pt/SiO₂ catalyst after different treatments.

<i>Treatment</i>	<i>Temperature (°C)</i>	<i>Cobalt phase</i>	<i>Isomer Shift (mm s⁻¹)</i>	<i>Hyperfine Field (kOe)</i>	<i>Quadrupole Splitting (mm s⁻¹)</i>	<i>Spectral Contribution (%)</i>
<i>After reduction</i>	20	<i>Co(0) bulk</i>	-0.1	310	-	43
		<i>Co(0) SPM</i>	0.2	-	-	57
<i>During FTS reaction</i>	200	<i>Co(0) bulk</i>	-0.2	288	-	31
		<i>Co(0) SPM</i>	0.0	-	-	69
<i>RH = 7.5%</i>	200	<i>Co(0) bulk</i>	-0.2	289	-	35
		<i>Co(0) SPM</i>	-0.1	-	-	65
<i>RH = 14%</i>	200	<i>Co(0) bulk</i>	-0.2	288	-	33
		<i>Co(0) SPM</i>	-0.1	-	-	67
<i>RH = 20%</i>	200	<i>Co(0) bulk</i>	-0.2	289	-	31
		<i>Co(0) SPM</i>	-0.1	-	-	69
<i>RH = 25%</i>	200	<i>Co(0) bulk</i>	-0.2	289	-	33
		<i>Co(0) SPM</i>	-0.1	-	-	67
<i>RH = 57%</i>	200	<i>Co(0) bulk</i>	-0.2	295	-	31
		<i>Co(0) SPM</i>	-0.1	-	-	44
		<i>Co²⁺</i>	0.9	-	1.8	24
<i>After reaction</i>	20	<i>Co(0) bulk</i>	-0.1	308	-	32
		<i>Co(0) SPM</i>	0.1	-	-	37
		<i>Co²⁺</i>	1.0	-	2.5	31

<i>Reduced</i>	<i>20</i>	<i>Co(0) bulk</i>	<i>-0.1</i>	<i>312</i>	<i>-</i>	<i>38</i>
		<i>Co(0) SPM</i>	<i>0.1</i>	<i>-</i>	<i>-</i>	<i>31</i>
		<i>Co²⁺</i>	<i>1.0</i>	<i>-</i>	<i>2.4</i>	<i>31</i>

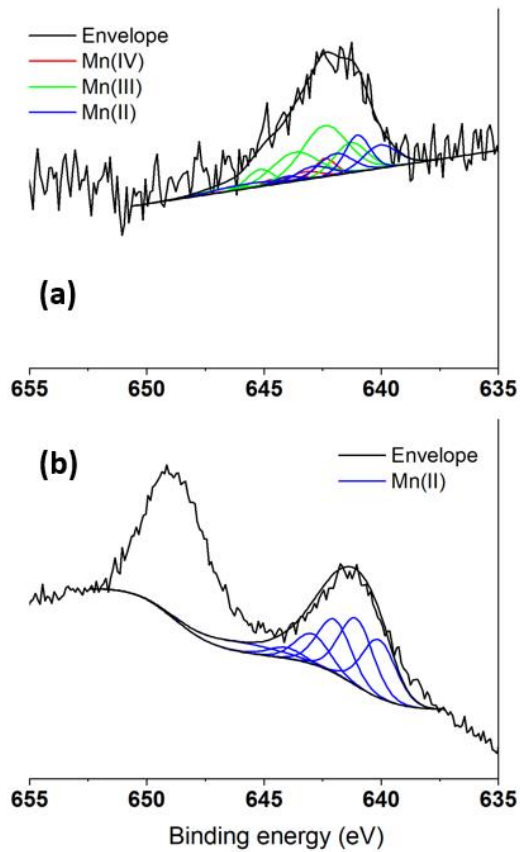


Figure B5. XPS spectra of CoMn(0.2)Pt/SiO₂ (a,b) after (a) calcination and (b) subsequent reduction at 350 °C (black: experimental data and the fitted envelope; red: the fitted Mn(IV) contributions; green: the fitted Mn(III) contributions; blue: fitted Mn(II) contributions; the XPS fit model was taken from Ref. [53]).

Chapter 4

Elucidating deactivation of titania-supported cobalt Fischer-Tropsch catalysts under simulated high conversion conditions

Abstract

The study of titania-supported cobalt nanoparticles is relevant for industrial Fischer-Tropsch synthesis (FTS). Herein, we report about various deactivation pathways of cobalt supported on P25 titania (cobalt loading 2-8 wt%) under simulated high conversion conditions using *in situ* Mössbauer spectroscopy. A fraction of metallic cobalt was oxidized under humid FTS conditions. The absolute amount of oxidized cobalt was ~ 1.2 wt% independent of the cobalt loading, indicating that specific cobalt-titanol interactions are involved in the oxidation process. The formation of cobalt-titanate-like compounds was only observed under very high water-to-hydrogen ratios in the absence of carbon monoxide. Steam considerably enhances cobalt sintering under FTS conditions. As such, deactivation under humid FTS conditions is not only caused by cobalt oxidation but also by enhancing sintering of the active phase.

This chapter was published as: L.M. van Koppen, A.I. Dugulan, G.L. Bezemer, and E.J.M. Hensen, *J. Catal.*, 2023, **420**, 44-57.

4.1 Introduction

Fischer-Tropsch synthesis (FTS) is a surface-catalyzed polymerization reaction that converts a feed of synthesis gas ($\text{CO} + \text{H}_2$) to fuels and chemicals [1]. Cobalt catalysts are preferred in industry when the synthesis gas is derived from natural gas and long-chain paraffins are targeted [2]. Structure sensitivity of the FTS reaction catalyzed by cobalt dictates that the optimum size of cobalt nanoparticles is around 6-8 nm [3], [4]. As such, it is important to understand the stability of cobalt nanoparticles for successful industrial applications [5].

One can distinguish short- and long-term deactivation of the catalyst in cobalt-based FTS [6]. Short-term deactivation is well studied [5], [7], [8] and can be reversed by mild hydrogen treatment [9]. Long-term deactivation, on the other hand, is less reversible, making it significant in industrial practice. Long-term deactivation is not well understood, and several factors can contribute to the loss of catalytic activity over time. The most common ones considered are oxidation of the active metal phase [10]–[13], strong-metal support interactions (SMSI) [14]–[16], carbon deposition [17]–[19] and cobalt sintering [20]–[22].

Investigations on supported cobalt catalysts are typically done using irreducible oxide supports such as SiO_2 [16], [23], [24] and Al_2O_3 [2], [25], [26]. Reducible oxides such as TiO_2 , are also of practical interest [27]–[30]. The support reducibility can result in the formation of cobalt-support compounds [31], [32]. The formation of such compounds can lead to significant irreversible deactivation.

Water is a main product of the FTS reaction, because the main pathway for O removal from the surface upon CO dissociation is through the production of water. High partial pressures of steam (humidity) can result in deactivation through oxidation as well as enhanced sintering. Thermodynamics dictate that spherical cobalt nanoparticles smaller than about 4 nm oxidize relevant $\text{H}_2\text{O}/\text{H}_2$ ratios during FTS conditions [11]. However, bulk oxidation of supported cobalt catalysts under such (simulated) industrial FTS conditions is often not observed in experiments, which can be due to the fact that typical catalysts contain larger particles or due to kinetic limitations of water dissociation [5], [10], [13], [33], [34]. The effect of steam on sintering under FTS conditions has been investigated [21], [34], [35]. The combination of high partial pressure of steam and carbon monoxide accelerates agglomeration of the active metal phase. The exact mechanisms at play are still a matter of discussion. Kliewer et al. proposed that surface wetting by cobalt oxide/hydroxide species forms a bridge between metallic particles that promotes coalescence [29]. With the size of such bridges limited by the metallic particle size, indicating that initial dispersion is key to resisting water induced

sintering. Moodley et al. suggested Ostwald ripening by sub-carbonyl species as the dominant mechanism, which is enhanced by the presence of water [7].

In this work, we investigate the deactivation pathways of titania-supported cobalt catalysts under humid FTS and model oxidation conditions. The chemical state of cobalt is investigated under conditions close to those encountered in industrial practice using *in situ* Mössbauer emission spectroscopy (MES) [36]. Here, we expand on previous ^{57}Co MES studies that showed the effect of steam on the sintering of cobalt catalysts supported on carbon nanofibers [34], [35] by studying cobalt supported on a titania support. The MES measurements are supplemented by ICP, XRD, TEM and STEM-EDX, while the catalytic performance was determined during the MES measurements as well as separately in a microflow reactor.

4.2 Experimental methods

4.2.1 Catalyst preparation

Supported cobalt catalysts were prepared by incipient wetness impregnation of P25 titania (Evonik Degussa, pore volume 0.3 mL/g, BET surface area 50 m²/g, Anatase/Rutile 85:15) followed by drying in air at 120 °C for 6 hours. The impregnation solutions were obtained by dissolving the appropriate amount of $\text{Co}(\text{NO}_3)_2 \cdot 6\text{H}_2\text{O}$ ($\geq 98.0\%$, Sigma Aldrich) in dehydrated ethanol. Four catalysts were prepared with a cobalt loading between 2 and 8 wt%. The resulting samples are denoted by $\text{Co}(x)/\text{TiO}_2$, where x represents the intended weight loading. Two more catalysts were later prepared for additional studies following the same approach. Following impregnation and drying, the samples were calcined at 350 °C for 2 hours in stagnant air (rate 5 °C/min). Part of these prepared catalysts was spiked with radioactive ^{57}Co by pore volume impregnation using a solution containing 90 MBq ^{57}Co in 0.1 M HNO_3 . These radioactive samples were dried at 120 °C for 12 hours and subsequently used for Mössbauer spectroscopy.

4.2.2 Characterization

Inductively coupled plasma-optical emission spectrometry

Inductively coupled plasma-optical emission spectrometry (ICP-OES) spectrometer (Spectroblue, AMETEK Inc.) was used for elemental analysis. For analyzing the cobalt content of the catalysts, approximately 25 mg of the sample was dissolved in a mixture of 2 mL of concentrated HNO_3 (65%) and 5 mL of concentrated H_2SO_4 (95-98%). The mixture was heated by a heating plate set to 250 °C until fully dissolved. After cooling to room temperature, demineralized water was added through a

reflux and homogenized. The solutions were subsequently diluted for ICP-OES measurements with demineralized water using volumetric flasks. ICP-OES analysis was conducted in duplo. A calibration line was prepared using a standard Co solution with concentrations between 0 and 6 mg/L. The cobalt concentration was determined using the 228.616 and 238.892 nm wavelengths and the average was reported.

X-ray diffraction

X-ray diffraction (XRD) patterns were recorded on a Bruker D2 Phaser using a Cu K α radiation source and a 2 mm slit. Data was collected using a time per step of 0.15 min and a step size of 0.1° in the 2 θ range of 10–60°. Background subtractions were applied, and reference spectra were obtained using the Diffrac.Eva software by Bruker.

Electron microscopy

Surface averaged particle sizes and particle size distributions were determined using transmission electron microscopy (TEM). TEM measurements were performed on a FEI Tecnai 20 electron microscope operated at an electron acceleration voltage of 200 kV with a LaB6 filament. Typically, a small amount of the sample was ground and suspended in pure ethanol, sonicated, and dispersed over a Cu grid with a holey carbon film.

The nanoscale distribution of elements in the samples was studied using scanning transmission electron microscopy–energy-dispersive X-ray spectroscopy (STEM-EDX). Measurements were carried out on a FEI cubed Cs-corrected Titan operating at 300 kV. Samples were crushed, sonicated in ethanol, and dispersed on a holey Cu support grid. Elemental analysis was done with an Oxford Instruments EDX detector X-MaxN 100TLE.

***In situ* Mössbauer emission spectroscopy**

Mössbauer emission spectroscopy (MES) was carried out at various temperatures using a constant acceleration spectrometer set up in a triangular mode with a moving single-line K₄Fe(CN)₆·3H₂O absorber enriched in ⁵⁷Fe. The velocity scale was calibrated with a ⁵⁷Co:Rh source and a sodium nitroprusside absorber. Zero velocity corresponds to the peak position of the K₄Fe(CN)₆·3H₂O absorber measured with the ⁵⁷Co:Rh source, positive velocities correspond to the absorber moving towards the source. To be able to measure under *in situ* Fischer-Tropsch conditions, a high pressure MES cell is used [36], which is described in detail in literature [35].

Mössbauer spectra were fitted using the MossWinn 4.0 program [37]. The spectra of very small superparamagnetic species were fitted using the two-state magnetic relaxation model of Blume and Tjon, which assumes the presence of a fluctuating magnetic field which jumps between the values of $+H$ and $-H$ along the z -axis with an average frequency τ [38]. Here, H typically equals 500 kOe and τ can vary between 10^{-9} and 10^{-12} s $^{-1}$. The Mössbauer spectra of larger particles were fitted using a hyperfine sextuplet, resulting from the local magnetic field experienced by bulk metallic particles. The experimental uncertainties in the calculated Mössbauer parameters, estimated using Monte Carlo iterations by the MossWinn 4.0 program and including experimental uncertainties were as follows: IS and QS ± 0.01 mm s $^{-1}$ for the isomer shift and quadrupole splitting, respectively; $\pm 3\%$ for the spectral contribution; ± 3 kOe for the hyperfine field.

Typically, 300 mg of radioactivity-spiked and 100 mg of non-radioactive catalyst (sieve fraction 250-500 μm) was loaded into two separate compartments of the reactor cell. FTS experiments were performed *in situ* following reduction at 340 °C for 2 hours in 100 mL/min flow of pure H $_2$. Reactions were done at 200 °C and 20 bar, while the H $_2$ /CO was kept at 4 throughout and steam was fed to vary the relative humidity. Water was evaporated and mixed with the incoming feed gas using a Bronkhorst controlled evaporator mixer (CEM). The reported relative humidity are determined solely by the fed steam, excluding the steam produced by the Fischer-Tropsch reaction. Wax products were collected in a downstream hot catch pot, and water was retrieved in a subsequent cold catch pot. An online Trace GC Ultra from Thermo Fisher Scientific equipped with a RT-Silica bond column and a flame ionization detector as well as a Stabilwax column and a thermal conductivity detector was used to analyse the gaseous products. Model oxidation experiments were performed *in situ* following a reduction treatment at 340 °C for 2 hours in 100 mL/min of pure H $_2$. Such reactions were done at a temperature of 220 °C and a pressure of 20 bar with a constant relative humidity (RH) of 25% and a varying H $_2$ partial pressure.

4.2.3 Catalytic activity measurements

The catalytic performance was determined in a single-pass flow reactor system (Microactivity Reference unit, PID Eng&Tech) operated at a temperature of 220°C or 240 °C, a total pressure of 20 bar and a H $_2$ /CO ratio of 4. In a typical experiment, 50 mg of catalyst (sieve fraction 125-250 μm) mixed with SiC particles of the same sieve fraction to a total volume of 3 mL was placed in a tubular reactor with an internal diameter of 9 mm. The temperature was controlled via a thermocouple, located in the centre of the catalytic bed. Reduction was first performed in a flow of H $_2$ at 350 °C for

2 hours after heating at a rate of 5 °C/min. Subsequently, the reactor was cooled to 220°C and the gas feed composition was changed to reaction conditions. A constant space velocity (SV) of 60 L g_{cat}⁻¹ h⁻¹, was applied for all catalysts, which resulted in a CO conversion between 1 and 5%. A TRACE1300 GC instrument from Thermo Fisher Scientific equipped with a RT-Silica bond column and a flame ionization detector as well as a Porabond-Q column and a thermal conductivity detector was used to measure the gas composition of the reactor effluent. The Weisz–Prater criterion was calculated to confirm operations did not run under internal mass transfer limitations. At the applied reaction conditions, no CO₂ was observed and the selectivity toward oxygenates on a molar carbon basis was less than 1%. Liquid products and waxes were collected in a cold trap placed after the reactor. Ar was used as an internal standard in the CO/H₂ feed mixture. The CO conversion (X_{CO}) was determined in the following manner:

$$X_{CO} = 1 - \frac{F_{Ar,in}F_{CO,out}}{F_{CO,in}F_{Ar,out}} \quad (1)$$

where $F_{Ar,in}$ is the volumetric Ar flow in the reactor feed, $F_{CO,in}$ is the volumetric CO flow in the reactor feed, $F_{Ar,out}$ and $F_{CO,out}$ are the respective volumetric flows of Ar and CO out of the reactor system.

The carbon-based selectivity of hydrocarbon compound C_i (S_{Ci}) was calculated using:

$$S_{Ci} = \frac{F_{Ar,in}F_{Ci}v_i}{F_{Ar,out}F_{CO,in}X_{CO}} \quad (2)$$

where F_{Ci} is the volumetric flow of hydrocarbon compound C_i out of the reactor, and v_i is the stoichiometric factor of the hydrocarbon compound.

The cobalt time-yield (CTY) was determined using the following equation:

$$CTY = \frac{F_{CO,in}X_{CO}}{m_{Co}} \quad (3)$$

where m_{Co} is the weight of cobalt used in the catalytic reaction determined through ICP analysis.

4.3 Results and Discussion

4.3.1 Fresh catalyst characterization

A set of four Co/TiO₂ catalysts was prepared by incipient wetness impregnation with intended cobalt loadings of 2, 4, 6 and 8 wt.%. The actual cobalt loadings determined by ICP analysis are given in Table 1, which point to some deviations from the targeted values.

Table 1. Cobalt loading and average metal particle of Co/TiO₂ catalysts.

Catalyst	Co loading (wt%) ^a	Particle size (nm) ^b
Co(2)/TiO ₂	3.0	13.3 ± 6.4
Co(4)/TiO ₂	5.0	13.4 ± 6.6
Co(6)/TiO ₂	5.6	12.0 ± 4.8
Co(8)/TiO ₂	7.4	11.0 ± 4.6

^aDetermined by ICP analysis; ^bDetermined by TEM analysis of reduced and passivated samples.

Figure 1 shows representative TEM images of the catalysts after reduction at 340 °C for 2 h in pure H₂ and subsequent passivation at room temperature in a flow of 5% O₂ in He. The average size and size distribution of the cobalt nanoparticles was determined by analysing approximately 150 particles in ca. 8 images per sample. The TEM images show that cobalt is well dispersed over the surface in all catalysts without any large agglomerated forms of cobalt. The average particle sizes given in Table show that the size of the reduced cobalt particles does not depend on the cobalt loading within the accuracy limits. This agrees with findings reported by Van Deelen et al. [39] that reduction of size-controlled cobalt particles, which were obtained through colloidal methods and loaded on P25 titania by impregnation, leads to nearly similar sizes of the final metallic cobalt particles.

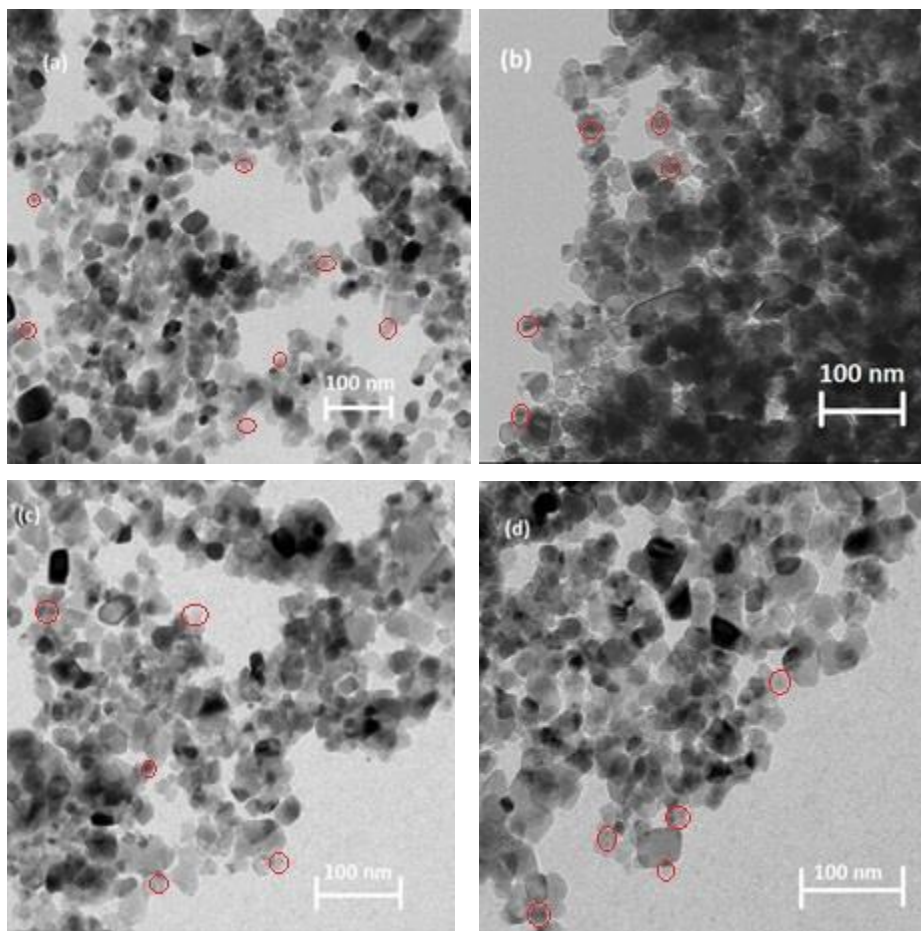


Figure 1. Representative TEM images of (a) Co(2)/TiO₂, (b) Co(4) /TiO₂, (c) Co(6)/TiO₂ and (d) Co(8)/TiO₂ following reduction at 340 °C for 2 h and passivation in 5% O₂ in He at room temperature. A few particles have been highlighted to assist the viewer.

The X-ray diffractograms of the calcined precursors are given in Figure 2. The samples show only diffraction lines due to anatase and rutile TiO₂, which is expected for P25 TiO₂ [40]. Features due to cobalt oxide are not observed, indicative of the high dispersion of cobalt oxide in the calcined precursor. The X-ray diffractograms of the reduced and passivated samples were similar to those of the calcined samples.

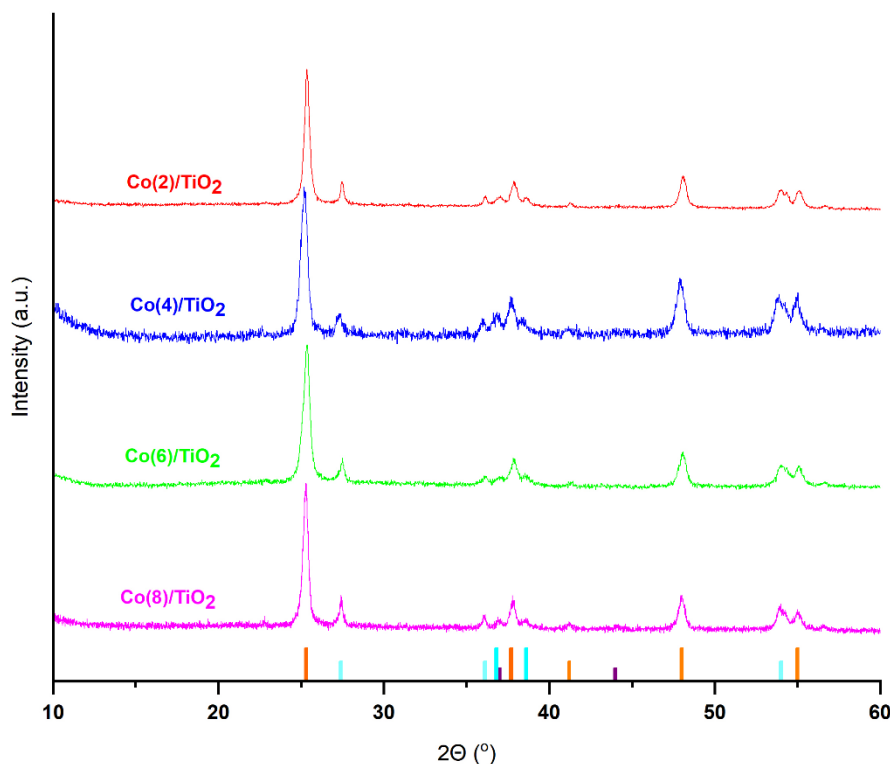


Figure 2. X-ray diffractograms of Co(2)/TiO₂, Co(4)/TiO₂, Co(6)/TiO₂, and Co(8)/TiO₂ after calcination at 350 °C. The strongest diffraction lines of anatase TiO₂(orange), rutile TiO₂ (cyan) and Co₃O₄ (dark purple) are indicated at the bottom.

4.3.2 *In situ* Mössbauer spectroscopy of reduced catalysts

Mössbauer spectra of the catalysts after reduction at 340 °C for 2 h are given in Figure 3. The Mössbauer fit parameters of the reduced catalysts are listed in Tables C3-C6. A sextuplet with an isomer shift (IS) of -0.1 mm s^{-1} and a hyperfine field (HF) of $\sim 323 \text{ kOe}$ observed for all catalyst samples is due to metallic cobalt. This sextuplet points to the presence of magnetically ordered metallic cobalt particles, which is common for cobalt particles larger than 6 nm [34]. The absence of a singlet feature of superparamagnetic metallic cobalt means that the fraction of very small cobalt nanoparticles with a size smaller than 6 nm in these samples is below the detection limit. This result is in line with the TEM analysis of the reduced catalysts. This aspect is important, as it has been well established that the FTS reaction on cobalt is structure sensitive with the CO conversion strongly decreasing for particles smaller than 6 nm [4]. In addition to the dominant metallic cobalt phase, all spectra contain a doublet with an IS of 1.0 mm s^{-1} and a quadrupole splitting (QS) of 2.0 mm s^{-1} , which can be assigned to a dispersed Co²⁺-oxide phase. The contribution of this oxidic phase is largest (47%) for Co(2)/TiO₂. When the reduction is prolonged to 10 h, the oxide phase spectral contribution decreased to 22%. The requirement of a longer reduction is likely the result of the increased cobalt-

titania interaction on this sample, and the reduced hydrogen spill over from metallic cobalt particles onto the support. The catalysts with a higher cobalt loading have a smaller contribution of cobalt-oxide. The presence of a certain fraction of cobalt oxide species that are more difficult to reduce can be due to the relatively strong cobalt-titania interactions as will be discussed below [41]. Despite these differences, the spectral parameters of the metallic contribution following reduction are the same for all samples, which confirms that the cobalt loading on titania cannot be used to obtain metallic cobalt particles of different size upon reduction at 340 °C. This is in line with the nearly similar sizes of the metallic cobalt particles as determined by TEM analysis (Figure 1).

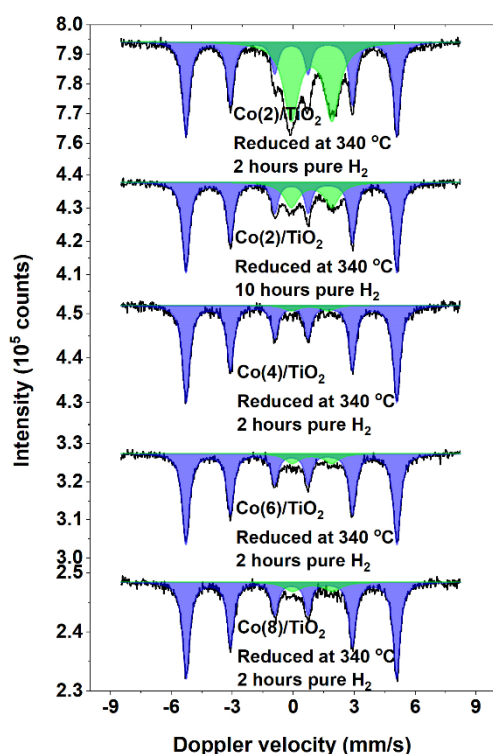


Figure 3. Mössbauer spectra of reduced Co/TiO₂ catalysts at 340 °C in pure hydrogen: black lines represent the experimental spectra, blue the fitted bulk metallic cobalt and green the fitted cobalt oxide doublet.

4.3.3 *In situ* Mössbauer emission spectroscopy during the FTS reaction

In situ Mössbauer spectra were recorded as a function of the steam partial pressure at a temperature of 200 °C, a total pressure of 20 bar, and a H₂/CO ratio of 4. The steam content in the feed is expressed as the relative humidity (RH) at the applied conditions. Table C1 details the feed compositions for the different RH measurements. The actual RH during the Mössbauer measurements are slightly higher, as additional steam is produced by the FTS reaction. However, in a typical experiment with a CO

conversion of approximately 15%, the amount of produced steam is small compared to the amount of steam in the feed. When no steam is added, the RH due to the FTS reaction is ca. 1.5%, which is substantially lower than the RH of 7.5% of the first humidity step. Spectra were recorded for at least 48 h at each humidity step, except for RHs of 25% and 57% where the steam treatment was prolonged to 5 days and 11 days, respectively. This was done to understand the influence of prolonged exposure as encountered in industrial practice. We started by measuring MES spectra at 200 °C without steam added. The results in Table C3-C6 show that the cobalt distribution is very similar to the distribution obtained during room-temperature measurements after reduction in H₂.

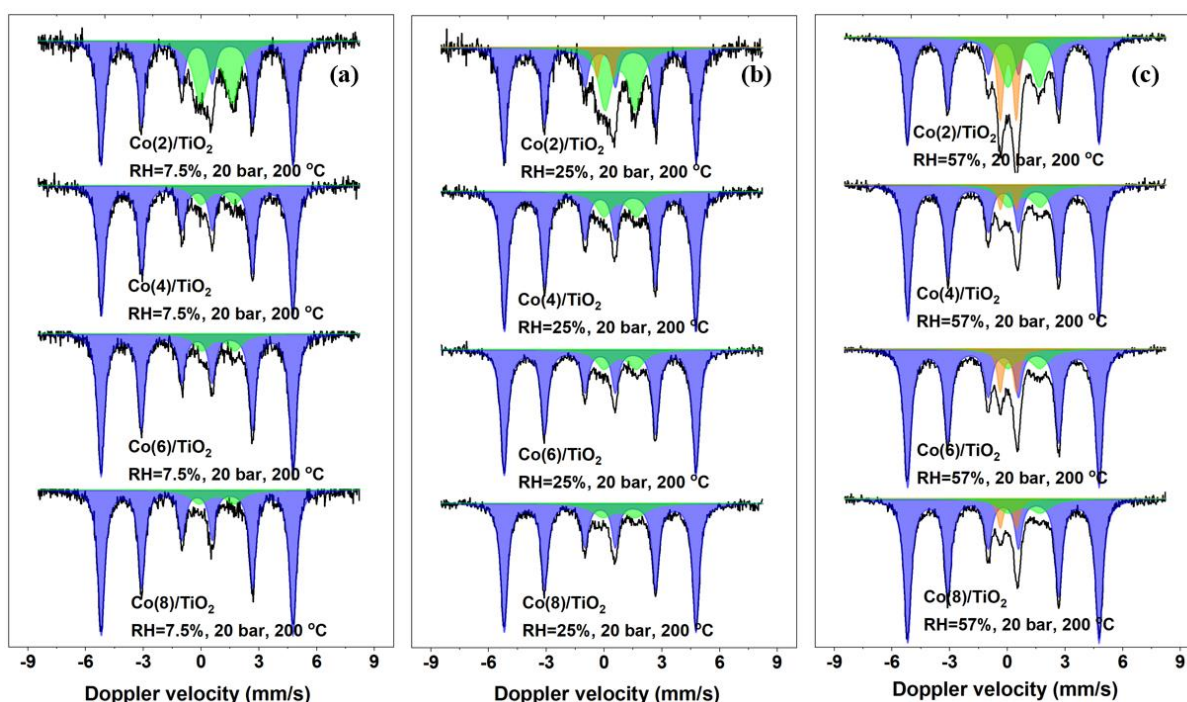


Figure 4. *In situ* Mössbauer spectra of the Co/TiO₂ catalysts under FTS conditions at a relative humidity of (a) 7.5%, (b) 25% and (c) 57%. The black lines represent the experimental spectra, the blue ones the fitted metallic cobalt sextuplet and the orange and green ones the fitted cobalt oxide doublets.

When exposed to a relatively low partial pressure of steam (RH 7.5%), the spectra of all catalysts contain the same metallic and oxidic features as observed directly after reduction (Figure 4a). The predominant sextuplet has an IS of -0.2 mm s⁻¹ and a HF of ~310 kOe as measured at 200 °C and is independent of the cobalt loading, implying that the samples still contain magnetically ordered metallic cobalt particles. The oxidic doublet has an IS of 0.8 mm s⁻¹ and a QS of 1.8 mm s⁻¹. The parameters point to a high dispersion of the Co²⁺-oxide species, the large quadrupole splitting

reflecting the low coordination of the cobalt atoms. While the contribution of this doublet is the same as under dry FTS conditions for Co(6)/TiO₂ and Co(8)/TiO₂, the contribution has increased for Co(2)/TiO₂ (from 23% to 33%) and Co(4)/TiO₂ (from 5% to 13%), pointing to cobalt oxidation. As the spectra do not show a significant change in the HF field for the metallic particles, these findings are likely not due to preferential oxidation of large or small particles, which would shift the average magnetic field to lower or higher values, respectively. Moreover, we can exclude a mechanism where only the surface of the metal particles is oxidized, as the fraction of oxidic cobalt formed in the Co(2)/TiO₂ and Co(4)/TiO₂ catalysts (10% and 8% respectively) exceeds the contribution of surface cobalt at the dispersion determined by TEM (d_{average} 13 nm, dispersion 6%). This will be further supported by the catalytic activity measurements presented below. Taken together, these results suggest mobility of cobalt species under the given conditions, leading to the formation of oxidized cobalt species in close interaction with the support as schematically shown in Figure 5.

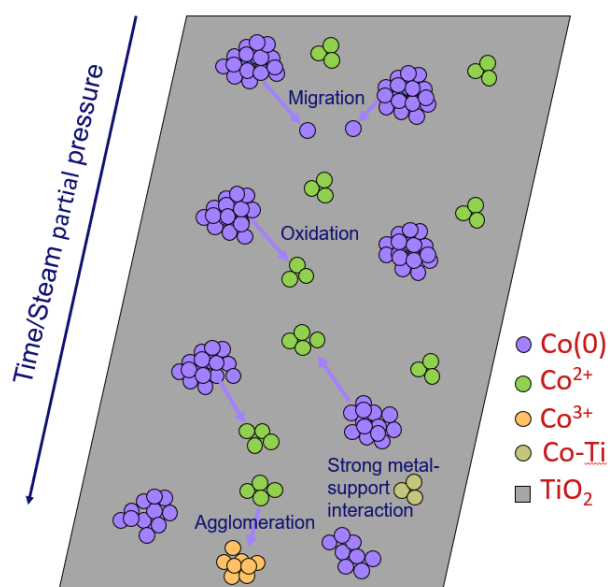


Figure 5. Schematic representation of the different cobalt species present in the catalyst and their evolution during the FTS reaction under changing conditions.

When the humidity is increased to RH values of 14% and 20%, further oxidation is observed. The spectral contribution of the oxidic cobalt phase is given in Table 2 for all catalysts, while the Mössbauer fit parameters can be found in Tables C3-C6. Unfortunately, the spectral contribution for the Co(4)/TiO₂ catalyst after 48 h at RH 25% and 57% are not available due to a malfunction of the hardware during the long-term measurements. The spectra obtained at a relative humidity of 25% are shown in Figure 4b. At this RH, the Co(2)/TiO₂ sample contains an additional cobalt oxide state with

an IS of 0.4 mm s^{-1} and a QS of 0.2 mm s^{-1} . The parameters can be assigned to Co^{3+} . The observation of Co^{3+} is most likely an artifact of the Mössbauer effect for ^{57}Co , where Co^{3+} is formed during the Auger cascade following the decay of the ^{57}Co probe [42]–[45]. Such a Co^{3+} signal is even present in the Mössbauer emission spectrum of ^{57}Co -doped CoO , which only contains Co^{2+} [42]. Surrounding Co^{2+} atoms can stabilize the Co^{3+} state, which is formed during the Auger cascade, long enough to be measured. As ^{57}Co probe atoms with more direct Co^{2+} neighbours are more likely to show this stabilized Co^{3+} state, the observation of Co^{3+} species by MES can be used as a qualitative indication for the dispersion of oxidic cobalt [46]–[48]. Thus, the data suggests that a larger amount of oxidic cobalt in the Co(2)/TiO_2 catalyst was present as slightly aggregated cobalt oxide than in the other catalysts at RH 25%. Nevertheless, such a contribution becomes visible for the samples containing more cobalt upon increasing the humidity to 57% (Figure 4c). These findings indicate that, at elevated steam pressure, the amount of oxidic cobalt increases and the domain size of these oxidic structures becomes larger as schematically shown in Figure 5. Since the measured HF of the metallic cobalt did not change, it is unlikely that higher humidity leads to oxidation of the larger metallic cobalt particles. Such a mechanism would have resulted in a change of the HF, because the HF is an average of the HFs of the metallic particles with different sizes. As such, we can conclude that the increasing amount of oxidic cobalt formed at higher humidity results in the growth of a cobalt oxide phase. It is likely that this phase is still highly dispersed as initially the Co^{3+} after-effect was absent.

Table 2. Contribution of cobalt oxide phase (Co^{2+} and Co^{3+} species) as determined from MES spectra recorded at 200°C under varying FTS conditions.

<i>Treatment</i>	$\text{H}_2\text{O}/\text{H}_2$	<i>Treatment length (hrs)</i>	<i>Spectral contribution cobalt oxide (%)</i>			
			<i>Co(2)/TiO₂</i>	<i>Co(4)/TiO₂</i>	<i>Co(6)/TiO₂</i>	<i>Co(8)/TiO₂</i>
RH 0%	0	48	23	5	9	8
RH 7.5%	0.25	48	33	13	11	10
RH 14%	0.50	48	34	14	12	11
RH 20%	0.75	48	35	14	13	13
RH 25%	1.0	48	36	N/A	14	13
	1.0	120	37	16	14	14

RH 57%	1.0	48	37	N/A	17	16
	1.0	120	40	N/A	19	17
	1.0	264	43	20	22	17

Despite the similar initial cobalt particle size in the reduced samples, the evolution of cobalt oxide following exposure to steam under FTS conditions is seemingly different. Figure 6 shows the absolute amount of oxidic cobalt formed as a function of the RH for the various samples. Within the experimental error, the samples contain a comparable amount of oxidic cobalt, which indicates that the extent of oxidation does not depend on the cobalt loading. The amount of oxidic cobalt increases with the steam pressure. Already at a low oxidizing potential ($\text{H}_2\text{O}/\text{H}_2$ 0.25, RH 7.5%), significant oxidation of metallic cobalt is observed for all prepared catalysts compared to the small contributions of cobalt oxide after reduction. The amount of oxidic cobalt increases to approximately 1.2 wt% cobalt under the harshest applied conditions (RH 57%). We tentatively propose that this is due to the interaction of Co^{2+} with support hydroxyl groups, *i.e.*, titanol groups. P25 titania contains about 5 titanol groups per nm^2 [49]. Assuming a Co^{2+} :titanol stoichiometry of 2, the complete coverage of such surface groups would result in a cobalt loading of 1.2 wt%. The data can thus be interpreted in terms of oxidation of cobalt species under humid FTS conditions and their migration to stable locations at the support. When more cobalt is oxidized, these species might lead to highly dispersed cobalt oxide particles as suggested by the observation of a Co^{3+} signal. Nevertheless, we should also mention that there might be a role of the exposed anatase and rutile surfaces of titania with the P25 titania containing about 15% rutile [40]. In the past, the impact of different titania phases on cobalt sintering and the formation of metal-support compounds has been suggested [50]–[52]. The important corollary of these findings is that oxidation of cobalt is a possible pathway in the deactivation of titania-supported cobalt nanoparticle catalysts during the FTS reaction. Thermodynamic considerations showed that cobalt oxidation under FTS conditions is not favorable for cobalt metal particles larger than 4 nm [11]. The present results show that oxidation of cobalt can occur under industrially relevant conditions for cobalt particles larger than 6 nm. The observed oxidation does not involve oxidation of metallic cobalt particles and, following the discussion above, also not from oxidation of a surface layer of the metallic cobalt nanoparticles as found for cobalt on silica [53]. Kliewer et al. mentioned that oxidation of cobalt on titania results in cobalt oxide/hydroxide species that anchor to the titania support [29]. Based on the latter suggestions and the current findings, we propose that the mobility of metallic cobalt species in combination with the oxidizing conditions due

to water play a role in oxidizing cobalt forming dispersed cobalt oxide interacting with titanol groups as sketched in Figure 5. Thus, whilst bulk oxidation did not occur under humid FTS conditions in line with the conclusions of Van Steen et al. [11], our findings show that dispersed oxidic cobalt can be formed in titania-supported cobalt catalysts under realistic FTS conditions. It is likely that the strong cobalt-titania support interactions play a critical role here, as oxidation was not observed for cobalt nanoparticles supported on carbon nanofibers treated under similar reaction conditions [35]. Beck et al. [54], [55] found that metallic platinum particles enhance the formation of oxygen vacancies in titania at a relatively low reduction temperature. Although we did not study the reduction of the titania surface for our catalysts, we argue that, even if oxygen vacancies would have formed under reducing conditions, these would be hydroxylated in the presence of steam. For instance, an STM study reported that H₂O dissociates on oxygen vacancies of titania already at 120 K by donating a proton to an adjacent oxygen and forming a bridged hydroxyl group [56]–[58]. The reducibility of small oxidic cobalt particles in synthesis gas can be affected by the presence of oxygen vacancies. Recent work by Qiu et al. indicated that oxygen vacancies in the titania support material enhance the reducibility of especially relatively small cobalt oxide particles [59]. Thus, the presence of steam, which keeps the surface in an oxidized/hydroxylated state, might inhibit reduction of the small cobalt oxide particles. The work by Kliewer et al. [29] reported that the presence of oxidic cobalt on titania can enhance the sintering of the active phase. If significant sintering of metallic cobalt occurred under humid FTS, an increase of the HF parameter would be observed. However, this parameter remains constant throughout the humid treatments for all catalyst samples (Tables C3-C6). Upon reduction of the oxidic cobalt formed during FTS, an increased metallic cobalt content is observed for all catalyst samples. This increased degree of reduction indicates growth of the oxidic cobalt domains, as small oxidic particles are typically more difficult to reduce [15]. This is in good agreement with the observation of after-effect Co³⁺ species, as its observation can be attributed to larger oxidic agglomerates. So, whilst no increase in the measured HF is observed between the freshly reduced and spent reduced state (Tables C3-C6), the improved reducibility points towards the agglomeration of oxidic cobalt during humid FTS. We also considered the alternative deactivation pathway under simulated high CO conversion conditions through formation of metal-support compounds [52], [60]. Such studies have shown before that cobalt titanate readily forms at high humidity, especially for a pure anatase titania support. We did not even observe cobalt titanate species under our harshest humid FTS conditions of RH 57%. Compared to literature where a H₂O/H₂ ratio of 70 was used in the absence of CO, our highest H₂O/H₂ ratio of 1 can nevertheless explain this difference.

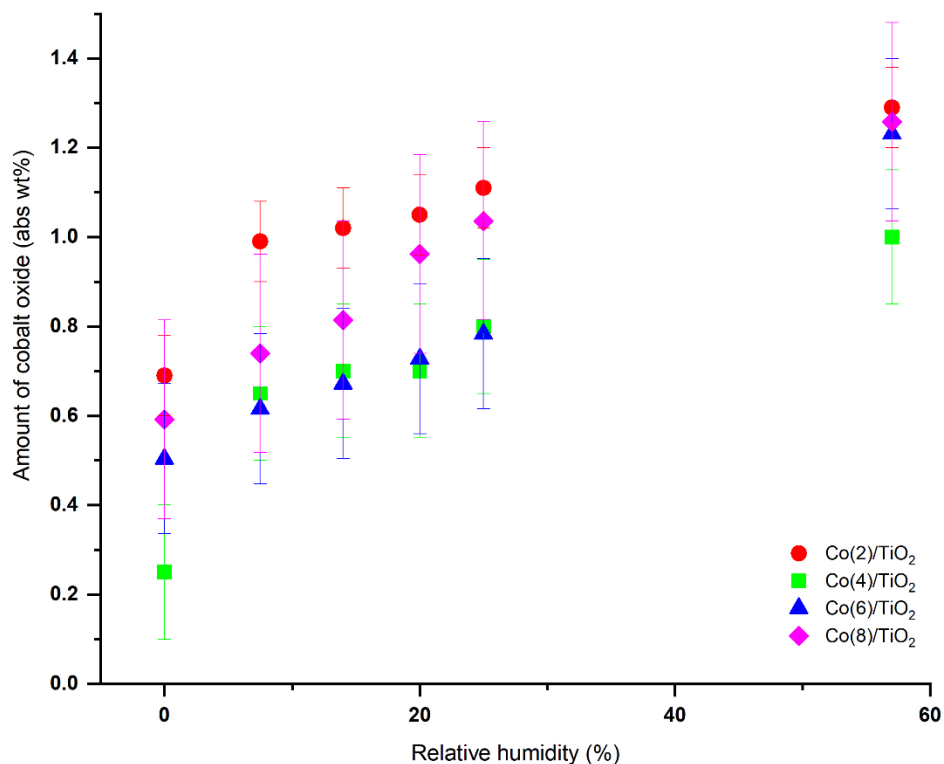


Figure 6. Amount of cobalt oxide in Co/TiO₂ catalysts under humid Fischer-Tropsch conditions (200 °C, 20 bar, H₂/CO = 4) as determined by Mössbauer spectroscopy at 200 °C as a function of the relative humidity (red: Co(2)/TiO₂, green: Co(4)/TiO₂, blue: Co(6)/TiO₂, magenta: Co(8)/TiO₂).

4.3.4 Sintering under humid Fischer-Tropsch conditions

Our findings indicate that the active cobalt phase in titania-supported FTS catalysts can sinter upon partial oxidation under humid FTS conditions and subsequent reduction. Under the given measurement conditions, the HF parameter does not allow picking up such sintering of the metallic cobalt nanoparticles. Our previous work on carbon-supported cobalt, however, showed very clearly enhanced sintering of cobalt nanoparticles upon steam treatment in the presence of CO [34]. Accordingly, we studied the sintering of cobalt on titania in more detail by reducing Co(2)/TiO₂ at a lower temperature of 300 °C in order to obtain initially smaller metallic cobalt particles. The resulting MES spectra are given in Figure 7 and the corresponding Mössbauer parameters are listed in Table C7. Compared to reduction at 340 °C, the spectra contain a much larger contribution of oxidic cobalt, both in the form of Co²⁺ (36%) and Co³⁺ (39%) next to a metallic cobalt contribution of 25%, characterized by the usual sextuplet for larger than 6 nm cobalt nanoparticles. To study sintering, we recorded MES spectra at a higher temperature of 200 °C. The higher measurement temperature can result in the loss of magnetic ordering for relatively small cobalt nanoparticles. This is evident from

the spectra recorded at 200 °C (Figure 7) after heating in a flow of inert argon, where the metallic cobalt phase is now characterized by a singlet with an IS of 0.0 mm s⁻¹, in addition to the sextuplet representative of bulk metallic cobalt particles. The loss of magnetic ordering of a fraction of the cobalt nanoparticles at a higher measurement temperature implies that their size is smaller than 6 nm [34]. We refer to these particles as superparamagnetic (SPM) cobalt. The contribution of SPM cobalt is 29%, while the contribution of bulk cobalt is 16%. The combined spectral contribution of bulk and SPM cobalt is 45%, which is significantly larger than the metallic contribution of 25% derived from spectra recorded at room temperature. When measuring at elevated temperatures, difference in the Debye temperature of the different phases can lead to over- or underestimation of the spectral contributions [61]. Accordingly, we explain the difference in spectral contribution between the room-temperature and 200 °C measurements under inert conditions to the higher Debye temperatures of the metallic phases in comparison with the oxidic cobalt phases. Additionally, the contribution from Co³⁺ declined significantly from 39% to 14%, whilst the Co²⁺ contribution increased from 36% to 41%. This suggests that the above-discussed Mössbauer after-effects are less pronounced at elevated temperatures. Nevertheless, despite the differences between room-temperature and 200 °C measurements, the Mössbauer data at the higher temperature can still be used for a qualitative analysis of sintering as will be done in the following.

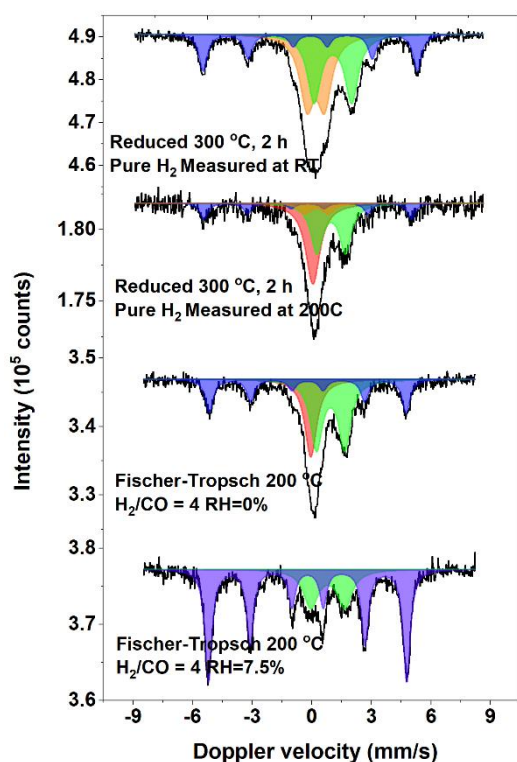


Figure 7. *In situ* Mössbauer spectra measured of Co(2)/TiO₂ following reduction at 300 °C and exposure to different FTS conditions: black lines represent the experimental spectra, blue ones the fitted metallic bulk cobalt sextuplet, red ones the small metallic cobalt singlet, and the orange and green ones the fitted cobalt oxide doublets.

Upon introduction of dry synthesis gas, the SPM cobalt feature in the spectrum recorded at 200 °C remains with an IS of -0.1 mm s^{-1} and a spectral contribution of 26%. Under these conditions, the Co³⁺ doublet is no longer present, and the spectral contribution of the Co²⁺ doublet has increased from 41% to 45%. The combined spectral contribution of oxidic cobalt thus decreased from 55% to 45% whilst the temperature remained the same, indicating some reduction occurs under these conditions, likely of the largest oxidic cobalt species. The remaining spectral contribution of 29% is made up by relatively large, magnetically ordered metallic cobalt particles. Upon addition of steam to the feed, the SPM cobalt contribution is immediately lost, even at a low RH of 7.5%. Under these slightly humid FTS conditions, the bulk metallic contribution increased from 29% to 74% with the residual 26% corresponding to Co²⁺. These results clearly show that the addition of steam to the synthesis gas feed leads to mobility of cobalt on the titania surface, resulting in further reduction of dispersed oxidic cobalt as well as sintering of small metallic particles. These findings support the previous hypothesis that carbon monoxide and steam have a synergistic effect towards sintering [21], [34], [35] and that

this also occur on titania. Kliewer et al. [29] suggested that the presence of oxidic cobalt on the titania facilitates sintering of the metallic phase due to coalescence following reduction. The present findings support such a mechanism as both an increased reduction degree and particle growth are observed simultaneously. The improved reduction is likely also facilitated by hydrogen spill-over, which is facilitated by the presence of steam [62], [63]. Overall, these phenomena can contribute to cobalt sintering and a higher cobalt reduction degree, despite the increasing oxidizing potential due to the higher steam pressure.

4.3.5 Characterization used catalysts

To complement the Mössbauer data obtained under humid FTS conditions, STEM-EDX measurements were performed on reduced-passivated and used Co(4)/TiO₂. The term ‘used catalysts’ refers to the non-radioactive catalyst samples obtained from the Mössbauer cell under the same humid FTS treatments as the Mössbauer samples. As such, these measurements provide *ex situ* information about the state of the catalyst following the deactivation studies. For each sample, 8 EDX maps were obtained on different areas of the sample. Two representative maps of the reduced and passivated Co(4)/TiO₂ are shown in Figure 8a-b. These are broadly in keeping with the earlier bright-field TEM measurements discussed above, showing the presence of cobalt particles with sizes in the range of 10-16 nm dispersed over the titania support.

Representative maps of used Co(4)/TiO₂ following high humidity FTS conditions are given in Figure 8c-d. The cobalt particles are larger than in the reduced-passivated sample with sizes in the 16-22 nm range. This is despite the fact that the HF of the metallic cobalt phase during humid FTS did not increase, highlighting again that this parameter is not sensitive enough to detect the sintering occurring under these conditions. This supports the earlier conclusion that steam addition to the synthesis gas feed leads to cobalt sintering. However, some small cobalt particles (5-8 nm) can still be observed in some of the STEM-EDX maps. These small particles may be due to the small amount of cobalt that was not reduced according to MES (Table C4), even after re-reduction following exposure to high humidity FTS conditions. Based on the particle size distribution shown in Table 1, this could correspond to relatively small cobalt particles with a size smaller than 8.5 nm. Regardless, this data shows that, besides the evident oxidation, sintering is also a significant deactivation pathway on titania-supported cobalt catalysts during humid FTS.

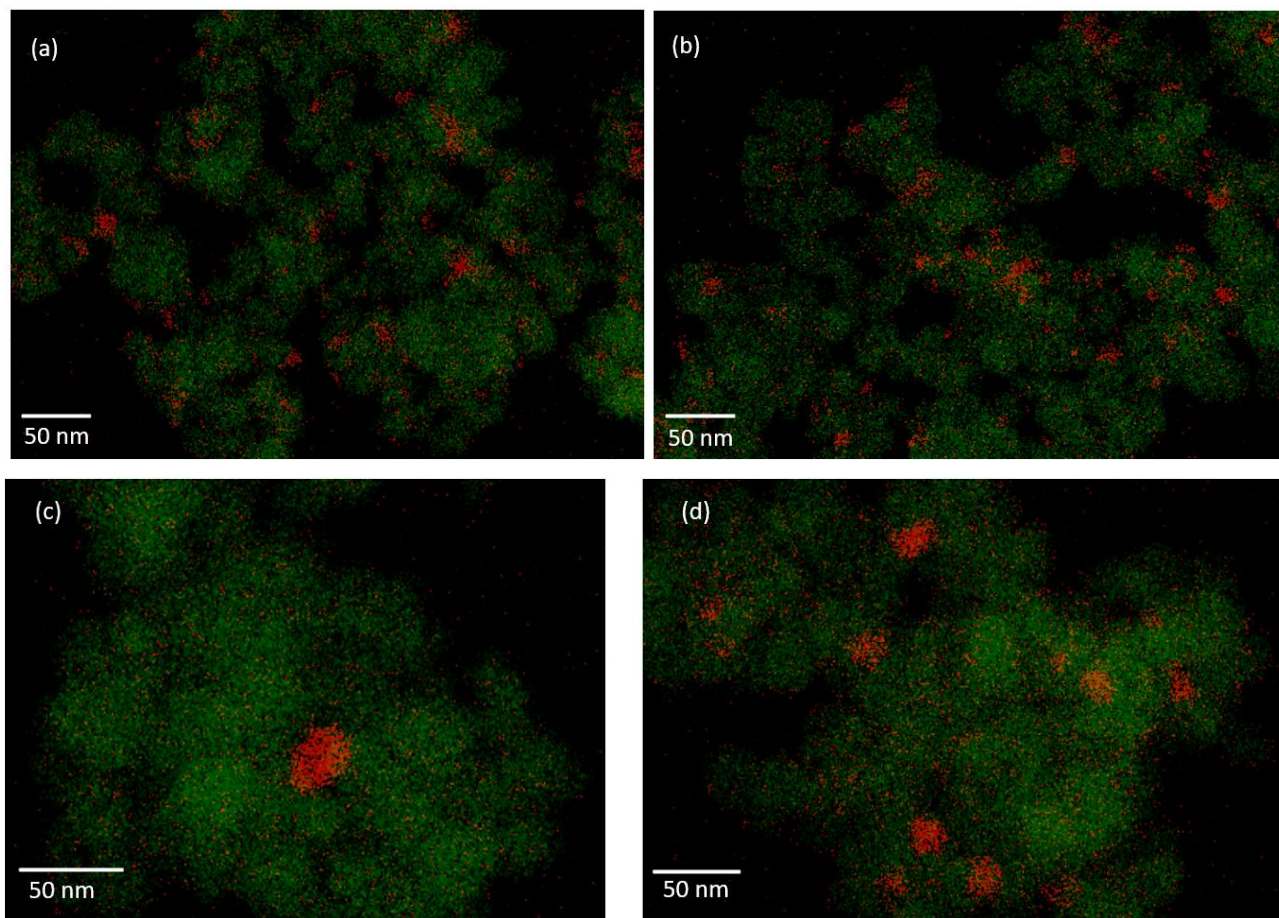


Figure 8: EDX mappings of (a-b) a reduced and passivated and (c-d) a used Co(4)/TiO₂ catalyst: the cobalt mapping is shown in red and the titania mapping in dark green.

4.3.6 Oxidation in the absence of CO

To study the oxidation behavior of Co/TiO₂ at higher oxidizing potential in the absence of CO, we subjected Co(4)/TiO₂ to model oxidation conditions (Figure 9). This sample was selected, because it combines a relatively low cobalt loading with good cobalt reducibility. The Mössbauer spectra were measured *in situ* at 220 °C and 20 bar at a constant RH of 25%, while varying the H₂O/H₂ ratio in the feed. The compositions used in these model oxidation measurements are given in Table C2. The Mössbauer parameters obtained during these experiments are collected in Table C8. Following 2 h reduction in pure hydrogen at 340 °C, a bulk metallic cobalt phase (83%) was observed with an IS of -0.1 mm s⁻¹ and a HF of 309 kOe measured at 220 °C. The residual spectral contribution belongs to dispersed Co²⁺-oxide with an IS of 0.8 mm s⁻¹ and a QS of 1.7 mm s⁻¹. The spectra obtained at a H₂O/H₂ ratio of 10 contains the same two cobalt features, but the spectral contribution of the bulk

metallic cobalt was lower at 65% with the other 35% corresponding to the dispersed Co^{2+} -oxidic phase. Increasing the $\text{H}_2\text{O}/\text{H}_2$ ratio to 50 by reducing the H_2 partial pressure resulted in a further increase of the cobalt oxide content to 55%. When the ratio was further increased to 70, a new cobalt oxide doublet was observed (55%) with an IS of 0.5 mm s^{-1} and a QS of 1.2 mm s^{-1} , which corresponds to a second Co^{2+} feature distinctively different from the other Co^{2+} species. At such a high $\text{H}_2\text{O}/\text{H}_2$ ratio, the formation of cobalt titanates can be envisioned. In CoTiO_3 , Co also has a formal 2+ oxidation state but a different coordination environment than in CoO . The Mössbauer parameters of this Co^{2+} phase are very similar to those reported for ferrous titanate (FeTiO_3) [64]. Thus, we infer that cobalt titanate phase was formed. When hydrogen is fully removed from the feed, full oxidation is observed with the cobalt-titanate feature, having a high spectral contribution of 76% and dispersed cobalt oxide making up the remainder. Following these lengthy model oxidation treatments, the reduction of the fully oxidized catalyst was investigated. Notably, a degree of reduction of only 18% was obtained following reduction at 340°C for 2 h. The dominant Co^{2+} feature could only be removed by reduction at 450°C , further strengthening the hypothesis that this doublet corresponded to cobalt titanate [65]. Contrary to the previous humid FTS measurements, no Co^{3+} features were observed during model oxidation. These findings suggest that, in the absence of CO, the agglomeration of the oxidic cobalt domains is significantly less pronounced. The slight gradual decrease of the HF from 309 kOe in the reduced state to 307 kOe at the highest $\text{H}_2\text{O}/\text{H}_2$ ratio of 70 also indicates that the metallic particles are becoming smaller, as the measured HF follows from the average particle size. This either suggests that larger metallic particles are oxidized before smaller ones or that gradual oxidation of the surface of cobalt particles occurs. Both mechanisms can explain the observed drop in HF. Contrary to humid FTS conditions, under the highly oxidizing conditions in these measurements the oxidic cobalt species react with the titania support to form metal-support compounds as previously reported by Wolf et al. [52]. This is also shown schematically in Figure 5. So, although the inclusion of cobalt in CoTiO_3 -like surface compounds would represent a significant deactivation pathway, these compounds are only formed under unusual conditions of very high $\text{H}_2\text{O}/\text{H}_2$ ratio (>70), which are less relevant to practical FTS.

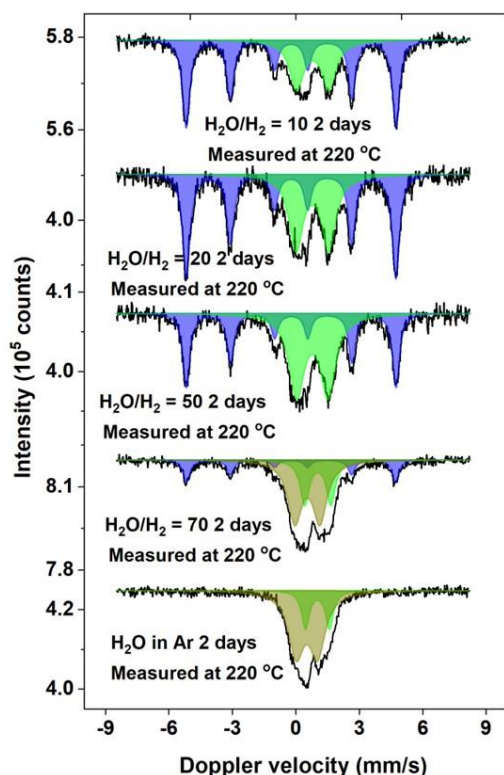


Figure 9. *In situ* Mössbauer spectra measured of Co(4)/TiO₂ following model oxidation treatments: black lines represent the experimental spectra, blue ones the fitted metallic bulk cobalt sextuplet, and dark yellow and green ones the fitted cobalt oxide doublets.

4.3.7 Deactivation pathways on the titania support

Based on the present findings we sketched a deactivation mechanism for Co/TiO₂ in Figure 10. We propose that, under low oxidizing potential ($RH = 7.5\text{--}20\%$, $H_2O/H_2 < 1$), the presence of steam during FTS conditions results in sintering of small metallic particles as well as the formation of dispersed oxidic cobalt on the titania support. The formation of oxidic cobalt complexes with the titania support has been earlier observed following deposition of cobalt on titania in aqueous media [66]. Whilst we cannot determine the exact nature of the oxidic cobalt observed in this work, it is very likely that such structures are formed. The cobalt oxidation degree increases with at higher oxidizing potential of the reaction mixture. Depending on the presence of carbon monoxide, different deactivation pathways are followed. With carbon monoxide present, it is likely that mobile cobalt carbonyl species contribute to further growth of the oxidic cobalt species into larger domains and facilitate sintering of the metallic cobalt via Ostwald ripening as has been previously observed [7]. A density functional theory study showed that the formation of cobalt carbonyl species is energetically favourable under practical FTS conditions, even in the presence of adsorbed water [67]. The loss of

metallic cobalt lowers the FTS activity, while re-reduction can result in the loss of the metallic cobalt surface area due to sintering through coalescence. Due to the relatively low oxidizing potential ($H_2O/H_2 = 1$) under our humid FTS conditions, no formation of cobalt-titanate compounds is observed. However, without CO, the mobility of cobalt seems hampered, as no larger oxidic cobalt domains are observed in the form of Co^{3+} despite the high degree of oxidation. When the oxidizing potential is significantly increased ($H_2O/H_2 = 70$) the formation of $CoTiO_3$ -like structures is observed, formed by the strong interaction of the dispersed oxidic cobalt with the titania support. Reduction of these structures requires much higher temperatures, meaning that a larger amount of cobalt is no longer accessible for catalysis.

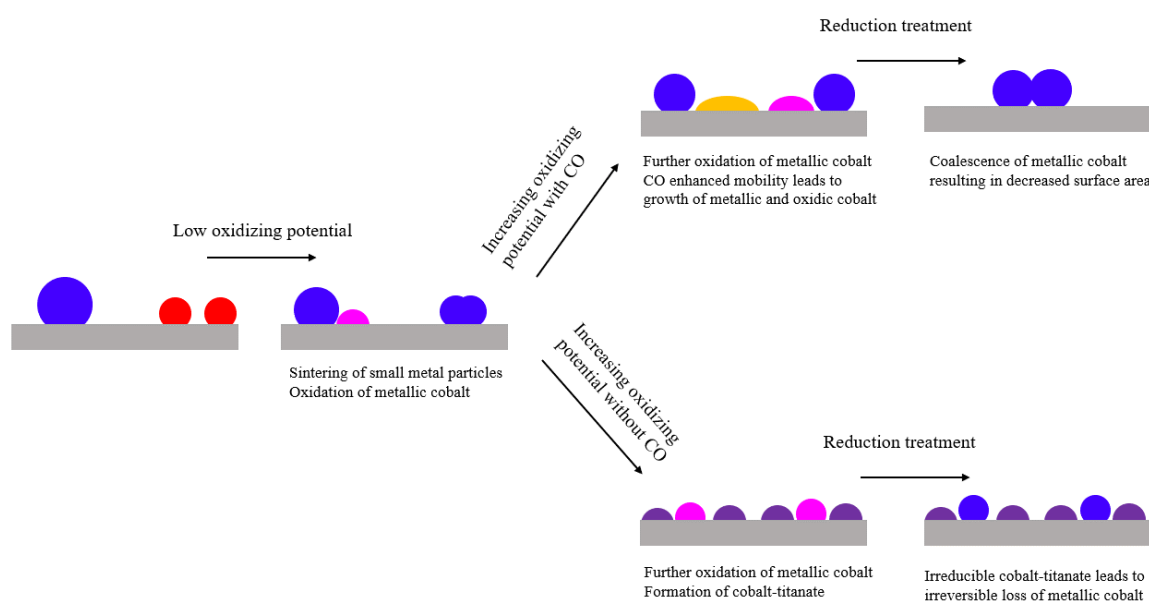


Figure 10. Schematic representation of deactivation mechanisms observed for Co/TiO₂ catalysts. Shown are small metallic SPM cobalt (red), bulk metallic cobalt (dark blue), dispersed oxidic cobalt (magenta), aggregated oxidic cobalt (orange), cobalt-titanate (dark purple), and titania (grey).

4.3.8 Catalytic performance

The catalytic activity continuously measured on-stream during the Mössbauer measurements is given in Figure 11. The results of the sample with the lowest cobalt loading (Co(2)/TiO₂) are not shown, as the conversion was too low. The other catalysts show very similar activity trends in terms of a slow decrease of the CO conversion with increasing humidity. It is important to note that the opposite has also been reported, namely that water co-feeding can increase FTS activity [68], [69]. Additionally, the introduction of steam to the reactor feed results in a small decrease of the CO and H₂ partial pressures, which can affect the catalytic activity due to the negative reaction order in CO and positive

order in H_2 [70], [71]. Therefore, additional measurements were performed under dry conditions following the 5-day treatment at $RH = 25\%$. This did not lead to significant activity differences. As such, the observed deactivation can be linked to the gradual oxidation of the active metallic cobalt along with mild sintering, resulting in a decrease of the cobalt specific activity of approximately 20% for all catalysts when comparing dry and $RH = 57\%$ conditions. This activity loss exceeds the loss of metallic cobalt between dry and high humidity conditions for all catalysts, indicating that oxidation of metallic cobalt can only explain part of the deactivation. It underlines that sintering, as observed by STEM-EDX (Figure 8), also significantly contributes to deactivation. Full surface oxidation of metallic cobalt particles can be excluded as a mechanism, as the formation of a (thin) surface oxide layer on metallic cobalt particles would render the active catalytic sites completely inaccessible for catalysis, resulting in a far greater activity loss already at relatively low oxidizing potential ($RH = 7.5\%$).

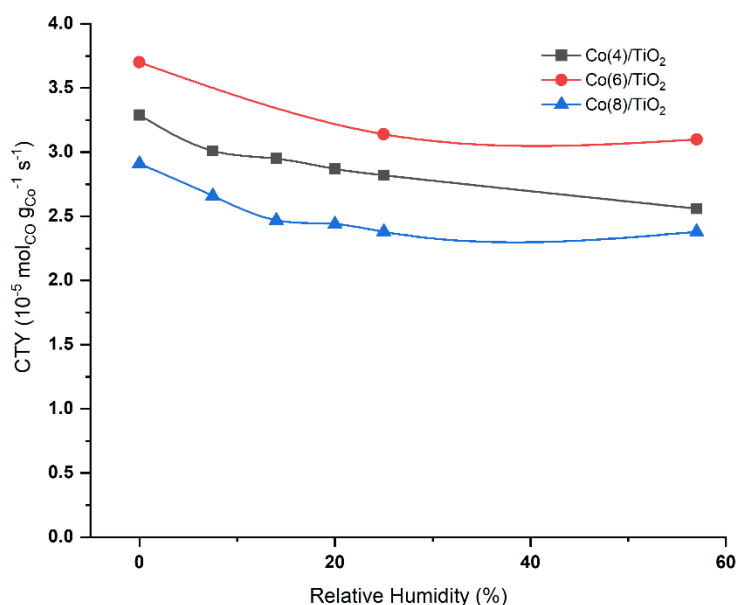


Figure 11. *In situ* FTS activity of the Co(x)/TiO₂ catalysts during humid FTS measurements in the Mössbauer cell. The CTY determined at steady state at the applied conditions is plotted against the RH. (Co(4)/TiO₂: black squares, Co(6)/TiO₂: red circles, Co(8)/TiO₂: blue triangles).

Besides catalytic activity measurements in the *in situ* MES cell, the performance of the cobalt catalysts was measured in a high-pressure fixed-bed plug-flow reactor at 220 °C, 20 bar, a H_2/CO ratio of 4, and a space velocity of 60 L g_{cat}⁻¹ h⁻¹. The corresponding results for fresh and used catalysts are collected in Table 3. Note that the fresh catalysts were reduced at 340 °C for 2 h, while the used catalysts retrieved after the *in situ* MES measurements were re-reduced according to the same

procedure. The activity normalized on the amount of cobalt (CTY) was in the range of $1.7 - 2.2 \cdot 10^{-5} \text{ mol}_{\text{CO}} \text{ g}_{\text{Co}}^{-1} \text{ s}^{-1}$ for the fresh reduced catalysts. The Co(2)/TiO₂ catalyst shows a substantially higher CTY after exposure to humid Fischer-Tropsch conditions. This strong increase is likely the result of the higher cobalt reduction degree, following the harsh humid FTS conditions employed. We previously showed that 47% of cobalt remained oxidic when the fresh catalyst was reduced for 2 h at 340 °C, whereas only 18% remained oxidic after 2 h at the same reduction temperature for the used catalyst. As the catalysts for these activity measurements were reduced *in situ* for 2 h, one would expect significant differences in the amount of metallic cobalt and, thus, the catalytic performance. This higher degree of reduction for the used catalysts counteracts the negative impact of sintering on the activity. In good agreement with this, the CTY of the used Co(2)/TiO₂ catalyst is approximately 50% higher than that of the fresh catalyst. The relatively strong increase in activity suggests that deactivation due to sintering was minimal. However, the used catalyst shows a significantly larger contribution of C₅+ hydrocarbon products at the expense of methane. It has been previously shown that an increase in the cobalt particle size results in an increased C₅+ selectivity under high pressure FTS conditions [4], although this effect becomes much less pronounced for cobalt particles larger than 10 nm. Therefore, this change in selectivity can be in part explained by sintering of metallic particles. The increase in CO conversion likely leads to an increased selectivity towards C₅+ products. The used Co(4)/TiO₂ catalyst is less active than the fresh one, as expected since the STEM-EDX maps clearly show significant sintering of the cobalt particles. In this case, there was no benefit for the increased reducibility of the used catalyst compared to its fresh state. However, contrary to the Co(2)/TiO₂ catalyst, the used Co(4)/TiO₂ catalyst shows a higher selectivity towards methane compared to the fresh one. This shift in selectivity could be the result of the lower CO conversion, as lower CO conversion typically shifts the selectivity towards C₁ products due to the lower coverage of the surface with chain-growth monomers. The two catalysts with the highest weight loadings show almost identical CTY values, which are comparable to what was observed for the fresh Co(4)/TiO₂ catalyst. This underlines the structural similarity between these catalysts with the comparable particle sizes resulting in similar catalytic performance. The two fresh catalysts exhibit a similar selectivity towards C₅+ hydrocarbons, but lower than for the Co(4)/TiO₂ catalyst, despite the higher CO conversion. Nevertheless, the observed changes are relatively small and the obtained product distributions are typical for the FTS reaction under our hydrogen-rich conditions.

Table 3. Catalytic performance data for the cobalt catalysts (plug-flow reactor operated at 220 °C, 20 bar and $H_2/CO = 4$, $SV = 60 \text{ L g}_{\text{cat}}^{-1} \text{ h}^{-1}$)

<i>Catalyst</i>	<i>Conversion</i> (%)	<i>C₁</i> <i>selectivity</i> (%)	<i>C₂-C₄</i> <i>selectivity</i> (%)	<i>C₅₊</i> <i>selectivity</i> (%)	<i>CTY</i> (10^{-5} mol_{CO} $\text{g}_{Co}^{-1} \text{ s}^{-1}$)
Co(2)/TiO ₂	2	12	7	81	1.6
Co(2)/TiO ₂ used	4	5	3	92	2.5
Co(4)/TiO ₂	3	7	7	86	2.1
Co(4)/TiO ₂ used	1	14	10	76	1.2
Co(6)/TiO ₂	5	11	9	80	1.9
Co(8)/TiO ₂	5	15	9	76	1.9

4.4 Conclusion

By combining Mössbauer spectroscopy with TEM, we showed that reduction of a calcined cobalt on titania precursor led to sintering. Independent of the initial cobalt loading in the 2-8 wt% range, the final size of the reduced cobalt metal particles was the same (ca. 12 nm). *In situ* Mössbauer spectroscopy demonstrated partial oxidation of metallic cobalt under humid FTS conditions. The extent of cobalt oxidation increased with the steam partial pressure. Comparing the different catalysts, it was found that the absolute amount of oxidized cobalt was the same for all samples. This could be linked to cobalt oxide strongly interacting with titanol groups of the support. The formation of cobalt-titanate-like compounds was only observed under very high oxidizing potential and in the absence of CO. As such, our results indicate that such compounds do not readily form under practical FTS conditions. The data point to a strong impact of humid FTS conditions on the sintering of small metallic cobalt particles, where oxidic cobalt wets the titania support, facilitating cobalt sintering in synthesis gas and under reduction conditions. STEM-EDX maps confirmed the much larger cobalt particles in catalysts employed under humid FTS conditions in comparison to reduced samples.

Bibliography

- [1] E. Iglesia, Design, synthesis, and use of cobalt-based Fischer-Tropsch synthesis catalysts, *Appl. Catal. A Gen.*, vol. 161, no. 1–2, pp. 59–78, 1997, doi: 10.1016/S0926-860X(97)00186-5.
- [2] E. Rytter, N. E. Tsakoumis, and A. Holmen, On the selectivity to higher hydrocarbons in Co-based Fischer-Tropsch synthesis, *Catal. Today*, vol. 261, pp. 3–16, 2016, doi: 10.1016/j.cattod.2015.09.020.
- [3] J. P. den Breejen, P. B. Radstake, G. L. Bezemer, J. H. Bitter, V. Frøseth, A. Holmen, and K. P. de Jong, On the Origin of the Cobalt Particle Size Effects in Fischer-Tropsch Catalysis, *J. Am. Chem. Soc.*, vol. 131, no. 20, pp. 7197–7203, 2009, doi: 10.1021/ja901006x.
- [4] G. L. Bezemer, J. H. Bitter, H. P. C. E. Kuipers, H. Oosterbeek, J. E. Holewijn, X. Xu, F. Kapteijn, A. J. van Dillen, and K. P. de Jong, Cobalt Particle Size Effects in the Fischer-Tropsch Reaction Studied with Carbon Nanofiber Supported Catalysts, *J. Am. Chem. Soc.*, vol. 128, no. 12, pp. 3956–3964, 2006, doi: 10.1021/ja058282w.
- [5] N. E. Tsakoumis, M. Rønning, Ø. Borg, E. Rytter, and A. Holmen, Deactivation of cobalt based Fischer-Tropsch catalysts: A review, *Catal. Today*, vol. 154, no. 3–4, pp. 162–182, 2010, doi: 10.1016/j.cattod.2010.02.077.
- [6] P. J. van Berge and R. C. Everson, Cobalt as an alternative Fischer-Tropsch catalyst to iron for the production of middle distillates, in *Studies in Surface Science and Catalysis*, vol. 107, no. 15, pp. 207–212, 1997. doi: 10.1016/S0167-2991(97)80336-9.
- [7] D. Moodley, M. Claeys, E. van Steen, P. van Helden, D. Kistamurthy, K.-J. Weststrate, H. Niemantsverdriet, A. Saib, W. Erasmus, and J. van de Loosdrecht, Sintering of cobalt during FTS: Insights from industrial and model systems, *Catal. Today*, vol. 342, pp. 59–70, 2020, doi: 10.1016/j.cattod.2019.03.059.
- [8] E. Rytter and A. Holmen, Deactivation and regeneration of commercial type fischer-tropsch co-catalysts—A mini-review, *Catalysts*, vol. 5, no. 2, pp. 478–499, 2015, doi: 10.3390/catal5020478.
- [9] Z. Yu, Ø. Borg, D. Chen, E. Rytter, and A. Holmen, Role of surface oxygen in the preparation and deactivation of carbon nanofiber supported cobalt Fischer-Tropsch catalysts, *Top. Catal.*, vol. 45, no. 1–4, pp. 69–74, 2007, doi: 10.1007/s11244-007-0242-7.
- [10] M. Wolf, B. K. Mutuma, N. J. Coville, N. Fischer, and M. Claeys, Role of CO in the Water-Induced Formation of Cobalt Oxide in a High Conversion Fischer-Tropsch Environment, *ACS Catal.*, vol. 8, no. 5, pp. 3985–3989, 2018, doi: 10.1021/acscatal.7b04177.
- [11] E. Van Steen, M. Claeys, M. E. Dry, J. Van De Loosdrecht, E. L. Viljoen, and J. L. Visagie, Stability of nanocrystals: Thermodynamic analysis of oxidation and re-reduction of cobalt in water/hydrogen mixtures, *J. Phys. Chem. B*, vol. 109, no. 8, pp. 3575–3577, 2005, doi: 10.1021/jp045136o.
- [12] P. J. Van Berge, J. Van De Loosdrecht, S. Barradas, and A. M. Van Der Kraan, Oxidation of cobalt based Fischer-Tropsch catalysts as a deactivation mechanism, *Catal. Today*, vol. 58, no. 4, pp. 321–334, 2000, doi: 10.1016/S0920-5861(00)00265-0.
- [13] J. van de Loosdrecht, B. Balzhinimaev, J. A. Dalmon, J. W. Niemantsverdriet, S. V. Tsybulya, A. M. Saib, P. J. van Berge, and J. L. Visagie, Cobalt Fischer-Tropsch synthesis: Deactivation by oxidation?, *Catal. Today*, vol. 123, no. 1–4, pp. 293–302, 2007, doi: 10.1016/j.cattod.2007.02.032.
- [14] W. Zhou, J.-G. Chen, K.-G. Fang, and Y.-H. Sun, The deactivation of Co/SiO₂ catalyst for Fischer-Tropsch synthesis at different ratios of H₂ to CO, *Fuel Process. Technol.*, vol. 87, no. 7, pp. 609–616, 2006, doi: 10.1016/j.fuproc.2006.01.008.
- [15] G. Prieto, A. Martínez, P. Concepción, and R. Moreno-Tost, Cobalt particle size effects in Fischer-Tropsch synthesis: structural and in situ spectroscopic characterisation on reverse micelle-synthesised Co/ITQ-2 model catalysts, *J. Catal.*, vol. 266, no. 1, pp. 129–144, 2009, doi: 10.1016/j.jcat.2009.06.001.
- [16] M. Wolf, E. K. Gibson, E. J. Olivier, J. H. Neethling, C. R. A. Catlow, N. Fischer, and M. Claeys, In-depth characterisation of metal-support compounds in spent Co/SiO₂ Fischer-Tropsch model catalysts, *Catal. Today*, vol. 342, pp. 71–78, 2020, doi: 10.1016/j.cattod.2019.01.065.
- [17] C. H. Bartholomew, Mechanisms of catalyst deactivation, *Appl. Catal. A Gen.*, vol. 212, no. 1–2, pp. 17–60, 2001, doi: 10.1016/S0926-860X(00)00843-7.
- [18] M. Sadeqzadeh, S. Chambrey, J. Hong, P. Fongarland, F. Luck, D. Curulla-Ferré, D. Schweich, J. Bousquet, and A. Y. Khodakov, Effect of different reaction conditions on the deactivation of alumina-supported cobalt Fischer-Tropsch catalysts in a milli-fixed-bed reactor: Experiments and modeling, *Ind. Eng. Chem. Res.*, vol. 53, no. 17, pp. 6913–6922, 2014, doi: 10.1021/ie4040303.
- [19] A. M. Saib, D. J. Moodley, I. M. Ciobîc, M. M. Hauman, B. H. Sigwebela, C. J. Weststrate, J. W. Niemantsverdriet, and J. Van De Loosdrecht, Fundamental understanding of deactivation and regeneration of cobalt Fischer-Tropsch synthesis catalysts, *Catal. Today*, vol. 154, no. 3–4, pp. 271–282, 2010, doi: 10.1016/j.cattod.2010.02.008.
- [20] M. Rahmati, M. S. Safdari, T. H. Fletcher, M. D. Argyle, and C. H. Bartholomew, Chemical and Thermal Sintering

- of Supported Metals with Emphasis on Cobalt Catalysts during Fischer-Tropsch Synthesis, *Chemical Reviews*, vol. 120, no. 10, pp. 4455–4533, 2020, doi: 10.1021/acs.chemrev.9b00417.
- [21] M. Claeys, M. E. Dry, E. van Steen, P. J. van Berge, S. Booyens, R. Crous, P. van Helden, J. Labuschagne, D. J. Moodley, and A. M. Saib, Impact of Process Conditions on the Sintering Behavior of an Alumina-Supported Cobalt Fischer–Tropsch Catalyst Studied with an in Situ Magnetometer, *ACS Catal.*, vol. 5, no. 2, pp. 841–852, 2015, doi: 10.1021/cs501810y.
- [22] M. D. Argyle, T. S. Frost, and C. H. Bartholomew, Cobalt fischer-tropsch catalyst deactivation modeled using generalized power law expressions, *Top. Catal.*, vol. 57, no. 6–9, pp. 415–429, 2014, doi: 10.1007/s11244-013-0197-9.
- [23] A. Carvalho, V. V. Ordonsky, Y. Luo, M. Marinova, A. R. Muniz, N. R. Marcilio, and A. Y. Khodakov, Elucidation of deactivation phenomena in cobalt catalyst for Fischer-Tropsch synthesis using SSITKA, *J. Catal.*, vol. 344, pp. 669–679, 2016, doi: 10.1016/j.jcat.2016.11.001.
- [24] B. Ernst, S. Libs, P. Chaumette, and A. Kiennemann, Preparation and characterization of Fischer–Tropsch active Co/SiO₂ catalysts, *Appl. Catal. A Gen.*, vol. 186, no. 1–2, pp. 145–168, 1999, doi: 10.1016/S0926-860X(99)00170-2.
- [25] H. Karaca, J. Hong, P. Fongarland, P. Roussel, A. Griboval-Constant, M. Lacroix, K. Hortmann, O. V. Safonova, and A. Y. Khodakov, In situ XRD investigation of the evolution of alumina-supported cobalt catalysts under realistic conditions of Fischer-Tropsch synthesis, *Chem. Commun.*, vol. 46, no. 5, pp. 788–790, 2010, doi: 10.1039/B920110F.
- [26] A. Rochet, V. Moizan, F. Diehl, C. Pichon, and V. Briois, Quick-XAS and Raman operando characterisation of a cobalt alumina-supported catalyst under realistic Fischer-Tropsch reaction conditions, *Catal. Today*, vol. 205, pp. 94–100, 2013, doi: 10.1016/j.cattod.2012.08.021.
- [27] T. O. Eschemann and K. P. de Jong, Deactivation Behavior of Co/TiO₂ Catalysts during Fischer–Tropsch Synthesis, *ACS Catal.*, vol. 5, no. 6, pp. 3181–3188, 2015, doi: 10.1021/acscatal.5b00268.
- [28] T. O. Eschemann, J. H. Bitter, and K. P. De Jong, Effects of loading and synthesis method of titania-supported cobalt catalysts for Fischer-Tropsch synthesis, *Catal. Today*, vol. 228, pp. 89–95, 2014, doi: 10.1016/j.cattod.2013.10.041.
- [29] C. E. Kliewer, S. L. Soled, and G. Kiss, Morphological transformations during Fischer-Tropsch synthesis on a titania-supported cobalt catalyst, *Catal. Today*, vol. 323, pp. 233–256, 2019, doi: 10.1016/j.cattod.2018.05.021.
- [30] M. Mehrbod, M. Martinelli, A. G. Martino, D. C. Cronauer, A. Jeremy Kropf, C. L. Marshall, and G. Jacobs, Fischer-Tropsch synthesis: Direct cobalt nitrate reduction of promoted Co/TiO₂ catalysts, *Fuel*, vol. 245, no. February, pp. 488–504, 2019, doi: 10.1016/j.fuel.2019.02.083.
- [31] S. J. Tauster, S. C. Fung, and R. L. Garten, Strong metal-support interactions. Group 8 noble metals supported on titanium dioxide, *J. Am. Chem. Soc.*, vol. 100, no. 1, pp. 170–175, 1978, doi: 10.1021/ja00469a029.
- [32] S. J. Tauster, S. C. Fung, R. T. K. Baker, and J. A. Horsley, Strong Interactions in Supported-Metal Catalysts, *Science*, vol. 211, no. 4487, pp. 1121–1125, 1981, doi: 10.1126/science.211.4487.1121.
- [33] H. Karaca, O. V. Safonova, S. Chambrey, P. Fongarland, P. Roussel, A. Griboval-Constant, M. Lacroix, and A. Y. Khodakov, Structure and catalytic performance of Pt-promoted alumina-supported cobalt catalysts under realistic conditions of Fischer–Tropsch synthesis, *J. Catal.*, vol. 277, no. 1, pp. 14–26, 2011, doi: 10.1016/j.jcat.2010.10.007.
- [34] G. L. Bezemer, T. J. Remans, A. P. van Bavel, and A. I. Dugulan, Direct Evidence of Water-Assisted Sintering of Cobalt on Carbon Nanofiber Catalysts during Simulated Fischer–Tropsch Conditions Revealed with in Situ Mössbauer Spectroscopy, *J. Am. Chem. Soc.*, vol. 132, no. 25, pp. 8540–8541, 2010, doi: 10.1021/ja103002k.
- [35] L. M. van Koppen, A. Iulian Dugulan, G. Leendert Bezemer, and E. J. M. Hensen, Sintering and carburization under simulated high conversion on a cobalt-based Fischer-Tropsch catalyst; manganese oxide as a structural promotor, *J. Catal.*, vol. 413, pp. 106–118, 2022, doi: 10.1016/j.jcat.2022.06.020.
- [36] M. W. J. Crajé, A. M. Van der Kraan, J. Van de Loosdrecht, and P. J. Van Berge, The application of Mössbauer emission spectroscopy to industrial cobalt based Fischer-Tropsch catalysts, *Catal. Today*, vol. 71, no. 3–4, pp. 369–379, 2002, doi: 10.1016/S0920-5861(01)00464-3.
- [37] Z. Klencsár, MossWinn—methodological advances in the field of Mössbauer data analysis, *Hyperfine Interact.*, vol. 217, no. 1–3, pp. 117–126, 2013, doi: 10.1007/s10751-012-0732-2.
- [38] J. A. Tjon and M. Blume, Mössbauer Spectra in a Fluctuating Environment II. Randomly Varying Electric Field Gradients, *Phys. Rev.*, vol. 165, no. 2, pp. 456–461, 1968, doi: 10.1103/PhysRev.165.456.
- [39] T. W. van Deelen, J. J. Nijhuis, N. A. Krans, J. Zečević, and K. P. de Jong, Preparation of Cobalt Nanocrystals Supported on Metal Oxides To Study Particle Growth in Fischer–Tropsch Catalysts, *ACS Catal.*, vol. 8, no. 11, pp. 10581–10589, 2018, doi: 10.1021/acscatal.8b03094.
- [40] T. Ohno, K. Sarukawa, K. Tokieda, and M. Matsumura, Morphology of a TiO₂ Photocatalyst (Degussa, P-25) Consisting of Anatase and Rutile Crystalline Phases, *J. Catal.*, vol. 203, no. 1, pp. 82–86, 2001, doi:

- 10.1006/jcat.2001.3316.
- [41] M. Voß, D. Borgmann, and G. Wedler, Characterization of Alumina, Silica, and Titania Supported Cobalt Catalysts, *J. Catal.*, vol. 212, no. 1, pp. 10–21, 2002, doi: 10.1006/jcat.2002.3739.
- [42] G. K. Wertheim, Hyperfine Structure of Divalent and Trivalent Fe^{57} in Cobalt Oxide, *Phys. Rev.*, vol. 124, no. 3, pp. 764–767, 1961, doi: 10.1103/PhysRev.124.764.
- [43] G. K. Wertheim, Chemical effects of nuclear transformations in Moessbauer spectroscopy, *Acc. Chem. Res.*, vol. 4, no. 11, pp. 373–379, 1971, doi: 10.1021/ar50047a003.
- [44] H. Pollak, Fe^{3+} ion Lifetime in CoO Deduced from the Auger and Mössbauer Effects, *Phys. status solidi*, vol. 2, no. 6, pp. 720–724, 1962, doi: 10.1002/pssb.19620020609.
- [45] A. Cruset and J. M. Friedt, Mössbauer study of the valence state of ^{57}Fe after ^{57}Co decay in CoFe_2O_4 , *Phys. Status Solidi*, vol. 45, no. 1, pp. 189–193, 1971, doi: 10.1002/pssb.2220450120.
- [46] C. Wivel, B. S. Clausen, R. Candia, S. Mørup, and H. Topsøe, Mössbauer Emission Studies of Calcined Co-Mo/ Al_2O_3 Catalysts: Catalytic Significance of Co Precursors, *J. Catal.*, vol. 87, no. 2, pp. 497–513, 1984, doi: 10.1016/0021-9517(84)90210-0.
- [47] H. Topsøe, B. S. Clausen, R. Candia, C. Wivel, and S. Mørup, In situ Mossbauer emission spectroscopy studies of unsupported and supported sulfided Co-Mo hydrodesulfurization catalysts: Evidence for and nature of a Co-Mo-S phase, *J. Catal.*, vol. 68, no. 2, pp. 433–452, 1981, doi: 10.1016/0021-9517(81)90114-7.
- [48] J. A. R. Van Veen, E. Gerkema, A. M. Van Der Kraan, P. A. J. M. Hendriks, and H. Beens, A ^{57}Co Mössbauer emission spectrometric study of some supported CoMo hydrodesulfurization catalysts, *J. Catal.*, vol. 133, no. 1, pp. 112–123, 1992, doi: 10.1016/0021-9517(92)90189-0.
- [49] H. P. Boehm, Chemical Identification of Surface Groups, in *Advances in Catalysis*, 1966, pp. 179–274. doi: 10.1016/S0360-0564(08)60354-5.
- [50] B. M. Xaba and J. P. R. de Villiers, Sintering Behavior of TiO_2 -Supported Model Cobalt Fischer–Tropsch Catalysts under H_2 Reducing Conditions and Elevated Temperature, *Ind. Eng. Chem. Res.*, vol. 55, no. 35, pp. 9397–9407, 2016, doi: 10.1021/acs.iecr.6b02311.
- [51] R. Y. Abrokwhah, M. M. Rahman, V. G. Deshmane, and D. Kuila, Effect of titania support on Fischer–Tropsch synthesis using cobalt, iron, and ruthenium catalysts in silicon-microchannel microreactor, *Mol. Catal.*, vol. 478, p. 110566, 2019, doi: 10.1016/j.mcat.2019.110566.
- [52] M. Wolf, E. K. Gibson, E. J. Olivier, J. H. Neethling, C. R. A. Catlow, N. Fischer, and M. Claeys, Water-Induced Formation of Cobalt-Support Compounds under Simulated High Conversion Fischer–Tropsch Environment, *ACS Catal.*, vol. 9, no. 6, pp. 4902–4918, 2019, doi: 10.1021/acscatal.9b00160.
- [53] C. Lancelot, V. V. Ordonsky, O. Stéphan, M. Sadeqzadeh, H. Karaca, M. Lacroix, D. Curulla-Ferré, F. Luck, P. Fongarland, A. Griboval-Constant, and A. Y. Khodakov, Direct Evidence of Surface Oxidation of Cobalt Nanoparticles in Alumina-Supported Catalysts for Fischer–Tropsch Synthesis, *ACS Catal.*, vol. 4, no. 12, pp. 4510–4515, 2014, doi: 10.1021/cs500981p.
- [54] A. Beck, H. Frey, M. Becker, L. Artiglia, M. G. Willinger, and J. A. van Bokhoven, Influence of Hydrogen Pressure on the Structure of Platinum–Titania Catalysts, *J. Phys. Chem. C*, vol. 125, no. 41, pp. 22531–22538, 2021, doi: 10.1021/acs.jpcc.1c05939.
- [55] A. Beck, P. Rzepka, K. P. Marshall, D. Stoian, M. G. Willinger, and J. A. van Bokhoven, Hydrogen Interaction with Oxide Supports in the Presence and Absence of Platinum, *J. Phys. Chem. C*, vol. 126, no. 41, pp. 17589–17597, 2022, doi: 10.1021/acs.jpcc.2c05478.
- [56] S. Wendt, R. Schaub, J. Matthiesen, E. K. Vestergaard, E. Wahlström, M. D. Rasmussen, P. Thostrup, L. M. Molina, E. Lægsgaard, I. Stensgaard, B. Hammer, and F. Besenbacher, Oxygen vacancies on $\text{TiO}_2(110)$ and their interaction with H_2O and O_2 : A combined high-resolution STM and DFT study, *Surf. Sci.*, vol. 598, no. 1–3, pp. 226–245, 2005, doi: 10.1016/j.susc.2005.08.041.
- [57] M. Henderson, The interaction of water with solid surfaces: fundamental aspects revisited, *Surf. Sci. Rep.*, vol. 46, no. 1–8, pp. 1–308, 2002, doi: 10.1016/S0167-5729(01)00020-6.
- [58] P. A. Thiel and T. E. Madey, The interaction of water with solid surfaces: Fundamental aspects, *Surf. Sci. Rep.*, vol. 7, no. 6–8, pp. 211–385, 1987, doi: 10.1016/0167-5729(87)90001-X.
- [59] C. Qiu, Y. Odarchenko, Q. Meng, S. Xu, I. Lezcano-Gonzalez, P. Olalde-Velasco, F. Maccherozzi, L. Zanetti-Domingues, M. Martin-Fernandez, and A. M. Beale, Resolving the Effect of Oxygen Vacancies on Co Nanostructures Using Soft XAS/X-PEEM, *ACS Catal.*, vol. 12, no. 15, pp. 9125–9134, 2022, doi: 10.1021/acscatal.2c00611.
- [60] M. Wolf, N. Fischer, and M. Claeys, Water-induced deactivation of cobalt-based Fischer–Tropsch catalysts, *Nat. Catal.*, vol. 3, no. 12, pp. 962–965, 2020, doi: 10.1038/s41929-020-00534-5.
- [61] H. J. Lipkin, Some simple features of the Mossbauer effect, *Ann. Phys. (N. Y.)*, vol. 18, no. 2, pp. 182–197, 1962, doi: 10.1016/0003-4916(62)90066-0.
- [62] K. Shun, K. Mori, S. Masuda, N. Hashimoto, Y. Hinuma, H. Kobayashi, and H. Yamashita, Revealing hydrogen

- spillover pathways in reducible metal oxides, *Chem. Sci.*, vol. 13, no. 27, pp. 8137–8147, 2022, doi: 10.1039/D2SC00871H.
- [63] S.-W. Ho, Surface Hydroxyls and Chemisorbed Hydrogen on Titania and Titania Supported Cobalt, *J. Chinese Chem. Soc.*, vol. 43, no. 2, pp. 155–163, 1996, doi: 10.1002/jccs.199600023.
- [64] J. D. Cashion, E. R. Vance, and D. H. Ryan, Mössbauer study of the temperature dependence of electron delocalization in mixed valence freudenbergite, *J. Am. Ceram. Soc.*, vol. 103, no. 10, pp. 5496–5501, 2020, doi: 10.1111/jace.17190.
- [65] R. Riva, H. Miessner, R. Vitali, and G. Del Piero, Metal–support interaction in Co/SiO₂ and Co/TiO₂, *Appl. Catal. A Gen.*, vol. 196, no. 1, pp. 111–123, 2000, doi: 10.1016/S0926-860X(99)00460-3.
- [66] T. Petsi, G. D. Panagiotou, C. S. Garoufalidis, C. Kordulis, P. Stathi, Y. Deligiannakis, A. Lycourghiotis, and K. Bourikas, Interfacial Impregnation Chemistry in the Synthesis of Cobalt Catalysts Supported on Titania, *Chem. - A Eur. J.*, vol. 15, no. 47, pp. 13090–13104, 2009, doi: 10.1002/chem.200900760.
- [67] K. K. B. Duff, L. Spanu, and N. D. M. Hine, Impact of Carbonyl Formation on Cobalt Ripening over Titania Surface, *J. Phys. Chem. C*, vol. 121, no. 29, pp. 15880–15887, 2017, doi: 10.1021/acs.jpcc.7b05371.
- [68] E. Rytter, Ø. Borg, N. E. Tsakoumis, and A. Holmen, Water as key to activity and selectivity in Co Fischer-Tropsch synthesis: γ -alumina based structure-performance relationships, *J. Catal.*, vol. 365, pp. 334–343, 2018, doi: 10.1016/j.jcat.2018.07.003.
- [69] E. Rytter and A. Holmen, Perspectives on the Effect of Water in Cobalt Fischer-Tropsch Synthesis, *ACS Catal.*, vol. 7, no. 8, pp. 5321–5328, 2017, doi: 10.1021/acscatal.7b01525.
- [70] W. Chen, R. Pestman, B. Zijlstra, I. A. W. Filot, and E. J. M. Hensen, Mechanism of Cobalt-Catalyzed CO Hydrogenation: 1. Methanation, *ACS Catal.*, vol. 7, no. 12, pp. 8050–8060, 2017, doi: 10.1021/acscatal.7b02757.
- [71] R. Pestman, W. Chen, and E. Hensen, Insight into the Rate-Determining Step and Active Sites in the Fischer-Tropsch Reaction over Cobalt Catalysts, *ACS Catal.*, vol. 9, no. 5, pp. 4189–4195, 2019, doi: 10.1021/acscatal.9b00185.

Appendix C

Table C1. Mössbauer experimental conditions for reactive Fischer-Tropsch humidity tests. All tests were performed at 200 °C with a total pressure of 20 bar.

<i>Reaction</i>	<i>He (mL/min)</i>	<i>H₂ (mL/min)</i>	<i>CO (mL/min)</i>	<i>Water (g/h)</i>	<i>Steam (mL/min)</i>
<i>RH = 0%</i>	75	20	5	0	0
<i>RH = 7.5%</i> <i>H₂/H₂O = 4</i>	55	20	5	0.24	5
<i>RH = 14%</i> <i>H₂/H₂O = 2</i>	55	20	5	0.48	10
<i>RH = 20%</i> <i>H₂/H₂O = 1.3</i>	55	20	5	0.72	15
<i>RH = 25%</i> <i>H₂/H₂O = 1</i>	55	20	5	0.96	20
<i>RH = 57%</i> <i>H₂/H₂O = 1</i>	0	20	5	0.96	20

Table C2. Mössbauer experimental conditions for model oxidation tests. All tests were performed at 220 °C with a total pressure of 20 bar.

<i>Reaction</i>	<i>Ar (mL/min)</i>	<i>H₂ (mL/min)</i>	<i>Water (g/h)</i>	<i>Steam (mL/min)</i>
<i>H₂O/H₂ = 10</i> <i>RH = 25%</i>	78	2	0.96	20
<i>H₂O/H₂ = 20</i> <i>RH = 25%</i>	79	1	0.96	20
<i>H₂O/H₂ = 50</i> <i>RH = 25%</i>	79.6	0.4	0.96	20
<i>H₂O/H₂ = 70</i> <i>RH = 25%</i>	79.7	0.3	0.96	20
<i>H₂O/Ar</i>	80	0	0.96	20

<i>RH</i> = 25%

Table C3. Fit parameters of Mössbauer spectra of the Co(2)/TiO₂ catalyst after different treatments.

<i>Treatment</i>	<i>Temperature</i> (°C)	<i>Cobalt</i> <i>phase</i>	<i>Isomer</i> <i>Shift</i> (mm s ⁻¹)	<i>Hyperfine</i> <i>Field</i> (kOe)	<i>Quadrupole</i> <i>Splitting</i> (mm s ⁻¹)	<i>Spectral</i> <i>Contribution</i> (%)
<i>After</i> <i>reduction</i>	20	<i>Co(0) bulk</i>	-0.1	323	-	78
		<i>Co</i> ²⁺	0.9	-	2.0	22
<i>During</i> <i>FTS</i> <i>reaction</i>	200	<i>Co(0) bulk</i>	-0.2	310	-	77
		<i>Co</i> ²⁺	0.8	-	1.8	23
<i>RH</i> = 7.5%	200	<i>Co(0) bulk</i>	-0.2	310	-	67
		<i>Co</i> ²⁺	0.8	-	1.7	33
<i>RH</i> = 14%	200	-	-	-	-	-
<i>RH</i> = 20%	200	<i>Co(0) bulk</i>	-0.2	310	-	65
		<i>Co</i> ²⁺	0.7	-	1.8	30
		<i>Co</i> ³⁺	0.4	-	0.2	5
<i>RH</i> = 25%	200	<i>Co(0) bulk</i>	-0.2	310	-	63
		<i>Co</i> ²⁺	0.7	-	1.8	30
		<i>Co</i> ³⁺	0.4	-	0.2	7
<i>RH</i> = 57%	200	<i>Co(0) bulk</i>	-0.2	310	-	57
		<i>Co</i> ²⁺	0.8	-	1.7	25
		<i>Co</i> ³⁺	0.1	-	0.8	18
<i>After</i> <i>reaction</i>	20	<i>Co(0) bulk</i>	-0.1	322	-	48
		<i>Co</i> ²⁺	0.9	-	2.0	30
		<i>Co</i> ³⁺	0.2	-	0.8	22
<i>Reduced</i>	20	<i>Co(0) bulk</i>	-0.1	323	-	82
		<i>Co</i> ²⁺	0.9	-	2.0	18

Table C4. Fit parameters of Mössbauer spectra of the Co(4)/TiO₂ catalyst after different treatments.

<i>Treatment</i>	<i>Temperature</i> (°C)	<i>Cobalt</i> <i>phase</i>	<i>Isomer</i> <i>Shift</i> (mm s ⁻¹)	<i>Hyperfine</i> <i>Field</i> (kOe)	<i>Quadrupole</i> <i>Splitting</i> (mm s ⁻¹)	<i>Spectral</i> <i>Contribution</i> (%)
<i>After</i> <i>reduction</i>	20	<i>Co(0) bulk</i>	-0.1	322	-	95
		<i>Co</i> ²⁺	0.8	-	1.8	5
<i>During</i> <i>FTS</i> <i>reaction</i>	200	<i>Co(0) bulk</i>	-0.2	309	-	95
		<i>Co</i> ²⁺	0.9	-	1.8	5
<i>RH = 7.5%</i>	200	<i>Co(0) bulk</i>	-0.2	309	-	87
		<i>Co</i> ²⁺	0.9	-	1.8	13
<i>RH = 14%</i>	200	<i>Co(0) bulk</i>	-0.2	309	-	86
		<i>Co</i> ²⁺	0.8	-	1.7	14
<i>RH = 20%</i>	200	<i>Co(0) bulk</i>	-0.2	309	-	86
		<i>Co</i> ²⁺	0.8	-	1.6	14
<i>RH = 25%</i>	200	<i>Co(0) bulk</i>	-0.2	309	-	84
		<i>Co</i> ²⁺	0.8	-	1.7	16
<i>RH = 57%</i>	200	<i>Co(0) bulk</i>	-0.2	309	-	80
		<i>Co</i> ²⁺	0.9	-	1.7	15
		<i>Co</i> ³⁺	0.1	-	0.9	5
<i>After</i> <i>reaction</i>	20	<i>Co(0) bulk</i>	-0.1	321	-	78
		<i>Co</i> ²⁺	0.9	-	2.1	13
		<i>Co</i> ³⁺	0.1	-	0.9	9
<i>Reduced</i>	20	<i>Co(0) bulk</i>	-0.1	323	-	96
		<i>Co</i> ²⁺	0.9	-	2.1	4

Table C5. Fit parameters of Mössbauer spectra of the Co(6)/TiO₂ catalyst after different treatments.

<i>Treatment</i>	<i>Temperature</i> (°C)	<i>Cobalt</i> <i>phase</i>	<i>Isomer</i> <i>Shift</i> (mm s ⁻¹)	<i>Hyperfine</i> <i>Field</i> (kOe)	<i>Quadrupole</i> <i>Splitting</i> (mm s ⁻¹)	<i>Spectral</i> <i>Contribution</i> (%)
<i>After</i> <i>reduction</i>	20	<i>Co(0) bulk</i>	-0.1	323	-	90
		<i>Co</i> ²⁺	0.9	-	1.9	10
<i>During</i> <i>FTS</i> <i>reaction</i>	200	<i>Co(0) bulk</i>	-0.2	310	-	91
		<i>Co</i> ²⁺	0.8	-	1.8	9
<i>RH = 7.5%</i>	200	<i>Co(0) bulk</i>	-0.2	310	-	89
		<i>Co</i> ²⁺	0.9	-	1.7	11
<i>RH = 14%</i>	200	-	-	-	-	-
<i>RH = 20%</i>	200	<i>Co(0) bulk</i>	-0.2	310	-	87
		<i>Co</i> ²⁺	0.8	-	1.7	13
<i>RH = 25%</i>	200	<i>Co(0) bulk</i>	-0.2	309	-	86
		<i>Co</i> ²⁺	0.8	-	1.7	14
<i>RH = 57%</i>	200	<i>Co(0) bulk</i>	-0.2	310	-	78
		<i>Co</i> ²⁺	0.8	-	1.7	11
		<i>Co</i> ³⁺	0.1	-	0.8	11
<i>After</i> <i>reaction</i>	20	<i>Co(0) bulk</i>	-0.1	322	-	81
		<i>Co</i> ²⁺	0.9	-	2.2	15
		<i>Co</i> ³⁺	0.2	-	0.9	4
<i>Reduced</i>	20	<i>Co(0) bulk</i>	-0.1	323	-	98
		<i>Co</i> ²⁺	0.9	-	2.0	2

Table C6. Fit parameters of Mössbauer spectra of the Co(8)/TiO₂ catalyst after different treatments.

<i>Treatment</i>	<i>Temperature</i> (°C)	<i>Cobalt</i> <i>phase</i>	<i>Isomer</i> <i>Shift</i> (mm s ⁻¹)	<i>Hyperfine</i> <i>Field</i> (kOe)	<i>Quadrupole</i> <i>Splitting</i> (mm s ⁻¹)	<i>Spectral</i> <i>Contribution</i> (%)
<i>After</i> <i>reduction</i>	20	<i>Co(0) bulk</i>	-0.1	322	-	89
		<i>Co</i> ²⁺	1.0	-	1.9	11
<i>During</i> <i>FTS</i> <i>reaction</i>	200	<i>Co(0) bulk</i>	-0.2	309	-	92
		<i>Co</i> ²⁺	0.8	-	1.6	8
<i>RH = 7.5%</i>	200	<i>Co(0) bulk</i>	-0.2	309	-	90
		<i>Co</i> ²⁺	0.8	-	1.8	10
<i>RH = 14%</i>	200	<i>Co(0) bulk</i>	-0.2	310	-	89
		<i>Co</i> ²⁺	0.8	-	1.7	11
<i>RH = 20%</i>	200	<i>Co(0) bulk</i>	-0.2	309	-	87
		<i>Co</i> ²⁺	0.7	-	1.7	13
<i>RH = 25%</i>	200	<i>Co(0) bulk</i>	-0.2	309	-	86
		<i>Co</i> ²⁺	0.8	-	1.7	14
<i>RH = 57%</i>	200	<i>Co(0) bulk</i>	-0.2	309	-	83
		<i>Co</i> ²⁺	0.8	-	1.7	10
		<i>Co</i> ³⁺	0.1	-	0.8	7
<i>After</i> <i>reaction</i>	20	<i>Co(0) bulk</i>	-0.1	321	-	79
		<i>Co</i> ²⁺	0.9	-	2.2	12
		<i>Co</i> ³⁺	0.2	-	0.9	9
<i>Reduced</i>	20	<i>Co(0) bulk</i>	-0.1	322	-	97
		<i>Co</i> ²⁺	0.9	-	2.0	3

Table C7. Fit parameters of Mössbauer spectra of the Co(2)/TiO₂ catalyst after various experiments.

<i>Treatment</i>	<i>Temperature</i> (°C)	<i>Cobalt</i> <i>phase</i>	<i>Isomer</i> <i>Shift</i> (mm s ⁻¹)	<i>Hyperfine</i> <i>Field</i> (kOe)	<i>Quadrupole</i> <i>Splitting</i> (mm s ⁻¹)	<i>Spectral</i> <i>Contribution</i> (%)
<i>After</i> <i>reduction</i>	20	<i>Co(0) bulk</i>	-0.1	319	-	25
		<i>Co</i> ³⁺	0.2	-	0.8	39
		<i>Co</i> ²⁺	1.0	-	1.8	36
<i>After</i> <i>reduction</i>	200	<i>Co(0) bulk</i>	-0.2	309	-	16
		<i>Co(0) SPM</i>	0.0	-	-	29
		<i>Co</i> ³⁺	0.1	-	0.8	14
		<i>Co</i> ²⁺	0.9	-	1.4	41
<i>During</i> <i>FTS</i> <i>reaction</i>	200	<i>Co(0) bulk</i>	-0.2	308	-	29
		<i>Co(0) SPM</i>	-0.1	-	-	26
		<i>Co</i> ²⁺	0.9	-	1.4	45
<i>RH</i> = 7.5%	200	<i>Co(0) bulk</i>	-0.2	310	-	74
		<i>Co</i> ²⁺	0.8	-	1.8	26

Table C8. Fit parameters of Mössbauer spectra of the Co(4)/TiO₂ catalyst after model oxidation experiments.

<i>Treatment</i>	<i>Temperature</i> (°C)	<i>Cobalt</i> <i>phase</i>	<i>Isomer</i> <i>Shift</i> (mm s ⁻¹)	<i>Hyperfine</i> <i>Field</i> (kOe)	<i>Quadrupole</i> <i>Splitting</i> (mm s ⁻¹)	<i>Spectral</i> <i>Contribution</i> (%)
<i>After</i> <i>reduction</i>	220	<i>Co(0) bulk</i>	-0.2	309	-	83
		<i>Co</i> ²⁺	0.8	-	1.7	17
<i>H</i> ₂ <i>O</i> / <i>H</i> ₂ = 10	220	<i>Co(0) bulk</i>	-0.2	308	-	65
		<i>Co</i> ²⁺	0.8	-	1.5	35
<i>H</i> ₂ <i>O</i> / <i>H</i> ₂ = 20	220	<i>Co(0) bulk</i>	-0.2	308	-	59
		<i>Co</i> ²⁺	0.8	-	1.5	41
<i>H</i> ₂ <i>O</i> / <i>H</i> ₂ = 50	220	<i>Co(0) bulk</i>	-0.2	308	-	45
		<i>Co</i> ²⁺	0.8	-	1.5	55

$H_2O/H_2 = 70$	220	<i>Co(0) bulk</i>	-0.2	307	-	19
		Co^{2+}	1.0	-	1.2	26
		Co^{2+}	0.5	-	1.2	55
H_2O/Ar	220	Co^{2+}	1.0	-	1.1	24
		Co^{2+}	0.5	-	1.0	76
After reduction at 340 °C for 2 hours	20	<i>Co(0) bulk</i>	-0.1	321	-	18
		Co^{2+}	0.9	-	2.0	46
		Co^{2+}	0.9	-	0.8	36
After reduction at 340 °C for 8 hours	20	<i>Co(0) bulk</i>	-0.1	323	-	31
		Co^{2+}	1.2	-	1.3	20
		Co^{2+}	0.7	-	1.3	49
After reduction at 400 °C for 4 hours	20	<i>Co(0) bulk</i>	-0.1	321	-	74
		Co^{2+}	0.9	-	1.0	26
After reduction at 450 °C for 2 hours	20	<i>Co(0) bulk</i>	-0.1	321	-	100

Chapter 5

Tuning stability of titania-supported Fischer-Tropsch catalysts: impact of surface area and noble metal promotion

Abstract

Cobalt oxidation is a relevant deactivation pathway of titania-supported cobalt catalysts used in Fischer-Tropsch synthesis (FTS). To work towards more stable catalysts, we studied the effect of the surface area of the titania support and noble metal promotion on cobalt oxidation under simulated high conversion conditions. Mössbauer spectroscopy was used to follow the evolution of cobalt during reduction and FTS operation as a function of the steam pressure. The reduction of the oxidic cobalt precursor becomes more difficult due to stronger metal-support interactions when the titania surface area is increased. The reducibility was so low for cobalt on GP350 titania (surface area 283 m²/g) that the catalytical activity was negligible. Although cobalt was more difficult to reduce on P90 titania (94 m²/g) than on commonly used P25 titania (50 m²/g), Co/P90 combined increased resistance against cobalt sintering and higher FTS performance than Co/P25. The addition of platinum to Co/P90 led to a higher reduction degree of cobalt and also increased the cobalt dispersion, resulting in a catalyst formulation with promising performance at relatively low steam pressure. Nevertheless, the stronger cobalt-titania interactions result in more extensive deactivation at high steam pressure due to oxidation.

This chapter is under review for publication in Catalysis Today.

5.1. Introduction

Fischer-Tropsch synthesis (FTS) is the reaction of synthesis gas (syngas), a mixture of CO and H₂, to long-chain hydrocarbons and other useful chemicals [1]. Since syngas can also be derived from renewable sources [2], [3], FTS is a promising alternative for producing transportation fuels for sectors that are hard to decarbonize such as heavy-duty transport and aviation. As most industrial chemical processes, FTS utilizes a catalyst to improve the kinetics and selectivity of the reaction [4]. Commercially, iron [5] and cobalt [6] are used as the active phase for the FTS reaction. Cobalt FTS provides excellent selectivity towards long-chain hydrocarbons and is the preferred catalyst for processing of syngas derived from natural gas [7], [8]. Moreover, in future Power-to-Liquid (PTL) scenarios, cobalt is also the catalyst of choice, due to its low CO₂ production, low oxygenate selectivity, that is lost to the water stream, and excellent selectivity to C₅₊ hydrocarbons [9]. Efficient catalysts require relatively large cobalt particles due to the structure sensitivity effect [10], [11]. An important aspect of practical FTS is the deactivation suffered by cobalt-containing catalyst [12]. Given the high price of cobalt, it is very important to not only understand the mechanisms underlying deactivation of such catalysts but also improve catalyst formulations to mitigate deactivation [13].

In general, the following main deactivation pathways can be discerned in cobalt-based FTS, namely (i) poisoning, (ii) carbon effects, (iii) sintering, (iv) oxidation and (v) strong metal-support interactions (SMSI) [12]. Typical poisoning agents are sulfur [14] and nitrogen compounds [15], [16], while alkali metals can also reduce the performance significantly [17], [18]. Careful cleaning of the syngas feed avoids most of such poisoning problems. Instead, carbon effects, sintering, oxidation and SMSI are intrinsic to the FTS reaction and, therefore, depend on the catalyst structure and composition as well as the experimental conditions. To improve future catalyst design, these deactivation mechanisms and the extent to which they contribute will need to be fully understood. For this reason, *in situ* and *operando* characterization, studying catalysts in their actual working state, is of utmost importance [19].

The high partial pressures of CO and surface coverage with carbon species can have two distinctive effects. First, carbon species can block access to the active sites. Although FTS is generally considered to be a reaction that does not produce coke [20], the formation of carbonaceous products with a low hydrogen content has been argued to contribute to catalyst deactivation [21]. Selective blockage of some of the active sites has been shown to enhance FTS selectivity [22], [23]. Second, the presence

of carbon atoms at the surface can also lead to the formation of cobalt carbides, either surface or bulk carbides, which are much less active than metallic cobalt and have different selectivity profile [24].

Sintering of cobalt-based FTS catalysts is the result of many factors such as the relatively high operating temperature close to the Hüttig temperature of cobalt [25], the exothermicity of the reaction, and high partial pressures of steam at practical CO conversion levels [14]. Previous studies have pointed out the synergistic effect between carbon monoxide and steam towards cobalt sintering [26]–[28]. Both coalescence due to particle migration [29] and Ostwald ripening [30], [31] through migration of cobalt atoms have been suggested as important sintering mechanisms.

The formation of large amounts of water by-product can also cause the oxidation of the surface of cobalt metal particles. Thermodynamic studies have shown that bulk oxidation of metallic cobalt particles is only favorable when the particles are smaller than 4 nm under realistic FTS conditions [32]. However, experimental studies have demonstrated that supported cobalt particles can be oxidized in the presence of co-fed water [33]–[36]. As such, surface and bulk oxidation of cobalt needs to be considered as a relevant deactivation mechanism.

Deactivation through strong metal-support interactions (SMSI) is obviously strongly dependent on the support material. On carbon-based supports, often used as model systems, no deactivation through SMSI is observed [27], [28], [37]–[39]. However, deactivation is apparent when metal oxide supports are used. Typical support materials used for the FTS reaction are irreducible oxides, such as SiO₂ [40]–[47] and Al₂O₃ [26], [31], [47]–[55], while a reducible oxide such as TiO₂ is also of practical interest [29], [36], [47], [56]–[61]. Whilst these support materials have the benefit of anchoring the cobalt more strongly than for instance carbon, this stronger interaction can also lead to the formation of metal-support compounds (MSC) under FTS conditions [62]–[66].

In this work, we investigate the effect of titania as a support material for cobalt nanoparticles under humid FTS conditions that simulate high CO conversion. We vary the surface area of titania and study the impact of platinum as a reduction promoter for the optimum titania to counter possible oxidation during humid FTS operation. The chemical state and structure of cobalt is investigated under conditions close to those encountered in industrial practice using *in situ* Mössbauer emission spectroscopy (MES) [67]. We expand on a previous ⁵⁷Co MES study in which we showed how steam can lead to oxidation and sintering of cobalt nanoparticles on P25 titania [34]. The MES measurements are supplemented by XRD, *quasi in situ* XPS, TEM and STEM-EDX. The catalytic performance was measured during MES and, separately, in a fixed-bed microflow reactor.

5.2. Experimental methods

5.2.1 Catalyst preparation

Supported cobalt catalysts were prepared by incipient wetness impregnation of P25 titania (Evonik Degussa, pore volume 0.3 mL/g, BET surface area 50 m²/g, Anatase/Rutile 85:15), P90 titania (Evonik Degussa, BET surface area 94 m²/g), and GP350 titania (Cristal ActivTM, Millennium Chemicals, BET surface area 283 m²/g, phase-pure anatase) followed by drying in air at 120 °C for 6 hours. The impregnation solutions were obtained by dissolving the appropriate amount of Co(NO₃)₂·6H₂O (≥98.0%, Sigma Aldrich) in dehydrated ethanol and, when required, an appropriate amount of Pt(NH₃)₄(NO₃)₂ (≥99.995%, Sigma Aldrich). A total of four catalysts were prepared with a cobalt loading of 4 wt%. One catalyst was promoted with platinum at an atomic cobalt/platinum ratio of 200. The resulting samples are denoted by CoPt/S and Co/S for the promoted and unpromoted catalysts respectively, where S stands for the support being P25, P90 or GP350. For Mössbauer emissions spectroscopy measurements, a portion of the dried catalysts was spiked with radioactive ⁵⁷Co by pore volume impregnation using a solution containing 90 MBq ⁵⁷Co in 0.1 M HNO₃. These radioactive samples were dried at 120 °C for 12 hours.

5.2.2 Characterization

X-ray diffraction

X-ray diffraction (XRD) patterns were recorded on a Bruker D2 Phaser using a Cu K α radiation source and a 2 mm slit. Data was collected using a time per step of 0.15 min and a step size of 0.1° in the 2 θ range of 10–60°. Background subtractions were applied, and reference spectra were obtained using the Diffrac.Eva software by Bruker.

Electron microscopy

Surface averaged particle sizes and particle size distributions were determined using transmission electron microscopy (TEM). TEM measurements were performed on a FEI Tecnai 20 electron microscope operated at an electron acceleration voltage of 200 kV with a LaB6 filament. Typically, a small amount of the sample was ground and suspended in pure ethanol, sonicated, and dispersed over a Cu grid with a holey carbon film.

The nanoscale distribution of elements in the samples was studied using scanning transmission electron microscopy–energy-dispersive X-ray spectroscopy (STEM-EDX). Measurements were carried out on a FEI cubed Cs-corrected Titan operating at 300 kV. Samples were crushed, sonicated

in ethanol, and dispersed on a holey Cu support grid. Elemental analysis was done with an Oxford Instruments EDX detector X-MaxN 100TLE.

***Quasi in situ* X-ray photoelectron spectroscopy (XPS)**

The oxidation state of cobalt was studied by *quasi in situ* XPS using a Kratos AXIS Ultra 600 spectrometer equipped with a monochromatic Al K α X-ray source (Al K α 1486.6 eV). Survey and region scans were recorded at pass energies of respectively 160 eV and 40 eV. The step size was 0.1 eV and the background pressure during the measurements was kept below 10^{-9} mbar.

A high-temperature reaction cell (Kratos, WX-530) was used to pre-treat the sample mounted on an alumina stub before XPS analysis. This setup allows *in vacuo* sample transfer of a pre-treated sample into the analysis chamber. Reduction was performed in a pure H₂ flow at atmospheric pressure and temperatures between 340 and 650 °C. After reduction, the reaction cell was evacuated to a pressure below 10^{-9} mbar. Then, the sample was cooled to 150 °C and transferred to the analysis chamber. Data analysis was done with the CasaXPS software (version 2.3.22PR1.0). The binding energy scale was corrected for surface charging by setting the Ti 2p_{3/2} peak of TiO₂ at a binding energy of 458.5 eV.

***In situ* Mössbauer emission spectroscopy**

Mössbauer emission spectroscopy (MES) was carried out at various temperatures using a constant acceleration spectrometer set up in a triangular mode with a moving single-line K₄Fe(CN)₆·3H₂O absorber enriched in ⁵⁷Fe. The velocity scale was calibrated with a ⁵⁷Co:Rh source and a sodium nitroprusside absorber. Zero velocity corresponds to the peak position of the K₄Fe(CN)₆·3H₂O absorber measured with the ⁵⁷Co:Rh source, positive velocities correspond to the absorber moving towards the source. Measurements under Fischer-Tropsch conditions were carried out in a high-pressure MES cell [67], which is described in detail in literature [28].

Mössbauer spectra were fitted using the MossWinn 4.0 program [68]. The spectra of very small metallic superparamagnetic species were fitted using the two-state magnetic relaxation model of Blume and Tjon, which assumes the presence of a fluctuating magnetic field which jumps between the values of +H and -H along the z-axis with an average frequency τ [69]. Here, H typically equals 500 kOe and τ can vary between 10^{-9} and 10^{-12} s⁻¹. The Mössbauer spectra of larger metallic particles were fitted using a hyperfine sextuplet, resulting from the local magnetic field experienced by bulk metallic particles. Oxidic contributions are fitted using doublets, with a quadrupole splitting following

their non-spherical charge distribution. The experimental uncertainties in the calculated Mössbauer parameters, estimated using Monte Carlo iterations by the MossWinn 4.0 program and including experimental uncertainties were as follows: IS and QS $\pm 0.01 \text{ mm s}^{-1}$ for the isomer shift and quadrupole splitting, respectively; $\pm 3\%$ for the spectral contribution; $\pm 3 \text{ kOe}$ for the hyperfine field.

Typically, 300 mg of ^{57}Co -spiked and 100 mg of non-radioactive catalyst (sieve fraction 250-500 μm) was loaded into two separate compartments of the reactor cell. FTS experiments were performed *in situ* following reduction between 340 $^{\circ}\text{C}$ and 400 $^{\circ}\text{C}$ for 2 hours in a 100 mL/min flow of pure H_2 . Reactions were done at 200 $^{\circ}\text{C}$ and 20 bar, while the H_2/CO was kept at 4 throughout and steam was fed to vary the relative humidity. Water was evaporated and mixed with the incoming feed gas using a Bronkhorst controlled evaporator mixer (CEM). The relative humidity reported is based on the steam fed in this way, excluding steam generated by the Fischer-Tropsch reaction. Wax products were collected in a downstream hot catch pot, and water was retrieved in a subsequent cold catch pot. An online Trace GC Ultra from Thermo Fisher Scientific equipped with a RT-Silica bond column and a flame ionization detector as well as a Stabilwax column and a thermal conductivity detector was used to analyze the gaseous products.

5.2.3 Catalytic activity measurements

The catalytic performance was determined in a single-pass flow reactor system (Microactivity Reference unit, PID Eng&Tech) operated at a temperature of 220 $^{\circ}\text{C}$ or 240 $^{\circ}\text{C}$, a total pressure of 20 bar and a H_2/CO ratio of 4. In a typical experiment, 50 mg of catalyst (sieve fraction 125-250 μm) mixed with SiC particles of the same sieve fraction to a total volume of 3 mL was placed in a tubular reactor with an internal diameter of 9 mm. The temperature was controlled via a thermocouple, located in the center of the catalytic bed. Reduction was first performed in a flow of H_2 at 340 $^{\circ}\text{C}$ for 2 hours after heating at a rate of 5 $^{\circ}\text{C}/\text{min}$. Subsequently, the reactor was cooled to 220 $^{\circ}\text{C}$ and the gas feed composition was changed to reaction conditions. A constant space velocity (SV) of 60 $\text{L g}_{\text{cat}}^{-1} \text{ h}^{-1}$, was applied for all catalysts, which resulted in a CO conversion between 1 and 5%. A TRACE1300 GC instrument from ThermoFischer Scientific equipped with a RT-Silica bond column and a flame ionization detector as well as a Porabond-Q column and a thermal conductivity detector was used to measure the gas composition of the reactor effluent. Based on the Weisz–Prater criterion, internal mass transfer limitations could be excluded. At the applied reaction conditions, no CO_2 was observed and the selectivity toward oxygenates on a molar carbon basis was less than 1%. Liquid products and waxes were collected in a cold trap placed after the reactor. Ar (9 vol% in CO) was used as an internal

standard in the CO/H₂ feed mixture. The CO conversion (X_{CO}) was determined in the following manner:

$$X_{CO} = 1 - \frac{F_{Ar,in}F_{CO,out}}{F_{CO,in}F_{Ar,out}} \quad (1)$$

where $F_{Ar,in}$ is the volumetric Ar flow in the reactor feed, $F_{CO,in}$ is the volumetric CO flow in the reactor feed, $F_{Ar,out}$ and $F_{CO,out}$ are the respective volumetric flows of Ar and CO out of the reactor system.

The carbon-based selectivity of hydrocarbon compound C_i (S_{Ci}) was calculated using:

$$S_{Ci} = \frac{F_{Ar,in}F_{Ci}v_i}{F_{Ar,out}F_{CO,in}X_{CO}} \quad (2)$$

where F_{Ci} is the volumetric flow of hydrocarbon compound C_i out of the reactor, and v_i is the stoichiometric factor of the hydrocarbon compound.

The cobalt time-yield (CTY) was determined using the following equation:

$$CTY = \frac{F_{CO,in}X_{CO}}{m_{Co}} \quad (3)$$

where m_{Co} is the weight of cobalt used in the catalytic reaction.

5.3. Results and Discussion

5.3.1 Characterization of titania supported catalysts

A set of three Co/TiO₂ catalysts without Pt reduction promoter was prepared by incipient wetness impregnation at a cobalt loading of 4 wt.% using different titania supports covering surface areas in the range of 50 – 283 m²/g. The X-ray diffractograms of the calcined precursors are given in Figure D8. The samples show only diffraction lines due to anatase and rutile TiO₂, which is expected for catalysts based on P25 [70] and P90 [71] TiO₂. The catalyst based on GP350 only contains anatase according to XRD analysis as per specifications. The absence of diffraction lines due to cobalt oxide points to the high dispersion of the cobalt oxide precursor.

Table 1. Average metal oxide particle size, Co/Ti ratio, and reducibility of Co(Pt)/TiO₂ catalysts.

Catalyst	Co/Ti (calcined) ^a	Reduction temperature (°C)	Co/Ti (reduced) ^a	DOR(%) ^b	Cobalt particle size (nm) ^c
Co/P25	0.163	340	0.041	43	13.4 ± 6.6
Co/P90	0.062	340	0.029	28	8.0 ± 3.4
		500	0.007	92	
		650	0.032	100	
CoPt/P90	0.027	340	0.019	79	
Co/GP350	0.034	340	0.024	3	4.6 ± 2.6
		450	0.063	4	

^a Atomic Co/Ti ratio determined by XPS, ^b Degree of reduction determined by XPS. ^c Determined by TEM analysis of reduced and passivated samples.

Figure 1 shows representative TEM images of the catalysts after reduction at 340 °C for 2 hours in pure H₂ and subsequent passivation at room temperature in a flow of 5% O₂ in He. The images show the clear difference between the structure of the more conventional P25 and P90 supports and the GP350 support. The GP350 support is obtained by hydrolysis of titanium oxychloride [72], resulting in anatase particles smaller than 10 nm, which agglomerate to form flower-like clusters as can be seen in the TEM images. This high-surface-area titania is thus prepared in a different way than the flame synthesized P25 and P90 supports that are produced from a sulfate source, and this means that the

GP350 support should be free of sulfur, which is a known FTS poison. The average size and size distribution of the cobalt nanoparticles was determined by analyzing approximately 150 particles in ca. 8 images per sample. On average, the cobalt particle size decreases from 13.4 nm for Co/P25 to 8.0 nm for Co/P90 and 4.6 nm for Co/GP350, indicating that smaller cobalt particles are obtained with increasing surface area of the titania support. The TEM images show that the cobalt phase is well dispersed over the surface without any large agglomerates of cobalt. The contrast differences between the various catalysts may suggest a lower cobalt reduction degree of especially the sample based on the high-surface-area titania support (Co/GP350) as compared to Co/P25.

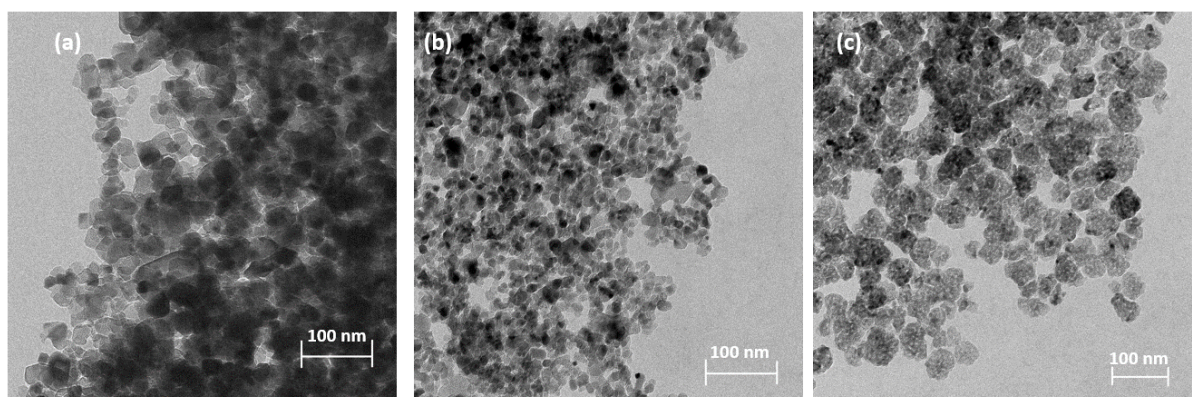


Figure 1. Representative TEM images of (a) Co/P25, (b) Co/P90, and (c) Co/GP350 following reduction at 340 °C for 2 hours and passivation in 5% O₂ in He at room temperature.

The surface of the catalysts was characterized using *quasi in situ* XPS. Survey scans revealed no contributions from unexpected elements on any of the measured samples, as such the presence of alkali metals and sulfur on the catalyst surface were excluded. The Co 2p_{3/2} spectra of the calcined catalysts and the catalysts reduced at 340 °C catalysts are given in Figure 2. Fitting was done using the model of Biesinger et al. [73]. Additional spectra obtained at higher reduction temperatures can be found in Figure D6. The atomic ratio of cobalt to titanium (Co/Ti ratio) of the oxidic precursors decreases as expected with the increasing surface area of the titania support and is consistent with the expected decrease by a factor of two for P90 compared to P25, and by a factor of five for GP350. During reduction, the differences in the Co/Ti ratios become much smaller, suggesting agglomeration of the cobalt phase during the reduction of cobalt oxide to metallic cobalt [36], [74]. Titania overlayer formation can also explain this, which has previously been observed under reducing conditions [29]. The decrease in the Co/Ti ratio is most pronounced for Co/P25 and least for Co/GP350. The contribution of metallic cobalt as determined by fitting of the Co 2p_{3/2} spectra was used to calculate

the degree of reduction (DOR). The DOR of Co/P25 amounts to 43% after reduction at 340 °C. While the DOR for Co/P90 is significantly lower at 28%, only a very small amount of cobalt is reduced in Co/GP350 according to XPS. These findings clearly demonstrate that the cobalt oxide reducibility is significantly more difficult when the cobalt-titania interactions become stronger due to the higher surface area of the titania support [47]. We speculate that the reduction of cobalt oxide will lead to significantly larger metallic cobalt particles due to sintering as observed for Co/P25. The much smaller particles observed in Co/GP350 after reduction at 340 °C are likely cobalt oxide particles, as suggested by the very low DOR of 3% according to XPS. We also reduced the Co/P90 and Co/GP350 catalysts at higher temperatures. The XPS spectra of these samples are given in Figure D6 and the analysis results in Table 1. When Co/P90 is reduced at 500 and 650 °C, (nearly) full cobalt reduction was obtained. Reduction at 500 °C already showed a strong decrease in the Co/Ti ratio, indicative of a decreasing dispersion of cobalt, or alternative the formation of metal-support compounds (CoTiO_x). Moreover, in the Ti $2p_{3/2}$ spectra, shown in Figure D9, contributions corresponding to Ti^{3+} [75] are evident, besides the main features of Ti^{4+} [76]. This is likely the result of the partial reduction of the surface of TiO_2 to Ti^{3+} at the high reduction temperatures. Interestingly, the Co/Ti ratio increased again upon reduction at 650 °C and the Ti XPS spectrum does not show a contribution of Ti^{3+} anymore. Phase transformation of titania is enabled by vacancies in the titania lattice and oxygen defects and takes place around 600 °C. Transformation of the smaller anatase particles into bigger rutile crystals results in a loss of titania surface area. The increase of the atomic Co/Ti ratio suggests that cobalt sintering proceeded slower than support collapse. Reduction of Co/GP350 at 450 °C did not improve the DOR, although the Co/Ti ratio was also significantly higher. This could imply some segregation of Ti species from Co, as for instance may occur during reduction of Co_3O_4 to CoO . Alternatively, it could well be that similar to the case of Co/P90 reduction, loss of titania surface area has taken place. Formation of the rutile phase is not expected at 450 °C, although sintering of the very small anatase crystals to bigger crystals would also result in the loss of support surface area.

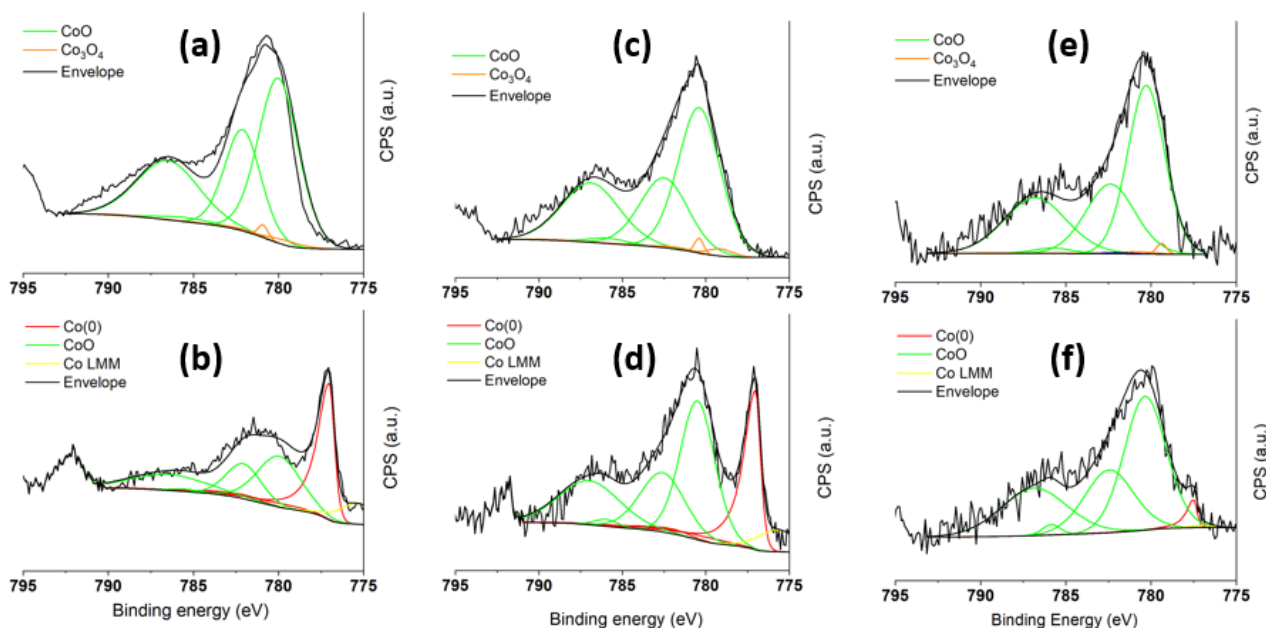


Figure 2. Co $2p_{3/2}$ XPS spectra of Co/P25 (a,b), Co/P90 (c,d), and Co/GP350 (e,f) after (a,c,e) calcination and (b,d,f) subsequent reduction at 340 °C (black: experimental data and the fitted envelope; red: the fitted metallic Co(0) contributions; green: the fitted CoO contributions; orange: fitted Co_3O_4 contributions; yellow: the Co auger LMM peak).

5.3.2 *In situ* Mössbauer spectroscopy of reduced catalysts

Mössbauer spectra of the catalysts after reduction at 340 °C for 2 hours are given in Figure 3a. The Mössbauer fit parameters of the reduced catalysts are listed in Tables D2-D4. The sextuplet with an isomer shift (I.S.) of -0.1 mm s^{-1} and a hyperfine field (H.F.) of $\sim 323 \text{ kOe}$ observed for all catalyst samples is due to metallic cobalt. This contribution comes from magnetically ordered metallic cobalt particles, which is common for cobalt particles larger than 6 nm [27]. The absence of a singlet indicates that these samples do not contain superparamagnetic cobalt, meaning that all metallic cobalt particles are larger than 6 nm. This implies that a significant part of the small cobalt particles seen by TEM are oxidic in nature, which is consistent with the substantial contribution of a dispersed Co^{2+} -oxide phase in the MES spectra as represented by a doublet with an I.S. of 1.0 mm s^{-1} and a quadrupole splitting (Q.S.) of 2.0 mm s^{-1} [77]. The contribution of cobalt oxide is significantly higher for Co/P90 and Co/GP350 than for Co/P25. The latter sample shows a nearly complete reduction of cobalt, while the reduction degree in the other two samples is about half. The DOR values according to MES after reduction at 340 °C are significantly higher than those according to XPS analysis. A tentative explanation for this discrepancy can be found in the size of the metallic and oxidic cobalt particles. As observed for Co/P25 and for other typical Co on titania catalysts [36], [74], substantial sintering

of cobalt takes place during the reduction to the metallic phase. For instance, the metallic cobalt particles in reduced Co/P25 are significantly larger than 10 nm. Given that the inelastic mean free path of cobalt 2p electrons is in the range of 1-2 nm in the XPS experiment, only a small fraction of the cobalt atoms in metallic cobalt particles are probed. As the cobalt oxide particles are much smaller due to the strong interactions with titania, it is likely that a larger fraction of the cobalt oxide phase is probed by XPS. In principle, Mössbauer spectroscopy probes all Co nuclei, being more representative for the overall reduction degree of cobalt. This line of reasoning can explain the discrepancies in the DOR noted here between MES and XPS. While XPS shows a DOR for Co/P25 of 43%, the DOR according to MES is 95%. The DOR according to XPS and MES for Co/P90 are respectively 28% and 40%. The largest difference in DOR as probed by XPS and MES is for Co/GP350 with respective values of 3% and 54%. This could imply the presence of a few very large metallic cobalt particles, which is not clearly supported by the MES hyperfine field nor the TEM analysis. A possible alternative explanation might be that the metallic cobalt phase is partially covered by titanium, decreasing effectively the XPS signal. The formation of such titania layers on cobalt has been reported for P25 titania [29], [58]. Recent work showed the formation of TiO_x bilayers on Ni particles in Ni/TiO₂ during reduction at 400 °C [78]. Such effects may be expected to be even stronger for the Co/GP350 catalyst, given its much higher surface area. Moreover, Wolf et al. reported that cobalt tends to form more metal-support compounds with phase-pure anatase [66]. As cobalt was not fully reduced for Co/P90 and Co/GP350 in the first step, additional reduction treatments were applied. First, the reduction time was extended by 2 hours at 340 °C, which only marginally improved the DOR for both catalysts, i.e., from 40% to 49% for Co/P90 and from 54% to 59% on the GP350 support. Afterwards, an additional 2-hour reduction at 400 °C for GP350 further increased the DOR to 84%. Despite these differences, the spectral parameters of the metallic cobalt phase following their final reduction are the same for all samples, indicating that the metallic cobalt particles are not too different in size.

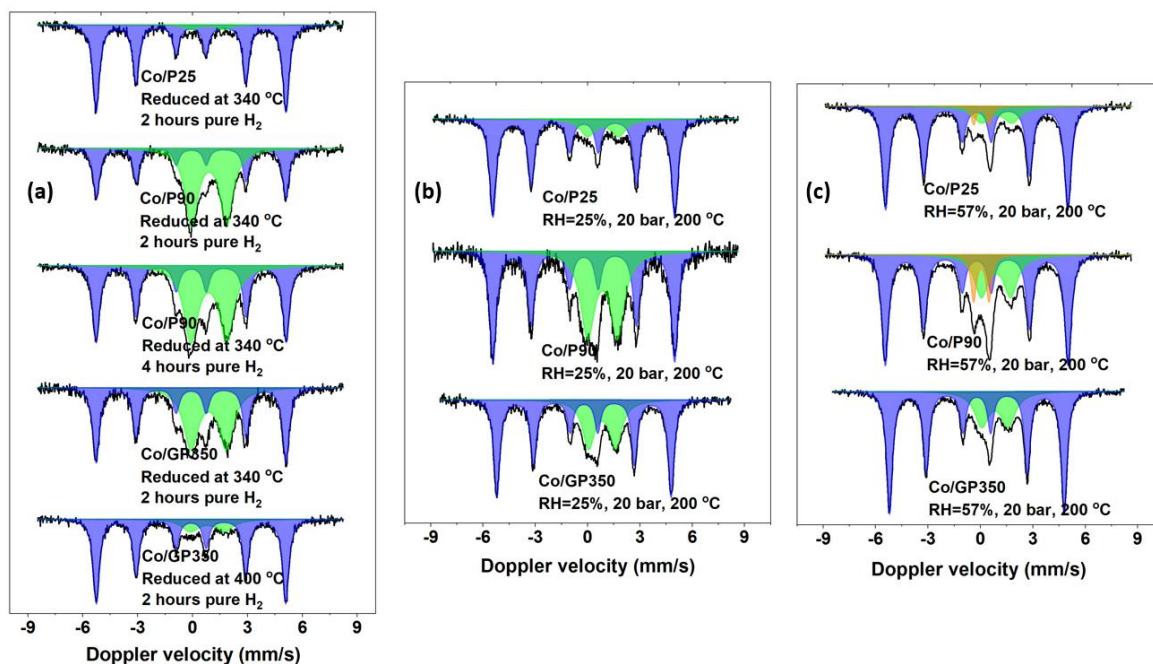


Figure 3. *In situ* Mössbauer spectra of the Co/TiO₂ catalysts (a) following reduction, and under FTS conditions at a relative humidity of (b) 25%, and (c) 57%. The black lines represent the experimental spectra, the blue ones the fitted bulk metallic cobalt sextuplet, and the orange and green ones the fitted oxidic cobalt doublets.

5.3.3 *In situ* Mössbauer emission spectroscopy during the FTS reaction

In situ Mössbauer emission spectra were recorded as a function of the steam partial pressure at a temperature of 200 °C, a total pressure of 20 bar, and a H₂/CO ratio of 4. The steam content in the feed is expressed as the relative humidity (RH) at the applied conditions. Table D1 details the feed compositions for the different RH measurements. Spectra were recorded for at least 48 h at each humidity step, except for RHs of 25% and 57% where the steam treatment was prolonged to 5 days and 11 days, respectively. This was done to understand the influence of prolonged exposure as encountered in industrial practice. Under dry FTS conditions (RH = 0%) measured at 200 °C, the metallic cobalt contribution of Co/P25 remained the same as after initial reduction. In contrast, the metallic contribution for Co/P90 increased from 49% after reduction to 64% during dry FTS conditions, as can be seen in Table 2. This increase of metallic cobalt at 200 °C can be caused by two effects, it is partially the result of a difference in Debye temperature of the metallic and oxidic cobalt phases [79], but it is also due to improved reducibility under the mildly reducing FTS conditions. This is evident from the measurement performed at room temperature following the dry FTS conditions given in Table D3, which showed an increase to 58% metallic cobalt compared to 49% for

the freshly reduced catalyst. The conversion of the Co/GP350 catalyst was very low under dry FTS conditions. An extra reduction at 400 °C resulted in a metallic cobalt contribution of 84% when measured at room temperature and 81% when measured at 200 °C.

Table 2. Contribution of the different cobalt phases as determined from MES spectra recorded at 200 °C under varying FTS conditions.

Treatment	H_2O/H_2	Spectral contribution cobalt (%)					
		Co/P25		Co/P90		Co/GP350	
		Co^0	Co-oxide	Co(0)	Co-oxide	Co(0)	Co-oxide
Reduced ^a	0	95	5	49	51	84	-
RH 0%	0	95	5	64	36	81	19
RH 7.5%	0.25	87	13	60	40	73	27
RH 14%	0.50	86	14	58	42	66	24
RH 20%	0.75	86	14	57	43	66	24
RH 25%	1.0	84	16	56	44	67	23
Reduced ^a	0	95	5	79	21	76	24
RH 0%	0	91	9	74	26	78	22
RH 57%	1.0	80	15 / 5	65	24 / 11	75	25

^aReduced spectra were recorded at room temperature.

Following dry FTS conditions, the humidity was increased during the MES measurements. The evolution of the metallic cobalt contribution is given in Table 2. Figure 3b shows the MES spectra for the catalyst at RH = 25%, demonstrating a gradual shift from bulk metallic cobalt to oxidic cobalt for all three samples. The spectra at RH = 25% can be fitted with a bulk metallic cobalt contribution (I.S. = -0.2 mm s^{-1} , H.F. in the 308 - 310 kOe) and an oxidic cobalt contribution (I.S. = 0.8 mm s^{-1} , Q.S. = $1.6\text{-}1.7 \text{ m s}^{-1}$). The latter spectral features of the oxidic feature represent well-dispersed Co^{2+} species, which are similar to the oxidic phase remaining in the initially reduced catalysts. Despite this, the Co/P90 sample contains significantly more oxidic cobalt than the other catalysts at RH = 25%. On the other hand, the oxidic cobalt contribution was already the highest among the three catalysts after reduction and operation under dry conditions (RH = 0%). Comparing the oxidic contributions between dry FTS and RH = 25% conditions, we can observe that operating at RH = 25% leads to more extensive oxidization of metallic cobalt in the order of Co/GP350 (from 81 to 67%) > Co/P25

(from 95 to 84%) > Co/P90 (from 64 to 56%). After treatment at RH = 25%, the catalysts were reduced again at 340 °C for 2 hours. The resulting spectral parameters in Tables D2-D4 show an increase in the DOR for Co/P90 and Co/GP350 compared to the DOR after the reduction. As smaller cobalt oxide particles are typically more difficult to reduce than larger ones [47], this can be taken as an indication that the catalyst exhibit a lower dispersion after the oxidation-reduction treatment. This effect is more pronounced for the Co/P90 catalyst, for which the DOR amounted to 79% after the second reduction step in comparison to 40% after the initial one. After this intermittent reduction step, the samples were exposed to the highest humidity of RH = 57%. This led to a new oxidic cobalt contribution for the Co/P25 and Co/P90 catalysts (Figure 3c). The spectral parameters of this phase ($IS = 0.0-0.1 \text{ mm s}^{-1}$, $QS = 0.8-0.9 \text{ mm s}^{-1}$) correspond to those of Co^{3+} , which is a signature of agglomerated Co^{2+} as explained in our previous work [36]. As such, the appearance of this contribution in Co/P25 and Co/P90 indicates significant sintering of cobalt in the oxide form. This less dispersed cobalt oxide phase is not observed in Co/GP350 treated at RH = 57%, despite the already large contribution of this phase. This might be the result of the high surface area of this support or a role of the anatase surface. The mobility of oxidic cobalt at high RH observed here for Co/P25 and Co/P90 is consistent with the mobility observed for oxidic cobalt on P25 support [36]. Compared to the catalyst following the RH = 25% conditions, the total amount of oxide following the highest humidity is lower for the Co/P90 and Co/GP350 catalysts, as seen in Table 2, this is likely the result of the increased DOR obtained after the intermittent reduction treatment, but alternatively sintering of cobalt oxide to larger metallic particles as reported by Claeys' group [34] can also explain this finding. The latter is supported by the observation that the H.F. increased for both the P90 (308 to 310 kOe) and GP350 (310 to 311 kOe) catalysts at RH = 57% compared to RH = 25% conditions.

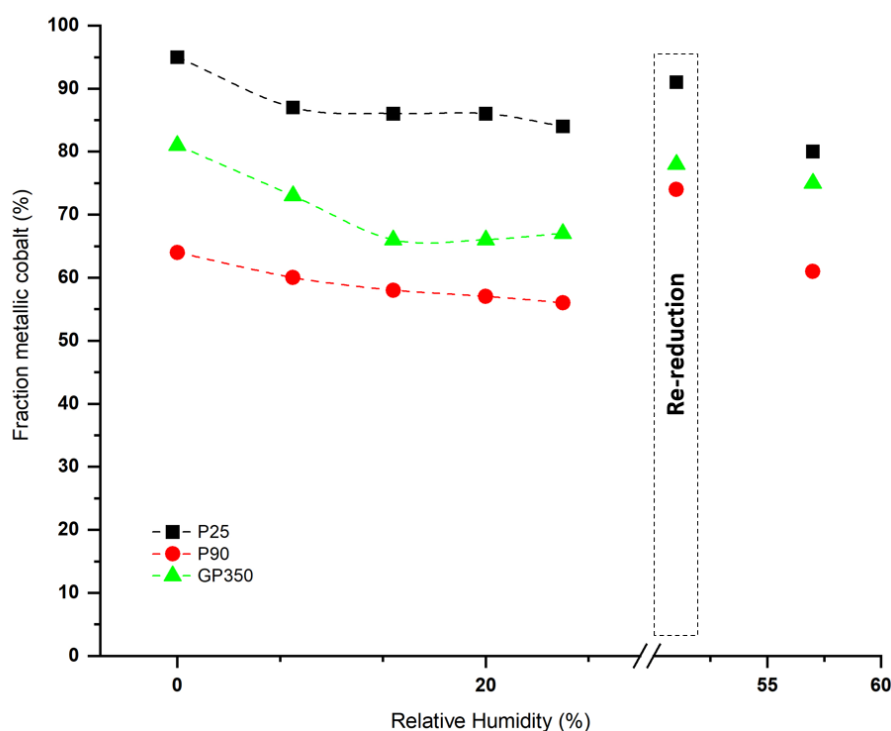


Figure 4. Fraction of metallic cobalt in Co/TiO₂ catalysts under humid Fischer-Tropsch conditions (200 °C, 20 bar, H₂/CO = 4) as determined by Mössbauer spectroscopy at 200 °C as a function of the relative humidity. The axis break points to the reduction treatment carried out after the RH = 25% treatment and before the RH = 57% treatment (reduction in H₂, at 340 °C for 2 hours). The data inside the dashed box pertain to the catalyst directly after reduction at 200 °C.

Figure 4 shows the relative amount of metallic cobalt in the three titania-supported cobalt catalysts under the increasing humid conditions. The trend for the three catalysts is qualitatively similar with a gradual decrease during the first steps and a small increase at the highest humidity conditions, which is due to the reduction step after RH = 25%. This clearly shows that the increased oxidation observed does not correlate with the titania surface area. Compared to Co/P25, Co/P90 and Co/GP350 with a higher surface area exhibit a lower cobalt reducibility, which results in a higher contribution of oxidic cobalt throughout the prolonged FTS testing as a function of the humidity. Whilst the P90 support showed the highest initial contribution of cobalt oxide, this contribution did not increase as strong as for the other two catalysts. The DOR upon initial reduction was highest for Co/P25 and this catalyst was most prone to cobalt oxidation under simulated high conversion conditions. All three titania-supported cobalt catalysts show significant oxidation of cobalt (10-15%) when operating at increased steam pressure. A re-reduction is capable to restore the degree of reduction. The observation that oxidation does take place during conditions that can be reached during industrial FTS requires the

design of catalysts that are capable to endure such conditions. Below, we will show results of platinum addition to improve stability, but first we will discuss used catalyst characterization.

5.3.4 Used catalyst characterization

The MES data were complemented by STEM-EDX measurements of reduced-passivated and used Co/P90 for comparison with STEM-EDX images of Co/P25 presented in our previous work [36]. The term ‘used catalysts’ refers to the non-radioactive catalyst samples obtained from the Mössbauer cell under the same humid FTS treatments as the Mössbauer samples. As such, these measurements provide *ex situ* information about the state of the catalyst following the deactivation studies. For each sample, eight EDX maps were obtained on different areas of the sample. Two representative maps of the reduced and passivated Co/P90 are shown in Figure 5a-b. These images show well-dispersed cobalt over the titania support, with a few larger cobalt particles around 8-12 nm.

Representative maps of the used Co/P90 catalyst following high humidity FTS are given in Figure 5c-d. Contrary to EDX mappings performed on the P25 sample, no significant sintering is observed for this catalyst. The cobalt remains well dispersed over the titania and only a few larger cobalt particles can be seen with sizes of approximately 8-12 nm, similar to the reduced and passivated sample. This suggests that cobalt is far less mobile on this support compared to Co/P25, which can be linked to the higher surface area of P90 titania. So, although this stronger interaction with the support decreases the DOR as observed before, it also results in less sintering during FTS operation under practical high CO conversion conditions.

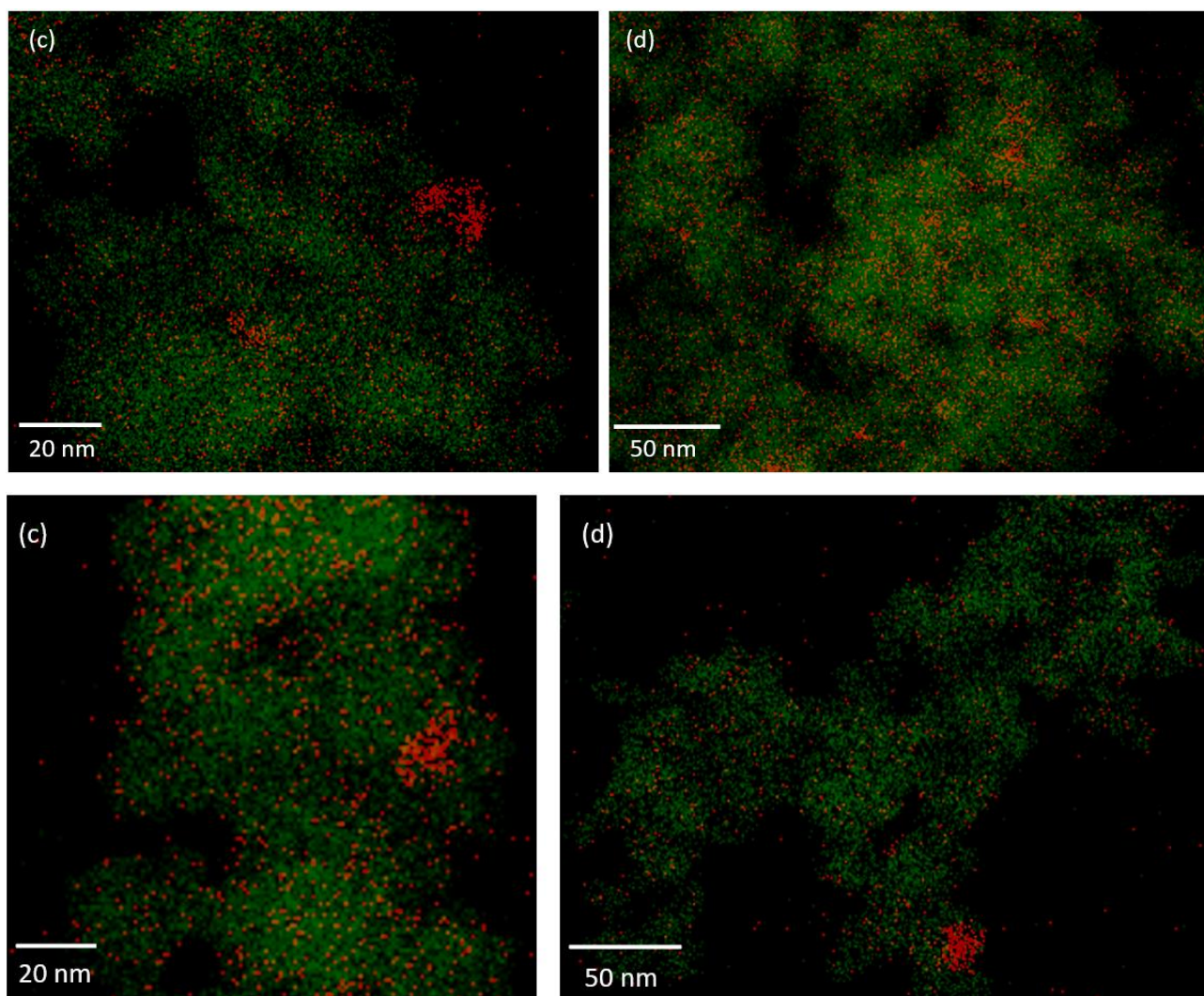


Figure 5. EDX mappings of (a-b) a reduced and passivated Co/P90 catalyst and (c-d) a used Co/P90 catalyst: the cobalt mapping is shown in red and the titania mapping in dark green.

5.3.5 Platinum promotion

To improve cobalt reducibility on the P90 support we studied the addition of platinum as a reduction promoter. To this end, an identical catalyst on the P90 titania support was prepared with the only difference that platinum was added to the impregnation solution. The X-ray diffractogram of the calcined precursor is given in Figure D8 together with that of the non-promoted catalyst. Both diffractograms only shows diffraction lines belonging to anatase and rutile as expected for the P90 support without indications of other cobalt or platinum phases, indicative of their high dispersion.

Quasi in situ XPS spectra of the Co 2p_{3/2} region of calcined and reduced CoPt/P90 catalyst are given in Figure 6. The Co/Ti ratios for the calcined and reduced catalysts as well as their DOR are given in

Table 1. Compared to the platinum-free counterpart (Figure 2), the feature due to metallic cobalt is much more pronounced, indicative of a higher DOR. This is expected, as platinum is known to act as a reduction promoter [57], [80]. After reduction at 340 °C for 2 hours, the DOR for CoPt/P90 according to XPS is 79%, substantially higher than the DOR of 28% for Co/P90 after the same reduction treatment. The Co/Ti ratio for the calcined precursor is significantly smaller in the presence of platinum, which may hint at a lower dispersion of the cobalt oxide phase upon calcination. Furthermore, the Co/Ti ratio of the CoPt/P90 catalyst following a reduction at 340 °C is smaller (0.019) to that found on the Co/P90 catalyst (0.029) following the same treatment. However, the platinum-promoted catalyst shows significantly higher contribution of metallic cobalt at the surface, which introduces complexity when comparing the results, since it has been found in the past that oxidic cobalt typically loses much of its cobalt dispersion upon reduction on the titania support [36], [74]. When looking at the Co/P90 catalyst following a reduction at 500 °C, a DOR is found that is much comparable to the one obtained on the CoPt/P90 system after reduction at 340 °C. Comparing the Co/Ti ratios between these two measurements paints a very different picture, as a ratio of only 0.007 is found on the Co/P90 catalyst after this treatment, implying a positive effect on the metallic cobalt dispersion due to the platinum promoter.

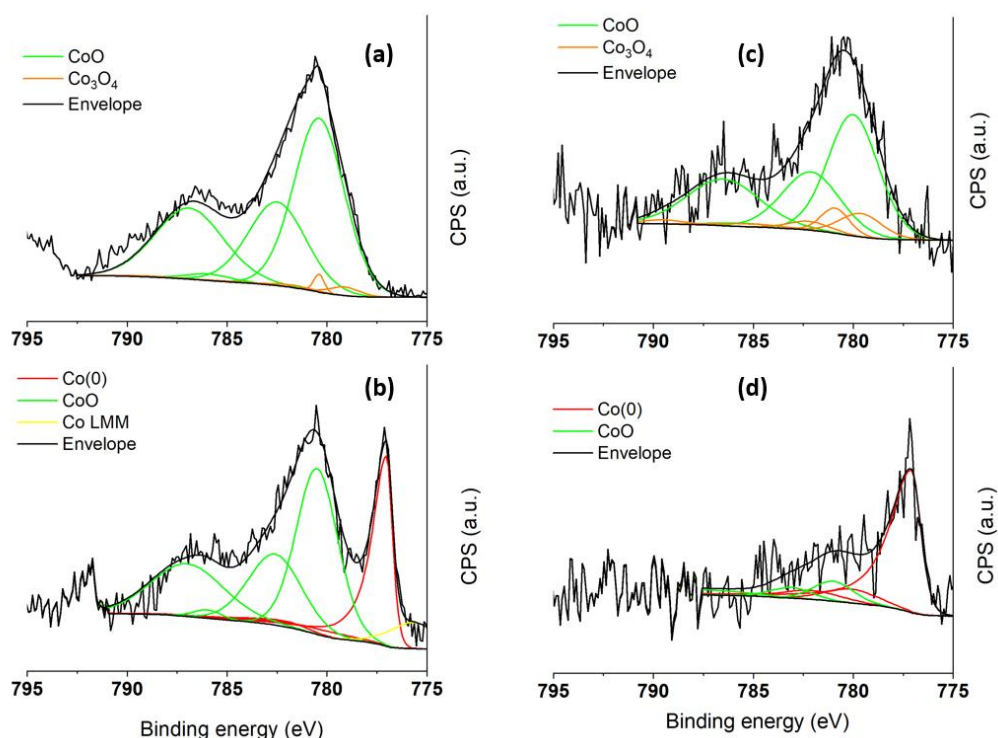


Figure 6. Co 2p_{3/2} XPS spectra of Co/P90 (a,b) and CoPt/P90 (c,d), after (a,c) calcination and (b,d) subsequent reduction at 340 °C (black: experimental data and the fitted envelope; red: the fitted metallic Co(0) contributions; green: the fitted CoO contributions; orange: fitted Co₃O₄ contributions; yellow: the Co auger LMM peak; the XPS fit model was taken from Ref. [73]).

5.3.6 *In situ* Mössbauer spectroscopy of reduced catalysts

The Mössbauer spectrum of the promoted catalyst after reduction at 340 °C for 2 hours is given in Figure 7a along with the reduced spectra of the non-promoted Co/P90 catalyst. The Mössbauer fit parameters of the reduced catalyst are listed in Table D5. The reduced promoted catalyst shows a sextuplet with an I.S. of -0.1 mm s^{-1} and a H.F. of 317 kOe, which points to magnetically ordered metallic cobalt with a size larger than 6 nm [27]. The absence of a singlet contribution shows that these large particles are the predominant metallic cobalt phase. The H.F. of the metallic particles for the platinum-promoted sample is smaller than that of the corresponding sample without platinum. This difference points to a higher dispersion of these particles in the platinum-promoted catalyst, which was also observed through XPS analysis. Next to the metallic phase, an oxidic contribution is observed with I.S. = 1.0 mm s^{-1} and Q.S. = 1.9 mm s^{-1} , which represents dispersed Co²⁺-oxide, and indicates non-complete reduction. However, the DOR observed through Mössbauer for CoPt/P90 is

71%, which is significantly higher than without platinum (49%). This is in good agreement with the XPS analysis and highlights the beneficial effect of the reduction promoter.

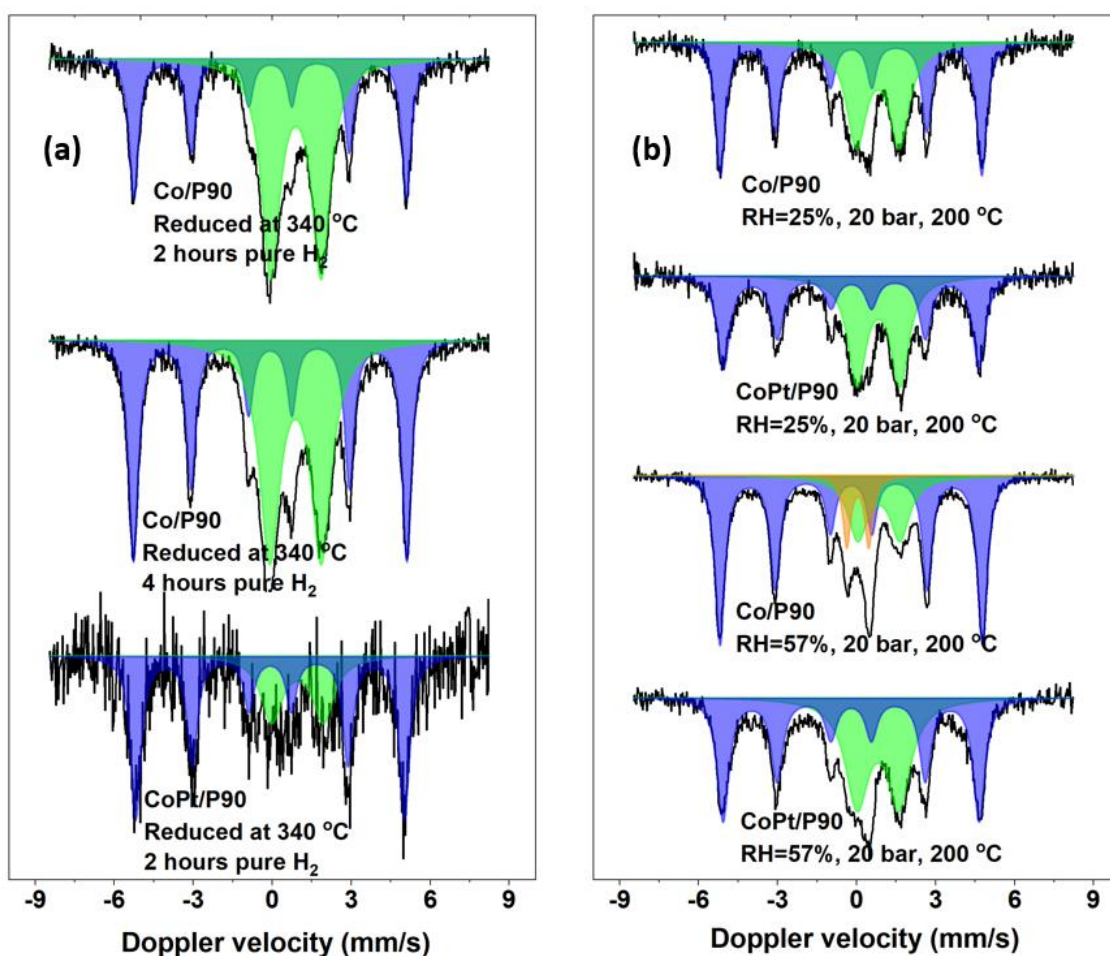


Figure 7. *In situ* Mössbauer spectra of the Co(Pt)/P90 catalysts (a) following reduction, and under FTS conditions at a relative humidity of (b) 25% and 57%. The black lines represent the experimental spectra, the blue ones the fitted bulk metallic cobalt sextuplet, and the orange and green ones the fitted oxidic cobalt doublets.

5.3.7 *In situ* Mössbauer emission spectroscopy during the FTS reaction

In situ Mössbauer spectra were measured during FTS measurements for the platinum-promoted sample, according to the conditions given in Table D1. The platinum-promoted catalyst shows the same Mössbauer features as the non-promoted counterpart when changing from dry to RH = 25% conditions, as shown in Figure 7b. A sextuplet is observed corresponding to bulk magnetically ordered cobalt with an I.S. of -0.2 mm s^{-1} and a H.F. of 302 kOe for the CoPt/P90 catalyst at 200 °C. Next to the sextuplet, there is an oxidic doublet with an I.S. of 0.8 mm s^{-1} and a Q.S. of 1.6 mm s^{-1} , indicative

of dispersed Co^{2+} . The first humidity steps show a gradual increase in the contribution of oxidic cobalt (Table 3), which is in the same order of magnitude as the previously measured non-promoted Co/P90 catalyst.

When the relative humidity is further increased to 57%, the promoted catalyst behaves differently from the non-promoted sample in the sense that the second oxidic cobalt doublet due to agglomerated cobalt does not appear (Figure 7b). This suggests that the presence of platinum suppresses the mobility of oxidic cobalt during humid FTS operation. Despite not observing the agglomerated oxidic cobalt phase, the platinum-promoted catalyst contains much more oxidized cobalt at $\text{RH} = 57\%$, compared to the non-promoted sample. From the significantly lower H.F. of the bulk metallic phase for the CoPt/P90 catalyst of 302 kOe compared to the one for Co/P90 of 310 kOe measured at 200 °C, we can infer that the metallic cobalt particles are smaller in CoPt/P90, even after this high humidity treatment. Smaller metallic particles are likely to have a stronger interaction with the support, which results in increased TiO_x overlayer formation. Formation of such overlayers anchors the cobalt more strongly, leading to less severe sintering but facilitating oxidation. So, whilst platinum improves cobalt dispersion and initial cobalt reducibility, further investigation is required in formulating titania-based catalysts that withstand oxidation during operation.

Table 3. Contribution of the different cobalt phases as determined from MES spectra recorded at 200 °C under varying FTS conditions.

Treatment	$\text{H}_2\text{O}/\text{H}_2$	Spectral contribution cobalt (%)			
		Co/P90		CoPt/P90	
		Co^0	Co-oxide	Co^0	Co-oxide
Reduced ^a	0	49	51	71	29
RH 0%	0	64	36	63	37
RH 7.5%	0.25	60	40	58	42
RH 14%	0.50	58	42	55	45
RH 20%	0.75	57	43	55	45
RH 25%	1.0	56	44	54	46
Reduced ^a	0	79	21	81	19
RH 0%	0	74	26	71	29
RH 57%	1.0	65	24 / 11	54	46

^aReduced spectra were recorded at room temperature.

5.3.8 Catalyst testing

The catalytic activity measured during the Mössbauer experiments is given in Figure 8. The data, including selectivity values are also presented in Table D7. The water gas shift selectivity was between 0.3% for all catalysts up to testing at 25% RH and increased to 2-3% for the 57% RH test condition. The activity rates observed for the Co/GP350 catalysts were very low, around $4 \times 10^{-6} \text{ mol}_{\text{CO}} \text{ g}_{\text{Co}}^{-1} \text{ s}^{-1}$, an order of magnitude below the other catalytic samples. The other catalysts show very similar activity trends in terms of a slow decrease of the catalytic activity with increasing humidity. This clearly points to deactivation of cobalt due to oxidation by co-fed water, as well as metallic cobalt sintering. The introduction of steam to the reactor feed results in a small decrease of the CO and H₂ partial pressures. Subsequently, at the high humidity conditions (RH = 57%), the removal of inert results in an increase of the CO and H₂ partial pressure, which both affect the catalytic activity due to the negative reaction order in CO and positive order in H₂ [81], [82]. As such, these data allow only for a qualitative comparison of the catalytic performance of the various samples.

The lowest activity, if we disregard the Co/GP350 outlier, was seen for the Co/P25 system between 2.5 and $3.2 \times 10^5 \text{ mol}_{\text{CO}} \text{ g}_{\text{Co}}^{-1} \text{ s}^{-1}$. The use of the higher titania surface area P90 support resulted in 70-80% higher performance with activity levels between 4.5 and $5.4 \times 10^5 \text{ mol}_{\text{CO}} \text{ g}_{\text{Co}}^{-1} \text{ s}^{-1}$. Interestingly, the use of the P90 support also showed a significant increase in the C₅₊ selectivity compared to the conventional P25 titania catalyst that coincides with a decrease in the methane selectivity. Typically, when operating at elevated pressure, larger metallic cobalt particles show higher C₅₊ selectivity compared to smaller ones. Here, however, the improved performance points at the opposite, as particles closer to 6-8 nm are known to be more active for FTS [10]. As such, the improved C₅₊ selectivity might simply be the result of the higher CO conversion. For both the Co/P25 and Co/P90 catalysts, a decrease in dry FTS activity is observed after re-reduction following the treatment at RH = 25%, indicated by the data in the dashed box in Figure 8. This irreversible activity loss is likely the result of metallic cobalt sintering as well as the formation of TiO_x overlayers. STEM-EDX measurements showed that sintering is much less pronounced when the P90 support is used. Therefore, the fact that more irreversible activity loss is observed on the Co/P90 catalyst compared to the Co/P25 sample, suggests that the formation of TiO_x overlayers is much more significant on the titania with the larger surface. This finding can also explain why a negligible activity was observed on the Co/GP350 catalyst, because the very high surface area of this support results in even stronger interaction between titania and the reduced metallic cobalt, causing almost complete coverage of the metallic cobalt by titania overlayers. So, whilst Mössbauer can probe metallic cobalt, due to its nature

as a bulk technique, the cobalt is not accessible at the surface for catalysis, which was also clearly observed in XPS.

When looking at the addition of platinum on the P90 support, improved activity is observed when the reduction promoter is present from 5.4 to $5.9 \times 10^5 \text{ mol}_{\text{CO}} \text{ g}_{\text{Co}}^{-1} \text{ s}^{-1}$ and additionally, the selectivity towards long-chain hydrocarbons is reduced by about 7%. Both these observations point towards a higher cobalt dispersion in the presence of the promoter, which was also observed in Mössbauer and XPS analysis. However, whilst the catalyst is initially more active, it also shows stronger deactivation during the humid FTS treatments. When comparing the activity after re-reduction, the difference is most significant with the CoPt/P90 showing a CTY of 4.0 and $4.4 \times 10^5 \text{ mol}_{\text{CO}} \text{ g}_{\text{Co}}^{-1} \text{ s}^{-1}$ for the Co/P90 catalyst. Under these conditions the platinum promoted catalyst still shows a lower H.F. of 319 kOe compared to 322 kOe for the non-promoted sample, suggesting that the difference is not the result of extensive sintering. Instead, we suggest that the improved dispersion of metallic cobalt leads to stronger interaction of cobalt with the titania support, resulting in more extensive TiO_x overlayer formation and less metallic cobalt being accessible for catalysis.

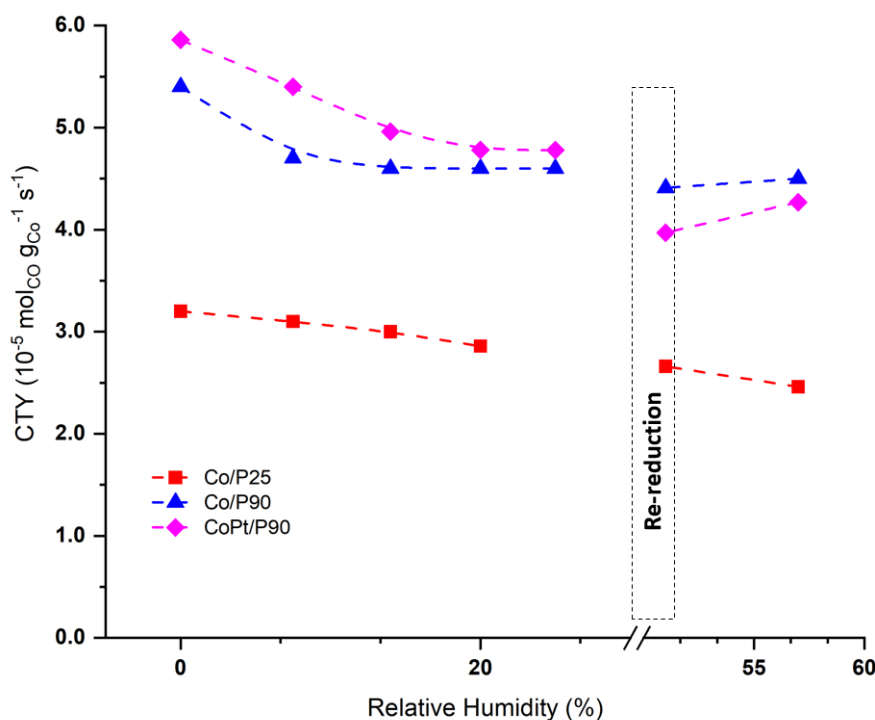


Figure 8. *In situ* FTS activity of the Co(Pt)/TiO₂ catalysts during humid FTS measurements in the Mössbauer cell. The CTY determined at steady state at the applied conditions is plotted against the RH. (Co/P25: red squares, Co/P90: blue triangles, CoPt/P90: magenta diamonds).

Besides catalytic activity measurements in the *in situ* MES cell, the performance of the cobalt catalysts was measured in a high-pressure fixed-bed plug-flow reactor at 220 °C, 20 bar, a H₂/CO ratio of 4, and a space velocity of 60 L g_{cat}⁻¹ h⁻¹. The corresponding results for fresh and used catalysts are collected in Table 4. The fresh catalysts were reduced at 340 °C for 2 hours. The used catalysts retrieved after the *in situ* MES measurements were re-reduced according to the same procedure. The GP350 supported catalysts were also tested, but no conversion was observed on these systems, even when reduction was prolonged at higher temperatures up to 450 °C. This agrees with the activity measured under *in situ* MES conditions. As the GP350 support does not contain sulfur from the preparation nor alkali metals as confirmed by XPS, we can exclude poisoning as an explanation. Instead, it is reasonable to conclude that formation of extensive TiO_x overlayers blocks some of the cobalt metal active phase. For the other catalysts based on P25 and P90, the CTY was in the range of 1.2 - 3.7 10⁻⁵ mol_{CO} g_{Co}⁻¹ s⁻¹ for the freshly reduced and used catalysts. The Co/P90 catalytic activity reported here was obtained after significant time on stream due to technical problems with the GC detector. As the time on stream was extended, we observed an increase in CO conversion, we suspect this is due to further reduction of cobalt, which was found to be difficult through MES and XPS. Due to this extended treatment, the final conversion obtained on this sample is substantially higher than intended, above 10%. As such, the higher CO conversion for this sample makes comparison of the product distribution less meaningful, although no significant differences are observed between the fresh and used Co/P90 catalysts. We can however compare the CTY, which is found to be significantly higher for Co/P90 compared to Co/P25, in good agreement with the activity measured *in situ* during MES. This improved activity is even more pronounced when comparing the used catalysts. For both Co/P25 and Co/P90, a decrease in catalytic activity is observed between the freshly reduced and used state, which is caused by sintering of metallic cobalt. This effect is however less pronounced for the Co/P90 catalyst as followed amongst others from the STEM-EDX data. This is different than what was observed in the *in situ* activity, where the Co/P90 catalyst deactivated more significantly than the Co/P25 catalyst. We explain this more substantial deactivation to the formation of TiO_x overlayers formed during reduction and under the mildly reducing conditions of the FTS reaction. However, the used catalyst tested here were oxidized by passivation and exposed to air before being reduced again for FTS. As reduction-oxidation-reduction (ROR) cycles can remove TiO_x overlayers [13], [29], [83], it is plausible that this occurred in our used samples, explaining the less severe deactivation. So, whilst the formation of TiO_x overlayers has a strong negative effect on the catalyst activity, it is reversible, making the P90 support for cobalt particles very promising for FTS applications due to the increased

sintering resistance of the supported cobalt. Additionally, the use of platinum greatly assists in cobalt reducibility and even further enhances the cobalt dispersion, resulting in an improved catalytic activity. As long as the RH remains below 25%, this should be the preferred catalyst formulation. For higher humidity application, further investigations are required to reduce the susceptibility to formation TiO_x overlayers and cobalt oxidation.

Table 4. Catalytic performance data for the cobalt catalysts (plug-flow reactor operated at 220 °C, 20 bar and $\text{H}_2/\text{CO} = 4$, $\text{SV} = 60 \text{ L g}_{\text{cat}}^{-1} \text{ h}^{-1}$). *Test results were obtained after three consecutive reduction and FT activity treatments.

<i>Catalyst</i>	<i>Conversion (%)</i>	<i>C₁ selectivity (%)</i>	<i>C₂-C₄ selectivity (%)</i>	<i>C₅+ selectivity (%)</i>	<i>CTY ($10^{-5} \text{ mol}_{\text{CO}}$ $\text{g}_{\text{Co}}^{-1} \text{ s}^{-1}$)</i>
Co/P25	3	7	7	86	2.1
Co/P25 used	1	14	10	76	1.2
Co/P90*	13	9	10	81	3.7
Co/P90 used	4	8	7	85	2.8
Co/GP350	0	0	0	0	0

5.4 Conclusion

By combining Mössbauer spectroscopy with *ex situ* characterization, we showed that reduction of a calcined cobalt on titania is hindered by a higher surface area of the titania support. On P90 and GP350 that have a higher surface area than the common P25 titania support, the increased cobalt-titania interactions result in significantly lower cobalt reduction. *In situ* Mössbauer spectroscopy demonstrated partial oxidation of metallic cobalt under humid FTS conditions for Co/P90 as was earlier found for Co/P25. There was no correlation between the extent of cobalt oxidation and the surface area of the titania support. The low reduction degree of cobalt in Co/GP350, which may also be related to TiO_x overlayer formation, resulted in a negligible FTS activity. Although cobalt reduction in Co/P90 was also lower than in Co/P25, the cobalt mobility on Co/P90 was lower, resulting in less cobalt sintering during FTS operation. Promotion of Co/P90 with platinum led to a higher DOR and a higher catalytic performance. However, despite the addition of the platinum promoter, oxidation occurred under high humid FTS conditions. Deactivation was even more significant in this case, which is due to the stronger interaction of dispersed metallic cobalt with the titania support. Nevertheless, compared to P25 the use of P90 with a higher surface area is promising for stably dispersing cobalt with an improved catalytic performance in the FTS reaction.

Bibliography

- [1] M. E. Dry, “The Fischer-Tropsch process: 1950-2000,” *Catal. Today*, vol. 71, no. 3–4, pp. 227–241, 2002, doi: 10.1016/S0920-5861(01)00453-9.
- [2] G. Maschio, A. Lucchesi, and G. Stoppato, “Production of syngas from biomass,” *Bio. Tech.*, vol. 48, no. 2, pp. 119–126, 1994, doi: 10.1016/0960-8524(94)90198-8.
- [3] K. Zhao, Q. Bkour, X. Hou, S. W. Kang, J. C. Park, M. G. Norton, J.-I. Yang, and S. Ha, “Reverse water gas shift reaction over CuFe/Al₂O₃ catalyst in solid oxide electrolysis cell,” *Chem. Eng. J.*, vol. 336, pp. 20–27, 2018, doi: 10.1016/j.cej.2017.11.028.
- [4] A. de Klerk, “Fischer-Tropsch Process,” in *Kirk-Othmer Encyclopedia of Chemical Technology*, Hoboken, NJ, USA: John Wiley & Sons, Inc., 2013. doi: 10.1002/0471238961.fiscdekl.a01.
- [5] E. de Smit and B. M. Weckhuysen, “The renaissance of iron-based Fischer-Tropsch synthesis: on the multifaceted catalyst deactivation behaviour,” *Chem. Soc. Rev.*, vol. 37, no. 12, p. 2758, 2008, doi: 10.1039/b805427d.
- [6] E. Iglesia, “Design, synthesis, and use of cobalt-based Fischer-Tropsch synthesis catalysts,” *Appl. Catal. A Gen.*, vol. 161, no. 1–2, pp. 59–78, 1997, doi: 10.1016/S0926-860X(97)00186-5.
- [7] E. Rytter, N. E. Tsakoumis, and A. Holmen, “On the selectivity to higher hydrocarbons in Co-based Fischer-Tropsch synthesis,” *Catal. Today*, vol. 261, pp. 3–16, 2016, doi: 10.1016/j.cattod.2015.09.020.
- [8] P. J. van Berge and R. C. Everson, “Cobalt as an alternative Fischer-Tropsch catalyst to iron for the production of middle distillates,” in *Stud. in Surf. Sci. and Catal.*, 1997, pp. 207–212. doi: 10.1016/S0167-2991(97)80336-9.
- [9] S. Drünert, U. Neuling, T. Zitscher, and M. Kaltschmitt, “Power-to-Liquid fuels for aviation – Processes, resources and supply potential under German conditions,” *Appl. Energy*, vol. 277, p. 115578, 2020, doi: 10.1016/j.apenergy.2020.115578.
- [10] G. L. Bezemer, J. H. Bitter, H. P. C. E. Kuipers, H. Oosterbeek, J. E. Holewijn, X. Xu, F. Kapteijn, A. J. van Dillen, and K. P. de Jong, “Cobalt Particle Size Effects in the Fischer-Tropsch Reaction Studied with Carbon Nanofiber Supported Catalysts,” *J. Am. Chem. Soc.*, vol. 128, no. 12, pp. 3956–3964, 2006, doi: 10.1021/ja058282w.
- [11] J. P. den Breejen, P. B. Radstake, G. L. Bezemer, J. H. Bitter, V. Frøseth, A. Holmen, and K. P. de Jong, “On the Origin of the Cobalt Particle Size Effects in Fischer-Tropsch Catalysis,” *J. Am. Chem. Soc.*, vol. 131, no. 20, pp. 7197–7203, 2009, doi: 10.1021/ja901006x.
- [12] N. E. Tsakoumis, M. Rønning, Ø. Borg, E. Rytter, and A. Holmen, “Deactivation of cobalt based Fischer-Tropsch catalysts: A review,” *Catal. Today*, vol. 154, no. 3–4, pp. 162–182, 2010, doi: 10.1016/j.cattod.2010.02.077.
- [13] E. Rytter and A. Holmen, “Deactivation and Regeneration of Commercial Type Fischer-Tropsch Co-Catalysts—A Mini-Review,” *Catalysts*, vol. 5, no. 2, pp. 478–499, 2015, doi: 10.3390/catal5020478.
- [14] C. H. Bartholomew, “Mechanisms of catalyst deactivation,” *Appl. Catal. A Gen.*, vol. 212, no. 1–2, pp. 17–60, 2001, doi: 10.1016/S0926-860X(00)00843-7.
- [15] V. V. Ordonsky, A. Carvalho, B. Legras, S. Paul, M. Virginie, V. L. Sushkevich, and A. Y. Khodakov, “Effects of co-feeding with nitrogen-containing compounds on the performance of supported cobalt and iron catalysts in Fischer-Tropsch synthesis,” *Catal. Today*, vol. 275, pp. 84–93, 2016, doi: 10.1016/j.cattod.2015.12.015.
- [16] W. Ma, G. Jacobs, D. E. Sparks, B. Todici, D. B. Bukur, and B. H. Davis, “Quantitative comparison of iron and cobalt based catalysts for the Fischer-Tropsch synthesis under clean and poisoning conditions,” *Catal. Today*, vol. 343, pp. 125–136, 2020, doi: 10.1016/j.cattod.2019.04.011.
- [17] A. H. Lillebø, E. Patanou, J. Yang, E. A. Blekkan, and A. Holmen, “The effect of alkali and alkaline earth elements on cobalt based Fischer-Tropsch catalysts,” *Catal. Today*, vol. 215, pp. 60–66, 2013, doi: 10.1016/j.cattod.2013.03.030.
- [18] C. M. Balonek, A. H. Lillebø, S. Rane, E. Rytter, L. D. Schmidt, and A. Holmen, “Effect of alkali metal impurities on Co-Re catalysts for Fischer-Tropsch synthesis from biomass-derived syngas,” *Catal. Letters*, vol. 138, no. 1–2, pp. 8–13, 2010, doi: 10.1007/s10562-010-0366-4.
- [19] B. M. Weckhuysen, “Preface: recent advances in the in-situ characterization of heterogeneous catalysts,” *Chem. Soc. Rev.*, vol. 39, no. 12, p. 4557, 2010, doi: 10.1039/c0cs90031a.
- [20] P. G. Menon, “Coke on catalysts-harmful, harmless, invisible and beneficial types,” *J. of Mol. Catal.*, vol. 59, no. 2, pp. 207–220, 1990, doi: 10.1016/0304-5102(90)85053-K.
- [21] C. H. Bartholomew, “Carbon Deposition in Steam Reforming and Methanation,” *Catal. Rev.*, vol. 24, no. 1, pp. 67–112, 1982, doi: 10.1080/03602458208079650.
- [22] K. Cheng, V. Subramanian, A. Carvalho, V. V. Ordonsky, Y. Wang, and A. Y. Khodakov, “The role of carbon pre-coating for the synthesis of highly efficient cobalt catalysts for Fischer-Tropsch synthesis,” *J. Catal.*, vol. 337, pp. 260–271, 2016, doi: 10.1016/j.jcat.2016.02.019.
- [23] W. Chen, T. F. Kimpel, Y. Song, F.-K. Chiang, B. Zijlstra, R. Pestman, P. Wang, and E. J. M. Hensen, “Influence of Carbon Deposits on the Cobalt-Catalyzed Fischer-Tropsch Reaction: Evidence of a Two-Site Reaction Model,” *ACS Catal.*, vol. 8, no. 2, pp. 1580–1590, 2018, doi: 10.1021/acscatal.7b03639.

- [24] M. Claeys, M. E. Dry, E. van Steen, E. du Plessis, P. J. van Berge, A. M. Saib, and D. J. Moodley, "In situ magnetometer study on the formation and stability of cobalt carbide in Fischer–Tropsch synthesis," *J. Catal.*, vol. 318, pp. 193–202, 2014, doi: 10.1016/j.jcat.2014.08.002.
- [25] M. Wolf, "Thermodynamic assessment of the stability of bulk and nanoparticulate cobalt and nickel during dry and steam reforming of methane," *RSC Adv.*, vol. 11, no. 30, pp. 18187–18197, 2021, doi: 10.1039/D1RA01856F.
- [26] M. Claeys, M. E. Dry, E. van Steen, P. J. van Berge, S. Booyens, R. Crous, P. van Helden, J. Labuschagne, D. J. Moodley, and A. M. Saib, "Impact of Process Conditions on the Sintering Behavior of an Alumina-Supported Cobalt Fischer–Tropsch Catalyst Studied with an in Situ Magnetometer," *ACS Catal.*, vol. 5, no. 2, pp. 841–852, 2015, doi: 10.1021/cs501810y.
- [27] G. L. Bezemer, T. J. Remans, A. P. van Bavel, and A. I. Dugulan, "Direct Evidence of Water-Assisted Sintering of Cobalt on Carbon Nanofiber Catalysts during Simulated Fischer–Tropsch Conditions Revealed with in Situ Mössbauer Spectroscopy," *J. Am. Chem. Soc.*, vol. 132, no. 25, pp. 8540–8541, 2010, doi: 10.1021/ja103002k.
- [28] L. M. van Koppen, A. I. Dugulan, G. L. Bezemer, and E. J. M. Hensen, "Sintering and carbidization under simulated high conversion on a cobalt-based Fischer–Tropsch catalyst; manganese oxide as a structural promotor," *J. Catal.*, vol. 413, pp. 106–118, 2022, doi: 10.1016/j.jcat.2022.06.020.
- [29] C. E. Kliewer, S. L. Soled, and G. Kiss, "Morphological transformations during Fischer–Tropsch synthesis on a titania-supported cobalt catalyst," *Catal. Today*, vol. 323, pp. 233–256, 2019, doi: 10.1016/j.cattod.2018.05.021.
- [30] D. Kistamurthy, A. M. Saib, D. J. Moodley, J. W. Niemantsverdriet, and C. J. Weststrate, "Ostwald ripening on a planar Co/SiO₂ catalyst exposed to model Fischer–Tropsch synthesis conditions," *J. Catal.*, vol. 328, pp. 123–129, 2015, doi: 10.1016/j.jcat.2015.02.017.
- [31] W. Janse Van Rensburg, P. Van Helden, D. J. Moodley, M. Claeys, M. A. Petersen, and E. Van Steen, "Role of Transient Co-Subcarbonyls in Ostwald Ripening Sintering of Cobalt Supported on γ -Alumina Surfaces," *J. of Phys. Chem. C*, vol. 121, no. 31, pp. 16739–16753, 2017, doi: 10.1021/acs.jpcc.7b01907.
- [32] J. van de Loosdrecht, B. Balzhinimaev, J. A. Dalmon, J. W. Niemantsverdriet, S. V. Tsybulya, A. M. Saib, P. J. van Berge, and J. L. Visagie, "Cobalt Fischer–Tropsch synthesis: Deactivation by oxidation?," *Catal. Today*, vol. 123, no. 1–4, pp. 293–302, 2007, doi: 10.1016/j.cattod.2007.02.032.
- [33] M. Wolf, B. K. Mutuma, N. J. Coville, N. Fischer, and M. Claeys, "Role of CO in the Water-Induced Formation of Cobalt Oxide in a High Conversion Fischer–Tropsch Environment," *ACS Catal.*, vol. 8, no. 5, pp. 3985–3989, 2018, doi: 10.1021/acscatal.7b04177.
- [34] M. Wolf, N. Fischer, and M. Claeys, "Capturing the interconnectivity of water-induced oxidation and sintering of cobalt nanoparticles during the Fischer–Tropsch synthesis in situ," *J. Catal.*, vol. 374, pp. 199–207, 2019, doi: 10.1016/j.jcat.2019.04.030.
- [35] E. Rytter and A. Holmen, "Perspectives on the Effect of Water in Cobalt Fischer–Tropsch Synthesis," *ACS Catal.*, vol. 7, no. 8, pp. 5321–5328, 2017, doi: 10.1021/acscatal.7b01525.
- [36] L. M. van Koppen, A. I. Dugulan, G. L. Bezemer, and E. J. M. Hensen, "Elucidating deactivation of titania-supported cobalt Fischer–Tropsch catalysts under simulated high conversion conditions," *J. Catal.*, vol. 420, pp. 44–57, 2023, doi: 10.1016/j.jcat.2023.02.019.
- [37] Z. Yu, Ø. Borg, D. Chen, B. C. Enger, V. Frøseth, E. Rytter, H. Wigum, and A. Holmen, "Carbon Nanofiber Supported Cobalt Catalysts for Fischer–Tropsch Synthesis with High Activity and Selectivity," *Catal. Letters*, vol. 109, no. 1–2, pp. 43–47, 2006, doi: 10.1007/s10562-006-0054-6.
- [38] Ø. Borg, Z. Yu, D. Chen, E. A. Blekkan, E. Rytter, and A. Holmen, "The effect of water on the activity and selectivity for carbon nanofiber supported cobalt Fischer–Tropsch catalysts," *Top. Catal.*, vol. 57, no. 6–9, pp. 491–499, 2014, doi: 10.1007/s11244-013-0205-0.
- [39] N. E. Tsakoumis, R. Dehghan, R. E. Johnsen, A. Voronov, W. Van Beek, J. C. Walmsley, Ø. Borg, E. Rytter, D. Chen, M. Rønning, and A. Holmen, "A combined in situ XAS-XRPD-Raman study of Fischer–Tropsch synthesis over a carbon supported Co catalyst," *Catal. Today*, vol. 205, pp. 86–93, 2013, doi: 10.1016/j.cattod.2012.08.041.
- [40] A. Carvalho, V. V. Ordonsky, Y. Luo, M. Marinova, A. R. Muniz, N. R. Marcilio, and A. Y. Khodakov, "Elucidation of deactivation phenomena in cobalt catalyst for Fischer–Tropsch synthesis using SSITKA," *J. Catal.*, vol. 344, pp. 669–679, 2016, doi: 10.1016/j.jcat.2016.11.001.
- [41] B. Ernst, S. Libs, P. Chaumette, and A. Kiennemann, "Preparation and characterization of Fischer–Tropsch active Co/SiO₂ catalysts," *Appl. Catal. A Gen.*, vol. 186, no. 1–2, pp. 145–168, 1999, doi: 10.1016/S0926-860X(99)00170-2.
- [42] A. Y. Khodakov, J. Lynch, D. Bazin, B. Rebours, N. Zanier, B. Moisson, and P. Chaumette, "Reducibility of cobalt species in silica-supported Fischer–Tropsch catalysts," *J. Catal.*, vol. 168, no. 1, pp. 16–25, 1997, doi: 10.1006/jcat.1997.1573.
- [43] A. Y. Khodakov, A. Griboval-Constant, R. Bechara, and V. L. Zhlobenko, "Pore Size Effects in Fischer Tropsch Synthesis over Cobalt-Supported Mesoporous Silicas," *J. Catal.*, vol. 206, no. 2, pp. 230–241, 2002, doi: 10.1006/jcat.2001.3496.
- [44] J. S. Jung, S. W. Kim, and D. J. Moon, "Fischer–Tropsch Synthesis over cobalt based catalyst supported on different mesoporous silica," *Catal. Today*, vol. 185, no. 1, pp. 168–174, 2012, doi: 10.1016/j.cattod.2012.02.002.

- [45] M. Wolf, H. Kotzé, N. Fischer, and M. Claeys, "Size dependent stability of cobalt nanoparticles on silica under high conversion Fischer–Tropsch environment," *Far. Dis.*, vol. 197, pp. 243–268, 2017, doi: 10.1039/C6FD00200E.
- [46] J. P. den Breejen, A. M. Frey, J. Yang, A. Holmen, M. M. van Schooneveld, F. M. F. de Groot, O. Stephan, J. H. Bitter, and K. P. de Jong, "A Highly Active and Selective Manganese Oxide Promoted Cobalt-on-Silica Fischer–Tropsch Catalyst," *Top. Catal.*, vol. 54, no. 13–15, pp. 768–777, 2011, doi: 10.1007/s11244-011-9703-0.
- [47] M. Voß, D. Borgmann, and G. Wedler, "Characterization of Alumina, Silica, and Titania Supported Cobalt Catalysts," *J. Catal.*, vol. 212, no. 1, pp. 10–21, 2002, doi: 10.1006/jcat.2002.3739.
- [48] E. Rytter and A. Holmen, "On the support in cobalt Fischer–Tropsch synthesis—Emphasis on alumina and aluminates," *Catal. Today*, vol. 275, pp. 11–19, 2016, doi: 10.1016/j.cattod.2015.11.042.
- [49] J. Wang, P. A. Chernavskii, A. Y. Khodakov, and Y. Wang, "Structure and catalytic performance of alumina-supported copper-cobalt catalysts for carbon monoxide hydrogenation," *J. Catal.*, vol. 286, pp. 51–61, 2012, doi: 10.1016/j.jcat.2011.10.012.
- [50] C. Lancelot, V. V. Ordonsky, O. Stéphan, M. Sadeqzadeh, H. Karaca, M. Lacroix, D. Curulla-Ferré, F. Luck, P. Fongarland, A. Griboval-Constant, and A. Y. Khodakov, "Direct Evidence of Surface Oxidation of Cobalt Nanoparticles in Alumina-Supported Catalysts for Fischer–Tropsch Synthesis," *ACS Catal.*, vol. 4, no. 12, pp. 4510–4515, 2014, doi: 10.1021/cs500981p.
- [51] H. Karaca, J. Hong, P. Fongarland, P. Roussel, A. Griboval-Constant, M. Lacroix, K. Hortmann, O. V. Safonova, and A. Y. Khodakov, "In situ XRD investigation of the evolution of alumina-supported cobalt catalysts under realistic conditions of Fischer–Tropsch synthesis," *Chem. Commun.*, vol. 46, no. 5, pp. 788–790, 2010, doi: 10.1039/B920110F.
- [52] H. Karaca, O. V. Safonova, S. Chambrey, P. Fongarland, P. Roussel, A. Griboval-Constant, M. Lacroix, and A. Y. Khodakov, "Structure and catalytic performance of Pt-promoted alumina-supported cobalt catalysts under realistic conditions of Fischer–Tropsch synthesis," *J. Catal.*, vol. 277, no. 1, pp. 14–26, 2011, doi: 10.1016/j.jcat.2010.10.007.
- [53] A. Rochet, V. Moizan, F. Diehl, C. Pichon, and V. Briois, "Quick-XAS and Raman operando characterization of a cobalt alumina-supported catalyst under realistic Fischer–Tropsch reaction conditions," *Catal. Today*, vol. 205, pp. 94–100, 2013, doi: 10.1016/j.cattod.2012.08.021.
- [54] M. Sadeqzadeh, S. Chambrey, J. Hong, P. Fongarland, F. Luck, D. Curulla-Ferré, D. Schweich, J. Bousquet, and A. Y. Khodakov, "Effect of different reaction conditions on the deactivation of alumina-supported cobalt Fischer–Tropsch catalysts in a milli-fixed-bed reactor: Experiments and modeling," *Ind. Eng. Chem. Res.*, vol. 53, no. 17, pp. 6913–6922, 2014, doi: 10.1021/ie4040303.
- [55] E. Rytter, Ø. Borg, N. E. Tsakoumis, and A. Holmen, "Water as key to activity and selectivity in Co Fischer–Tropsch synthesis: γ -alumina based structure-performance relationships," *J. Catal.*, vol. 365, pp. 334–343, 2018, doi: 10.1016/j.jcat.2018.07.003.
- [56] T. O. Eschemann and K. P. de Jong, "Deactivation Behavior of Co/TiO₂ Catalysts during Fischer–Tropsch Synthesis," *ACS Catal.*, vol. 5, no. 6, pp. 3181–3188, 2015, doi: 10.1021/acscatal.5b00268.
- [57] T. O. Eschemann, J. Oenema, and K. P. de Jong, "Effects of noble metal promotion for Co/TiO₂ Fischer–Tropsch catalysts," *Catal. Today*, vol. 261, pp. 60–66, 2016, doi: 10.1016/j.cattod.2015.06.016.
- [58] T. O. Eschemann, J. H. Bitter, and K. P. De Jong, "Effects of loading and synthesis method of titania-supported cobalt catalysts for Fischer–Tropsch synthesis," *Catal. Today*, vol. 228, pp. 89–95, 2014, doi: 10.1016/j.cattod.2013.10.041.
- [59] F. Morales, D. Grandjean, F. M. F. de Groot, O. Stephan, and B. M. Weckhuysen, "Combined EXAFS and STEM-EELS study of the electronic state and location of Mn as promoter in Co-based Fischer–Tropsch catalysts," *Phys. Chem. Chem. Phys.*, vol. 7, no. 4, pp. 568–572, 2005, doi: 10.1039/B418286C.
- [60] F. Morales, D. Grandjean, A. Mens, F. M. F. de Groot, and B. M. Weckhuysen, "X-ray Absorption Spectroscopy of Mn/Co/TiO₂ Fischer–Tropsch Catalysts: Relationships between Preparation Method, Molecular Structure, and Catalyst Performance," *J. Phys. Chem. B*, vol. 110, no. 17, pp. 8626–8639, 2006, doi: 10.1021/jp0565958.
- [61] F. Morales, F. M. F. De Groot, P. Glatzel, E. Kleimenov, H. Bluhm, M. Hävecker, A. Knop-Gericke, and B. M. Weckhuysen, "In situ X-ray absorption of Co/Mn/TiO₂ catalysts for Fischer–Tropsch synthesis," *J. of Phys. Chem. B*, vol. 108, no. 41, pp. 16201–16207, 2004, doi: 10.1021/jp0403846.
- [62] S. J. Tauster, S. C. Fung, and R. L. Garten, "Strong metal-support interactions. Group 8 noble metals supported on titanium dioxide," *J. Am. Chem. Soc.*, vol. 100, no. 1, pp. 170–175, 1978, doi: 10.1021/ja00469a029.
- [63] S. J. Tauster, S. C. Fung, R. T. K. Baker, and J. A. Horsley, "Strong Interactions in Supported-Metal Catalysts," *Science*, vol. 211, no. 4487, pp. 1121–1125, 1981, doi: 10.1126/science.211.4487.1121.
- [64] M. Wolf, N. Fischer, and M. Claeys, "Water-induced deactivation of cobalt-based Fischer–Tropsch catalysts," *Nat. Catal.*, vol. 3, no. 12, pp. 962–965, 2020, doi: 10.1038/s41929-020-00534-5.
- [65] M. Wolf, E. K. Gibson, E. J. Olivier, J. H. Neethling, C. R. A. Catlow, N. Fischer, and M. Claeys, "In-depth characterization of metal-support compounds in spent Co/SiO₂ Fischer–Tropsch model catalysts," *Catal. Today*, vol. 342, pp. 71–78, 2020, doi: 10.1016/j.cattod.2019.01.065.

- [66] M. Wolf, E. K. Gibson, E. J. Olivier, J. H. Neethling, C. R. A. Catlow, N. Fischer, and M. Claeys, "Water-Induced Formation of Cobalt-Support Compounds under Simulated High Conversion Fischer–Tropsch Environment," *ACS Catal.*, vol. 9, no. 6, pp. 4902–4918, 2019, doi: 10.1021/acscatal.9b00160.
- [67] M. W. J. Crajé, A. M. Van der Kraan, J. Van de Loosdrecht, and P. J. Van Berge, "The application of Mössbauer emission spectroscopy to industrial cobalt based Fischer–Tropsch catalysts," *Catal. Today*, vol. 71, no. 3–4, pp. 369–379, 2002, doi: 10.1016/S0920-5861(01)00464-3.
- [68] Z. Klencsár, "MossWinn—methodological advances in the field of Mössbauer data analysis," *Hyperfine Interact.*, vol. 217, no. 1–3, pp. 117–126, 2013, doi: 10.1007/s10751-012-0732-2.
- [69] J. A. Tjon and M. Blume, "Mössbauer Spectra in a Fluctuating Environment II. Randomly Varying Electric Field Gradients," *Phys. Rev.*, vol. 165, no. 2, pp. 456–461, 1968, doi: 10.1103/PhysRev.165.456.
- [70] T. Ohno, K. Sarukawa, K. Tokieda, and M. Matsumura, "Morphology of a TiO₂ Photocatalyst (Degussa, P-25) Consisting of Anatase and Rutile Crystalline Phases," *J Catal.*, vol. 203, no. 1, pp. 82–86, 2001, doi: 10.1006/jcat.2001.3316.
- [71] T. A. Dontsova, O. I. Yanushevskaya, S. V. Nahirniak, A. S. Kutuzova, G. V. Krynets, and P. S. Smertenko, "Characterization of Commercial TiO₂ P90 Modified with ZnO by the Impregnation Method," *J. Chem.*, vol. 2021, pp. 1–11, 2021, doi: 10.1155/2021/9378490.
- [72] A. Desmartin-Chomel, J. L. Flores, A. Bourane, J. M. Clacens, F. Figueras, G. Delahay, A. G. Fendler, and C. Lehaut-Burnouf, "Calorimetric and FTIR Study of the Acid Properties of Sulfated Titanias," *J. Phys. Chem. B*, vol. 110, no. 2, pp. 858–863, 2006, doi: 10.1021/jp0530698.
- [73] M. C. Biesinger, B. P. Payne, A. P. Grosvenor, L. W. M. Lau, A. R. Gerson, and R. St. C. Smart, "Resolving surface chemical states in XPS analysis of first row transition metals, oxides and hydroxides: Cr, Mn, Fe, Co and Ni," *Appl. Surf. Sci.*, vol. 257, no. 7, pp. 2717–2730, 2011, doi: 10.1016/j.apsusc.2010.10.051.
- [74] T. W. van Deelen, J. J. Nijhuis, N. A. Krams, J. Zečević, and K. P. de Jong, "Preparation of Cobalt Nanocrystals Supported on Metal Oxides To Study Particle Growth in Fischer–Tropsch Catalysts," *ACS Catal.*, vol. 8, no. 11, pp. 10581–10589, 2018, doi: 10.1021/acscatal.8b03094.
- [75] M. C. Biesinger, L. W. M. Lau, A. R. Gerson, and R. St. C. Smart, "Resolving surface chemical states in XPS analysis of first row transition metals, oxides and hydroxides: Sc, Ti, V, Cu and Zn," *Appl. Surf. Sci.*, vol. 257, no. 3, pp. 887–898, 2010, doi: 10.1016/j.apsusc.2010.07.086.
- [76] M. Oku, K. Wagatsuma, and S. Kohiki, "Ti 2p and Ti 3p X-ray photoelectron spectra for TiO₂, SrTiO₃ and BaTiO₃," *Phys. Chem. Chem. Phys.*, vol. 1, no. 23, pp. 5327–5331, 1999, doi: 10.1039/a907161j.
- [77] C. Wivel, B. S. Clausen, R. Candia, S. Mørup, and H. Topsøe, "Mössbauer Emission Studies of Calcined Co-Mo/Al₂O₃ Catalysts: Catalytic Significance of Co Precursors," *J. Catal.*, vol. 87, no. 2, pp. 497–513, 1984, doi: 10.1016/0021-9517(84)90210-0.
- [78] M. Monai *et al.*, "Restructuring of titanium oxide overlayers over nickel nanoparticles during catalysis," *Science*, vol. 380, no. 6645, pp. 644–651, 2023, doi: 10.1126/science.adf6984.
- [79] H. J. Lipkin, "Some simple features of the Mossbauer effect," *Ann Phys (N Y)*, vol. 18, no. 2, pp. 182–197, 1962, doi: 10.1016/0003-4916(62)90066-0.
- [80] J. H. Den Otter, S. R. Nijveld, and K. P. De Jong, "Synergistic Promotion of Co/SiO₂ Fischer–Tropsch Catalysts by Niobia and Platinum," *ACS Catal.*, vol. 6, no. 3, pp. 1616–1623, 2016, doi: 10.1021/acscatal.5b02418.
- [81] W. Chen, R. Pestman, B. Zijlstra, I. A. W. Filot, and E. J. M. Hensen, "Mechanism of Cobalt-Catalyzed CO Hydrogenation: 1. Methanation," *ACS Catal.*, vol. 7, no. 12, pp. 8050–8060, 2017, doi: 10.1021/acscatal.7b02757.
- [82] R. Pestman, W. Chen, and E. Hensen, "Insight into the Rate-Determining Step and Active Sites in the Fischer–Tropsch Reaction over Cobalt Catalysts," *ACS Catal.*, vol. 9, no. 5, pp. 4189–4195, 2019, doi: 10.1021/acscatal.9b00185.
- [83] A. M. Saib, D. J. Moodley, I. M. Ciobîc, M. M. Hauman, B. H. Sigwebela, C. J. Weststrate, J. W. Niemantsverdriet, and J. Van De Loosdrecht, "Fundamental understanding of deactivation and regeneration of cobalt Fischer–Tropsch synthesis catalysts," *Catal. Today*, vol. 154, no. 3–4, pp. 271–282, 2010, doi: 10.1016/j.cattod.2010.02.008.

Appendix D

Table D1: Mössbauer experimental conditions for reactive Fischer-Tropsch humidity tests. All tests were performed at 200 °C with a total pressure of 20 bar.

<i>Reaction</i>	<i>He (mL/min)</i>	<i>H₂ (mL/min)</i>	<i>CO (mL/min)</i>	<i>Water (g/h)</i>	<i>Steam (mL/min)</i>
<i>RH = 0%</i>	75	20	5	0	0
<i>RH = 7.5%</i> <i>H₂/H₂O = 4</i>	55	20	5	0.24	5
<i>RH = 14%</i> <i>H₂/H₂O = 2</i>	55	20	5	0.48	10
<i>RH = 20%</i> <i>H₂/H₂O = 1.3</i>	55	20	5	0.72	15
<i>RH = 25%</i> <i>H₂/H₂O = 1</i>	55	20	5	0.96	20
<i>RH = 57%</i> <i>H₂/H₂O = 1</i>	0	20	5	0.96	20

Table D2: Fit parameters of Mössbauer spectra of the Co/P25 catalyst after different treatments.

<i>Treatment</i>	<i>Temperature (°C)</i>	<i>Cobalt phase</i>	<i>Isomer Shift (mm s⁻¹)</i>	<i>Hyperfine Field (kOe)</i>	<i>Quadrupole Splitting (mm s⁻¹)</i>	<i>Spectral Contribution (%)</i>
<i>Reduced for 2 h at 340 °C</i>	20	<i>Co(0) bulk</i>	-0.1	322	-	95
		<i>Co²⁺</i>	0.8	-	1.8	5
<i>During FTS reaction</i>	200	<i>Co(0) bulk</i>	-0.2	309	-	95
		<i>Co²⁺</i>	0.9	-	1.8	5
<i>RH = 7.5%</i>	200	<i>Co(0) bulk</i>	-0.2	309	-	87
		<i>Co²⁺</i>	0.9	-	1.8	13

<i>RH = 14%</i>	200	<i>Co(0) bulk</i>	-0.2	309	-	86
		<i>Co²⁺</i>	0.8	-	1.7	14
<i>RH = 20%</i>	200	<i>Co(0) bulk</i>	-0.2	309	-	86
		<i>Co²⁺</i>	0.8	-	1.6	14
<i>RH = 25%</i>	200	<i>Co(0) bulk</i>	-0.2	309	-	84
		<i>Co²⁺</i>	0.8	-	1.7	16
<i>Reduced for 2 h at 340 °C</i>	20	<i>Co(0) bulk</i>	-0.1	322	-	95
		<i>Co²⁺</i>	0.8	-	2.4	5
<i>RH = 57%</i>	200	<i>Co(0) bulk</i>	-0.2	309	-	80
		<i>Co²⁺</i>	0.9	-	1.7	15
		<i>Co³⁺</i>	0.1	-	0.9	5
<i>After reaction</i>	20	<i>Co(0) bulk</i>	-0.1	321	-	78
		<i>Co²⁺</i>	0.9	-	2.1	13
		<i>Co³⁺</i>	0.1	-	0.9	9
<i>Reduced for 2 h at 340 °C</i>	20	<i>Co(0) bulk</i>	-0.1	323	-	96
		<i>Co²⁺</i>	0.9	-	2.1	4

Table D3: Fit parameters of Mössbauer spectra of the Co/P90 catalyst after different treatments.

<i>Treatment</i>	<i>Temperature (°C)</i>	<i>Cobalt phase</i>	<i>Isomer Shift (mm s⁻¹)</i>	<i>Hyperfine Field (kOe)</i>	<i>Quadrupole Splitting (mm s⁻¹)</i>	<i>Spectral Contribution (%)</i>
<i>Reduced for 2 h at 340 °C</i>	20	<i>Co(0) bulk</i>	-0.1	322	-	40
		<i>Co²⁺</i>	0.9	-	1.9	60
<i>Reduced for 4 h at 340 °C</i>	20	<i>Co(0) bulk</i>	-0.1	323	-	49
		<i>Co²⁺</i>	0.9	-	2.0	51

<i>During FTS reaction</i>	200	<i>Co(0) bulk</i>	-0.2	309	-	64
		<i>Co²⁺</i>	0.8	-	1.8	36
<i>After FTS reaction</i>	20	<i>Co(0) bulk</i>	-0.1	322	-	58
		<i>Co²⁺</i>	0.9	-	2.2	42
<i>RH = 7.5%</i>	200	<i>Co(0) bulk</i>	-0.2	308	-	60
		<i>Co²⁺</i>	0.8	-	1.7	40
<i>RH = 14%</i>	200	<i>Co(0) bulk</i>	-0.2	309	-	58
		<i>Co²⁺</i>	0.8	-	1.7	42
<i>RH = 20%</i>	200	<i>Co(0) bulk</i>	-0.2	309	-	57
		<i>Co²⁺</i>	0.8	-	1.6	43
<i>RH = 25%</i>	200	<i>Co(0) bulk</i>	-0.2	308	-	56
		<i>Co²⁺</i>	0.8	-	1.6	44
<i>Reduced for 2 h at 340 °C</i>	20	<i>Co(0) bulk</i>	-0.1	322	-	79
		<i>Co²⁺</i>	0.9	-	2.1	21
<i>RH = 57%</i>	200	<i>Co(0) bulk</i>	-0.2	310	-	65
		<i>Co²⁺</i>	0.8	-	1.6	24
		<i>Co³⁺</i>	0.0	-	0.8	11
<i>After reaction</i>	20	<i>Co(0) bulk</i>	-0.1	322	-	60
		<i>Co²⁺</i>	0.9	-	2.1	31
		<i>Co³⁺</i>	0.1	-	0.9	9
<i>Reduced for 2 h at 340 °C</i>	20	<i>Co(0) bulk</i>	-0.1	323	-	82
		<i>Co²⁺</i>	0.9	-	2.1	18

Table D4: Fit parameters of Mössbauer spectra of the Co/GP350 catalyst after different treatments.

<i>Treatment</i>	<i>Temperature</i> (°C)	<i>Cobalt</i> <i>phase</i>	<i>Isomer</i> <i>Shift</i> (mm s ⁻¹)	<i>Hyperfine</i> <i>Field</i> (kOe)	<i>Quadrupole</i> <i>Splitting</i> (mm s ⁻¹)	<i>Spectral</i> <i>Contribution</i> (%)
<i>Reduced</i> <i>for 2h at</i> <i>340 °C</i>	20	<i>Co(0) bulk</i>	-0.1	322	-	54
		<i>Co</i> ²⁺	0.8	-	2.0	46
<i>Reduced</i> <i>for 4h at</i> <i>340 °C</i>	20	<i>Co(0) bulk</i>	-0.1	322	-	59
		<i>Co</i> ²⁺	0.8	-	2.0	41
<i>During</i> <i>FTS</i> <i>reaction</i>	200	<i>Co(0) bulk</i>	-0.2	311	-	54
		<i>Co</i> ²⁺	0.8	-	1.7	46
<i>Reduced</i> <i>for 2 h at</i> <i>400 °C</i>	20	<i>Co(0) bulk</i>	-0.1	322	-	84
		<i>Co</i> ²⁺	0.8	-	1.9	16
<i>During</i> <i>FTS</i> <i>reaction</i>	200	<i>Co(0) bulk</i>	-0.2	311	-	81
		<i>Co</i> ²⁺	0.7	-	1.4	19
<i>RH = 7.5%</i>	200	<i>Co(0) bulk</i>	-0.2	310	-	73
		<i>Co</i> ²⁺	0.8	-	1.6	27
<i>RH = 14%</i>	200	<i>Co(0) bulk</i>	-0.2	310	-	66
		<i>Co</i> ²⁺	0.8	-	1.6	34
<i>RH = 20%</i>	200	<i>Co(0) bulk</i>	-0.2	310	-	66
		<i>Co</i> ²⁺	0.8	-	1.6	34
<i>RH = 25%</i>	200	<i>Co(0) bulk</i>	-0.2	310	-	67
		<i>Co</i> ²⁺	0.8	-	1.6	33
<i>Reduced</i> <i>for 2h at</i> <i>340 °C</i>	20	<i>Co(0) bulk</i>	-0.1	322	-	76
		<i>Co</i> ²⁺	0.9	-	2.0	24

<i>RH = 57%</i>	200	<i>Co(0) bulk</i>	-0.2	311	-	75
		<i>Co²⁺</i>	0.8	-	1.5	25
<i>After reaction</i>	20	<i>Co(0) bulk</i>	-0.1	322	-	72
		<i>Co²⁺</i>	0.9	-	2.0	28
<i>Reduced for 2 h at 340 °C</i>	20	<i>Co(0) bulk</i>	-0.1	322	-	82
		<i>Co²⁺</i>	0.9	-	2.0	18

Table D5: Fit parameters of Mössbauer spectra of the CoPt/P90 catalyst after different treatments.

<i>Treatment</i>	<i>Temperature (°C)</i>	<i>Cobalt phase</i>	<i>Isomer Shift (mm s⁻¹)</i>	<i>Hyperfine Field (kOe)</i>	<i>Quadrupole Splitting (mm s⁻¹)</i>	<i>Spectral Contribution (%)</i>
<i>Reduced for 2h at 340 °C</i>	20	<i>Co(0) bulk</i>	-0.1	317	-	71
		<i>Co²⁺</i>	1.0	-	1.9	29
<i>During FTS reaction</i>	200	<i>Co(0) bulk</i>	-0.2	302	-	63
		<i>Co²⁺</i>	0.8	-	1.8	37
<i>RH = 7.5%</i>	200	<i>Co(0) bulk</i>	-0.2	302	-	58
		<i>Co²⁺</i>	0.8	-	1.7	42
<i>RH = 14%</i>	200	<i>Co(0) bulk</i>	-0.2	301	-	55
		<i>Co²⁺</i>	0.8	-	1.7	45
<i>RH = 20%</i>	200	<i>Co(0) bulk</i>	-0.2	302	-	55
		<i>Co²⁺</i>	0.8	-	1.7	45
<i>RH = 25%</i>	200	<i>Co(0) bulk</i>	-0.2	302	-	54
		<i>Co²⁺</i>	0.8	-	1.6	46
<i>Reduced for 2h at 340 °C</i>	20	<i>Co(0) bulk</i>	-0.1	319	-	81
		<i>Co²⁺</i>	0.9	-	2.2	19
<i>RH = 57%</i>	200	<i>Co(0) bulk</i>	-0.2	302	-	54
		<i>Co²⁺</i>	0.8	-	1.6	46

After reaction	20	<i>Co(0) bulk</i>	-0.1	318	-	54
		<i>Co²⁺</i>	0.9	-	2.1	46
Reduced for 2h at 340 °C	20	<i>Co(0) bulk</i>	-0.1	319	-	81
		<i>Co²⁺</i>	0.9	-	2.2	19

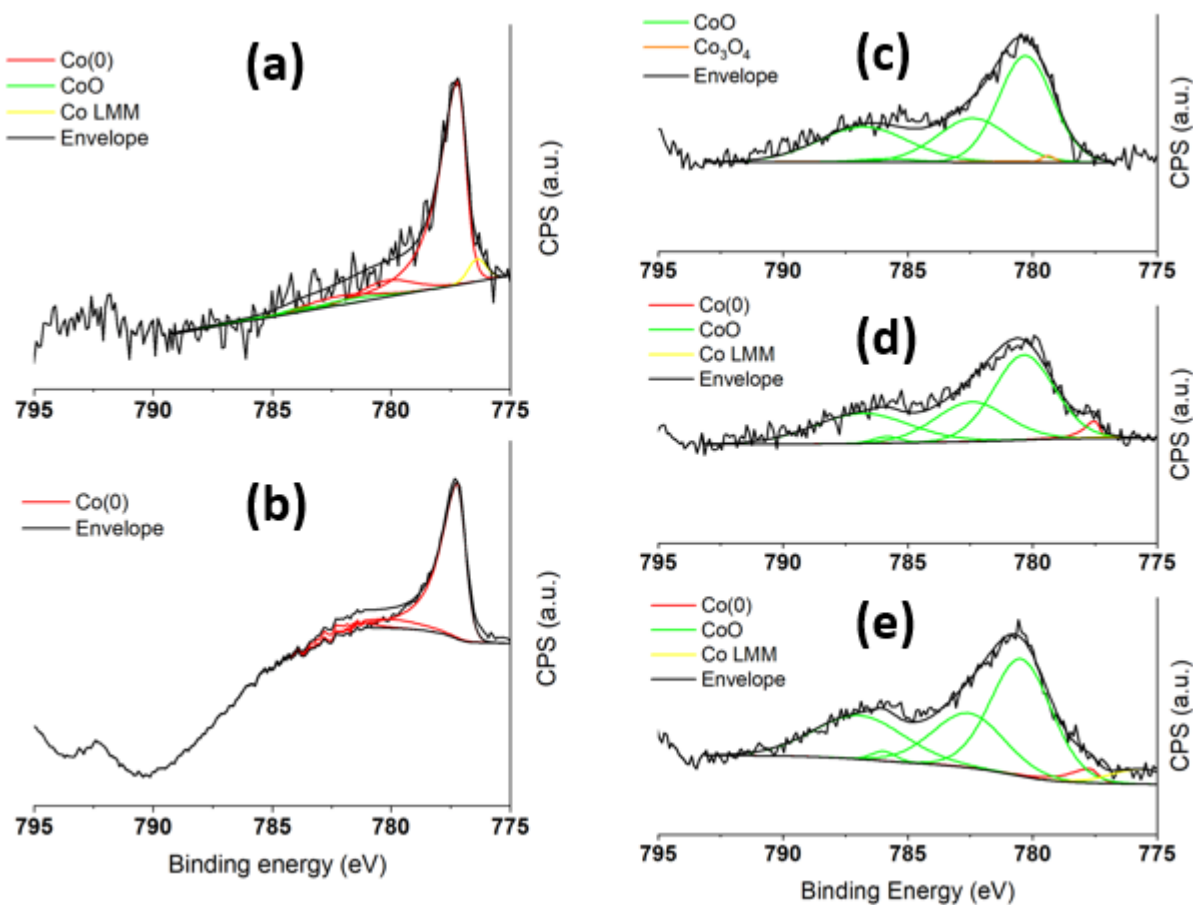


Figure D6: Co 2p_{3/2} XPS spectra of Co/P90 (a) after reduction at 500 °C, and (b) after reduction at 650 °C. And XPS spectra of Co/GP350 (c) after calcination at 350 °C, (d) after reduction at 340 °C and (e) after reduction at 450 °C. (black: experimental data and the fitted envelope; red: the fitted metallic Co(0) contributions; green: the fitted CoO contributions; yellow: the Co auger LMM peak; the XPS fit model was taken from Ref. [73]).

Table D7: Catalytic data obtained from *in situ* Mössbauer spectroscopy at 200 °C, 20 bar, H₂/CO = 4, and increasing relative humidity.

<i>Catalyst</i>	<i>Relative humidity (%)</i>	<i>C₁ selectivity (%)</i>	<i>CO₂ selectivity (%)</i>	<i>C₅₊ selectivity (%)</i>	<i>CTY (10⁻⁵ mol_{CO} g_{Co}⁻¹ s⁻¹)</i>
Co/P25	0	5	0.2	92	3.2
	7.5	4	0.3	93	3.1
	14	4	0.2	93	3.0
	20	5	0.2	93	2.9
	0	4	0.2	94	2.7
	57	2	3	93	2.5
Co/P90	0	2	0.2	97	5.4
	7.5	1	0.1	98	4.7
	14	1	0.1	98	4.6
	20	1	0.2	98	4.6
	25	1	0.1	97	4.6
	0	2	0.2	97	4.4
	57	2	1	97	4.5
CoPt/P90	0	9	0.2	87	5.9
	7.5	8	0	87	5.4
	14	8	0.1	88	5.0
	20	6	0.1	89	4.8
	25	7	0.1	88	4.8
	0	5	0.2	90	4.0
	57	3	2	91	4.3
	0	4	0	93	3.6

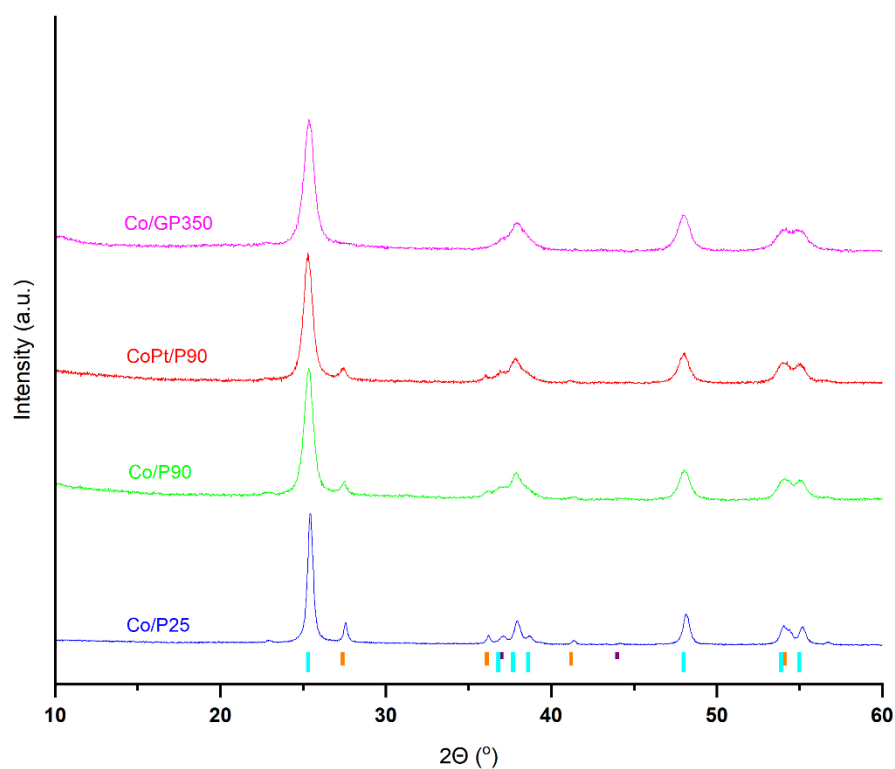


Figure D8: X-ray diffractograms of Co/P25, Co/P90, CoPt/P90 and Co/GP350 after calcination at 350 °C. The strongest diffraction lines of anatase TiO_2 (orange), rutile TiO_2 (cyan) and Co_3O_4 (dark purple) are indicated at the bottom.

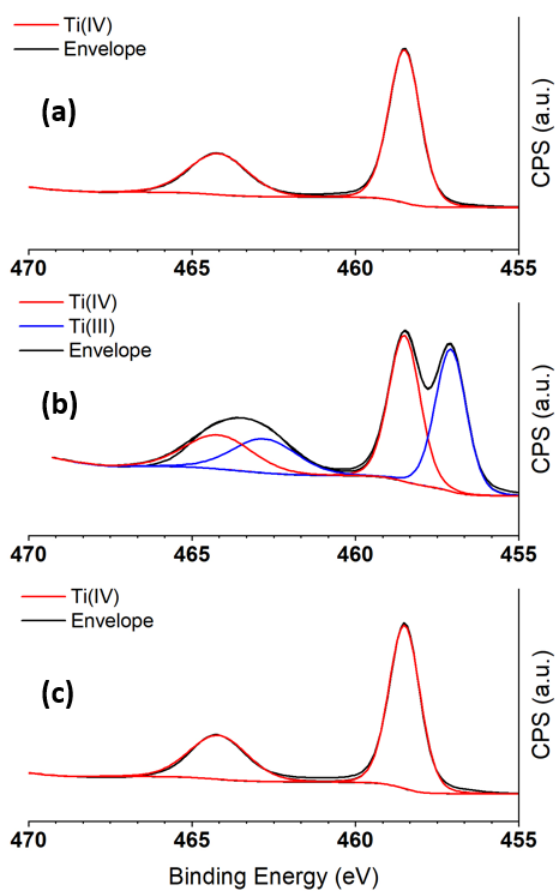


Figure D9: Ti 2p XPS spectra of Co/P90 (a) after reduction at 340 °C, (b) after reduction at 500 °C, and (c) after reduction at 650 °C (black: experimental data and the fitted envelope; red: the fitted Ti(IV) contributions; blue: the fitted Ti(III) contributions; the XPS fit model was taken from Ref. [73]).

Chapter 6

Summary and Outlook

In the coming decades, concerns about climate change are expected to push the energy and chemicals industry towards renewable sources away from the exploitation of fossil fuels. Although some of the demand for transportation fuels can be covered by electric vehicles, there will remain a demand for liquid fuels by sectors such as heavy-duty transport and aviation, which require diesel and kerosene. Fischer-Tropsch synthesis (FTS) is ideally suited to produce such fuels from other feedstock than oil. FTS is part of technology that can be described as XTL, or anything-to-liquids, including alternative resources such as biomass and CO₂ in addition to conventional ones as natural gas and coal. The feedstock for the FTS reaction itself is synthesis gas, a mixture of CO and H₂, which can be obtained through steam reforming, autothermal reforming or of natural gasification of natural gas, gasification of coal or biomass or reduction of CO₂ to CO by thermocatalytic (reverse water-gas shift) or electrocatalytic approaches using respectively green hydrogen or renewable electricity.

For successful commercial exploitation of the Fischer-Tropsch reaction, catalysts are required. The most commonly employed practical catalysts for the conversion of natural-gas-derived synthesis gas are based on cobalt. Whilst cobalt-based catalysts show excellent catalytic activity and selectivity towards long-chain hydrocarbons, they suffer from various deactivation mechanisms under FTS conditions. Developing more stable cobalt catalysts would greatly improve the economics of the FTS process and productivity and reduce the energy demand of the FTS process. To develop such catalysts, first we must have a thorough understanding of the exact deactivation mechanisms at play, how they relate to the experimental conditions and to what extent they contribute to the undesired deactivation. To obtain such information, *in situ* and operando characterization techniques are indispensable, as they allow to capture the structure of the catalyst under close to industrial conditions. Following the evolution of the catalyst at different experimental conditions can provide deeper insight into the deactivation of cobalt-based catalysts in the FTS reaction. In this work, we have focused on the effect of high partial pressures of steam, representative of high CO conversion conditions in the FTS reaction, on the deactivation of cobalt catalysts for different support materials as well as the influence of different promoters. The main

technique deployed in this work is *in situ* Mössbauer emission spectroscopy (MES) which, as a fingerprint technique based on the recoil-free emission and adsorption of gamma rays, provides valuable information on cobalt oxidation state, coordination, and particle size under realistic FTS conditions.

In **Chapter 2**, we investigated the deactivation of cobalt catalysts on carbon nanofibers, which served as a model support. By co-feeding steam with synthesis gas, we were able to observe a strong synergistic effect between steam and carbon monoxide towards the sintering of metallic cobalt through the use of *in situ* MES. This strong deactivation pathway showed the need for a structural promoter, which can anchor metallic cobalt and reduce sintering. To this end, we promoted the catalyst with manganese, which has previously been studied as an activity promoter for FTS. Although there was a small positive effect on the sintering behavior in the presence of manganese oxide, deactivation through carbidization of the active metallic cobalt to cobalt carbide (Co_2C) occurred, when the catalyst was exposed to a combination of steam and carbon monoxide. The amount of cobalt carbide formed was found to increase with the steam partial pressure, additionally the tendency towards carbidization was found to increase at a higher cobalt loading at the same cobalt-to-manganese ratio. Analysis of the catalyst surface with STEM-EDX after reaction revealed the formation of large manganese oxide agglomerates with sizes up to 200 nm, which were in close interaction with cobalt particles that were around 15 nm in size. Our findings suggest that the cobalt particles in close proximity with the manganese agglomerates are susceptible to carbidization by carbon monoxide. The formation of these structures is only possible due to the high mobility of both cobalt and manganese on the model carbon support when both steam and carbon monoxide are present.

We next studied the effect of manganese promoter on an oxide support that more strongly interacts with cobalt. For this purpose, we prepared catalysts with and without manganese on a silica support in **Chapter 3**. Here, we found that the introduction of manganese oxide in the catalyst formulation results in the formation of more dispersed cobalt particles. This is relevant for cobalt-based catalysts because of the well-known structure-sensitivity of the FTS reaction. Under relatively low steam partial pressure, the silica-supported cobalt catalyst showed excellent stability towards sintering, contrarily to what was observed on the carbon support. However, *in situ* MES demonstrated that high steam partial pressure led to the reaction of the metallic cobalt phase with the silica support, resulting in cobalt-silicate compounds, which are inactive in the FTS reaction. This strong metal-support interaction (SMSI) was more pronounced for the manganese-promoted catalyst, which

could be linked to the enhanced cobalt dispersion. As such, the findings in this chapter show that silica should only be considered as an FTS support material when low steam partial pressures can be maintained. Moreover, it is desirable to use relatively large (> 10 nm) cobalt particles to limit deactivation through SMSI.

In **Chapter 4**, we studied titania as a reducible carrier material for cobalt during operation under high humidity FTS conditions. We prepared a series of catalysts with cobalt weight loadings between 2 and 8%. Contrarily to the silica-supported catalysts, no deactivation through SMSI was observed under realistic FTS conditions. Using *in situ* MES, we found that much higher steam to hydrogen ratios (>70) were required to form cobalt-support compounds, cobalt-titanate, on P25 titania in the absence of carbon monoxide. Despite the absence of such SMSI, we observed the oxidation of part of the metallic cobalt upon introduction of steam, and the extent of oxidation increased with the partial pressure of steam. We observed that the absolute amount of oxidized cobalt was independent of the cobalt loading, strongly suggesting that the oxidation is related to the available titania support surface area. The amount of absolute oxidized cobalt was found to be in the range of 1.2 w% on all catalysts supported P25 titania, which appears to match reasonably with a monolayer coverage of the titanol groups by Co^{2+} ions. As such, it is likely that the limiting factor in the oxidation of cobalt is the surface concentration of titanols.

To further study this phenomenon, we expanded our study to two different titania support materials in **Chapter 5**, namely P90 and GP350. Whilst the P90 support is comparable to P25 except for the higher surface area of the former, the GP350 support has a unique structure of pure anatase with a very high surface area. XPS analysis showed that the reducibility of Co/P90 and Co/GP350 was impeded by stronger cobalt-titania interactions as compared with Co/P25. Under high steam partial pressure, we did not observe significantly more cobalt oxidation on the P90 and GP350 supports, as was expected from the substantially higher surface areas of these titanias. On the GP350 support, we observed indications for the coverage of cobalt by TiO_x overlayers, which strongly suppresses the catalytic activity. The results for Co/GP90 were very promising, as the formation of significant TiO_x layers was not observed while the stronger metal-support interactions still led to less sintering during humid FTS operation as compared to Co/P25, which was beneficial for the metallic particle size but also to prevent the expected more severe oxidation of cobalt, due to more exposed titanols. As a result, the catalytic performance of Co/P90 was substantially better than that of Co/P25. As the cobalt reduction degree for Co/P90 was lower than for Co/P25, we promoted the Co/P90 catalyst with a platinum reduction promoter, considering that platinum not only improved cobalt reducibility

during pre-treatment but could also counteract the oxidation under humid FTS operation. Further analysis of this sample showed the expected beneficial effect on the reducibility of cobalt, and it also led to the formation of more dispersed cobalt particles. Both aspects led to a further increase in the catalytic performance. Nevertheless, similar to the silica-based catalysts, the improved cobalt dispersion resulted in more significant deactivation under high steam partial pressure as indicated by *in situ* MES measurements. This deactivation due to oxidation was not counteracted by the platinum promoter.

The work in this thesis combined state-of-the-art *in situ* Mössbauer emission spectroscopy with extensive *ex situ* electron microscopy, spectroscopy characterization and catalytic activity measurements to provide insights into the deactivation of cobalt-based FTS catalysts. The work indicates the main pitfalls of the different supported cobalt catalysts, and through this we have gained a better understanding of what is needed for stable catalyst design. We expect that future works can build on this, by utilizing different promoters to stabilize the active cobalt phase from deactivation. This could be achieved by reducing the oxidizing potential, or by anchoring the cobalt more strongly, or instead by weakening the metal-support interaction.

The most significant advances presented in this thesis are the findings associated with oxidation of the active cobalt phase on the titania support. Although previous work doubted oxidation as a relevant deactivation mechanism, here we have demonstrated conclusively that oxidation can contribute to deactivation of cobalt FTS catalysts when operated under industrially relevant conditions. Moreover, we have shown ways to improve the oxidation resistance of titania-supported cobalt catalysts, which can form a lead for further work. This could include the use of promoters or further tweaking the support chemistry. We have also shown that silica as a support is not industrially relevant for the high humidity conditions encountered in a tubular fixed bed reactor, because it will lead at high humidity associated with high CO conversion to cobalt silicates that are inactive in the FTS reaction. Another important finding of this work is that manganese and platinum promotion has a more considerable effect on catalyst structure than previously understood. Both these promoters showed a beneficial effect on cobalt dispersion, which may help to guide the design of more stable catalysts with improved activity. As such, to the best of our knowledge, this thesis presents the most concise and comprehensive research into the fundamental processes determining cobalt deactivation in FTS on different support systems. With this work we have shown the importance of academic and industrial collaboration, which has provided relevant knowledge for the successful industrial exploitation of the Fischer-Tropsch reaction.

Acknowledgements

Finding the right words to describe the years that have led up to this thesis is difficult, much like the journey itself, character-building and challenging are some examples that come to mind. Starting this project, I was very aware of the typical PhD struggles, but the addition of a global pandemic was something I was ill prepared for. Being at the end of this 5+ year marathon, I know that I could not have done this without thanking the friends, colleagues and family that helped me along the way.

Firstly, I would like to offer a massive thanks to my 1st promoter, Emiel Hensen, who gave me the opportunity to do my PhD project in the IMC group. After prof. Gascon left the group in Delft, I was uncertain if I would stay in academia to pursue a PhD project, but then I saw the opportunity to join the group in Eindhoven. And after a somewhat nervous, but apparently successful interview, I got to tackle this joint project. Whilst I struggled to find my own footing in the first year of the project, your guidance and supervision helped guide me onto the right track. And through our meetings and many writing iterations I have gained both in confidence and scientific knowledge. Your help and feedback were fundamental in bringing this PhD thesis to a successful end, even if it took a bit longer than planned.

Secondly, I would like to give a big thanks to my first co-promotor, Iulian Dugulan, who stood beside me throughout the entire project and taught me a lot about being confident in the lab and especially Mössbauer spectroscopy. The Mössbauer group is lucky to have someone so active and invested as you, Iulian, you run countless experiments and collaborations and really help bring this perhaps underrated technique to the forefront in catalysis research and beyond. Though it wasn't all about science, often, especially during the pandemic, we'd just spend time talking in the lab (at a safe distance of course!), and I consider myself lucky to have had such a down-to-earth supervisor during this time.

And another big thank you goes to my second co-promotor, Leendert Bezemer, who not only acted as a company supervisor during my project but was constantly actively involved in shaping and reporting the research. Early on, at the end of my first year, if I'm not mistaken, we chose to regularly meet to discuss the state of things. Whilst I did not always have many results to share, to my dismay, these meetings always helped with creating new ideas or getting things back on track. Your levelheadedness, patience and knowledge were always appreciated in meetings and in writing our publications. And thank you for allowing me to present my work to the XTL community at the ETCA on two separate occasions.

I would like to thank my committee members, prof. dr. Atsushi Urakawa, prof. dr. Michael

Acknowledgements

Claeys, prof. dr. ir. John van der Schaaf, and prof. dr. ir. Martin van Sint Annaland for taking the time to diligently read and evaluate my thesis and being part of my defense ceremony.

Everyone knows that groups would cease to function without its support staff, and I owe thanks to many of these people in both IMC in Eindhoven, as well as FAME in Delft.

Emma, when I joined IMC back in 2018 it was immediately clear that your management and people skills were fundamental for the functioning of our group. You solved many problems and provided me as well as many others with countless pleasant conversations, when waiting for meetings or just in passing. Your advice was invaluable, and I hope you are enjoying your well-deserved retirement. Sue, you seem to have seamlessly stepped into the position left by Emma, and your aptitude in helping me plan my defense has been something I've relied on heavily. I'm wishing you all the best in your future endeavors at ASML!

Tiny, Brahim, Adelheid and Thijs. Without your effort I'm pretty sure very few, if any, of the machines in the lab would be working. Thank you for always being there to fix a problem, even if it was just with a piece of advice or some technical know-how. Adelheid, thank you for helping me with my ICP measurements and for advocating so strongly for a clean and safe work environment. Brahim, in my first year we went on a beam trip together with Jiachun and Jiaodong. You were key in making those experiments work, and this was also true back in Eindhoven. Thank you for the help with the TPR, isotherms and FTIR. Tiny, on you I've probably relied on the most in Eindhoven. You have helped me grasp the HP-FT set-up as well as the KRATOS. And were always around when something inevitably went wrong. Thank you for all that help, and for every laugh shared. Thijs, you are newer to the group, and we did not interact much, but thank you for your help in keeping the labs running as well as they do.

Then my home away from home, being part of two separate universities was challenging but it was made substantially easier effort by Ilse and Nicole. You helped me get settled into the reactor institute and were always available to help when I needed you. Michel, if not for your efforts the Mössbauer lab would not run as flawlessly and efficiently as it does. Your patient and thought through approach to solving all kinds of technical issues taught me a lot and helped me grow more comfortable with taking charge of the various parts and equipment. I learned much from you, not only technically but also scientifically, about the physics and electronics behind the Mössbauer phenomenon and equipment.

Damian and Shiyue, thank you for joining my defense as my paranymphs. Damian, you are the future of the Mössbauer representation in Eindhoven, a lot of pressure perhaps. But through our interactions in the lab, and seeing your work, I know that it is in great hands. You

Acknowledgements

tackle your project with a lot of energy and determination, and with your experimental aptitude and great mindset I'm sure you will excel. Shiyue, already early on in your project in our group we worked a lot together. Both the KRATOS and FT reactor were hotly contested equipment between the two of us and a few others. But our work in the lab was always pleasant and, on the days, where I needed to be in Delft I could always rely on you to take care of the set-ups. You have a difficult project, working with the Raney iron catalyst, but in your very capable hands I know you can bring it to a successful finish.

Keeping two offices meant many office mates came and went. Arno, and on rare occasions Peng, you kept me company though most of my time in Eindhoven. Sharing the office with you specifically Arno, was an interesting time, since you seemed to attract all kinds of pranks. You also invited me into the lunch group which made for some very entertaining afternoon breaks, so thank you. Peng, we did not talk much, but when you did come over from China, we enjoyed pleasant and thoughtful discussions about Fischer-Tropsch and Mössbauer. Thank you for that. Later I got to meet Yvette and Peerapol, I'm sorry to hear that you have left the group Yvette, I'm wishing you all the best in your future. And Peerapol best of luck with finishing your PhD! In Delft I had the pleasure of sharing an office with Michael and Xinmin, you were wonderful company, and I had some great conversations with the both of you. Xinmin best of luck with your future, and Michael I hope your start-up company continues to do well!

Arno, Sasha, Evgeny, Wilbert, Giulia, Tobias, Elisabet, Valery and Monica, the earlier mentioned lunch group, you were a big part in making me feel like at home in the IMC group, even if I never did say much. By now, most of you have successfully defended and moved on to new jobs, so I wish you all the best in your careers! Ferdy, Rim, Francesco, Dimitra, Florian, Jerome, and Anna. You all started later than me in the IMC group, and though it pains me to admit four of you will have defended before me, it was a pleasure getting to know you even over the difficult covid period. Whilst my trips to Eindhoven became few and far between, you were always there to talk to or share lunch with. Aleksei, I enjoyed our Dutch learning sessions in the lab, and I hope you are keeping it up, you were really good! Shiyue, Wei and Jiachun, together with Tobias you represent the experimental FT research in our group, and I'm thankful for having been able to discuss and work with you all. Especially Tobias you helped show me the way around various set-ups, most importantly the KRATOS and HP-FT, thank you so much for that. And Jiachun, you were there to help my experiments in the pandemic time, sharing the set-up with you was never a problem and we always made it work, thanks for that!

Acknowledgements

Not common in the acknowledgements, but I would like to apologize to Aleksei, Bart and Rim who had to share a room with me at conferences or at CAIA and succumbed to my apparent curse of making you win a bucket. To all the other members of IMC whom I've had the pleasure of meeting and working with but have not listed here, thank you for making me feel welcome.

I would also like to thank my fellow PhDs of the Mössbauer group in Delft. Maxim, you were there when I started and you, whilst you intended this or not, taught me a lot about being a PhD. You were determined and held on to your own ideas and visions, and I admired that immensely. Prasad, you struggled a lot with your project, but your perseverance was an inspiration to me as well. I'm wishing you both the very best in your future careers.

Then my parents, Tom and Linda, without you I would never have been here, and I don't just mean biologically. Your support and love throughout my entire life and education has been key in getting me to where I am today and being the person I am. I can't thank you enough for always being there for me throughout these years, you always listened even if my research sometimes sounded like witchcraft to you. Thank you for everything, I love you both very much. The rest of my family, thank you too for believing in me and listening to me during birthdays or family gatherings.

To my friends, Yoram, Jan-Paul, Willem, Jeroen and Victor. Thanks for all the good times that we shared during these 5+ years, I will always remember our festival experiences, or our city trips before that. Hanging out with you, even if just to play some games was always a great experience and helped keep me grounded throughout these years. We will have to plan another get together soon!

Then last but not least, Sebastian, we met through sheer luck on a silly online game when I started this whole project. Now 5 years later, I'm finished and set to move in with you. You gave me the love and support that I needed to soldier through this PhD project, and you never stopped believing that I could do it, even when I very much doubted it myself. You are set to start your own PhD now, and I will be ready to support you all the way like you did for me.

List of publications

Publications within the scope of this thesis

L.M. van Koppen, A.I. Dugulan, G.L. Bezemer, E.J.M. Hensen, Sintering and carbidization under simulated high conversion on a cobalt-based Fischer-Tropsch catalyst; manganese oxide as a structural promotor. *Journal of Catalysis*, 2022, **413**, 106-118.

L.M. van Koppen, A.I. Dugulan, G.L. Bezemer, E.J.M. Hensen, Elucidating deactivation of titania-supported cobalt Fischer-Tropsch catalysts under simulated high conversion conditions. *Journal of Catalysis*, 2023, **420**, 44-57.

L.M. van Koppen, A.I. Dugulan, G.L. Bezemer, E.J.M. Hensen, Manganese as a structural promoter in silica-supported cobalt Fischer-Tropsch catalysts under simulated high conversion conditions. *Journal of Catalysis – in review*.

L.M. van Koppen, A.I. Dugulan, E.J.M. Hensen, G.L. Bezemer, Tuning stability of titania-supported Fischer-Tropsch catalysts: impact of surface area and noble metal promotion. *Catalysis Today – in review*.

Publications outside the scope of this thesis

M.J. Valero Romero, J.G. Santaclara, L. Oar-Arteta, L. van Koppen, D.Y. Osadchii, J. Gascon, F. Kapteijn, Photocatalytic properties of TiO₂ and Fe-doped TiO₂ prepared by metal organic framework-mediated synthesis. *Chemical Engineering Journal*, **360**, 2019, 75-88.

A. Goryachev, A. Pustovarenko, G. Shterk, N.S. Alharji, A. Jamal, M. Albuali, L. van Koppen, I.S. Khan, A. Russkikh, A. Ramirez, T. Shoinkhorova, E.J.M. Hensen, J. Gascon, A Multi-Parametric Catalyst Screening for CO₂ Hydrogenation to Ethanol, *Chem. Cat. Chem.* **13**, 2021, 3324-3332.

J. Ren, C. Mebrathu, **L. van Koppen**, F. Martinovic, J.P. Hofmann, E.J.M. Hensen, R. Palkovits, Enhanced CO₂ methanation activity over La_{2-x}Ce_xNiO₄ perovskite-derived catalysts: Understanding the structure-performance relationships. *Chemical Engineering Journal*, **426**, 2021, 131760.

Oral presentations

L.M. van Koppen, A.I. Dugulan, G.L. Bezemer, E.J.M. Hensen, An in-situ Mössbauer Emission Spectroscopy study on manganese promotion on cobalt Fischer-Tropsch catalysts. NCC XXI, **March 2020**, Noordwijkerhout, the Netherlands.

Poster presentations

L.M. van Koppen, A.I. Dugulan, G.L. Bezemer, E.J.M. Hensen, The effect of manganese promotion on deactivation of cobalt Fischer-Tropsch catalysts supported on carbon nanofibers studied through in-situ Mössbauer Emission Spectroscopy. Catalysis: Fundamentals and Practice 2019, **July 2019**, Liverpool, the United Kingdom.

L.M. van Koppen, A.I. Dugulan, G.L. Bezemer, E.J.M. Hensen, Deactivation on titania supported cobalt catalysts; Oxidation at simulated high conversion. NCC XXIII, **May 2022**, Noordwijkerhout, the Netherlands.

Curriculum Vitae

Lukas Martin van Koppen was born in Rotterdam, the Netherlands, on January 21st, 1994. After completing his VWO education at the Sint Laurenscollege in Hillegersberg in 2012, he pursued a bachelor degree in Molecular Science and Technology (MST), a joint program by the universities of Leiden and Delft. In the second year, he chose to follow the Technology track and he completed his bachelor's thesis in the Reaction Physics and Nuclear Materials (RPNM) group of the Reactor Institute Delft at the Technische Universiteit Delft in 2015. He continued his education by enrolling in the master's program in Chemical Engineering at the Technische Universiteit Delft. His master's thesis project entitled '*Preparation of Fe/TiO₂ catalysts for non-oxidative methane conversion using metal-organic framework MIL-125(Ti) as Fe support and sacrificial template*' was carried out in the Catalysis Engineering group of prof. dr. Jorge Gascon. He successfully defended this work on April 20th, 2017. After completion of a three-month internship at Tata Steel in IJmuiden, where he developed a physical-mathematical model to describe tin-iron alloy layer formation, he obtained his master's degree in September 2017.

In February 2018, he started a PhD project in the Inorganic Materials and Catalysis group at the Technische Universiteit Eindhoven in a collaboration with the Technische Universiteit Delft and Shell Global Solutions International B.V under the supervision of prof. dr. ir. E.J.M. Hensen (Eindhoven), dr. ir. A.I. Dugulan (Delft), and dr. G.L. Bezemer (Shell). The project was focused on the development of detailed understanding of deactivation of cobalt-based Fischer-Tropsch catalysts during realistic operation conditions. The outcomes of this project, which have been presented at several conferences and published in peer-reviewed journals, have been summarized in this thesis.

